Politecnico di Torino

ScuDo
Scuola di Dottorato ~ Doctoral School
WHAT YOU ARE, TAKES YOU FAR

Doctoral Dissertation
Doctoral Program in Electrical Engineering (36^{th}cycle)

Modeling and Design of Wound-Field Synchronous Machines for Transportation Applications

Federica Graffeo

Supervisors:
Prof. S. Vaschetto, Supervisor
Prof A. Tenconi, Co-Supervisor

Politecnico di Torino
2023

I hereby declare that, the contents and organisation of this dissertation constitute my own original work and does not compromise in any way the rights of third parties, including those relating to the security of personal data.

. . . . . .

Federica Graffeo

Turin, 2023

I would like to dedicate this thesis to my loving family

Abstract

The energy transition toward a sustainable future demands adopting effective carbon-free solutions. Many governments are now focusing on achieving very low or net-zero greenhouse gas emissions by mid-century, driven by the increasing awareness of environmental concerns and the enactment of more stringent regulations. In this scenario, a significant impact on the emissions is due to the transportation sector, responsible for 23% of the global emissions of CO_2. Most of the transportation emissions are caused by cars, maritime transport, railways and heavy-duty vehicles.

In the path towards transport decarbonization, the production of green electric transport uses critical materials, including rare-earth elements. These elements are necessary for the production of permanent magnets, which are used in the majority of electric traction motors. However, the use of rare-earth elements has raised concerns related to environmental, economic, social, and technical sustainability, driving towards alternative solutions.

Wound-field synchronous machines have recently been garnering attention from the automotive industry as a compelling permanent magnet-free alternative motor, showing the potential of playing a crucial role in decarbonizing transports in the future. Wound-field synchronous motors have windings on the rotor, supplied in *dc* to generate the excitation field, replacing the role of the permanent magnets. The possibility of adjusting the excitation field simply by modifying the rotor current allows for: (i) generating high torques at low speeds without having to inject strong currents into the stator, (ii) extending the constant power speed range, maintaining high efficiencies also at high speeds, (iii) avoiding the risk of uncontrolled generations operations or demagnetization. However, the presence of a rotor current produces additional losses in the rotor and necessitates a system to bring the current to rotating parts, such as brushes and slip rings or wireless power transfer technologies.

Designing wound-field synchronous motors from scratch can be a lengthy process due to the additional degree of freedom introduced by the rotor current. This is especially true when relying on finite element tools or optimization algorithms. Although optimizations based on finite elements usually achieve the best results, the required computational burden makes this procedure impractical for fast evaluations intended for preliminary technical discussions. In this context, the main goal of this thesis is to develop a fast electromagnetic sizing procedure for salient-pole wound-field motors for traction applications. This process has been conceived to provide motor designers and engineers with a reliable and efficient way of determining the preliminary motor size, starting from a limited number of targets and constraints.

The process of designing wound-field machines requires accurate machine models able to predict the rated performance and assess the main characteristics and capabilities. Therefore, the study initially focuses on selecting the most appropriate machine modelling to be used in the sizing algorithm. In particular, an analytical model, a magnetic equivalent circuit and a parametric finite element model have been developed and compared in terms of accuracy and computational efficiency. The comparison of the three models has led to the conclusion that a combination of the analytical and finite element models represents the proper choice for the developed sizing code of wound-field motors.

The proposed sizing methodology consists of progressively increasing the air gap machine diameter until the desired performances are guaranteed while respecting the constraints. The process is achieved following two distinct steps. Initially, strictly analytical equations are used to establish a preliminary geometry under no-load conditions and in a negligible computational time. The obtained geometry is subsequently further refined through finite element simulations to ensure the rated load performances. Therefore, starting from the analytically sized lamination geometry, the second step only requires a limited computational time, albeit using finite element simulations. The proposed methodology is validated considering, as a case study, a reversely engineered salient-pole wound field traction motor, specifically the electric motor equipping the Renault ZOE.

The final part of the thesis deals with the methodology for developing lumped parameter thermal networks for synchronous machines, focusing on the identification of the parameters by means of experimental and optimization approaches.

Contents

List of Figures

List of Tables

Nomenclature

Roman Symbols

$\overline{E}$	Stator back e.m.f. phasor, (V)
$\overline{I_d}$	d-axis current phasor, (A)
$\overline{I_q}$	q-axis current phasor, (A)
$\overline{I}$	Stator current phasor, (A)
$\overline{V}$	Stator voltage phasor, (V)
$\mathbf{i}$	Current vector, (A)
$\mathbf{L}$	Inductance matrix, (H)
$\mathbf{M}$	Mutual inductance matrix, (H)
$\mathbf{R}$	Resistance matrix, (Ω)
$\mathbf{v}$	Voltage vector, (V)
C	Path of the circulation
A_s	Stator linear current density, (A/m)
AT	Ampere-Turns, (A)
AT_g	m.m.f. drop in the air gap, (A)
AT_t	m.m.f. drop in the stator teeth, (A)
AT_{gt}	Sum of the m.m.f. drop in air gap and in the stator teeth, (A)
AT_{rp}	m.m.f. drop in the rotor pole, (A)
AT_{ry}	m.m.f. drop in the rotor yoke, (A)
AT_{sy}	m.m.f. in the stator yoke, (A)

B Magnetic flux density, (T)

B_d d-axis magnetic flux density, (T)

B_g Air gap magnetic flux density, (T)

B_q q-axis magnetic flux density, (T)

B_s Magnetic flux density in the stator slot, (T)

B_t Magnetic flux density in the stator tooth, (T)

B_{g1} Fundamental value of the air gap flux density, (T)

B_{rp} Magnetic flux density in the rotor pole, (T)

B_{ry} Magnetic flux density in the rotor yoke, (T)

B_{sy} Magnetic flux density in the stator yoke, (Wb)

B_{t0} Magnetic flux density in the stator tooth portion closer to the air gap, (T)

C_s Machine constant, $(\mathrm{kVAmin/m^3})$

D_g Diameter at the air gap centre, (m)

D_{ri} Rotor inner diameter, (m)

D_{so} Stator outer diameter, (m)

D_{sy} Diameter at the centre of the yoke, (m)

dl Infinitesimal element of the circulation path, (m)

$e.m.f.$ Electromotive Force, (V)

E_s No-Load Stator Voltage, (V)

f Frequency, (Hz)

g Air gap length, (m)

g_0 Minimum air gap length, (m)

H Magnetic field, (A/m)

h_1 Inner tooth height, (m)

h_2 Tooth tip height, (m)

h_{p1} Rotor pole body length, (m)

H_p Magnetic field in the rotor pole, (A/m)

h_p Rotor pole length, (m)

h_{re} Lateral height of the rotor tip, (m)

H_{ry} Magnetic field in the rotor yoke, (A/m)

h_{ry} Height of the rotor yoke, (m)

h_{ry} Rotor yoke height, (m)

H_{st} Magnetic field in the stator tooth, (A/m)

h_{st} Stator tooth height, (m)

h_{sy} Stator yoke height, (m)

h_{us} Stator slot height occupied by the conductor, (m)

I_d d-axis current, (A)

I_q q-axis current, (A)

I_r Rotor current, (A)

I_{sc} Short-circuit current, (A)

J_r Rotor current density, (A/m^2)

J_s Stator current density, (A/m^2)

k_w Winding factor

k_b Portion of one electric pole occupied by the pole tip

k_{st} Lamination stacking factor

L Axial length, (m)

l Length, (m)

L_d d-axis inductance, (H)

L_q q-axis inductance, (H)

L_r Rotor inductance, (H)

L_σ Leakage inductance, (H)

L_{md} d-axis magnetizing inductance, (H)

L_{mq} q-axis magnetizing inductance, (H)

$m.m.f.$ Magnetomotive Force, (A)

M_{sr}	Mutual inductance between the stator and the rotor, (H)
N	Discretized layers of the stator tooth
n	Rotational speed, (rpm)
N_1	Stator equivalent number of turns in series per phase
N_r	Number of rotor coil turns per pole
N_s	Number of stator slots
N_y	Discretized layers of the air gap circumference
p	Pole pairs
P_{sf}	Permenace of the fringing air gap flux tube, (H)
p_{ss}	Specific permeance of the stator slot, (H/m)
P_{st}	Permenace of the main air gap flux tube, (H)
R_m	Magnetic reluctance, (H^{-1})
R_r	Rotor resistance, (Ω)
R_s	Stator resistance, (Ω)
R_{ss}	Stator slot magnetic reluctance, (H^{-1})
R_{st}	Stator tooth magnetic reluctance, (H^{-1})
R_{sy}	Stator yoke magnetic reluctance, (H^{-1})
S	Surface, (m^2)
S_n	Rated apparent power, (VA)
S_{rs}	Rotor slot surface, (m^2)
S_{ss}	Stator slot surface, (m^2)
T	Electromagnetic torque, (Nm)
V_d	d-axis voltage, (V)
V_q	q-axis voltage, (V)
V_r	Rotor voltage, (V)
V_s	Stator Voltage, (V)
w_s	Stator slot width, (m)

w_{cu} Rotor winding distance from tip, (m)

w_p Width of the pole, (m)

w_{s1} Bottom stator slot width, (m)

w_{s2} Top stator slot width, (m)

w_{st0} Stator tooth width at the air gap, (m)

w_{st} Stator tooth width, (m)

X_d d-axis reactance, (Ω)

X_q q-axis reactance, (Ω)

Z_c Turns in series per slot

Greek Symbols

α Potier coefficient

$\boldsymbol{\lambda}$ Flux linkage vector, (Vs)

$\boldsymbol{\Omega}$ Speed matrix, (rad/s)

$\cos\varphi$ Power factor

Λ_d d-axis flux linkage, (Vs)

Λ_q q-axis flux linkage, (Vs)

Λ_r Rotor flux linkage, (Vs)

μ_0 Vacuum permeability, (H/m)

$\mu_{r,st}$ Relative permeability of the stator tooth, (H/m)

$\mu_{r,sy}$ Relative permeability of the stator yoke, (H/m)

ω Electrical speed, (rad/s)

Φ_p Magnetic flux per pole, (Wb)

Φ_s Magnetic flux in the stator slot, (Wb)

Φ_t Magnetic flux in the stator tooth, (Wb)

Φ_{sp} Magnetic flux relative to one slot pitch, (Wb)

τ_s Slot pitch

θ Mechanical angle, (rad)

θ_e Electrical angle, (rad)

k_C Carter factor

Thermal Symbols

α_{th} Thermal diffusivity, $(\mathrm{m}^2/\mathrm{s})$

β Expansion coefficient, $(1/^\circ\mathrm{C})$

ε_r Emissivity coefficient

μ Fluid dynamic viscosity, $(\mathrm{kg}/\mathrm{s}/\mathrm{m})$

ν Fluid speed, (m/s)

ν_k Kinematic viscosity, $(\mathrm{m}^2/\mathrm{s})$

ρ Fluid density, $(\mathrm{kg}/\mathrm{m}^3)$

σ_c Stefan-Boltzmann constant, $(\mathrm{W}/\mathrm{m}^2/\mathrm{K}^4)$

ϑ_{ag} Temperature of the air gap, $(^\circ\mathrm{C})$

ϑ_a Ambient temperature, $(^\circ\mathrm{C})$

$\vartheta_{Cu,r}$ Temperature of the rotor copper, $(^\circ\mathrm{C})$

$\vartheta_{Cu,s}$ Temperature of the stator copper, $(^\circ\mathrm{C})$

ϑ_{hsg} Temperature of the housing, $(^\circ\mathrm{C})$

ϑ_{rot} Temperature of the rotor core, $(^\circ\mathrm{C})$

ϑ_{sy} Temperature of the stator yoke, $(^\circ\mathrm{C})$

$C_{Cu,r}$ Thermal capacitance of the rotor winding, $(\mathrm{J}/^\circ\mathrm{C})$

$C_{Cu,s}$ Thermal capacitance of the stator winding, $(\mathrm{J}/^\circ\mathrm{C})$

C_{hsg} Thermal capacitance of the housing, $(\mathrm{J}/^\circ\mathrm{C})$

c_p Specific heat capacity of the considered motor part, $(\mathrm{kg}/\mathrm{m}^3)$

C_{rot} Thermal capacitance of the rotor, $(\mathrm{J}/^\circ\mathrm{C})$

C_{shaft} Thermal capacitance of the shaft, $(\mathrm{J}/^\circ\mathrm{C})$

C_{sy} Thermal capacitance of the stator yoke, $(\mathrm{J}/^\circ\mathrm{C})$

C_{teeth} Thermal capacitance of the stator teeth, $(\mathrm{J}/^\circ\mathrm{C})$

C_{th} Generic thermal capacitance, $(\mathrm{J}/^\circ\mathrm{C})$

g_a Gravitational acceleration, $(\mathrm{m/s^2})$

h_c Thermal conduction coefficient, $(\mathrm{W/K/m^2})$

h_r Thermal radiation coefficient, $(\mathrm{W/K/m^2})$

h_{ag} Thermal forced convection coefficient of the air, $(\mathrm{W/m^2/K})$

h_{hsg} Height of the housing, (m)

h_{PM} Height of the permanent magnet, (m)

k_{air} Thermal conduction coefficient of the air, $(\mathrm{W/m/K})$

k_{ir} Thermal conduction coefficient of the iron, $(\mathrm{W/m/K})$

k_{PM} Portion of one electric pole occupied by the permanent magnet

L_{shaft} Shaft length, (m)

n_{teeth} Number of stator teeth

Nu Nusselt number

$P_{Fe,r}$ Iron losses on the rotor, (W)

$P_{Fe,s}$ Iron losses on the stator, (W)

$P_{J,r}$ Rotor Joule losses, (W)

$P_{J,s}$ Stator Joule losses, (W)

P_{PM} Rotor losses on permanent magnets, (W)

P_{rot} Rotor losses of PM machines, (W)

Pr Prandtl number

q_r Surface heat density, $(\mathrm{W/m^2})$

R_{airgap} Convection thermal resistance of the air gap, $(^\circ\mathrm{C/W})$

$R_{Cu,r}$ Thermal resistance between rotor winding and rotor core, $(^\circ\mathrm{C/W})$

$R_{Cu,s}$ Thermal resistance between stator winding and stator core, $(^\circ\mathrm{C/W})$

R_{hsg} Convection thermal resistance between housing and ambient, $(^\circ\mathrm{C/W})$

R_{ig} Radial thermal resistance of the interface gap between stator core and housing, $(^\circ\mathrm{C/W})$

R_{shaft} Axial thermal resistance of the shaft, $(^\circ\mathrm{C/W})$

R_{sy1} Radial thermal resistance of the inner half of the stator yoke, $(^{\circ}\mathrm{C/W})$

R_{sy2} Radial thermal resistance of the outer half of the stator yoke, $(^{\circ}\mathrm{C/W})$

R_{teeth} Radial thermal resistance of the stator teeth, $(^{\circ}\mathrm{C/W})$

Ra_f Rayleigh number of front surface

Ra_l Rayleigh number of lateral surface

Re Reynolds number

Re_{cr} Critical Reynolds number

S_{tooth} Cross-sectional area of one stator tooth, (m^2)

v Volume of the considered motor part, (m^3)

v_{hsg} Volume of the housing, (m^3)

v_{PM} Volume of the permanent magnets, (m^3)

v_{ry} Volume of the rotor yoke, (m^3)

v_{shaft} Volume of the shaft, (m^3)

v_{sy} Volume of the stator yoke, (m^3)

v_{teeth} Volume of the stator teeth, (m^3)

Acronyms / Abbreviations

BBW Brake By Wire

CFD Computational Fluid Dynamic

DC Direct Current

EU European Union

EV Electric Vehicles

FE Finite Elements

GDP Gross Domestic Product

GHG Greenhouse Gas

HDV Heavy-Duty Vehicles

IM Induction Motor

IPM Interior Permanent Magnet

LPTN Lumped Parameter Thermal network

MEC Magnetic Equivalent Circuit

MTPA Maximum Torque Per Ampere

PM Permanent Magnet

PSO Particle Swarm Optimization

REE Rare-Earth Elements

SRM Switched Reluctance Motor

SynRM Synchronous Reluctance Motor

US United States

WFSM Wound-Field Synchronous Motor

Chapter 1

Introduction

1.1 Background

Nowadays, many jurisdictions are focused on achieving very low or net-zero greenhouse gas (GHG) emissions by mid-century, driven by growing environmental awareness and more stringent regulations [1]. According to the International Energy Agency, global energy-related CO_2 emissions grew by 0.9% in 2022, reaching a new high of over 36.8 Gt, as depicted in Fig.1.1. Compared to the growth of the global Gross Domestic Product (GDP) of 3.2%, the resulting growth of CO_2 emissions in 2022 was significantly lower, a trend that had been in place for a decade until 2021.

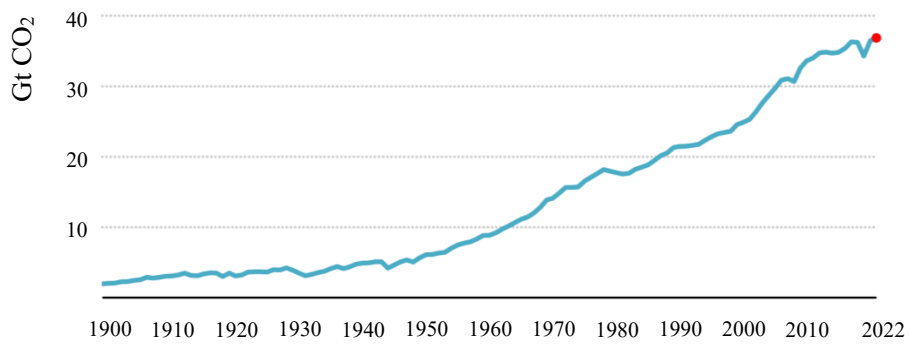

Fig. 1.1 Global CO2 emissions from energy combustion and industrial processes and their annual change, 1900-2022 [2].

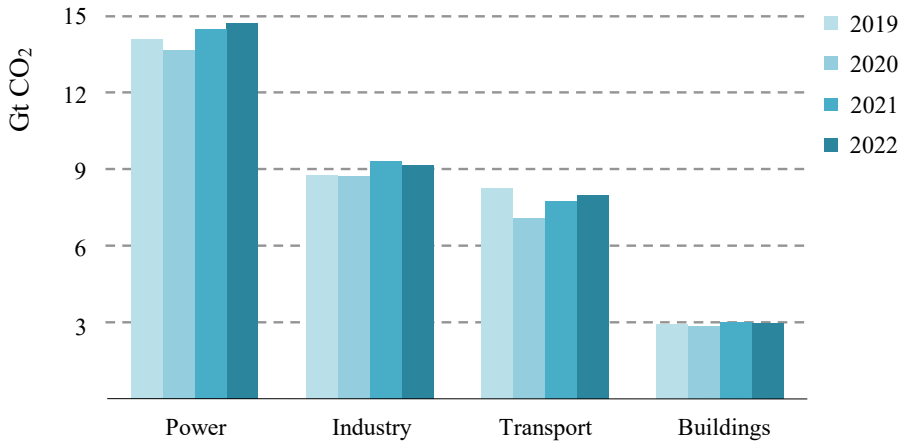

Fig. 1.2 Global CO_2 emissions by sector, 2019-2022 [2].

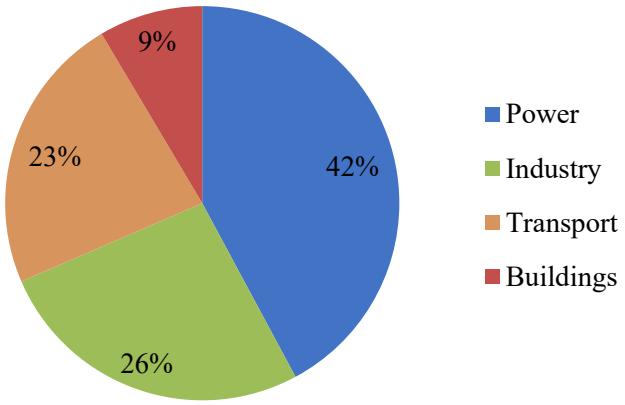

Fig. 1.3 Global CO_2 emissions by sector, 2022.

Increased deployment of clean energy technologies such as renewables, electric vehicles, and heat pumps helped prevent an additional 550 Mt in CO_2 emissions, despite gas-to-coal switching in many countries [2]. In this scenario, a significant impact on the emissions is due to the transportation sector, as shown in Fig.1.2 for the years 2019-2022. Based on the data for the year 2022, it is possible to extrapolate the pie-chart of Fig.1.3, concluding that the impact of the transportation sector on the global CO_2 emissions is 23%. According to a study of Transport & Environment, whilst for sectors like power, there is a clear commitment by the European Union (EU) to decarbonise by 2050, transport emissions are the only sector whose emissions are above 1990 levels, and officially, the EU still assumes transport emissions will only decrease by 60% [3].

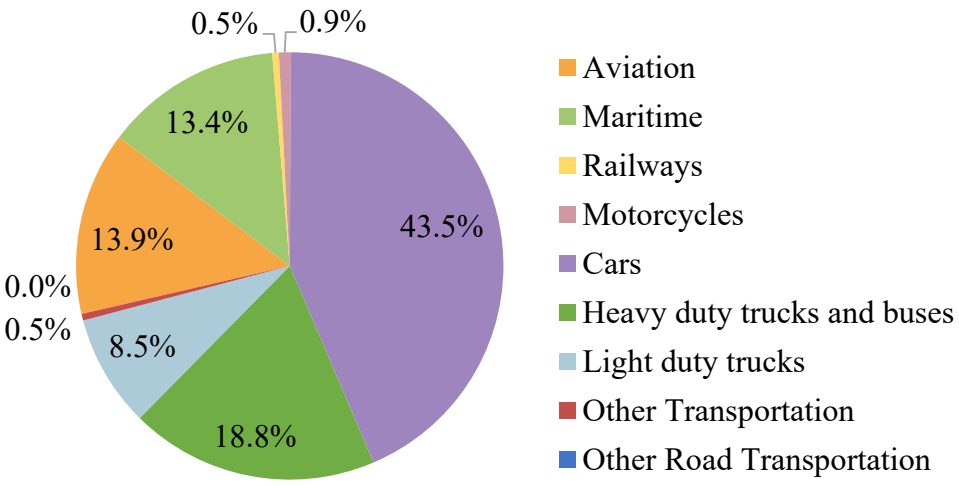

Fig. 1.4 EU GHG transport emissions share, 2019.

Figure 1.4 depicts the share of transport emissions in the EU for 2019; the data are shared by the European Environment Agency [4]. The chart shows how the majority of the emissions are caused by cars, maritime transport, aviation and heavy-duty vehicles. Although all sectors are important, the data show that decarbonising cars must represent a priority, also considering that the technology is already available. In 2017, the European Federation for Transport and Environment compared conventional diesel vehicles to Electric Vehicles (EVs) charging using different electricity mixes across Europe. The study demonstrated that even when powered by the most carbon-intensive electricity, the EVs still emit less GHG [5].

Heavy-duty vehicles (HDV) represent around a fifth of all EU transport emissions, a quarter if only road transport is considered, and its importance is expected to increase [3]. The future of climate action depends on the development and deployment of zero-emission trucks. In February 2023, the European Commission proposed to revise the HDV CO_2 standards in order to decarbonise the sector. The revised standards would set tailpipe CO_2 reduction targets for new vehicle sales of -45% in 2030, -65% in 2035, and -90% in 2040 [6]. City buses, urban delivery transport, and equipment at ports are leaders in heavy vehicle decarbonisation, as they can be recharged at a central location or at wireless pads along the way. Transport for heavier loads and longer distances opens up new challenges, particularly concerning the weight of the battery and the high power required for fast charging. To address the issue, chargers rated 3MW are under development and grid updates are expected to meet such challenging electrical requirements [1].

Aviation emissions have been increasing in Europe since 1990 and could double or triple by 2050 [7]. Aviation is at risk of having its emissions locked in due to the growth in passenger numbers and aircraft fleet, consuming the limited carbon budget to remain within the 1.5°C and 2°C targets [3]. Moreover, although electric aeroplanes have the potential to reduce emissions considerably, there are still a multitude of technological and regulatory issues that need to be addressed before they can become viable commercial technology. These challenges include developing more efficient batteries, creating new safety standards, and building the necessary charging infrastructure [8].

Finally, shipping is one of the largest GHG emitting sectors of the global economy, responsible for about 13% of the total EU GHG emissions. This speaks to the absolute necessity of including maritime transport in the development of an EU 2050 economy-wide decarbonisation strategy and the subsequent financial, investment and regulatory decisions that will be needed [3].

1.1.1 Rare-earth elements in electric transport

In the path towards transport decarbonisation, the production of electric transport makes use of critical materials, including Rare-Earth Elements (REE). Rare-earth elements are 17 chemical elements of the periodic table, sharing similar properties and often found together in geological deposits [5]. The peculiarity of REE is the capacity of generating a strong magnetic fields in limited volumes, allowing for the production of high-quality Permanent Magnets (PMs). The application of REE-PMs in electric motors increases torque and power density, resulting in compact and high-performance machines. Although the undeniable performance benefits, the use of REE-PMs has raised concerns related to environmental, economic, social, and technical sustainability [9, 10].

Environmental unsustainability

The damaging effects on the environment that derive from the extraction and refining of rare earth metals have been extensively documented [11–13]. Mining for REE minerals generates large volumes of toxic and radioactive material, causing air and water pollution, and land contamination [14].

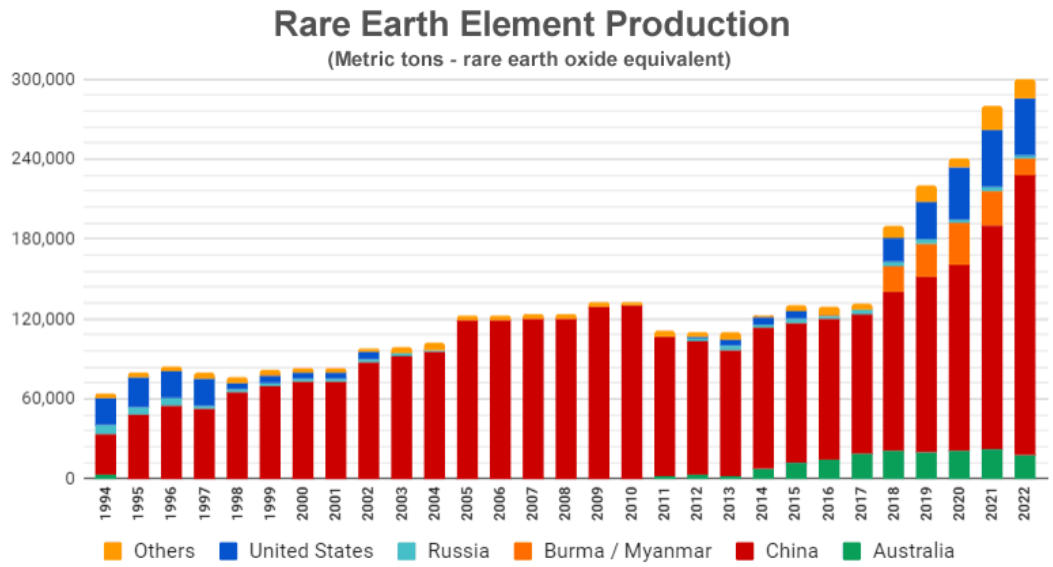

Fig. 1.5 Rare Earth Element Production Share using data from the United States Geological Survey [17].

Life cycle assessment research suggests that NdFeB magnets may be more damaging than other materials commonly used in electrical machines per unit mass. Although the actual environmental impact of NdFeB magnets may be still unclear, their elimination could still reduce the environmental footprint of electric traction motor manufacture, which in turn would reduce the environmental footprint of electrified transports [15]. In any case, mitigation of this phenomenon needs to be achieved through emission treatment technologies and also recycling of chemicals, closing illegal mines and raising environmental standards and regulations [16].

Unstable supply and fluctuation prices

Rare-earth elements are typically found in low concentrations and often mixed with other materials, making them difficult and expensive to mine. Their availability has raised concerns over the years and varies depending on the type of rare-earth element: the US Department of Energy identified a risk of supply conditions for Neodymium and Dysprosium, two of the principal components of PM motors [5].

Moreover, the total market capitalization of REE is mostly driven by China, which supplies about 80% of the available rare-earth minerals [5, 18]. This is well evident by looking at Fig.1.5. The lack of diversified suppliers and issues over availability make the REE market more prone to shocks, which is a concern for REE

buyers. Indeed, prices of rare-earth elements have experienced great fluctuations in recent years. In 2010-2011 a 12-fold increase was observed, mainly initiated by a strong reduction of Chinese exports and geopolitical tensions in a period of high demand [19].

Regardless of the final price of rare-earth magnets, it is generally acknowledged that their elimination from electrical machines will lead to a reduction in costs [20]. However, in choosing PM-free alternatives, attention must be paid not to shift the cost benefit to other components, e.g. power electronics and battery.

Performance & Safety

Although rare-earth magnets enable electric motors to achieve high torque density, some other performance aspects must be taken into account. First of all, their performances are temperature-dependent and generally worse with higher temperatures. The PMs are at risk for demagnetization, a process that will lead to a drastic drop in the motor torque capability. Demagnetization will occur if the PMs exceed a certain temperature threshold (Curie temperature), or if they are exposed to a high magnetic field. Vibrations and bumps can also lead to PM damage.

Rare-earth magnets cannot be "shut down", regardless of the functioning of the electric machine. Therefore, when rotating, PMs will generate voltages in the stator terminals even without applied electrical currents. These uncontrolled generation operations lead to a number of undesirable consequences and are especially dangerous in case of fault.

Finally, it is often beneficial that electric machines feature a certain degree of flux weakening capability, which is especially welcomed by the automotive sector. Flux weakening consists of decreasing the magnetic flux, with the aim of increasing the speed, as the motor reaches the available supply voltage. The presence of PMs makes this process hard and energetically expensive, as part of the stator current vector must be used with the scope of contrasting the PM magnetic flux. Moreover, this procedure must be performed carefully to avert the risk of demagnetization.

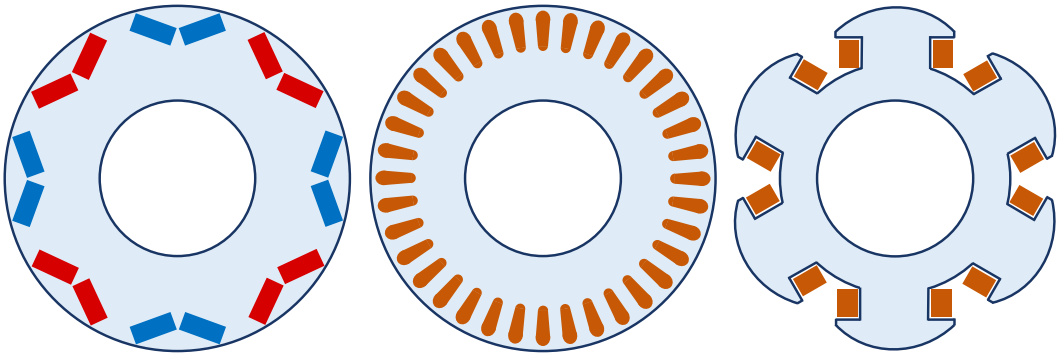

(a) (b) (c)

Fig. 1.6 Most commonly used electric motors in EVs: permanent magnet synchronous motors (a), induction motors (b), salient-pole wound-field synchronous motors (c).

1.1.2 Alternatives to REE magnets in electrical machines

Although PM motors are still the most commonly used machines in electric transport, the mentioned concerns related to REE-PMs are driving towards alternative solutions that reduce or eliminate the use of REE materials. This is especially true for electric vehicle applications, as the technology is more mature and ready for improvements. In the automotive sector, the Interior Permanent Magnet (IPM) motor, shown in Fig.1.6a, is the most preferred solution among the various PM motor topologies, as it shows important advantages in terms of output torque and constant power speed range [21]. For instance, Toyota Prius, Tesla Model 3, and Chevy Volt are equipped with IPM motors [22–24]. The two most employed PM-free alternatives are Induction Motors (IM) and salient-pole Wound-Field Synchronous Motors (WFSM), whose schematic representation is reported in Fig.1.6b and Fig.1.6c, respectively. Notable applications of IMs include the GM EV-1 vehicle and earlier models from the Tesla Motor Corporation, while applications of WFSMs can be found in the Renault ZOE and BMW iX3 [25–27]. Less common alternatives include both the topologies of reluctance motors, i.e. Synchronous Reluctance Motors (SynRMs) and Switched Reluctance Motors (SRMs), hybrid machine topologies with reduced REE materials, and ferrite-based motors. The possible alternatives to PM motors from the EV literature are discussed in the forthcoming, except for the WFSM, which is covered separately in Section 1.2.

Induction motors

Induction motors are free from permanent magnet materials. Their operating principle is based on inducing electrical currents in the rotor through the magnetic field generated by the stator currents. The induced rotor currents generate a magnetic field in turn, allowing for torque production. As the rotor current originates from the stator side, induction motors generally feature low power factors, leading to a low inverter usage factor. The absence of permanent magnets makes the IM a relatively inexpensive electric machine. Moreover, it is a well-known and reliable technology that does not need any system to bring current to the rotor side. However, rotor winding losses in induction motors result in lower efficiency and reduced cooling capabilities compared to PM motors. Improvements can be achieved with the use of a copper rotor cage instead of an aluminium one, as done by Tesla [15]. The main drawbacks of this option are the higher cost of copper and increased motor mass.

Reluctance motors

Reluctance Motors have a simple rotor structure only composed of steel laminations, without the need for permanent magnets or windings. The production of the torque is based on the particular rotor design, which exploits the physical property of magnetic flux to concentrate in the least magnetic reluctant paths.

Out of the two available topologies, synchronous reluctance motors generally use a conventional sinusoidally-fed stator, and the motor saliency allows locking the rotor to the stator magnetic field, synchronously. SynRMs are appealing in terms of robustness, high efficiency, low torque ripple, and simplicity [25]. However, they also feature a low power factor, affecting both performance and power electronic compactness, and reduced flux weakening capability.

Switched reluctance motors operate in a slightly different manner. The torque production is obtained by using the tendency of the rotor iron to reach the position of minimum reluctance. Concentrated stator windings are supplied by continuously switching coils, forcing the rotor to maintain rotation. SRMs have been shown to be robust and inexpensive to manufacture, and despite achieving high efficiency and a suitable constant power speed range, acoustic noise and torque ripple remain significant challenges to overcome.

Hybrid motors

The term "hybrid motor" is used in this document to refer to those machines that can operate with a reduced amount of REE permanent magnets. From this perspective, one possibility is to doubly excite the rotor with windings and permanent magnets. Using two excitation sources aims to combine the flux weakening capability of the WFSMs and the high efficiency and torque density of PM motors [28, 29]. Although the combination of the two sources opens up unlimited machine structures, generally, this is achieved at the expense of higher topological complexity.

Another possibility is to embed PM into a salient rotor structure, similar to SynRM rotor. Although one may categorize this motor simply as an IPM, the required amount of PMs is reduced thanks to a higher reluctance torque offered by the rotor saliency. This type of motor technology is used in the BMW i3 electric vehicle [15, 30]. However, these solutions do not eliminate the presence of PMs but only aim to decrease the required amount to different extents depending on the topology.

Ferrite-based motors

Permanent magnets can also be manufactured without the use of REE materials, turning to ferrite magnets. The ferrites are materials obtained from iron oxides and metallic elements, such as Barium or Strontium. Their main weakness is the low remanence flux density, which is about one-third of REE magnets. This poses a major obstacle to achieving competitive torque densities. A possible solution includes concentrating the flux from multiple magnets and exploiting rotor saliency to obtain reluctance torque. These machines are generally referred to as "PM-assisted motors", and it is worth noticing that they show improved efficiency and power factor with respect to induction motors [31]. However, ferrites have low coercivity, about one-fifth to one-third of REE magnets. Consequently, they are more susceptible to demagnetization risks. However, differently from REE magnets, the ferrite coercivity increases with temperature, making them less sensitive to sudden demagnetization. Additionally, their Curie temperature is higher than REE magnets.

1.2 The Wound-Field Synchronous Motor in traction applications

Wound-field synchronous motors have windings on the rotor, which are supplied in *dc* to generate the excitation field, eliminating the need for permanent magnets. The possibility of adjusting the excitation field simply by modifying the rotor current brings numerous advantages.

1.2.1 WFSM benefits

High torque at low speeds

The first advantage of the complete controllability over the excitation field is the ability to generate high torques at low speeds, without having to inject strong currents into the stator. Indeed, in the absence of the rotor winding, the maximum torque is limited by the current rating of the source. In the case of inverter-fed motors, oversizing the latter is often the solution adopted by designers to deal with the issue, with an inevitable increase in costs [32].

High power factor

Moreover, it is possible to regulate the reactive power exchanged by the machine through the rotor current and the value of the induced electromotive force associated with it. A high power factor enables to reduction of the section of the conductors of the stator winding and the size of the DC-link capacitor, with a clear saving in economic terms on the entire powertrain [33].

Extended constant power speed range

Wound-field machines feature a very wide speed range in which they can operate at constant power. In fact, by controlling the rotor current, it is possible to easily reduce the magnetic flux, resulting in optimal flux weakening capability [34].

Safety

Uncontrolled generations operations, discussed in Section 1.1.1, are avoided as the source of excitation can be easily removed by opening the rotor winding terminals.

1.2.2 WFSM limitations

Limited cooling capability

Similarly to IMs, the presence of a rotor current produces additional losses in the rotor. The heat extraction from the rotor conductors may become a limiting factor. However, with a well-planned design project and a control strategy in place, overheating can be prevented.

Additional switching devices

A further drawback is that additional switching devices are needed in the power electronics in order to control the *dc* rotor current, resulting in increased system complexity and, therefore, cost.

Supplying of rotating parts

The necessity to bring current to rotating parts may be the most limiting factor in WFMS's popularity in traction applications. This task has been historically accomplished by stationary carbon brushes in contact with rotating conductive rings. This technology generally arouses concerns about reliability and wear. However, unlike the commutators of DC machines, the brushes and slip rings of WFSMs are supplied with relatively low *dc* power, making their wear compatible with the requirements of transportation applications. Moreover, this limitation can be overcome by using wireless power transfer systems (see Section 1.2.3), as amply demonstrated in the context of aircraft on-board auxiliary generation [35, 36].

1.2.3 Excitation systems

A fundamental component of wound-field synchronous machines is the selected technology to excite the rotating rotor from the stationary source. The most common and economic excitation system consists of sliding contacts between stationary graphite brushes and rotating slip rings, which are also preferred when a fast dynamic response is needed. For instance, Renault successfully mounts brushes and slip rings to supply the rotor of the ZOE motor (see Chapter 5). However, sliding contacts generally cause concerns about maintenance and safety due to brush wear and possible sparking.

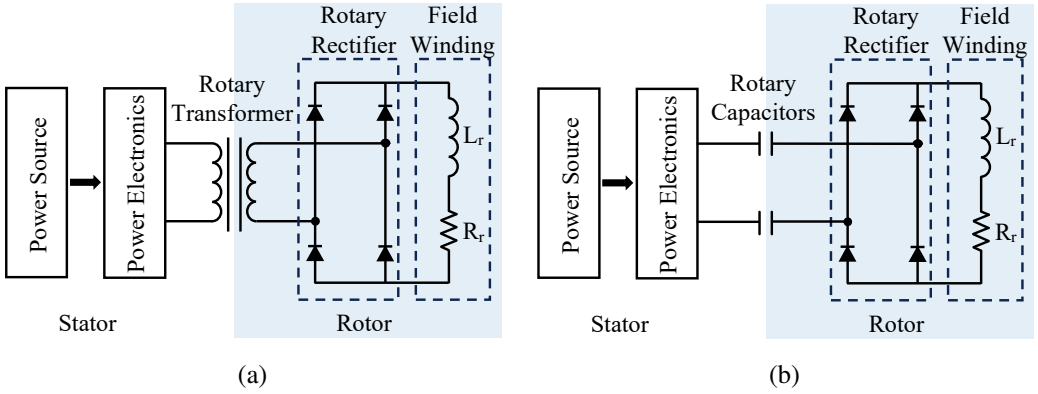

Fig. 1.7 Simplified circuit of inductive (a) and capacitive (b) power transfers.

In the past two decades, the progress in power electronics and wireless technology enabled the development of brushless exciters for WFSMs, overcoming these issues [37]. For instance, Brusa Elektronik also developed a wound-field motor for traction applications, namely the SSM 6.17.12, equipped with a contactless power transfer system [38]. Nonetheless, they suffer from worse dynamic performance, hinder access to the rotor winding for measurement and protection, and require an exciter machine installed on the main motor or generator shaft [36]. Certain applications, like aircraft power generation, employ an excitation system composed of a permanent magnet generator, another electric generator (exciter), and a rotating rectifier. Nevertheless, the resulting technology is more expensive [39]. namely the SSM 6.17.12 [45]. The two most popular wireless methods to transfer power to the rotor are currently rotary transformers and rotary capacitors, shown in Fig.1.7.

Inductive power transfer

The inductive power transfer is achieved through a rotary transformer and a rotating rectifier, and they represent an efficient non-contact alternative to brushes and slip rings [40–42]. The design of rotary transformers that operate at high frequencies is challenging as leakage inductances and parasitic capacitances directly impact the power converter performance. However, recent improvements in their performance make this solution more attractive than in the past [39]. In fact, suitable positioning of the conductors allows for to reduction of the leakage inductances and to improve the coupling between the windings. As a consequence, a larger air gap can be used, easing the strict construction tolerances of various components.

Capacitive power transfer

The rotary capacitors are composed of two conductive materials (generally hoops or parallel plates) separated by a dielectric material, in which one is rotating with respect to the other. The distance and orientation of the two conductive elements remain constant. The solution is mechanically robust and does not present structural integrity problems due to high rotational speeds [43]. However, capacitive coupling needs a large surface area and a small airgap length to transfer power efficiently, causing concerns in the eventual presence of mechanical vibrations [44]. Additionally, when a motor is spray-cooled or splashed with transmission oil, the capacitive coupler poses a safety risk due to the possibility of arcing.

1.2.4 Transport applications

Wound-field synchronous machines have been most commonly used as alternators in power plant applications, because of the ease of voltage regulation, simply achieved by adjusting the rotor current. Synchronous generators produce almost 95% of the world's electricity [45]. Nonetheless, wound-field synchronous machines have recently been garnering attention from the automotive industry as a compelling PM-free alternative motor. In addition to the mentioned Renault ZOE, the BMW iX3, and Brusa Elektronik SSM 6.17.12, General Motors has reported on the design and testing of a traction WFSM with wireless power transfer exciter [46]. ZF Friedrichshafen, a German multinational company producing components for the transport industry, has also recently announced the production of wound-field synchronous motors [47]. Figure 1.8 recollects some of the mentioned commercial wound-field motors.

Apart from the automotive industry, wound-field machines are used in the naval and aviation sectors. The use of electric propulsion systems in boats provides greater flexibility in speed regulation, unlike conventional thermal solutions. Moreover, simpler drivetrain solutions can be designed, thus increasing reliability [48, 49]. In the aviation sector, the combination of WFSM and superconducting technologies is the subject of various research activities, since high torques and power densities can be obtained, paving the way towards all-electric solutions for the aerial mobility of goods and people [50].

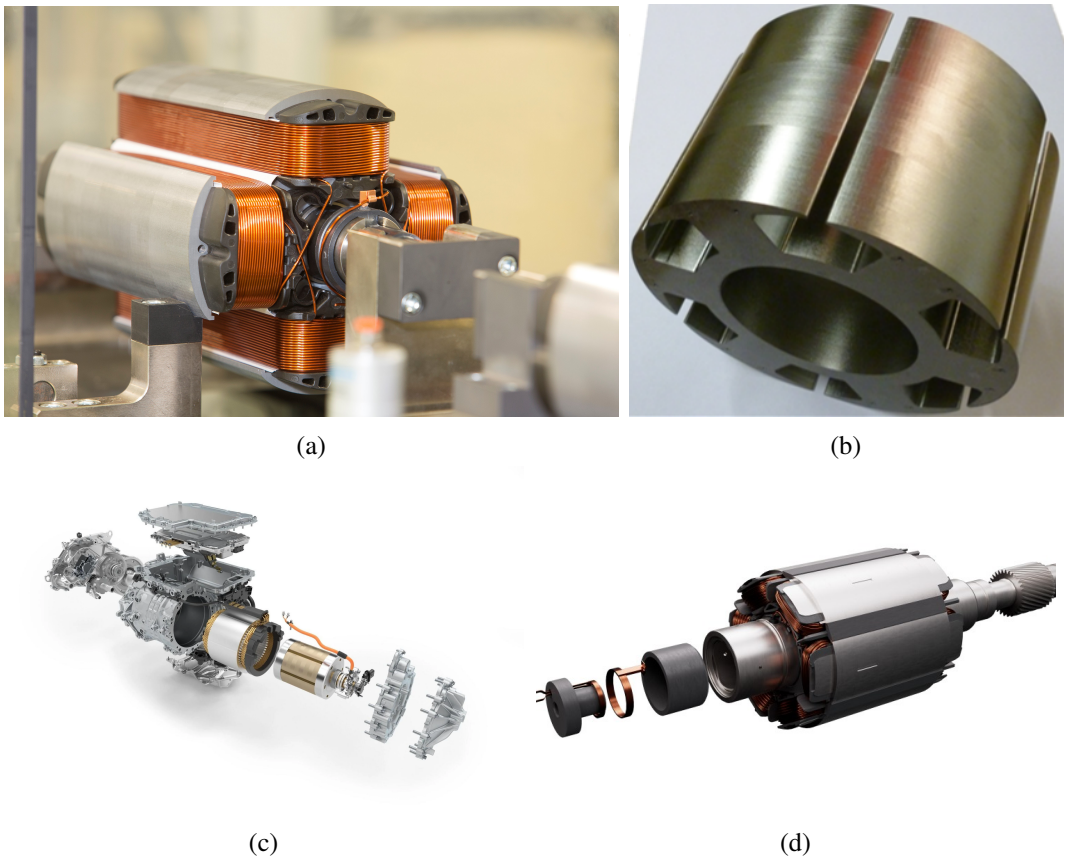

(a) (b)

(c) (d)

Fig. 1.8 Commercial WFSMs: (a) Renault Zoe [51], (b) Brusa Elektronik [38], (c) BMW iX3 motor [52], (d) ZF Friedrichshafen [47].

1.3 Reasearch objectives

In the described scenario, wound-field synchronous motors have proven to play a crucial role in decarbonizing transports, as seen in the recent trend in the automotive industry. The design of WFSMs is not a trivial task, as the third degree of freedom introduced by the rotor current significantly enlarges the design space. Designing WFSMs from scratch that cater to unique motor limitations, imposed by the specific application, can be a lengthy process, especially when relying on finite element (FE) tools or optimization algorithms. The most recent technical literature reports different design methodologies for WFSMs; however, most of them are based on finite element optimization procedures [49, 53–57]. Although optimizations based on FE simulations usually achieve the best design solution with the most accurate results, the required computational burden makes this procedure unpractical for

fast evaluations intended for preliminary technical discussions or for initial cost estimations. In this context, the aim of this thesis is to develop methodologies and fast tools for the analysis and the preliminary electromagnetic sizing of salient-pole wound-field synchronous motors for traction applications. The contributions of this study are recollected in seven chapters.

- Chapter 1 presented the current environmental and technological background, clearing the reasons that motivate this research to investigate salient-pole wound-field synchronous motors and to develop tools for the analysis and sizing.
- Chapter 2 focuses on the wound-field synchronous machine technology, highlighting specific structural and modelling aspects, representing the key elements for the development of the research objectives.
- Chapter 3 reports the adopted and developed analysis methodologies for wound-field machines. The explanation of the proposed machine models includes analytical equations, the magnetic equivalent circuit approach, and finally, the parametric finite element method.
- Chapter 4 describes the WFSM sizing procedure proposed by this research. The methodology is thoroughly explained, starting from the general algorithm flow and proceeding to the employed analytical equations supported by the machine finite element model.
- Chapter 5 deals with the validation of the sizing procedure. The commercial traction motor of the Renault ZOE is used as a baseline for the verification. The chapter also includes the analysis and reverse engineering of the ZOE sample, along with the conducted experimental tests.
- Chapter 6 focuses on electric machine thermal aspects, in particular presenting methodologies for the definition of the parameters of thermal models based on the lumped parameter thermal network approach.
- Chapter 7 draws the conclusion and reports possible future works.

Chapter 2

The Wound-Field Synchronous Machine

The wound-field synchronous machines are a well-known technology, as they have been historically used as generators for power plant applications. The principle of operation is based on the law of magnetic induction resulting from a uniform movement of relative rotation between an inductive magnetic field and a system of induced conductors properly connected. The electromechanical conversion is obtained by the interaction between the stator and rotor magnetic fields. The frequency (f) of the electromagnetic force (e.m.f.) induced is closely related to the rotation speed (n) and the number of pole pairs (p) of the inductor $\left(n = \frac{60f}{p}\right)$. In this chapter, noteworthy fundamentals of wound-field machines are provided for the sake of clarity. Important structural machine aspects are reported, as the particular air gap shape of salient pole-machines. Machine model and performance are therefore illustrated, together with adopted design methodologies form literature.

2.1 Structural aspects

Although detailed information about the machine structure and working principle are easily accessible through textbooks [58–60], most are intended for power plant alternators. This section reports some machine generalities from the perspective of traction motors and discusses notable structural aspects of salient-pole wound-field machines.

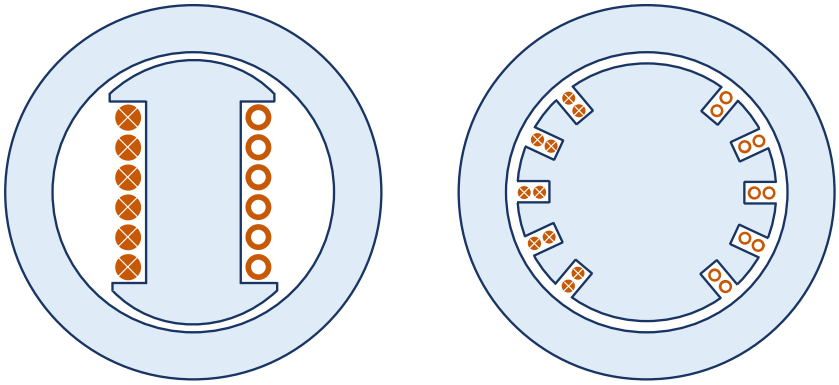

(a) (b)

Fig. 2.1 Wound field synchronous machine topologies: salient-pole (a), cylindrical rotor (b).

2.1.1 WFSM topologies

The WFSM has two possible rotor configurations: salient-pole machine, with projecting field poles, and non-salient pole machine (also called "cylindrical rotor"), without projecting field poles. The salient-pole machine presents a variable air gap, which contributes to its structural anisotropy, as depicted in Fig.2.1a. Consequently, the output torque of the salient-pole machine also includes a quota due to the machine's saliency. On the contrary, the cylindrical rotor machine (shown in Fig.2.1b) is characterized by a constant air gap, excluding the negligible contribution of the rotor slots, and therefore can be considered an isotropic machine.

The two rotor structures have been largely used in power plants with different applications. The cylindrical alternators are characterized by a more complex construction; they generally have smaller diameters and longer axial lengths, resulting in less available space to fit the poles. Thus, they are generally constructed with a low number of pole pairs (1 to 2); therefore, for a fixed frequency of 50-60Hz, they need to rotate at high rotational speeds (1500-3000rpm). Distributing the winding over the rotor surface results convenient to guaranteeing sufficient mechanical resistance, better arrangement and securing of the excitation winding [61]. The salient-pole motor is generally used for speeds around 100 to 400rpm, mainly for power stations and hydraulic turbines.

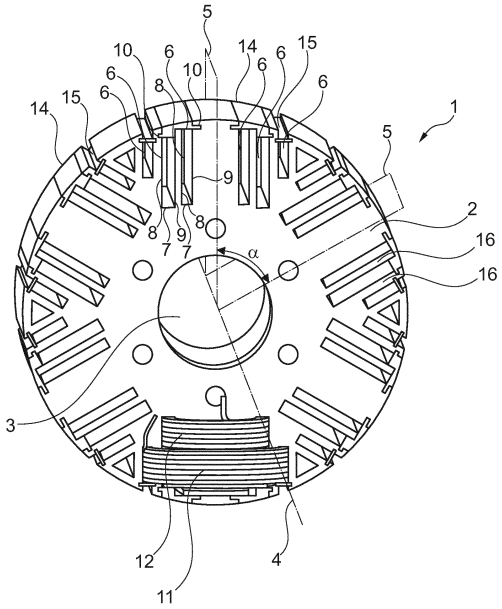

Fig. 2.2 BMW cylindrical rotor patent [62].

For what concerns the automotive application, the salient-pole motor has received more attention than its counterpart, probably because of its simple structure and the possibility of using the reluctance torque offered by the saliency. For instance, the Renault ZOE is equipped with a salient-pole synchronous motor (details are provided in Chapter 5). Brusa Elektronik and General Motors also reported on the design and testing of salient-pole WFSM [38, 46]. According to Fig.1.8c from [52] and considering [63], BMW is currently employing a salient-pole synchronous machine for its 5th-generation motors to propel the BMW iX3.

To the best author's knowledge, the cylindrical rotor machine cannot be currently found in any commercial vehicle. However, one of the first investigations of a WFSM with a cylindrical rotor as a potential solution for traction applications can be found in a 2018 patent from BMW [62]. The mentioned machine is shown in Figure 2.2.

2.1.2 Air gap of salient-pole machines

The non-constant air gap of the salient-pole machine plays a major role in the machine's performance. Different methodologies can be adopted for defining the shape of the air gap [64–67]. For instance, one common possibility is to shape the pole as a circumference, whose centre does not coincide with the machine centre but

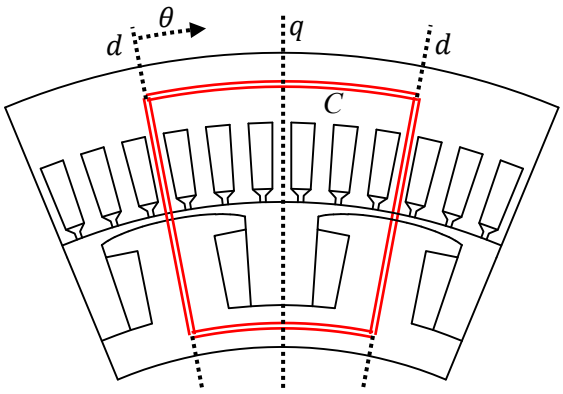

Fig. 2.3 Circulation circuit C.

generally falls into the rotor pole body. Another alternative consists of calculating the pole shaping by adopting a combination of different harmonics and optimizing according to the desired performance.

However, the solution generally adopted is to shape the air gap as the inverse of the cosine of the angle that starts from the d-axis. The machine d-axis is placed in the axis of minimum reluctance, i.e. through the centre of the pole body, as shown in Fig.2.3; the q-axis is electrically perpendicular to the d-axis. To understand the reason for this shaping, let's take into account Ampere's circuital law, which relates the circulation of a magnetic field around a closed loop to the electric current passing through the loop surface. The formulation is reported in equation (2.1), where C is the path of the circulation, H is the magnetic field, dl is the infinitesimal element of C, NI is the total current passing through C.

$$\oint_C H \cdot dl = NI \tag{2.1}$$

Let's apply Ampere's law to a salient-pole machine considering as circulation circuit the one shown in Fig.2.3, and suppose to supply the rotor turns N_r with the dc current I_r. In the hypothesis of negligible magneto motive force (mmf) required to magnetize the iron, the value of the air gap magnetic flux density B at the position θ of Fig.2.3 can be obtained.

$$H(\theta_e) \cdot g(\theta_e) = N_r \cdot I_r \quad \Rightarrow \quad B(\theta_e) = \frac{N_r \cdot I_r \cdot \mu_0}{g(\theta_e)} \tag{2.2}$$

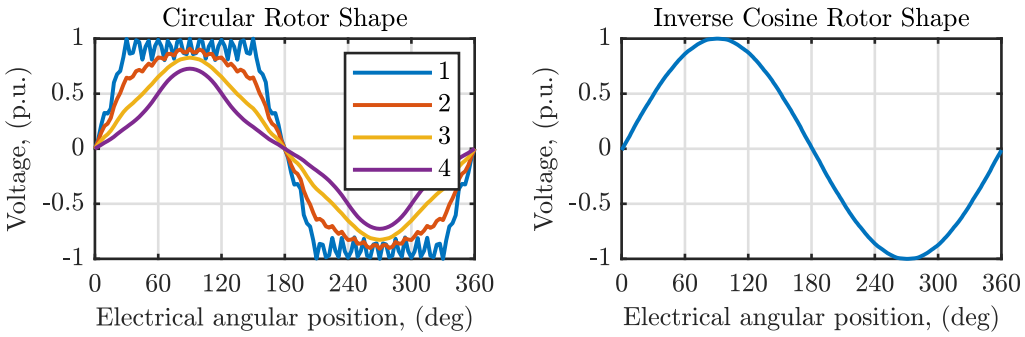

Fig. 2.4 No-load induced voltage for circular and inverse cosine rotor shape.

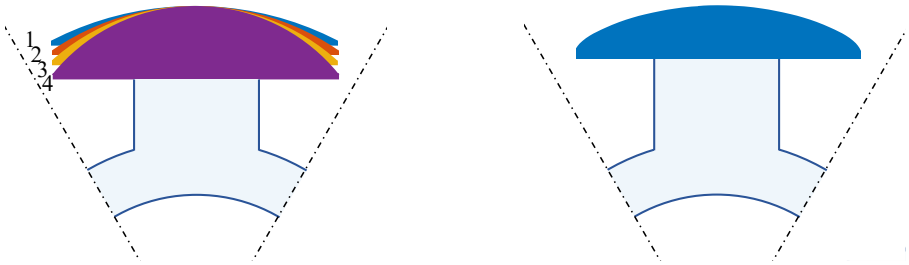

Fig. 2.5 Circular and inverse cosine rotor shape.

In equation (2.2), θ_e is the electrical angle $p \cdot \theta$, g is the air gap length, μ_0 is the vacuum permeability. Thus, the rotor can produce a sinusoidal waveform of B in the air gap (cosinusoidal for θ) only if the air gap length is shaped as in equation (2.3), resulting in a sinusoidal induced stator voltage.

$$g(\theta_e) = \frac{g_0}{\cos(\theta_e)} \qquad if \;\; 0 \leq \theta_e \leq \frac{\pi}{2} \tag{2.3}$$

For instance, Fig.2.4 shows the induced stator voltage for a circular and inverse cosine of the rotor pole shape in a demonstrative case study obtained through finite elements simulations. In particular, the effects of the circular shape rotor are reported for different centres of the circumference; going from 1 to 4, the centre tends to approach the air gap, as depicted in Fig.2.5. The reported results show how a more sinusoidal waveform is obtained by shaping the air gap as the inverse cosine of θ.

2.2 Steady-state model in *dq*-axes

The *dq*-model in steady-state conditions is used in the forthcoming chapters for the analysis and design of wound-field synchronous machines. Electrical machines are generally modelled through the electric and magnetic equations of the rotor and of the three phases of the stator. The equations can be expressed in vector form, in which the instantaneous values of any variables can be obtained as projections of the vector onto the magnetic axis of the corresponding phase. However, a simplification of the model can be obtained if the stationary frame of the three-phase windings (*abc*-frame) is replaced with an equivalent system of two-phase rotating windings (*dq*-frame). This can be achieved by applying the *abc*-$\alpha\beta$ and $\alpha\beta$-*dq* transformations [68, 69].

The transformation adopted in this research is amplitude-invariant. The used *dq*-frame model is individuated for sinusoidal steady-state conditions. The electric and magnetic matrix vectorial equations are reported in (2.4). Note that while the electric equations are always valid in steady-state conditions, the magnetic equations consider constant inductances, thus neglecting the saturation effects.

$$\begin{cases} \mathbf{v} = \mathbf{R}\mathbf{i} + \boldsymbol{\Omega}\boldsymbol{\lambda} \\ \boldsymbol{\lambda} = \mathbf{L}\mathbf{i} + \mathbf{M}\mathbf{i} \end{cases} \tag{2.4}$$

The vectors of the voltage, current and flux linkages are expressed in terms of the *d*-axis, *q*-axis and rotor components, as in (2.5).

$$\mathbf{v} = \begin{bmatrix} V_d \\ V_q \\ V_r \end{bmatrix}, \qquad \mathbf{i} = \begin{bmatrix} I_d \\ I_q \\ I_r \end{bmatrix}, \qquad \boldsymbol{\lambda} = \begin{bmatrix} \Lambda_d \\ \Lambda_q \\ \Lambda_r \end{bmatrix} \tag{2.5}$$

The resistance, speed, inductance and mutual inductance matrices are reported in equations (2.6) and (2.7), where R_s is the stator resistance, R_r is the rotor resistance, $\omega = 2\pi f$ is the electrical speed, L_d and L_q are the *d*- and *q*-axis inductances, L_r is the rotor inductance, M_{sr} is the mutual inductance between the stator and the rotor. Note that the cross-coupling inductances have been neglected.

$$\mathbf{R} = \begin{bmatrix} R_s & 0 & 0 \\ 0 & R_s & 0 \\ 0 & 0 & R_r \end{bmatrix}, \qquad \mathbf{\Omega} = \begin{bmatrix} 0 & -\omega & 0 \\ \omega & 0 & 0 \\ 0 & 0 & 0 \end{bmatrix} \tag{2.6}$$

$$\mathbf{L} = \begin{bmatrix} L_d & 0 & 0 \\ 0 & L_q & 0 \\ 0 & 0 & L_r \end{bmatrix}, \qquad \mathbf{M} = \begin{bmatrix} 0 & 0 & M_{sr} \\ 0 & 0 & 0 \\ M_{sr} & 0 & 0 \end{bmatrix} \tag{2.7}$$

The system of equations derived from (2.4) is reported in (2.8).

$$\begin{cases} V_d = R_s \cdot I_d - \omega \cdot \Lambda_q \\ V_q = R_s \cdot I_q + \omega \cdot \Lambda_d \\ V_r = R_r \cdot I_r \end{cases} \qquad \begin{cases} \Lambda_d = L_d \cdot I_d + M_{sr} \cdot I_r \\ \Lambda_q = L_q \cdot I_q \\ \Lambda_r = L_r \cdot I_r + M_{sr} \cdot I_d \end{cases} \tag{2.8}$$

Considering only the stator equations and substituting the magnetic equations into the electric ones:

$$\begin{cases} V_d = R_s \cdot I_d - \omega \cdot L_q \cdot I_q \\ V_q = R_s \cdot I_q + \omega \cdot L_d \cdot I_d + \omega \cdot M_{sr} \cdot I_r \end{cases} \tag{2.9}$$

Therefore, the stator equations can be written in the form of phasors and visualized in the diagram of Fig.2.6.

$$\overline{V} = \overline{E} + R_s \cdot \overline{I} + jX_d\overline{I_d} + jX_q\overline{I_q} \tag{2.10}$$

In equation (2.11), $\overline{E}$ is the induced no-load voltage, and it is considered:

$$\overline{I_d} = I_d + j0, \qquad \overline{I_q} = 0 + jI_q, \qquad \overline{E} = j\omega M_{sr} I_r \tag{2.11}$$

$$X_d = \omega L_d, \qquad X_q = \omega L_q \tag{2.12}$$

The parameters L_d, L_q are the sum of two contributions: the leakage inductance and the magnetizing inductance.

$$L_d = L_\sigma + L_{md}, \qquad L_q = L_\sigma + L_{mq} \tag{2.13}$$

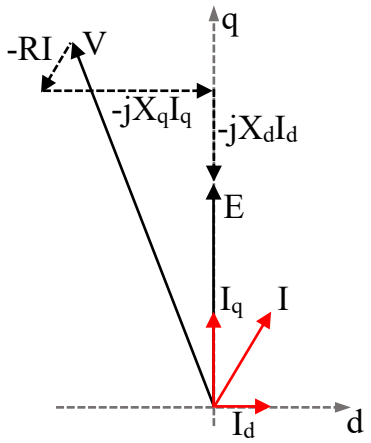

Fig. 2.6 Generic phasor diagram of wound-field motors.

Electromagnetic output torque

In the *dq*-frame, the output torque can be obtained through equation (2.14).

$$T = \frac{3}{2} \cdot p \cdot (\Lambda_d \cdot I_q - \Lambda_q \cdot I_d) \tag{2.14}$$

Substituting Λ_d and Λ_q into equation (2.14), the output torque can be alternatively written as in (2.15).

$$T = \frac{3}{2} \cdot p \cdot (M_{sr} \cdot I_r \cdot I_q + (L_d - L_q) \cdot I_d \cdot I_q) \tag{2.15}$$

Significant considerations can be extrapolated starting from the torque formulation in (2.15). The output torque is composed of two terms: the torque due to the excitation field and the torque due to the saliency. Supposing a zero rotor current, the torque profiles in the *dq*-frame become symmetrical with respect to the *q*-axis, as it is shown in Fig.2.7a; thus, the motor behaves as a synchronous reluctance motor. As the rotor current positively increases, see 2.7b-d, the torque profiles become asymmetric with respect to the *q*-axis and the Maximum Torque Per Ampere Profile (MTPA) tends to rotate toward negative values of *d*-currents. In case of not too strong iron saturation conditions, the *d*-axis inductance is greater than the *q*-axis inductance; therefore, being $L_d - L_q > 0$, positive values of *d*-currents must be provided in order to algebraically sum the reluctance and excitation torque contributions. The

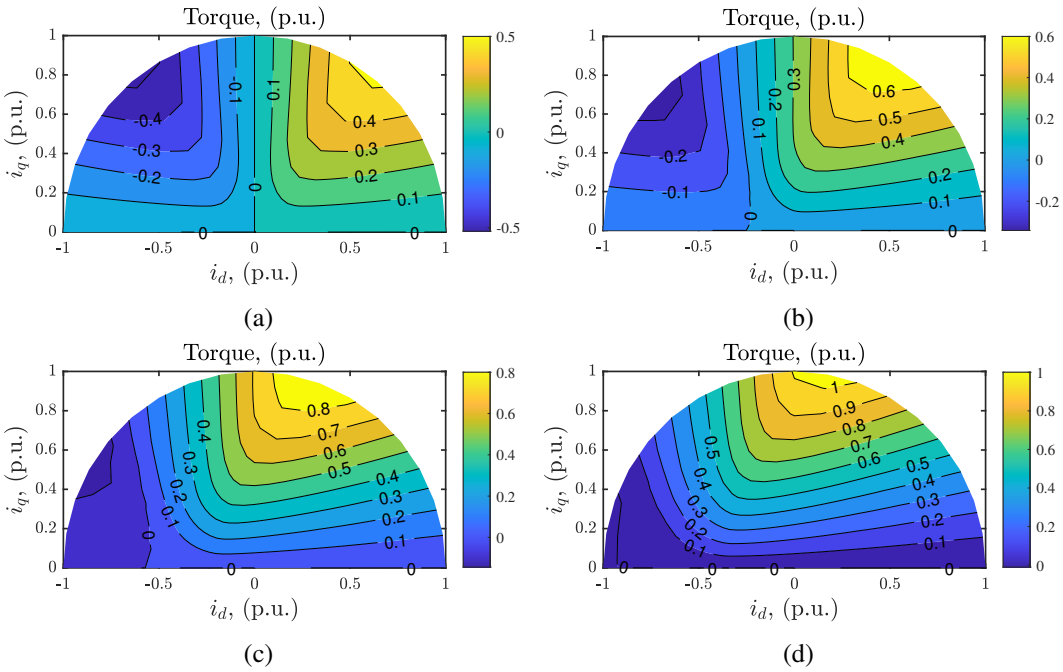

Fig. 2.7 i_d, i_q torque map for different rotor currents: 0p.u.(a), 0.3p.u.(b), 0.7p.u.(c), 1p.u.(d).

maximum torque per stator ampere is, therefore, in the first quadrant of the dq-axes. A further increase of the rotor current might cause a strong saturation of the machine iron to an extent in which $L_d \approx L_q$. In this case, the maximum torque per stator ampere profile coincides with the q-axis, as for isotropic machines; therefore, the motor behaves as a surface permanent magnet machine.

2.3 Steady-state machine performance

The fundamental parameters of the presented steady-state linear dq-model can be found through a series of tests conducted on the machine operating in sinusoidal steady-state conditions.

2.3.1 No-load characteristic

The no-load characteristic of wound-field machines refers to the correlation between the rotor current and the induced voltage at the open stator terminals while maintaining a fixed speed. During this state, the stator current does not circulate, resulting in

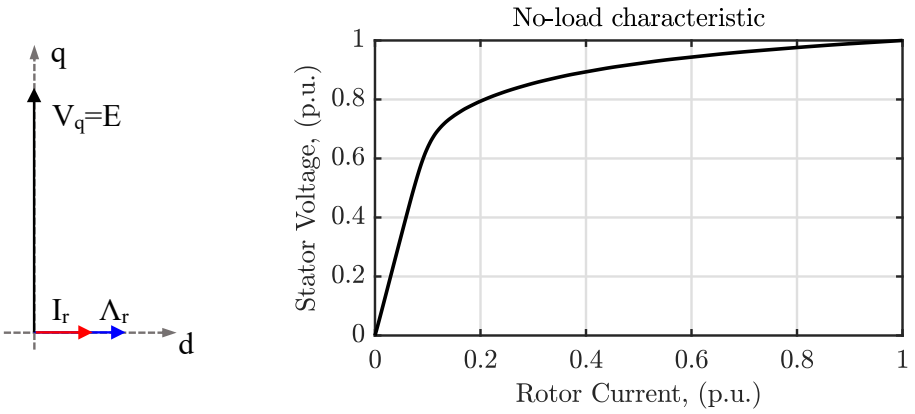

(a) (b)

Fig. 2.8 No-load characteristic.

both I_d and I_q being equal to zero. Thus, the system of equations (2.8) transforms into:

$$\begin{cases} V_d = 0 \\ V_q = \omega \cdot \Lambda_d \\ V_r = R_r \cdot I_r \end{cases} \qquad \begin{cases} \Lambda_d = M_{sr} \cdot I_r \\ \Lambda_q = 0 \\ \Lambda_r = L_r \cdot I_r \end{cases} \tag{2.16}$$

The obtained equations can be represented by the diagram in Fig.2.8a. Figure 2.8 shows a typical example of a no-load characteristic. The curve profile corresponds to the magnetization process of the machine and the saturation of the magnetic circuits.

Considering that the peak value of the induced no-load voltage coincides with the q-axis voltage (being $V_d = 0$), the parameter M_{sr} is expressed by equation (2.17).

$$M_{sr} = \frac{E}{\omega \cdot I_r} \tag{2.17}$$

2.3.2 Short-circuit characteristic

The short-circuit characteristic of wound-field machines refers to the correlation between the rotor current and the current induced in the stator terminals closed in short-circuit while maintaining a fixed speed. During this state, the stator voltage is zero, resulting in $V_d = V_q = 0$.

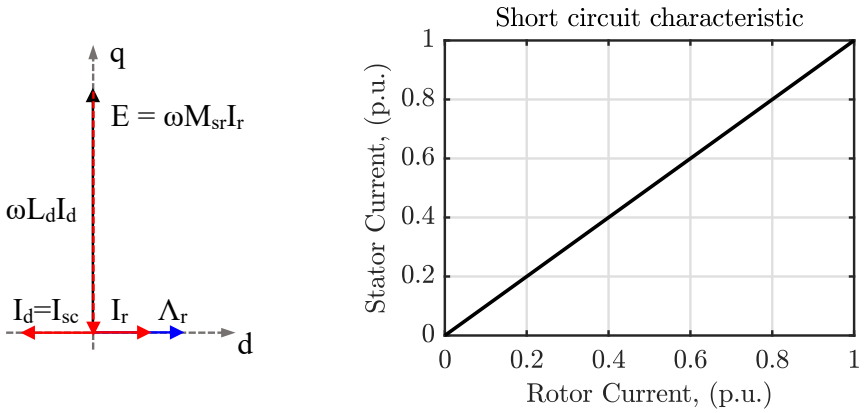

(a) (b)

Fig. 2.9 Short-circuit characteristic.

Thus, the system of equations (2.8) transforms into:

$$\begin{cases} 0 = R_s \cdot I_d - \omega \cdot \Lambda_q \\ 0 = R_s \cdot I_q + \omega \cdot \Lambda_d \\ V_r = R_r \cdot I_r \end{cases} \qquad \begin{cases} \Lambda_d = L_d \cdot I_d + M_{sr} \cdot I_r \\ \Lambda_q = L_q \cdot I_q \\ \Lambda_r = L_r \cdot I_r + M_{sr} \cdot I_d \end{cases} \tag{2.18}$$

In the hypothesis of a negligible value of the stator resistance, substituting the q-axis flux linkage equation into the d-axis voltage equation leads to (2.19), while substituting the q-axis flux linkage equation into the d-axis voltage equation leads to (2.20).

$$\Lambda_q = L_q \cdot I_q = 0 \tag{2.19}$$

$$\omega \cdot \Lambda_d = \omega \cdot L_d \cdot I_d + \omega \cdot M_{sr} \cdot I_r = 0 \tag{2.20}$$

The obtained equations can be represented by the diagram in Fig.2.9a. Figure 2.9 shows a typical example of a short-circuit characteristic. Equation (2.20) and Fig.2.9a show that the d-axis current tends to produce a magnetizing effect opposite to that produced by the excitation current. The resulting magnetic flux is, thus, modest, and the magnetic saturation is absent, regardless of the rotor current values. The amplitude of the short-circuit current in steady-state conditions is generally not dangerous for the machine and is comparable with its rated current.

Note that the short-circuit test allows obtaining the value of the synchronous inductance in the d-axis, using (2.20). In this case, the absolute value of the I_d current coincides with the peak value of the stator short-circuit current, being $I_q = 0$.

$$L_d = \frac{M_{sr} \cdot I_r}{I_{sc}} \tag{2.21}$$

2.3.3 The Potier diagram

Let's suppose that the no-load characteristic of the machine is known and to operate the machine as a generator closed on an inductive load, thus producing only negative values of the I_d current. As a consequence, a voltage V is obtained at the stator terminals, certainly lower than E, for a fixed value of the excitation current. The voltage V is represented by the ordinate of P in Fig.2.10. In this operation, the stator ampere-turns are demagnetizing and act as a real counter-excitation. The resulting total ampere-turns can be computed as an arithmetic difference:

$$AT_t = AT_r - AT_s \tag{2.22}$$

Dividing both members of this relation by the number of rotor turns, the analogous equivalence relation between the excitation currents is obtained:

$$I_t = I_r - \alpha \cdot I \tag{2.23}$$

Where α is the Potier coefficient and represents the value of the current, which, circulating in the rotor coils, produces the same magnetic effect as the unit load current circulating in the three stator phases.

$$\alpha = \frac{AT_s}{N_r \cdot I} \tag{2.24}$$

In the case of a negative current I_d, the value $\alpha \cdot I$ must therefore be subtracted from the excitation current I_r to obtain the resulting excitation current I_t. This excitation current is responsible for the production of the magnetic flux. On the no-load characteristic, the e.m.f. corresponds to this excitation current is represented by the ordinate $\overline{MR}$ of the graph in Fig.2.10. This e.m.f. is the result of the voltage

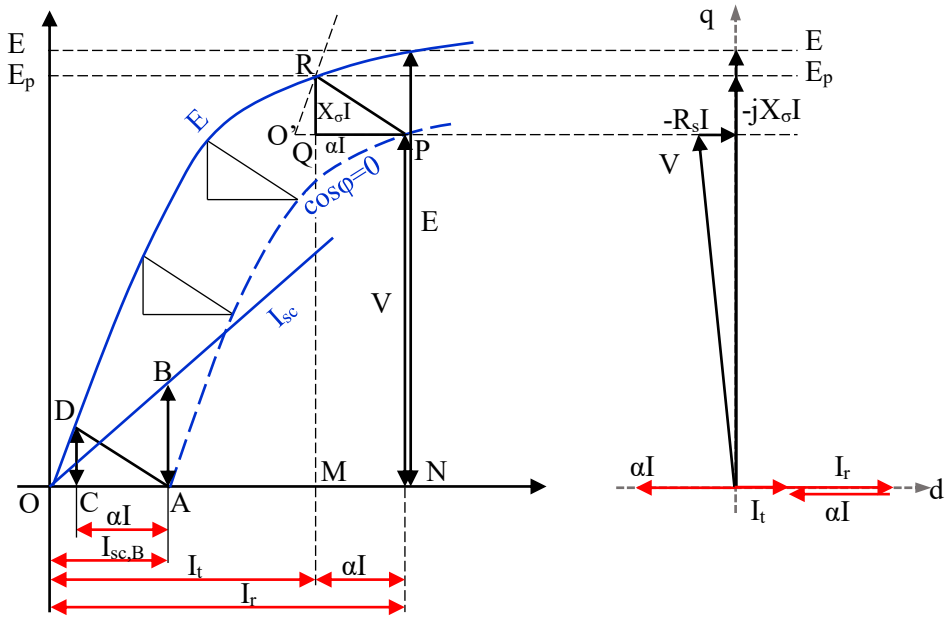

Fig. 2.10 Potier diagram.

V and the voltage drops R_sI and $j\omega L_\sigma I$, considering the phasor equation:

$$\overline{V} = \overline{E}_p + R_s \cdot \overline{I} + j\omega L_\sigma \cdot \overline{I} \tag{2.25}$$

Neglecting the stator resistance, the voltage $j\omega L_\sigma I$ coincides with the arithmetic difference $E - V$, i.e. the segment $\overline{QR}$. The right-angled triangle PQR, also known as the Potier triangle, has the property of representing the excitation current αI in the side $\overline{PQ}$ and the voltage drop $X_\sigma I$ in the side $\overline{QR}$ due to leakage reactance. By varying the load and simultaneously acting on the rotor current in order to keep the stator current fixed, the voltage at the stator terminals also varies. However, the voltage drops remain unchanged, since they are caused by the same stator current, and so does the Potier triangle. Therefore, the voltage at the terminals varies according to the curve $\cos\varphi = 0$ in Fig.2.10, obtained by translating the Potier triangle from point P. Its intersection with the abscissa axis determines a condition where the stator voltage is zero, i.e. the short-circuit. The abscissa $\overline{AO}$, thus, represents the value of the excitation current necessary to obtain the current I in the short-circuited stator winding. The current I is identified by the ordinate $\overline{BA}$, measured on the short-circuit characteristic in A.

For the complete determination of the Potier triangle, it is sufficient to know the no-load characteristic, the short-circuit characteristic and a point (P) of the $\cos\varphi = 0$ characteristic related to a certain current I. By reporting this current on the short-circuit characteristic in $\overline{AB}$, the abscissa $\overline{OA}$ is determined, which represents the short-circuit excitation $I_{sc,B}$ relative to the current I. Subsequently, moving the segment $\overline{OA}$ to $\overline{O'P}$ and determining point R by the intersection of the no-load characteristic with a line parallel to the linear part of the no-load characteristic and starting from O', the Potier triangle to be completed [70]. Based on this, since $\overline{QR} = \omega L_\sigma I$ and $\overline{QP} = \alpha I$, the leakage reactance and the Potier coefficient also remain determined, being simply the ratios:

$$L_\sigma = \frac{\overline{QR}}{\omega I} \tag{2.26}$$

$$\alpha = \frac{\overline{QP}}{I} \tag{2.27}$$

2.3.4 The q-axis inductance

The q-axis inductance can be computed considering the ratio betweeen the d- and q-magnetic flux density in the air gap induced by sinusoidal ampere-turns, as depicted in Fig.2.11, where k_b represents the portion of one electric pole occupied by the pole tip [60].

The d-axis magnetic flux density can be approximated as in (2.28), and therefore it is possible to compute the fundamental value.

$$B_d(\theta_e) = \begin{cases} B\cos(\theta_e), & -k_b \cdot \frac{\pi}{2} \leq \theta_e \leq k_b \cdot \frac{\pi}{2} \\ 0, & -\frac{\pi}{2} < \theta_e < -k_b \cdot \frac{\pi}{2} \ \vee \ k_b \cdot \frac{\pi}{2} < \theta_e < \frac{\pi}{2} \end{cases} \tag{2.28}$$

$$B_{d,1} = \frac{2}{\pi}\int_{-\pi/2}^{\pi/2} B_d \cos(\theta_e) d\theta_e = \frac{2}{\pi}\int_{-k_b\pi/2}^{k_b\pi/2} B\cos^2(\theta_e) d\theta_e \tag{2.29}$$

$$B_{d,1} = \frac{k_b \cdot \pi + \sin(k_b \cdot \pi)}{\pi} \cdot B \tag{2.30}$$

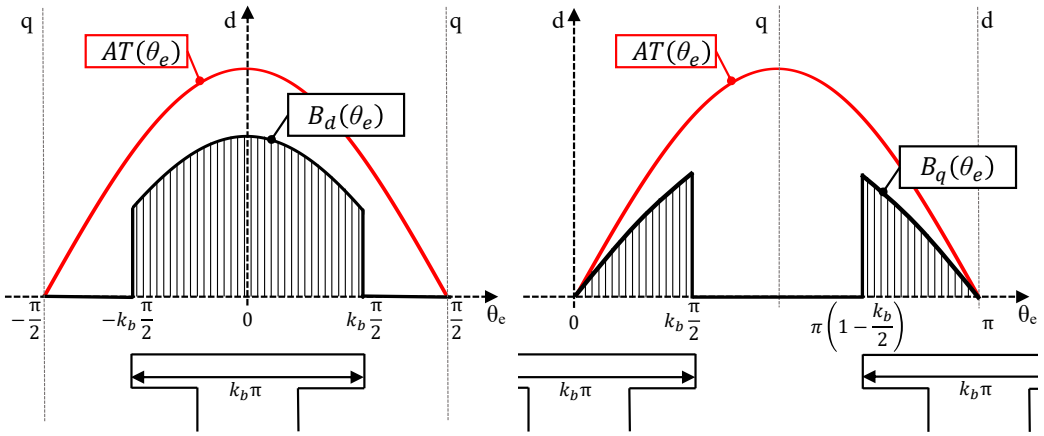

(a) (b)

Fig. 2.11 Air gap flux density and ampere-turns for the d-axis (a), and q-axis (b).

Dually, the q-axis magnetic flux density can be approximated as in (2.31), and therefore it is possible to compute the fundamental value.

$$B_q(\theta_e) = \begin{cases} B\sin(\theta_e), & -k_b \cdot \frac{\pi}{2} \leq \theta_e \leq k_b \cdot \frac{\pi}{2} \\ 0, & -\frac{\pi}{2} < \theta_e < -k_b \cdot \frac{\pi}{2} \ \vee \ k_b \cdot \frac{\pi}{2} < \theta_e < \frac{\pi}{2} \end{cases} \tag{2.31}$$

$$B_{q,1} = \frac{2}{\pi}\int_{-\pi/2}^{\pi/2} B_q \sin(\theta_e) d\theta_e = \frac{2}{\pi}\int_{-k_b\pi/2}^{k_b\pi/2} B\sin^2(\theta_e) d\theta_e \tag{2.32}$$

$$B_{q,1} = \frac{k_b \cdot \pi - \sin(k_b \cdot \pi)}{\pi} \cdot B \tag{2.33}$$

The d- and q-axis reactances can be thus computed by dividing the stator voltage induced by the magnetic flux density computed above by the stator current producing such flux density.

$$X_d = \frac{2\pi f \cdot N_s \cdot k_w \cdot L \cdot \tau_p \cdot \left(\frac{2}{\pi} \cdot B_{d,1}\right)}{I} \qquad X_q = \frac{2\pi f \cdot N_s \cdot k_w \cdot L \cdot \tau_p \cdot \left(\frac{2}{\pi} \cdot B_{q,1}\right)}{I} \tag{2.34}$$

The q-axis inductance can, thus, be obtained as in (2.35).

$$L_q = \frac{B_{q,1}}{B_{d,1}} \cdot L_d = \frac{k_b \cdot \pi - \sin(k_b \cdot \pi)}{k_b \cdot \pi + \sin(k_b \cdot \pi)} \cdot L_d \tag{2.35}$$

2.3.5 Common control strategies

The third degree of freedom introduced by the presence of the rotor current opens up many control strategies that can be implemented [55, 71–78].

- Loss Minimization, in which the aim is to minimize the total losses, both the stator and the rotor, hence maximizing the motor efficiency.
- Maximum Torque Per Stator Ampere (Stator MTPA), used to achieve the maximum torque for a fixed rotor current.
- Maximum Torque Per Rotor Ampere, used to achieve a certain torque with the minimum amount of rotor current. As a consequence, if the required torque can be achieved by purely reluctance torque, the rotor current is set to zero. The stator current components must be chosen according to the MTPA.
- Zero d-Axis Current is a special case in which the current vector is set in the q-direction. This methodology simplifies the control from three degrees of freedom to two. The remaining variables can be set with the aim of minimizing the losses.
- Unity Power Factor (UPF) control consists of maximizing the power factor, which is generally applied to fully utilize the power capability of the inverter.

2.4 Design procedures

Wound-field synchronous machines have been historically used as generators for power plant applications, where the rotor is connected to the prime mover, which can be a steam turbine, gas turbine or diesel engine, and the stator is connected to the power grid. In this scenario, the process of designing wound-field alternators is a consolidated and reliable procedure that generally exploits well-known coefficients and geometrical assumptions [58, 79, 80]. For example, the output power coefficient C_s, shown in Fig.2.12 and also known as the machine constant, is defined as a function of the apparent power and the number of poles, both dictated by the application. The parameter C_s allows defining the electric and magnetic loadings, i.e. the linear current density A_s and the air gap magnetic flux density B_g, ultimately obtaining a

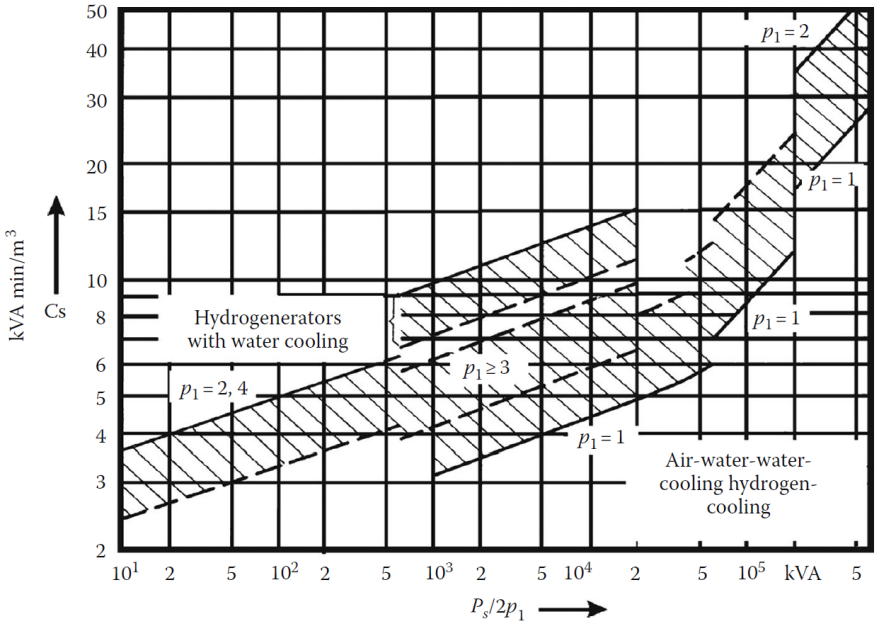

Fig. 2.12 The output power coefficient for synchronous generators [58].

fixed rotor volume. In (2.37), D_g is the air gap diameter, L is the axial length, S_n is the nominal apparent power, $\cos(\varphi)$ is the power factor, and n is the rotational speed.

$$C_s = \frac{\pi^2}{\sqrt{2}} \cdot k_w \cdot A_s \cdot B_g \tag{2.36}$$

$$D_g^2 \cdot L = \frac{S_n \cdot \cos(\varphi)}{C_s \cdot n} \tag{2.37}$$

Although the procedure followed for generators can serve as a basic framework for designing WFSM motors, it may not always align with the specific requirements of the application. Indeed, wound-field motors are often designed to operate in heavily saturated conditions, which is not a common assumption in designing generators. Furthermore, since traction motors are relatively smaller in size when compared to power plant alternators, some of the assumptions about the geometry of the machines may also become invalid.

To the best author's knowledge, the technical literature reports only a limited amount of documents dealing with the design of wound-field motors. A comprehensive study is presented in [44, 81, 82], where high-performance WFSMs were

designed, prototyped and experimentally characterized with brushes and slip rings and brushless capacitive power couplers. The machine designs were obtained through a mechanical, thermal and electromagnetic parametric model used in an optimization algorithm. Electromagnetic and thermal evaluations have been conducted through MATLAB, interfaced with FE and thermal equivalent circuit software.

FE optimization is also adopted in [83, 84], where genetic algorithms are used to find the best candidate for traction drives in hybrid electric vehicles and for a 48V battery electric vehicle, respectively. The study [85] focuses on selecting the number of stator slots and the number of poles, leading to three machine alternatives, of which the best design is electromagnetically optimised for use as a wheel hub drive in an electric vehicle. In [86], a wound-field synchronous motor is designed and optimized using a metamodel-based approach to maximize its efficiency over a custom set of load points, and the selected design is prototyped. In [87], six motor options are compared (including the WFSM), also relying on FE optimizations. The works presented in [53, 57] employ FE optimizations on predefined geometries with the aim of optimizing two specific parameters in the former and considering magnetic asymmetry in the latter. In [88], a wound-field motor is designed to be compared to a baseline IPM motor, fixating the main dimensions and optimizing for the peak torque and power and specific efficiency requirements.

An optimization algorithm is used on an analytical model in [89], where seven parameters are optimized within a fixed machine volume to maximize efficiency. The development of a population-based design tool that utilizes a magnetic equivalent circuit is proposed in [90], where the design tool is applied to perform multiobjective optimization of a 2-kW portable power generator, validated through the construction of a prototype. In [91], a WFSM prototype is studied and improved also through a magnetic equivalent circuit. The work [92] presents a specific design analysis on the possibility of using a subharmonic component of the stator magnetomotive force for brushless excitation, also proposed in [83], while [93] deals with a dual stator winding with connections change.

The conclusion is that the literature scenario is mostly focused on optimization algorithms generally coupled with FE simulations and, to a lesser extent, with analytical or magnetic equivalent circuit models. Nonetheless, the literature is more concentrated on papers dealing with the modelling of wound-field machines, as described in Chapter 3.

Chapter 3

Developed Machine Models

The process of designing wound-field machines requires accurate machine models able to predict the rated performance and assess the main characteristics and capabilities. Several WFSM models have been proposed and documented in the literature. A possible classification of the proposed models includes analytical models, magnetic equivalent circuits, and finite element simulations, excluding those models that are more suitable for control than design.

The analytical models generally require a certain number of assumptions to achieve closed-form analytical formulations. For instance, the magnetic permeability of iron is often assumed to be infinite. Neglecting the iron saturation may strongly limit the model's accuracy, depending on the actual machine operating conditions. Nevertheless, equation-based models commonly reach the best computational performance, as the time required to solve the model is typically negligible [94–100].

The Magnetic Equivalent Circuits (MECs) may represent a good compromise between analytical models and finite element simulations. In MEC models, the machine is partitioned into a finite number of magnetic reluctances connected through a network. The solution of the system of non-linear equations associated with the network provides the magnetic flux density of each discretized element, emulating the machine's behaviour. The computational time of MEC models is generally lower compared to finite element simulations. However, the solving efficiency strongly depends on the selected initial conditions and the adopted method for solving the system, possibly resulting in convergence problems [101–113].

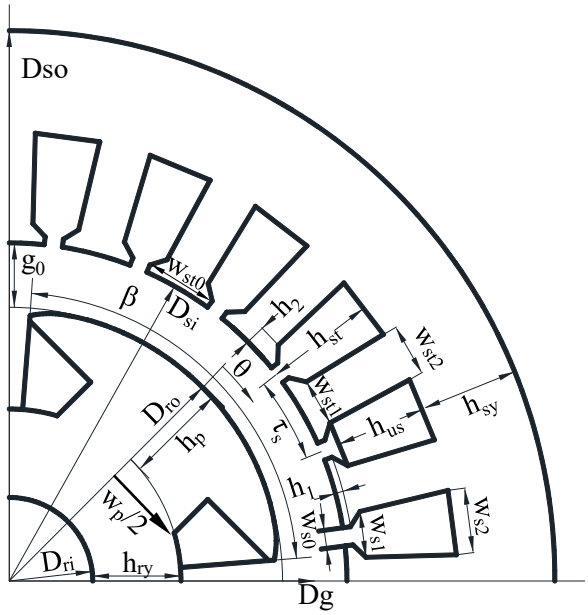

Fig. 3.1 Geometry sketch of a wound-field machine.

The finite element analysis is a numerical method of solving partial differential equations in two or three space variables. The popularity of finite element models (FEMs) is certainly due to the achieved level of results accuracy. However, an important role is played by the wide availability of both commercial and free FE software, which eases the analysis process through user-friendly interfaces and the possibility of communicating with other software, such as programming platforms. Although many techniques can be used to optimize the solving procedure, such as parallel computation and machine periodicity exploitation, the computational time still remains a burden for FE tools [49, 53–55, 114–120].

In this scenario, even though not necessarily in the field of transportation applications, combined analytical-numerical approaches are proposed in the literature as a trade-off between the computational speed of the analytical formulations and the accuracy of the numerical analyses [121–125]. These hybrid models are generally used in the modelling of wound-field synchronous generators rather than motors, as they ease the computation of the damper bar currents.

The following sections describe the WFSM models conceived in this research activity. In particular, an analytical model, a magnetic equivalent circuit and a parametric FE model have been developed and compared in terms of accuracy and

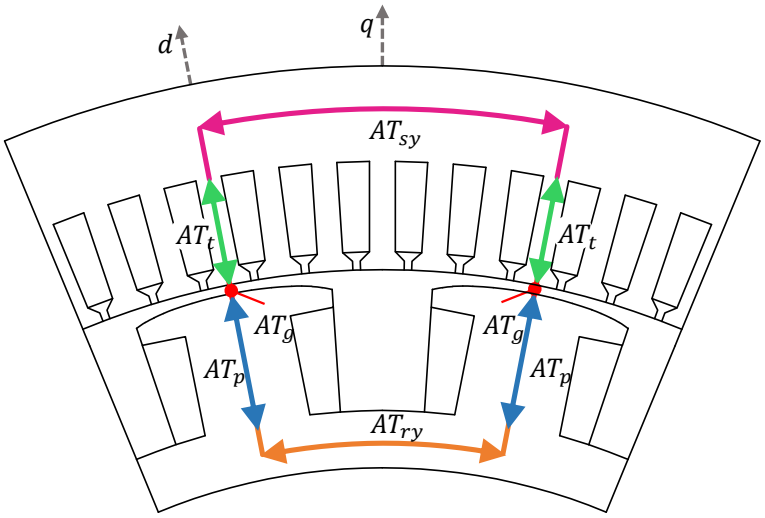

Fig. 3.2 Magnetic circuit along the d-axis.

computational efficiency in order to be used in a sizing algorithm for the design of wound-field synchronous motors. The geometric variables employed by the proposed machine models are recollected in Fig.3.1.

3.1 The analytical formulation

Analytical models often require complex mathematical formulations, which may not always result in a level of accuracy that justifies the effort. Nonetheless, they can still be a valuable tool in situations where symmetries can be exploited and assumptions can be made. This is the case of the no-load characteristic, as the magnetic flux is solely created by the rotor current and, therefore, directed along the d-axis. In this context, a straightforward analytical procedure for the computation of the no-load characteristic has been developed, considering the iron saturation, the distortion of the air gap flux density and the magnetic shunt of the stator slots [126].

3.1.1 The no-load characteristic computation

The computation of the no-load characteristic requires the estimation of the values $\{I_r, E_s\}$, meaning the value of the induced stator voltage E_s by the rotor current I_r, for different values of I_r. This characteristic can be obtained by scaling the characteristic

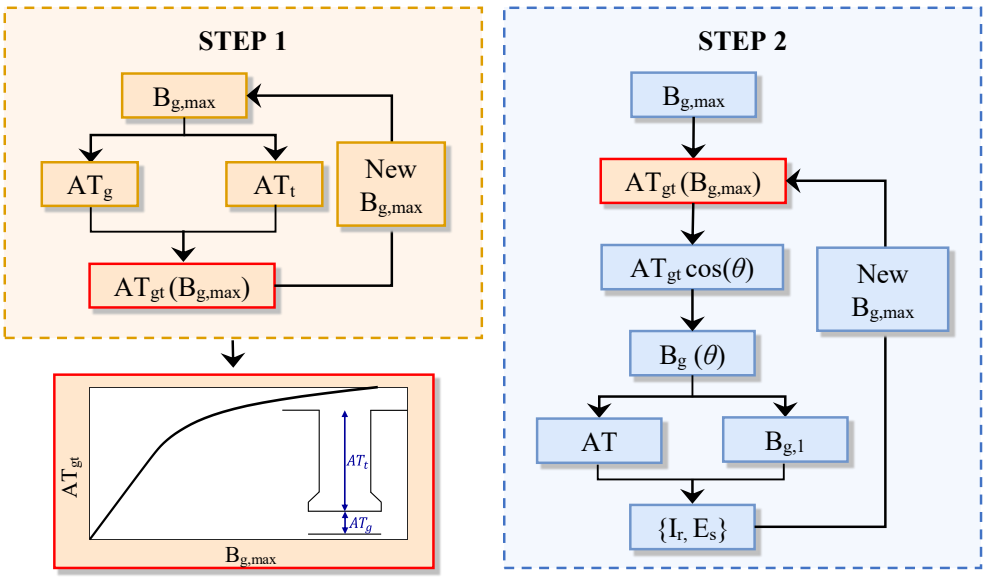

Fig. 3.3 Scheme of no-load characteristic computation.

$\{AT, B_{g1}\}$, where AT are the total ampere-turns required to magnetize the machine, while B_{g1} is the fundamental value of the magnetic flux density in the air gap.

The proposed computation of such characteristic is based on the segmentation of the magnetic circuit along the d-axis into five different parts, as shown in Fig.3.2, i.e. the air gap, the stator and rotor yoke, the stator teeth, and the rotor pole. The computational process is reported in the scheme of Fig 3.3, where $B_{g,max}$ is the maximum value of the magnetic flux density, AT_g and AT_t are the magnetomotive forces (m.m.f.) drop in the air gap and stator teeth, respectively, AT_{gt} is the sum of AT_g and AT_t.

The scheme shows that the procedure follows two different steps. In the first step, the m.m.f. drops of the air gap and the stator teeth are computed for different values of maximum magnetic flux density in the air gap. Therefore, assuming that the distortion of the magnetic flux density in the air gap is solely due to the saturation of the stator teeth, the remaining m.m.f. drops (rotor and stator yoke and rotor pole) are computed in the second step. The sum of all the m.m.f. drops provides the value of AT for a specific maximum magnetic flux density in the air gap. Repeating the computation for different values of $B_{g,max}$, the characteristic $\{AT, B_{g1}\}$ is obtained, and thus $\{I_r, E_s\}$. The following sections describe the procedure adopted in each of the presented steps.

STEP 1

Air Gap m.m.f. Drop

Step 1 starts with the computation of the m.m.f. drop in the air gap AT_g. The air gap length is assumed to be inversely proportional to the cosine of the angle that starts from the d-axis, as explained in Chapter 2. For a specific value of $B_{g,max}$, the value of the m.m.f. drop in the air gap is computed as in (3.1), where k_C is the Carter factor calculated for the average air gap length [79].

$$AT_g = \frac{B_{g,max}}{\mu_0} \cdot k_C \cdot g_0 \tag{3.1}$$

Stator Teeth m.m.f. Drop

The m.m.f. drop in the stator teeth is required to complete the second step. The amount of ampere-turns required to magnetize the circuit is significantly affected by the saturation of the stator teeth. Typically, in mild saturation conditions, it is assumed that the magnetic flux passing through one slot pitch (Φ_{sp}) is entirely funnelled in the teeth. Therefore, the magnetic flux density in the portion of the stator tooth closer to the air gap (B_{t0}) can be computed trough (3.2)-(3.3), where τ_s is the slot pitch, k_{st} is the lamination stacking factor and L is the machine axial length.

$$\Phi_{sp} = B_{g,max} \cdot \tau_s \cdot L \tag{3.2}$$

$$B_{t0} = \frac{\Phi_{sp}}{k_{st} \cdot w_{st}} \tag{3.3}$$

Nevertheless, when the tooth becomes highly saturated, the amount of magnetic flux in the slot becomes non-negligible, causing the magnetic shunt of the stator slots. This phenomenon is evaluated in the proposed procedure through an iterative method in order to consider the non-linear magnetic characteristic of the lamination material.

The teeth and the slots are divided into N layers, as depicted in Fig.3.4a, assuming parallel equipotential lines [127]. For each discretized layer, the magnetic flux of the stator tooth Φ_t and of the stator slot Φ_s are computed through (3.4)-(3.5), where w_s is the slot width of the considered layer, B_t and B_s are the tooth and slot magnetic

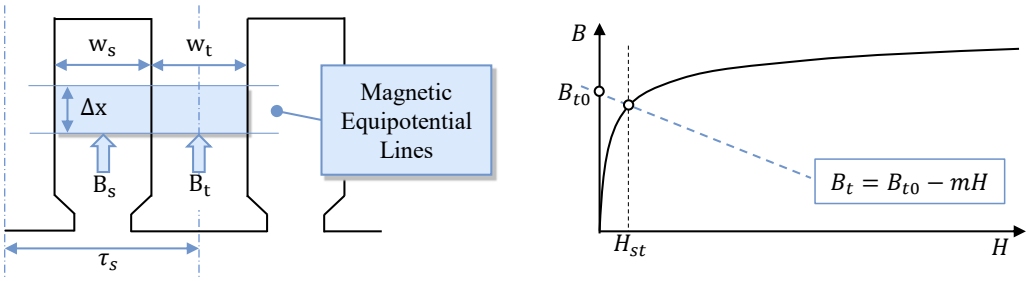

(a) (b)

Fig. 3.4 Shunt effect of the slot (a), teeth working point (b).

flux density, respectively. In equation (3.5), the first term represents the flux share in the stator slots, while the second is through the lamination sheets.

$$\Phi_t = B_t \cdot L \cdot k_{st} \cdot w_{st} \tag{3.4}$$

$$\Phi_s = B_s \cdot L \cdot w_s + B_s \cdot L \cdot (1 - k_{st}) \cdot w_{st} \tag{3.5}$$

The sum of Φ_t and Φ_s is the flux relative to one slot pitch Φ_{sp}.

$$\Phi_{sp} = \Phi_t + \Phi_s \tag{3.6}$$

Substituting (3.4) and (3.5) into (3.6), equation (3.7) can be obtained.

$$B_{t0} = B_t(H) + \frac{\mu_0}{k_{st}} \left(\frac{w_s}{w_{st}} + 1 - k_{st} \right) \cdot H_{st} = B_t(H) + m \cdot H_{st} \tag{3.7}$$

For a given value of the magnetic field in the stator tooth H_{st}, the magnetic flux density of the i-th layer of the tooth (B_t) can be found by intersecting the iron magnetic characteristic with the line in (3.7), as depicted in Fig.3.4b.

Based on these premises, the iterative procedure is obtained as shown in Fig.3.5, i.e. by implementing the following steps.

- Using equation (3.3), the value of B_{t0} is computed and assumed as the first initial guess of the magnetic flux density in the tooth (B_t).
- The magnetic field in the tooth H_{st} is computed entering the iron magnetic characteristic curve with the assumed value of B_t.

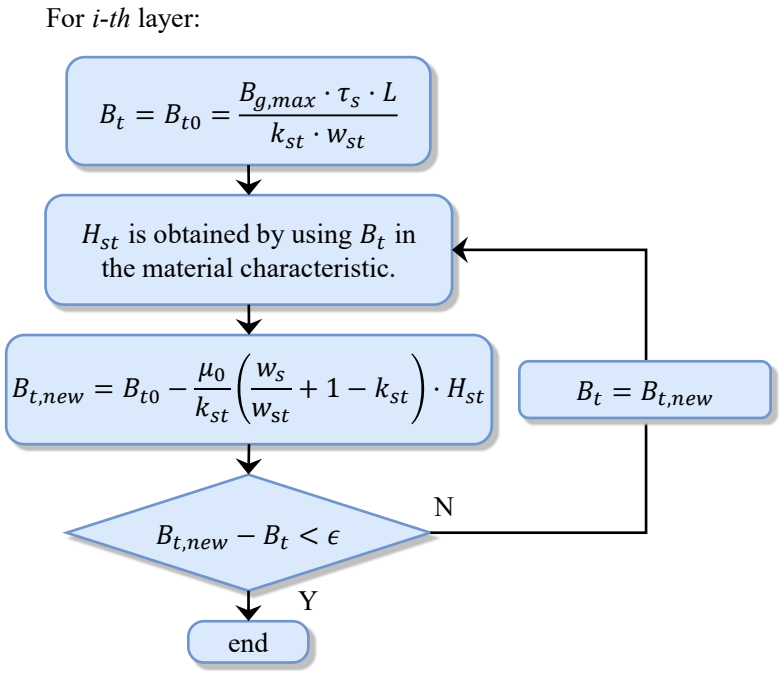

Fig. 3.5 Iterative procedure for the computation the magnetic flux density of the i-th tooth layer considering the slot magnetic shunt.

- The obtained value of H_{st} is used in equation (3.7) to compute the new value of the magnetic flux density in the tooth ($B_{t,new}$).
- If the assumed B_t differs from $B_{t,new}$ more than a defined tolerance ε, the procedure is repeated assuming $B_t = B_{t,new}$ otherwise the procedure is completed.

Note that the described procedure applies to one layer of the stator tooth and slot and for one value of the maximum magnetic flux density in the air gap. The total m.m.f drop in the tooth is found by summing the contribution of each layer, as in (3.8), where AT_t is a function of $B_{g,max}$, H_i is the magnetic field of the i-th tooth layer and Δx is the length of the layer.

$$AT_g(B_{g,max}) = \sum_{i=1}^{N} H_{st,i} \cdot \Delta x \tag{3.8}$$

The m.m.f. drop AT_{gt} is therefore obtained by summing AT_g and AT_t, computed through (3.1) and (3.8), for different values of $B_{g,max}$. This allows for the computation of the characteristic $\{AT_{gt}, B_{g,max}\}$, necessary for the second step.

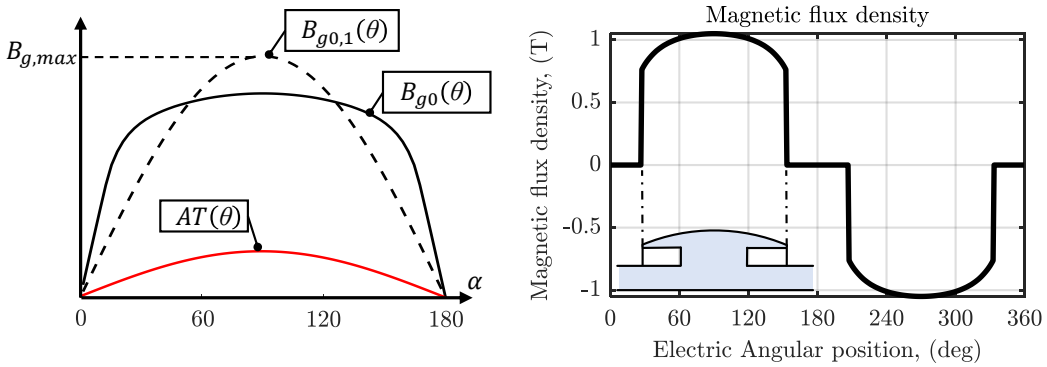

(a) (b)

Fig. 3.6 Air gap flux density distortion (a), typical air gap flux density (b).

STEP 2

Air Gap flux density waveform

Whereas the maximum value of the magnetic flux density was sufficient for obtaining the $\{AT_{gt}, B_{g,max}\}$ characteristic, an estimation of the actual distribution of the magnetic flux density is needed in the second step to determine the m.m.f. drop in the other parts of the machine. The adopted shape of the rotor pole as an inverse cosine results in a sinusoidal distribution of the m.m.f. at the air gap, at least in the area covered by the pole iron. In saturation conditions, the magnetic flux density waveform resulting from a sinusoidal m.m.f. becomes distorted along the circumference of the air gap, as shown in Fig.3.6a. Assuming the distortion to be caused mainly by the saturation of the teeth, the maximum value of the m.m.f. distribution at the air gap can be obtained from $\{AT_{gt}, B_{g,max}\}$, for a given value of $B_{g,max}$. The waveform of m.m.f. at the air gap can be thus described by the function in (3.9), where θ is the angle starting from the d-axis.

$$AT(\theta) = AT_{gt}(B_{g,max}) \cdot \cos(\theta) \tag{3.9}$$

Considering that in the area between two consecutive poles, i.e. in the q-axis direction, the presence of a large region of air causes the air gap flux density to drop abruptly, as depicted in Fig.3.6b, the distribution of B_g can be approximated as a piecewise function. The air gap flux density is considered different from zero only

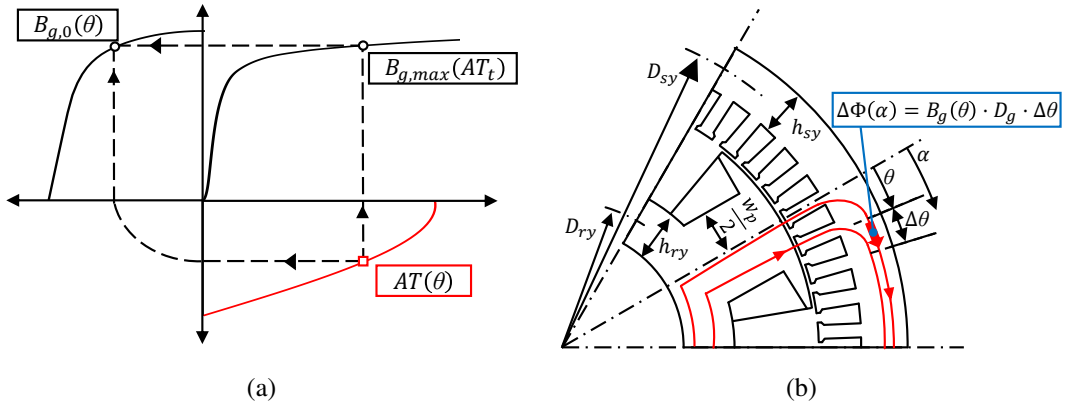

(a) (b)

Fig. 3.7 Distorted air gap flux density computation (a), computational procedure for the stator yoke m.m.f. drop (b).

for those values of θ in which the iron pole is present, as in (3.10), where $B_{g,0}$ is the air gap flux density when $k_b \to 1$, i.e. when the rotor pole tip tends to occupy the whole pole pitch.

$$B_g(\theta) = \begin{cases} B_{g,0}(\theta), & \theta \leq k_b \cdot \frac{\pi}{2} \\ 0, & \theta > k_b \cdot \frac{\pi}{2} \end{cases} \tag{3.10}$$

The magnetic flux density waveform $B_{g,0}$ is built considering the distorted distribution, following the procedure shown in Fig.3.7a [128]. At this stage, knowing the distribution of the magnetic flux density in the air gap, the m.m.f. drop of the stator and rotor yoke and rotor pole can be obtained, as well as the fundamental value of B_g. The formulation of the latter is expressed in (3.11).

$$B_{g1} = \frac{4}{\pi} \int_0^{\frac{\pi}{2}} B_g(\theta) \cdot \cos(\theta) \cdot d\theta \tag{3.11}$$

The computation of B_{g1} is discretized by dividing the air gap of half the pole into N_a layers, defining the variable θ_i as the angular coordinate of the centre of each layer.

Discetizing equation (3.11), the value of B_{g1} is determined.

$$B_{g1} = \frac{2}{N_a} \sum_{i=1}^{N_a} B_g(\theta_i) \cdot \cos(\theta_i) \tag{3.12}$$

Stator Yoke m.m.f. Drop

The magnetic flux density in the stator yoke is lowest in the d-axis and progressively increases towards the q-axis, as shown in Fig.3.7b. The value of the magnetic flux density in the stator yoke B_{sy} at the angular position α, referred to the d-axis, can be computed as in (3.13), where D_g is the diameter at the air gap centre, h_{sy} is the stator yoke height.

$$B_{sy}(\alpha) = \int_0^{\alpha} B_g(\theta) \cdot \frac{D_g}{2 \cdot h_{sy}} \cdot \frac{1}{k_{st} \cdot p} \cdot d\theta \tag{3.13}$$

For a discrete variable θ, the magnetic flux density in the yoke can be computed as in (3.14), where n_y is the number of considered yoke pieces at the coordinate α.

$$B_{sy}(\alpha) = \sum_{i=1}^{n_y(\alpha)} B_g(\theta_i) \cdot \frac{D_g}{2 \cdot h_{sy}} \cdot \frac{1}{k_{st} \cdot p} \cdot \Delta\theta \tag{3.14}$$

Ultimately, the required value of the m.m.f. drop in the stator yoke is obtained as in (3.15), where D_{sy} is the diameter at the centre of the yoke.

$$AT_{sy}(B_{g,max}) = \sum_{i=0}^{N_a} H(B_{sy}(\theta_i)) \cdot \frac{D_{sy}}{2p} \cdot \Delta\theta \tag{3.15}$$

Rotor Yoke and Pole m.m.f. Drop

The computation of the m.m.f. drop in the rotor yoke (AT_{ry}) and rotor pole (AT_{rp}) follows an easier procedure. Indeed, because of the absence of slots, a constant value of magnetic flux is assumed for each of the two machine parts, as depicted by the red flux lines in Fig.3.7b. Therefore, the required m.m.f. drop AT_{ry} and AT_{rp} depend on the flux per pole, which can be obtained through equation (3.16), while the value of the integral for the discrete variable θ is found as expressed in (3.17).

$$\Phi_p = 2 \int_0^{\frac{\pi}{2}} B_g(\theta) \cdot D_g \cdot L \cdot \frac{1}{2p} \cdot d\theta \tag{3.16}$$

$$\Phi_p = 2 \sum_{i=1}^{N_a} B_g(\theta_i) \cdot D_g \cdot L \cdot \frac{1}{2p} \cdot \frac{\pi}{2} \tag{3.17}$$

Therefore, the values of the magnetic flux density in the rotor yoke and pole are computed as in equations (3.18) and (3.19), where h_{ry} is the height of the rotor yoke and w_p is the width of the pole, and the same stacking factor is assumed for the stator and rotor cores.

$$B_{ry} = \frac{\Phi_p}{2} \cdot \frac{1}{h_{ry} \cdot L \cdot k_{st}} \tag{3.18}$$

$$B_p = \Phi_p \cdot \frac{1}{w_p \cdot L \cdot k_{st}} \tag{3.19}$$

From the magnetic characteristic, the magnetic field in the rotor yoke (H_{ry}) and in the pole (H_p) is obtained, and thus the values of the m.m.f. drop, considering D_{ri} the rotor inner diameter, h_{ry} the rotor yoke height and h_p the rotor pole length.

$$AT_{ry} = H_{ry} \frac{(D_{ri} + h_{ry}) \cdot \pi}{4p} \tag{3.20}$$

$$AT_p = H_p \cdot h_p \tag{3.21}$$

No-Load Characteristic

Finally, the $\{B_g, AT\}$ characteristic can be obtained by summing all the computed m.m.f. drops and repeating the procedure for different values of $B_{g,max}$.

$$AT_{tot} = AT_d + AT_t + AT_{sy} + AT_{ry} + AT_p \tag{3.22}$$

The obtained curve is manipulated to obtain the no-load characteristic $\{I_r, E_s\}$ for a given speed. The rotor current value is simply obtained by dividing AT by the number of rotor turns N_r. The no-load voltage E_s is obtained through (3.23), where k_w is the winding factor, and N_1 is the equivalent number of turns in series per phase.

$$E_s = \frac{2\pi}{\sqrt{2}} \cdot f \cdot k_w \cdot N_1 \cdot \left(\frac{2}{\pi} \cdot \tau_p \cdot L \cdot B_{g1} \right) \tag{3.23}$$

The proposed procedure is validated by means of simulations with the FE method, for two case study machines of 4 and 6 poles. Figure3.8 shows the obtained results, particularly the obtained no-load characteristic and the magnetic flux density distribu-

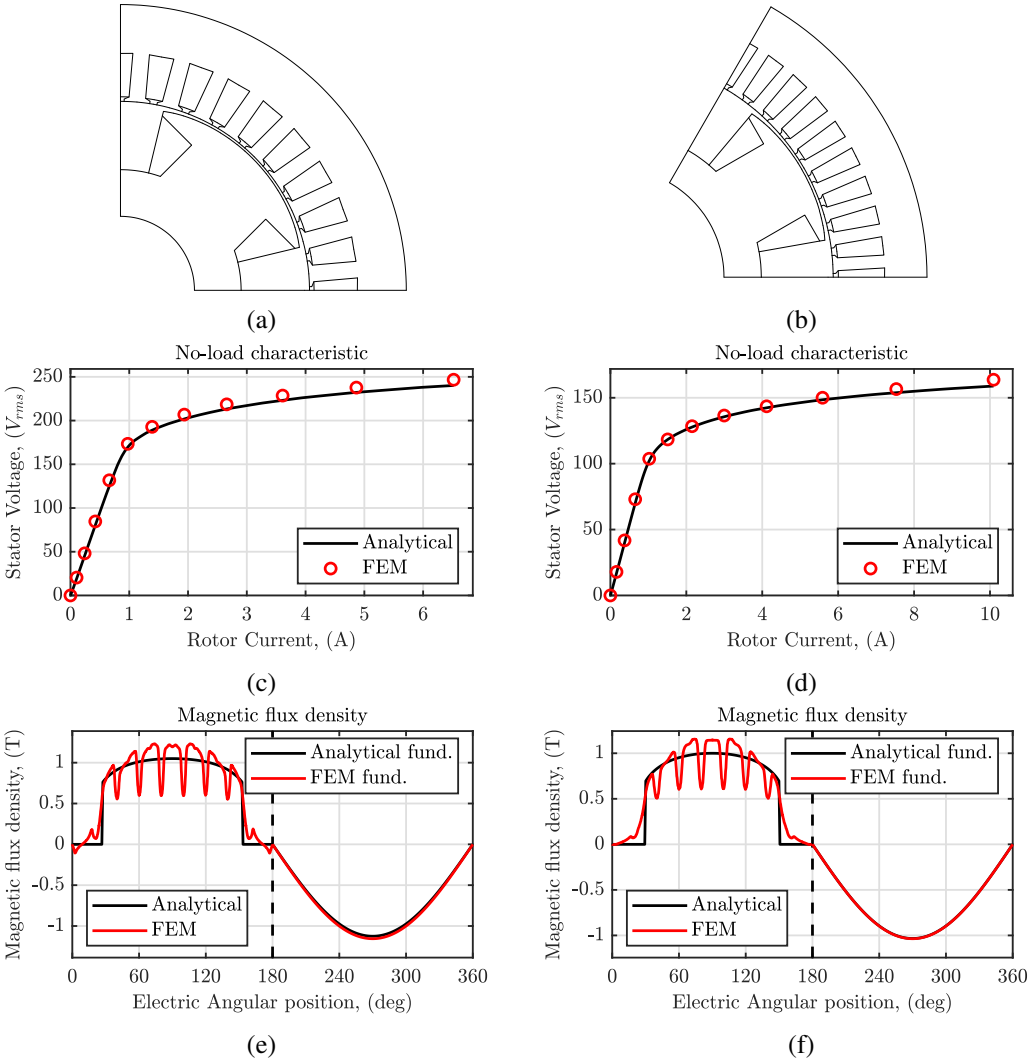

Fig. 3.8 Results for the 4-pole machine (a)-(c)-(e), and for the 6-pole machines (b)-(d)-(f).

tion for $B_{g,max} = 1T$, in terms of instantaneous values and fundamental components. The proposed procedure features low percentage errors in the whole range of the no-load characteristic. Specifically, in the saturation region, the maximum percentage error is 2.9%, reached by the highest rotor current of the 6-pole machine. Low percentage errors in this region are especially welcomed for this kind of motor that generally works in high saturation conditions. Slightly higher percentage errors occur in the linear part of the curve, albeit lower than 5%. The increase in the percentage errors is mainly due to the relatively small values of the measured quantities used as the reference for the error computation, considering that the maximum absolute error is lower than 3V.

3.2 The magnetic equivalent circuit

Magnetic equivalent circuits are based on the duality between electric and magnetic circuits. Voltages, currents and resistances become m.m.f. drops, magnetic fluxes and reluctances, respectively, in the magnetic circuit. In case saturation is taken into account, the magnetic reluctances are non-linear elements; thus, solving the circuit means solving a system of non-linear equations.

The most common method for solving the system is to apply Kirchoff's current law to find the unknown m.m.f. drops of each node of the circuit. In this model, the system is built using magnetic permeances to relate m.m.f. to source magnetic fluxes. An alternative to the nodal-based approach is the mesh-based approach, in which Kirchoff's voltage law is used to find the unknown magnetic fluxes in each loop of the circuit using the magnetic reluctances. Although the nodal-based MEC features an easier implementation due to the fact that the number of nodes in the circuit is fixed (while loops depend on the position between stator and rotor), the mesh-based model results in much better convergence performance. The reason is due to the different residual functions of the two approaches [107, 129].

In the context of magnetic equivalent circuits, a mesh-based model that includes rotation has been developed for wound field synchronous motors and presented in the forthcoming sections.

3.2.1 The equivalent circuit

Figure 3.9 shows the developed magnetic equivalent circuit. The circuit models one machine periodicity, and therefore, it is suitable for an arbitrary number of poles. The total number of reluctances depends on the machine geometry. To be specific, the stator yoke (R_{sy}) and the stator tooth reluctances (R_{st}) are equal to the number of teeth in one machine pole (n_s). The reluctances of the air gap (R_{ag}) depend on the connections between the stator teeth and the discretized number of elements of the rotor pole (N_{ri}) and interpolar air (N_{ra}). Leakage reluctances are also included according to [108]. These are considered in the stator slots (R_{ss}), in the rotor slots (R_{sr}), in the interpolar air (R_{ias} and R_{pp}). The pole body is approximated as one single reluctance (R_{rp}), while the rotor yoke is divided into three parts (R_{ry}).

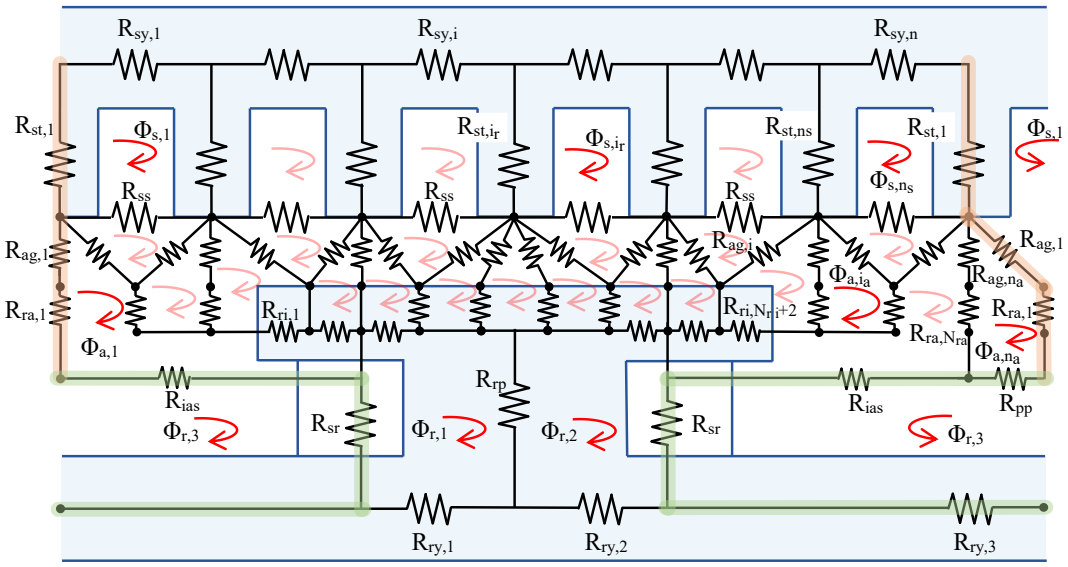

Fig. 3.9 Magnetic equivalent circuit of wound-field machines.

Depending on the number of magnetic reluctances and their connections, the total number of flux loops, shown with red arrows in Fig.3.9, is determined. In particular, based on the defined circuit, the number of stator flux loops Φ_s coincides with n_s, and the number of rotor flux loops is 3. However, the number of flux loops in the air gap Φ_a is not known a priori, as it depends on how many connections are formed between the stator teeth and the rotor sections. The reluctances representing a part of the machine composed of magnetic material are non-linear elements of the circuit. These are reported in the blue regions of Fig.3.9. The remaining reluctances, reported in the white regions, represent non-magnetic materials and thus are considered constant values.

The branches highlighted in orange and green include border reluctances. The border reluctances in the orange branch are in a position of magnetic symmetry. Hence, the same behaviour is expected by the two branches on the side of the modelled machine portions. The border reluctances in green belong to the same loop, namely *"r,3"*. In both cases, the adjacent pole features an antiperiodic behaviour with respect to the modelled one, as shown by the change in the direction of the flux loop arrows on the right border of Fig.3.9. Therefore, a sign minus will be included for the border reluctances in building the reluctance matrix of the magnetic equivalent circuit.

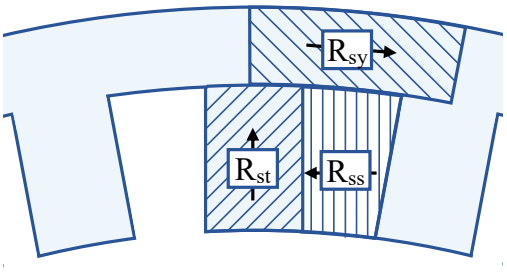

Fig. 3.10 Stator reluctances.

3.2.2 The magnetic reluctances

In order to solve the MEC, each magnetic reluctance of the circuit must be computed. The general formulation for the computation of magnetic reluctance is shown in (3.24), where l is the length of the considered magnetic flux tube, S is its surface, and μ_r is the relative magnetic permeability. The equation is simplified in the case of prismatic or cylindrical volumes where the surface is constant along the variable l, leading to (3.25). In the following sections, the computation of each magnetic reluctance is explained.

$$R_m = \int \frac{dl}{\mu_0 \cdot \mu_r(l) \cdot S(l)} \tag{3.24}$$

$$R_m = \frac{l}{\mu_0 \cdot \mu_r \cdot S} \tag{3.25}$$

Stator reluctances

The computation of the stator reluctances R_{sy}, R_{st}, R_{ss} is a relatively straightforward process. The considered flux tubes are shown in Fig.3.10. The stator tooth and stator yoke reluctances are computed through (3.26) and (3.27), where N_s is the number of stator slots, D_{so} is the stator outer diameter, h_{st} is the stator tooth height.

$$R_{st} = \frac{h_{st}}{\mu_0 \cdot \mu_{r,st} \cdot (L \cdot k_{st} \cdot w_{st})} \tag{3.26}$$

$$R_{sy} = \frac{\pi \cdot (D_{so} - h_{sy})/N_s}{\mu_0 \cdot \mu_{r,sy} \cdot (L \cdot k_{st} \cdot h_{sy})} \tag{3.27}$$

The stator slot leakage reluctance is computed through the formulation of the specific permeance of slots reported in [130]. In (3.28), the formulation for trapezoidal-shaped slots is shown, according to the geometric variables defined in Fig.3.1.

$$p_{ss} = \mu_0 \cdot \frac{h_{us}}{w_{s2}} \cdot \left[\frac{\left(\frac{w_{s1}}{w_{s2}}\right)^2 - \frac{w_{s1}^4}{4w_{s2}^4} - ln\left(\frac{w_{s1}}{w_{s2}}\right) - \frac{3}{4}}{\left(1 - \left(\frac{w_{s1}}{w_{s2}}\right)\right)\left(1 - \left(\frac{w_{s1}}{w_{s2}}\right)^2\right)^2} \right] \tag{3.28}$$

$$R_{ss} = \frac{1}{p_{ss} \cdot L} \tag{3.29}$$

Air gap reluctances

The air gap reluctances are formed between the stator teeth and the rotor sections. The connection between the i_s-th stator tooth and the i_r-th rotor section is supposed to exist only if a part of the rotor section is between the centres of the two adjacent slots, as shown in Fig.3.11a. In the figure, for instance, the rotor sections $i_r - 1$ and i_r are connected to the i_s tooth, but no connection exists with the $i_r + 1$ rotor section. The air gap reluctances are computed as the parallel combination of two reluctances, i.e. the inverse of the sum of two permeances (P_{st} and P_{sf}), as depicted in Fig.3.11a. The first permeance P_{st} represents the main flux between the stator tooth and the portion of the rotor section placed directly under the tooth. The second permeance P_{sf} represents the fringing flux from the tooth sides to the rotor section. Different scenarios can occur depending on the mutual position of the i_s-th stator tooth and the i_r-th rotor section, as later addressed.

The computation of the air gap permeance associated with the main flux is expressed in (3.30), where w_{sr} is the width of the overlapping portion of the stator tooth and the rotor section, and g is the air gap length. In the developed model, the air gap is assumed to be shaped as an inverse cosine; therefore, the value of g depends on the angular coordinate θ.

$$P_{st} = \frac{\mu_0 \cdot L \cdot w_{sr}}{g(\theta)} \tag{3.30}$$

The fringing permeance is obtained by integration over the width of the flux tube. The length of the flux is considered to be the sum of the air gap length and a quarter of

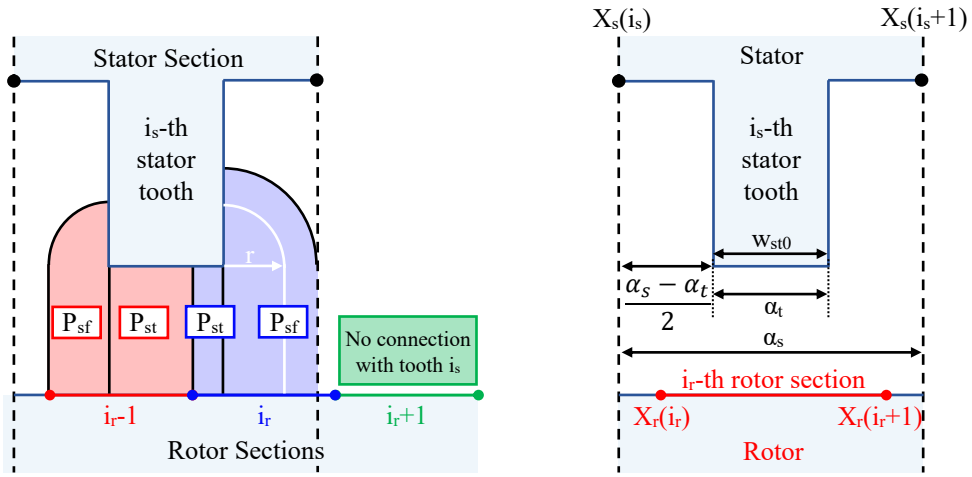

Fig. 3.11 Sketch of the i_s-th stator tooth and the i_r-th rotor section.

a circumference starting from the side of the slot and radius r, which thus represents the variable for the integration, as shown in white in Fig.3.11a.

$$P_{sf} = \int_{r_1}^{r_2} \frac{\mu_0 \cdot L}{\frac{\pi}{2} \cdot r + g(\theta)} dr \tag{3.31}$$

Through 3.30 and 3.31, the magnetic permeances P_{st} and P_{sf} are known if the width of the main tube flux w_{sr} and the bounds of integration r_1 and r_2 of the fringing flux are determined. The air gap reluctance is thus computed as in (3.32).

$$R_{ag} = \frac{1}{P_{ag}} = \frac{1}{P_{st} + P_{sf}} \tag{3.32}$$

According to Fig.3.11b, let's consider the variable x_s the angular position of the stator teeth, identified by the coordinates of the centres of the adjacent slots. The variable x_r identifies the angular position of the rotor sections. The angle α_s is the angular slot pitch in radians, and α_t is the angle of the tooth width at the air gap (w_{st0}).

$$\alpha_s = \frac{2\pi}{N_s} \tag{3.33}$$

$$\alpha_t = 2 \arcsin\left(\frac{w_{st0}}{D_g}\right) \tag{3.34}$$

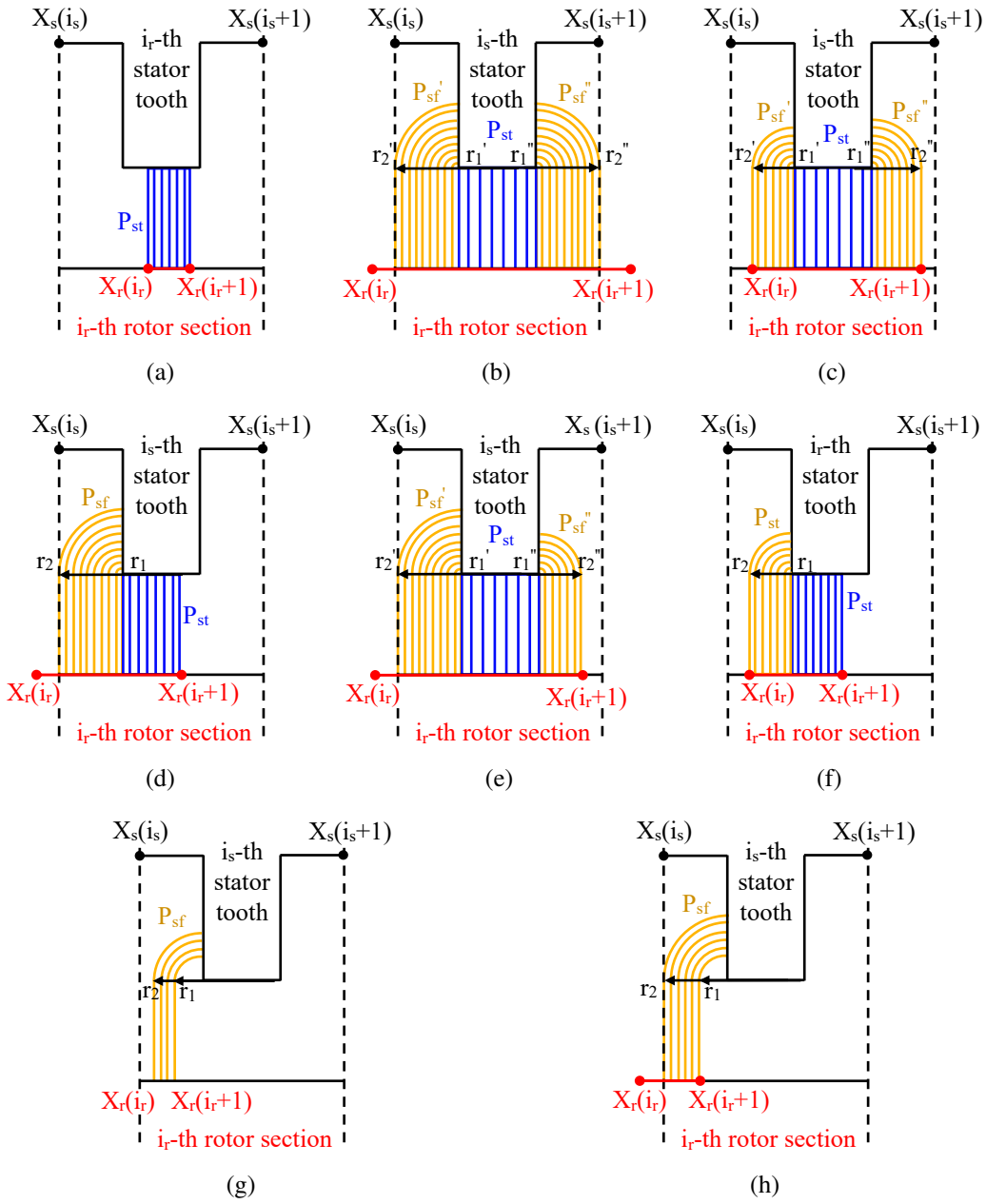

Fig. 3.12 Possible connection cases between the i_s-th stator tooth and the i_r-th rotor section.

In order to compute the air gap permeance, one must know how the i_s-th stator tooth connects to the i_r-th rotor section. Figure 3.12 shows eight of the thirteen considered possible cases of connection. For the economy of space, the conditions symmetric to the cases (d) to (h) are not reported. For example, Fig.3.12g has a dual case in which the fringing flux is on the right side of the tooth. The computation of

Table 3.1 Computation of the air gap reluctance for case (a).

	CASE (a)
Case conditions	$\begin{cases} x_r(i_r) > x_s(i_s) + \frac{\alpha_s - \alpha_t}{2} \\ x_r(i_r+1) < x_s(i_s+1) - \frac{\alpha_s - \alpha_t}{2} \end{cases}$
Main flux permeance	$P_{st} = \frac{\mu_0 \cdot L}{g} \left[(x_2(i_r+1) - x_2(i_r)) \cdot \frac{D_g}{2} \right]$
Fringing flux permeance	$P_{sf} = 0$

Table 3.2 Computation of the air gap reluctance for case (b).

	CASE (b)
Case conditions	$\begin{cases} x_r(i_r) < x_s(i_s) \\ x_r(i_r+1) > x_s(i_s+1) \end{cases}$
Main flux permeance	$P_{st} = \frac{\mu_0 \cdot L}{g} \left[\alpha_s \cdot \frac{D_g}{2} \right]$
Fringing flux permeance	$\begin{cases} r_1' = r_1'' = 0 \\ r_2' = r_2'' = \frac{\alpha_s - \alpha_t}{2} \cdot \frac{D_g}{2} \\ P_{sf} = 2 \cdot \int_{r_1'}^{r_2'} \frac{\mu_0 \cdot L}{\frac{\pi}{2} \cdot r + g} dr \end{cases}$

Table 3.3 Computation of the air gap reluctance for case (c).

	CASE (c)
Case conditions	$\begin{cases} x_r(i_r) > x_s(i_s) \quad \& \quad x_r(i_r) < x_s(i_s) + \frac{\alpha_s - \alpha_t}{2} \\ x_r(i_r+1) > x_s(i_s+1) \end{cases}$
Main flux permeance	$P_{st} = \frac{\mu_0 \cdot L}{g} \left[\alpha_s \cdot \frac{D_g}{2} \right]$
Fringing flux permeance	$\begin{cases} r_1' = r_1'' = 0 \\ r_2' = \left(x_s(i_s) + \frac{\alpha_s - \alpha_t}{2} - x_r(i_r) \right) \cdot \frac{D_g}{2} \\ r_2'' = \left(x_r(i_r) - x_s(i_s+1) + \frac{\alpha_s - \alpha_t}{2} \right) \cdot \frac{D_g}{2} \\ P_{sf} = \int_{r_1'}^{r_2'} \frac{\mu_0 \cdot L}{\frac{\pi}{2} \cdot r + g} dr + \int_{r_1''}^{r_2''} \frac{\mu_0 \cdot L}{\frac{\pi}{2} \cdot r + g} dr \end{cases}$

the air gap permeances is shown only for the first three cases since the others can be obtained through the same methodology. The case conditions, the computation of the main flux permeance and the fringing flux permeance are recollected in Table 3.1, Table 3.2, and Table 3.3 for cases (a), (b), and (c), respectively.

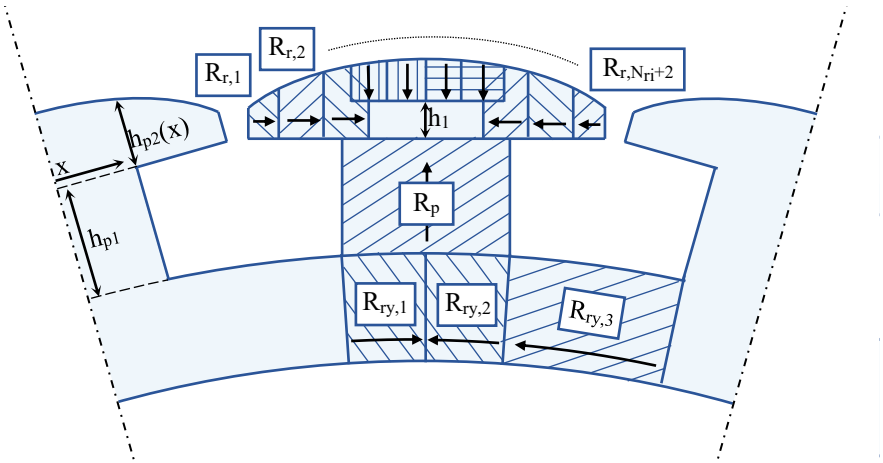

Fig. 3.13 Rotor iron reluctances.

Rotor iron reluctances

The values of the rotor reluctances are computed according to [108]. The configuration of the rotor iron reluctances is shown in Fig.3.13. The total number of pole tip reluctances depends on the selected number of discretized elements of the rotor pole N_{ri}. In particular, selecting N_{ri} nodes on the rotor pole tip leads to $N_{ri}+2$ reluctances considering the two external ones, as shown in Fig.3.9, in which $N_{ri}=8$. The configuration is designed so that flux flows tangentially in the pole tip on both sides of the pole body, while it flows radially directly above the rotor pole body, as indicated by the arrows in in Fig.3.13. The width of a pole tip section is computed as in (3.35), in which the numerator is the geometric arc occupied by the rotor pole tip.

$$w_{ri} = \frac{D_g \cdot \sin(k_b \cdot \frac{\pi}{2p})}{N_{ri}} \tag{3.35}$$

The value w_{ri} represents the length of the flux tubes of the tangential reluctance and the width of the flux tubes of the radial reluctances.

The height of each pole tip section can be evaluated through (3.36), where h_{p1} and the variable x are shown in Fig.3.13. The value h_{p2} represents the length of the flux tubes of the radial reluctance and the width of the flux tubes of the tangential reluctances.

$$h_{p2}(x) = \sqrt{\left(\frac{D_{ro}}{2} - g(x)\right)^2 - x^2} - \left(\frac{D_{ri}}{2} + h_{ry} + h_{p1}\right) \tag{3.36}$$

The flux tubes of the reluctances at the extremities of the pole tip have half the length of the other tangential reluctances.

$$R_{ri,1} = \frac{w_{ri}/2}{\mu_0 \cdot \mu_{ri}(1) \cdot L \cdot k_{st} \cdot h_{p2}\left(w_{ri} \cdot \left(\frac{N_{ri}}{2} - \frac{1}{4}\right)\right)} \tag{3.37}$$

$$R_{ri,N_{ri}+2} = \frac{w_{ri}/2}{\mu_0 \cdot \mu_{ri}(N_{ri}+2) \cdot L \cdot k_{st} \cdot h_{p2}\left(w_{ri} \cdot \left(\frac{N_{ri}}{2} - \frac{1}{4}\right)\right)} \tag{3.38}$$

The number of tangential reluctances depends on the machine geometry. Specifically, one can compute the total length occupied by the tangential reluctances as in (3.39), where l_t refers to half of the pole tip, and the variable $h_1 = 1/2 \cdot h_{p2}(N_{rt} \cdot w_{rt}/4)$ is reported in Fig.3.13.

$$l_t = \frac{N_{ri} \cdot w_{ri} - w_p}{2} + min\left(\frac{w_p}{4}, h_1\right) \tag{3.39}$$

Therefore, the number of tangential reluctances on half of the pole, excluding the extremity one, is the next higher integer of (3.40).

$$n_t = \frac{l_t}{w_{ri}} - \frac{1}{2} w_{ri} \tag{3.40}$$

The length of the innermost tangential reluctance l_{ti} cannot then be w_{ri}, but it is determined by the remaining length from l_t. Accordingly, the value of the reluctance is computed as in (3.42).

$$l_{ti} = l_t - (0.5 + n_t - 1) \cdot w_{ri} \tag{3.41}$$

$$R_{ri}(n_t) = \frac{l_{ti}}{\mu_0 \cdot \mu_{ri}(n_t) \cdot L \cdot k_{st} \cdot h_{p2}\left(w_{ri} \cdot (0.5 + n_t) - \frac{l_{ti}}{2}\right)} \tag{3.42}$$

The remaining tangential reluctances are computed similarly to (3.37), (3.38) and (3.42), but considering the length equal to w_{ri} and updating the function h_{p2} according to the position of the reluctance. The radial reluctance can also be obtained similarly, but using $h_{p2}(x) - h_1$ as length and w_{ri} as width of the flux tubes.

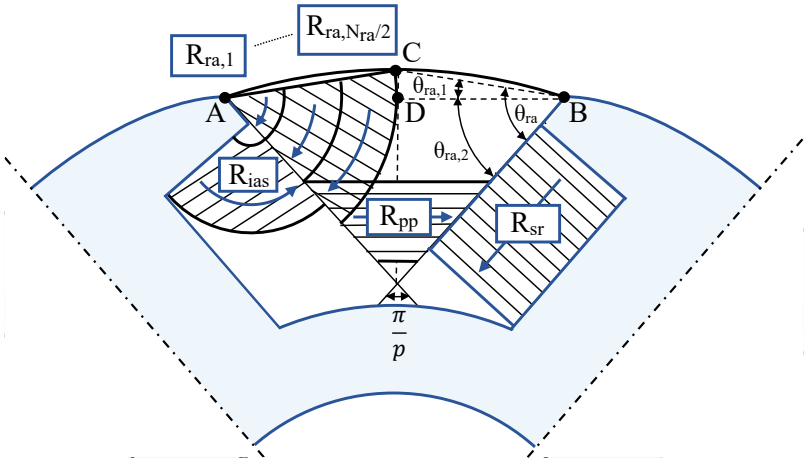

Fig. 3.14 Rotor interpolar air reluctances.

The computation of the rotor pole body reluctance is a straightforward procedure, as shown in (3.43).

$$R_p = \frac{h_{p1}}{\mu_0 \cdot \mu_{ri}(n_t) \cdot L \cdot k_{st} \cdot w_p} \tag{3.43}$$

The rotor yoke reluctances, $R_{ry,1}$, $R_{ry,2}$ and $R_{ry,3}$ feature that same flux tube surface, whose width coincides with the rotor yoke width, but different flux tube length. The length of $R_{ry,1}$ and $R_{ry,2}$ can be computed as in (3.44), while that of $R_{ry,3}$ as in (3.45).

$$l_{ry,12} = w_p \cdot \arcsin\left(\frac{w_p}{D_{ri} + h_{ry}}\right) \tag{3.44}$$

$$l_{ry,3} = \frac{D_{ri} + h_{ry}}{2} \cdot \left(\frac{\pi}{2} - 2 \cdot \arcsin\left(\frac{w_p}{D_{ri} + h_{ry}}\right)\right) \tag{3.45}$$

Rotor air reluctances

The configuration of the reluctances in the interpolar air is shown in Fig.3.14, where R_{ra} represents the rotor fringing, R_{pp} the rotor pole leakage, R_{ias} the fringing from the bottom of the pole, R_{sr} the rotor winding leakage [108].

The reluctances in the interpolar region R_{ra} are defined starting from the line that connects the corner of the rotor tip, point A of Fig.3.14, to the centre of the interpolar region at the radius $D_{si}/2 - g_{max}$, point C of Fig.3.14. The parameter g_{max} is the

maximum air gap length inside the rotor pole tip, computed as $g(k_b \cdot \pi/2)$. Therefore, the reluctances R_{ra} are not considered part of the air gap, with the advantage of simplifying the model [108]. The number of the reluctances in the interpolar region coincides with the discretized elements N_{ra}, as depicted in Fig.3.9.

The widths of the interpolar flux tubes w_{ra} are considered to be uniform and equal to the interpolar region length of both sides divided by the number of discretized elements N_{ra}. The length is approximated as the length of the arc centred with respect to the flux tube.

$$l_{ra,i} = \theta_{ra}\left(\frac{w_{ra}}{2} + w_{ra} \cdot (i-1)\right) \tag{3.46}$$

The angle θ_{ra} is shown in Fig.3.14, and its value can be computed by summing $\theta_{ra,1}$ and $\theta_{ra,2}$.

$$\overline{AB} = (D_{si} - 2 \cdot g_{max}) \cdot \sin\left(\frac{1}{2} \cdot (1-k_b) \cdot \frac{\pi}{p}\right) \tag{3.47}$$

$$\overline{CD} = \left(\frac{D_{si}}{2} - g_{max}\right) - \sqrt{\left(\frac{D_{si}}{2} - g_{max}\right)^2 - \left(\frac{\overline{AB}}{2}\right)^2} \tag{3.48}$$

$$\theta_{ra,1} = \arctan\left(\frac{\overline{CD}}{\overline{AB}/2}\right) \tag{3.49}$$

$$\theta_{ra,2} = \frac{1}{2} \cdot \left(\pi - \frac{\pi}{p}\right) \tag{3.50}$$

The reluctance representing the fringing through the bottom of the pole tip R_{ias} is computed as in (3.51), considering that the width of the flux tube includes the entire bottom of the pole tip except for a small section of length $w_{ri}/4$ at the outside edge.

$$R_{ias} = \frac{2}{\pi} \cdot L \cdot \ln\left(\frac{(w_{ri} \cdot N_{ri} - w_p)/2}{w_{ri}/4}\right) \tag{3.51}$$

The width of the flux tube that represents the leakage pole-to-pole (R_{ias}) is set to one-third of the height of the pole h_p [108]. The flux tube length is computed

through equation (3.52), considering the placement of the flux tube centre at the end of the fringing reluctances.

$$l_{pp} = \frac{\overline{AB}}{3} \cdot \left(\frac{1}{\cos(\theta_{ra,2})} - 1 \right) \cdot \sin\left(\frac{\pi}{2p} \right) \tag{3.52}$$

Finally, the field leakage reluctance is obtained considering a rectangular geometry. The value of the reluctance R_{sr} is computed as in (3.53), where w_f is the field winding width.

$$R_{sr} = \frac{3h_p}{\mu_0 L w_f} \tag{3.53}$$

3.2.3 The system of non-linear equations

The solution of the circuit in Fig.3.9 is obtained by applying the Kirchhoff's voltage law to each loop, creating a system of non-linear equations, as in (3.54). The matrix $\boldsymbol{A_R}$ is the reluctance matrix, $\boldsymbol{\Phi}$ is the vector containing the loop fluxes, and $\boldsymbol{F}$ is the vector of the m.m.f. sources, n_l is the sum of n_s, n_r and n_a, i.e. the total number of flux loops in the circuit.

$$\boldsymbol{A_R}^{[n_l \, x \, n_l]} \boldsymbol{\Phi}^{[n_l \, x \, 1]} = \boldsymbol{F}^{[n_l \, x \, 1]} \tag{3.54}$$

The vector of the loop fluxes $\boldsymbol{\Phi}$ contains the n_s loops in the stator, the $n_r = 3$ loops in the rotor, and the n_a loops in the air gap. These loop fluxes represent the unknowns of the problem to be solved.

$$\boldsymbol{\Phi} = [\Phi_{s,1} \ \ldots \ \Phi_{s,n_s} \quad \Phi_{a,1} \ \ldots \ \Phi_{a,n_a} \quad \Phi_{r,1} \ \ldots \ \Phi_{r,n_r}]^T \tag{3.55}$$

Similarly, the vector of the m.m.f. sources $\boldsymbol{F}$ contains the n_s m.m.f sources in the stator, the $n_r = 3$ m.m.f. loops in the rotor, and the n_a m.m.f. loops in the air gap. These values represent the inputs of the circuit.

$$\boldsymbol{F} = [F_{s,1} \ \ldots \ F_{s,n_s} \quad F_{a,1} \ \ldots \ F_{a,n_a} \quad F_{r,1} \ \ldots \ F_{r,n_r}]^T \tag{3.56}$$

The m.m.f. sources can be grouped into three sub-matrices associated with the stator, the rotor and the air gap. However, as no conductors are present in the air gap region, no m.m.f source exists in the air gap loops. The vector $\boldsymbol{F}$ can be then simply converted into (3.57).

$$\boldsymbol{F} = \left[\boldsymbol{F}_s^{[1\ x\ n_s]} \quad \boldsymbol{F}_r^{[1\ x\ n_r]} \quad \boldsymbol{0}^{[1\ x\ n_a]} \right]^T \tag{3.57}$$

The m.m.f sources in the stator depend on the stator winding matrix $\boldsymbol{N}_{abc}$ and the stator phase currents $\boldsymbol{i}_{abc}$.

$$\boldsymbol{F}_s^{[1\ x\ n_s]} = \boldsymbol{i}_{abc}^{[1\ x\ 3]} \boldsymbol{N}_{abc}^{[3\ x\ n_s]} \tag{3.58}$$

The stator winding matrix $\boldsymbol{N}_{abc}$ is built depending on the specific machine stator winding arrangement, for instance, distributed or concentrated, double or single layer, and ultimately depends on the number of slots per pole and per phase q, and the number of turns in series per phase in one slot Z_c. An example is provided in (3.59), relative to a 2-poles per slot per phase machine with single-layer distributed winding. The stator phase currents $\boldsymbol{i}_{abc}$ vector contains the instantaneous values of the currents, here developed as a consequence of imposing dq-currents.

$$\boldsymbol{N}_{abc} = \begin{bmatrix} Z_c & 0 & 0 & 0 & 0 & -Z_c \\ 0 & 0 & 0 & Z_c & Z_c & 0 \\ 0 & -Z_c & -Z_c & 0 & 0 & 0 \end{bmatrix} \tag{3.59}$$

The rotor m.m.f. sources exist only in the first two loops of the three rotor loops, according to Fig.3.9. In particular, the rotor m.m.f. sources vector is obtained through (3.60), considering that no m.m.f. source is present in the third loop of the rotor flux loops, see Fig.3.9.

$$\boldsymbol{F}_r^{[1\ x\ n_r]} = [-1\ \ 1\ \ 0] \cdot N_r \cdot I_r \tag{3.60}$$

The value of the unknowns can be computed through (3.54), if the reluctance matrix $\boldsymbol{A_R}$ is determined. The matrix of reluctances is based on the network topology and calculated through the reluctances computed in the previous section. A division into sub-matrices is reported in (3.61), in which $\boldsymbol{A}_s$ is associated with the stator

reluctances, $\boldsymbol{A}_r$ with the rotor reluctances, $\boldsymbol{A}_a$ with the air gap reluctances, while the off-diagonal matrices $\boldsymbol{A}_{a,s}$ and $\boldsymbol{A}_{a,r}$ represent the connection between the air gap and the stator, and the air gap and the rotor, respectively. No direct connection exists between the stator and the rotor.

$$\boldsymbol{A}_R = \begin{bmatrix} \boldsymbol{A}_s^{[n_s \, x \, n_s]} & \boldsymbol{0}^{[n_s \, x \, n_r]} & \boldsymbol{A}_{a,s}^{[n_s \, x \, n_a]} \\ \boldsymbol{0}^{[n_r \, x \, n_s]} & \boldsymbol{A}_r^{[n_r \, x \, n_r]} & \boldsymbol{A}_{a,r}^{[n_r \, x \, n_a]} \\ \boldsymbol{A}_{a,s}^T & \boldsymbol{A}_{a,r}^T & \boldsymbol{A}_r^{[n_a \, x \, n_a]} \end{bmatrix} \tag{3.61}$$

The matrix is populated according to the circuit theory for mesh-based solutions of networks. In particular, the generic element of the main diagonal in position (*i*,*i*) is the sum of all the reluctances of the *i*-th loop. The generic off-diagonal element in position (*j*,*k*) is the opposite of the sum of the reluctances in common between the *j*-th loop and the *k*-th loop. An example is given by equations (3.62) and (3.63).

$$\boldsymbol{A}_s(1,1) = R_{st,1} + R_{sy,1} + R_{st,2} + R_{ss} \tag{3.62}$$

$$\boldsymbol{A}_s(1,2) = \boldsymbol{A}_s(2,1) = -R_{st,2} \tag{3.63}$$

However, attention must be paid to the off-diagonal elements that include border reluctances. Let's consider the border reluctance $R_{st,1}$ of the circuit in Fig.3.9. A fictitious connection is imagined between loop 1 and loop n_s. Yet, loop n_s is actually connected to the loop n_s+1, whose flux has the same value as loop 1 but the opposite sign, because of the machine's antiperiodicity. Therefore, the connection between loop 1 and loop n_s must be corrected by changing the sign of the corresponding off-diagonal element.

$$\boldsymbol{A}_s(1,n_s) = \boldsymbol{A}_s(n_s,1) = +R_{st,1} \tag{3.64}$$

The same concept applies to the border reluctances of the air gap and of the rotor, as shown, for example, in (3.65) and (3.66).

$$\boldsymbol{A}_a(1,n_a) = \boldsymbol{A}_s(n_a,1) = R_{ag,1} + R_{ra,1} \tag{3.65}$$

$$\boldsymbol{A}_r(1,n_r) = \boldsymbol{A}_r(n_r,1) = +R_{sr} \tag{3.66}$$

Therefore, by inspection of the circuit, the reluctance matrix is automatically populated following the procedure explained in the previous sections. Based on how many reluctances are formed and which stator tooth and rotor section they connect, the topology changes and, therefore, the reluctance matrix. The key to considering this aspect is to verify whether two consecutive rotor sections connect to the same stator tooth. If such a connection exists, two consecutive air gap reluctances are included in the reluctance matrix element together with one or more rotor reluctance. On the contrary, if two consecutive stator teeth connect to the same rotor section, the element must include the two consecutive air gap reluctance and the stator leakage reluctance. Otherwise, if none of these two possibilities is verified, the element must include two consecutive air gap reluctances, one or more stator leakage reluctances, and one or more rotor reluctances.

3.2.4 The Newton-Raphson solution

The solution of the circuit is obtained through the Newton-Raphson method, whose complete procedure is shown in Fig.3.15. Rearranging equation (3.54), it is possible to obtain the residual function to be used in the procedure.

$$f(\boldsymbol{\Phi}) = \boldsymbol{A_R}\boldsymbol{\Phi} - \boldsymbol{F} = 0 \tag{3.67}$$

The procedure consists of iteratively approximating $f(\boldsymbol{\Phi})$ near the current iterate $\boldsymbol{\Phi}^k$ by the linear function $f_l(\boldsymbol{\Phi})$, and then using the solution as the next iterate until a certain tolerance is reached. The function $f_l(\boldsymbol{\Phi})$ is obtained as in (3.68), where $\boldsymbol{J_R}$ is the Jacobian matrix.

$$f_l(\boldsymbol{\Phi}) = f(\boldsymbol{\Phi}^k) + \boldsymbol{J_R}(\boldsymbol{\Phi}^k) \cdot (\boldsymbol{\Phi} - \boldsymbol{\Phi}^k) \tag{3.68}$$

As a first step, an initial guess of $\boldsymbol{\Phi}$ must be assumed. In particular, it is considered that the iron is unsaturated, and the relative permeability of each reluctance is equal to the maximum offered by the material. Based on this assumption, each reluctance of the circuit is computed, and the reluctance matrix is built. Using equation (3.54), the initial guess of the loop fluxes is obtained.

The subsequent step is to compute the flux flowing through each reluctance of the circuit. For instance, taking the circuit of Fig.3.9 as a reference, the flux in the

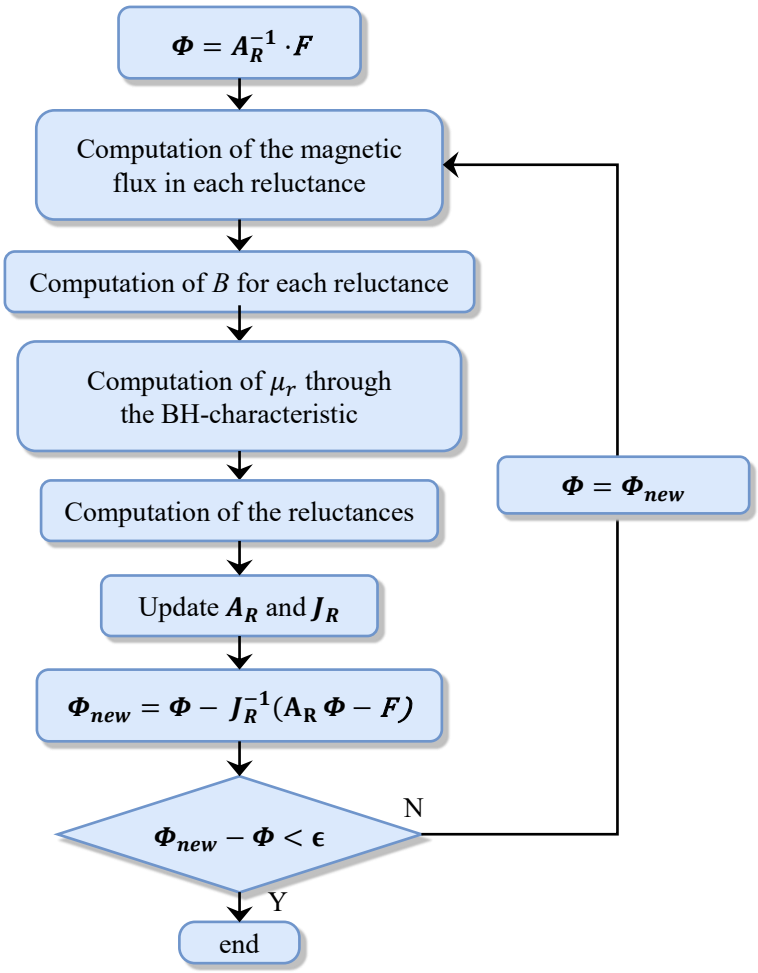

Fig. 3.15 Newthon-Raphson procedure.

reluctance $R_{sy,1}$ coincides with the flux loop 1, $\Phi_{s,1}$. On the contrary, the flux in $R_{st,2}$ is the difference between the flux in loop 1 and in loop 2, as in (3.69).

$$\Phi_{st,2} = \Phi_{s,1} - \Phi_{s,2} \tag{3.69}$$

Once the reluctance fluxes are known, the associated magnetic flux density is obtained by dividing by the surface of the corresponding flux tube. Thanks to the material magnetic characteristic, the magnetic permeability is retrieved, together with its derivative with respect to the magnetic flux density.

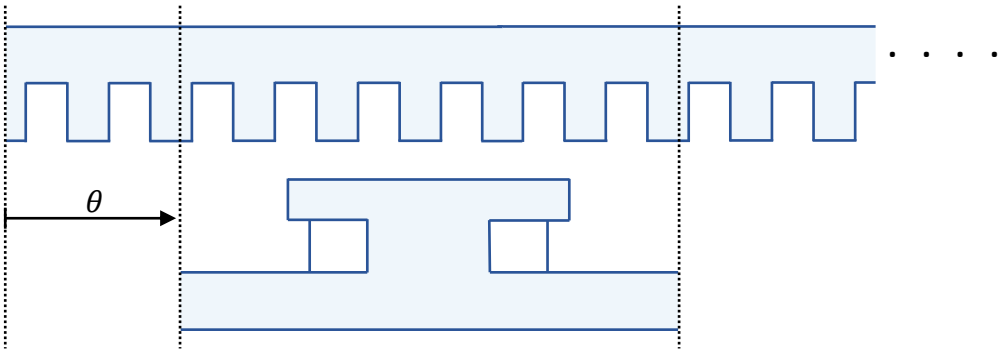

Fig. 3.16 Rotor interpolar air reluctances.

The obtained magnetic permeability is used to update the values of the reluctances, and, ultimately, the matrix $\boldsymbol{A_R}$. The derivative is used to update the Jacobian, as more thoroughly explained in Appendix A.

Finally, the new values of the loop flux vector are obtained as in (3.70), and compared to the starting values or the values of the previous iteration. If the defined tolerance is respected, the procedure is complete and the final results are obtained. Otherwise, the new loop flux vector is assumed as input, and the procedure is repeated.

$$\boldsymbol{\Phi}_{new} = \boldsymbol{\Phi} - \boldsymbol{J_R}^{-1}(\boldsymbol{A_R}\boldsymbol{\Phi} - \boldsymbol{F}) \tag{3.70}$$

3.2.5 The motion incorporation

At this stage, the model works only for a determined rotor position. In order to incorporate the motion in the magnetic equivalent circuit, a relative movement between the stator and the rotor must exist.

Although the rotor circuit can be built as a function of the rotor position [107], the alternative method proposed in this research is to slide the rotor circuit depending on the selected angular position and to connect the rotor to the corresponding stator section, as shown in Fig.3.16. This approach fixes the rotor network in the space and, therefore, the position of the rotor iron and the rotor air reluctances. The stator iron is repeated along the θ coordinate, while the rotor section coordinates are increased by θ. Then, the procedure to determine the air gap reluctances explained in Section 3.2.2 maintains its validity.

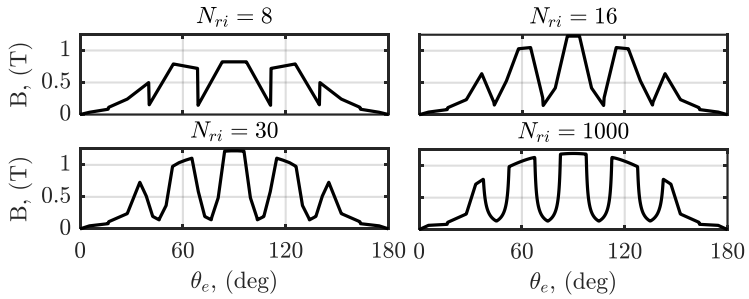

Fig. 3.17 Sensitivity analysis of the parameter N_{ri}.

However, the winding matrix N_{abc} must be built consistently when repeating the stator structure. For example, the matrix N_{abc} in (3.59) should be completed by appending by row the matrix $\boldsymbol{N}"_{abc}$, and then repeated as long as the selected angular position is included.

$$\boldsymbol{N}"_{abc} = \begin{bmatrix} -Z_c & 0 & 0 & 0 & 0 & Z_c \\ 0 & Z_c & Z_c & 0 & 0 & 0 \\ 0 & 0 & 0 & -Z_c & Z_c & 0 \end{bmatrix} \tag{3.71}$$

3.2.6 Comparison with FE simulations

The accuracy of the proposed magnetic equivalent circuit model depends on the selected discretization of the rotor sections, and in particular on the rotor iron elements N_{ri}. Figure 3.17 shows the impact of N_{ri} on the air gap flux density of a case study machine. The higher the number of rotor iron sections, the more accurate results are obtained, albeit with larger computational time. For example, for the cases with $N_{ri} \leq 30$ the time required to build the matrix and find the first solution is around 10ms, while for the case $N_{ri} = 1000$ is around 300ms, therefore 30 times more. Note that, to reach the convergence, the procedure is repeated a certain number of times, which may lead to significant differences in the final solving time. Nonetheless, it has been noted that generally less iterations are required with a higher number of rotor elements. A good compromise has been individuated in the case $N_{ri} = 30$.

The MEC model has been tested for different wound-field machines, including different numbers of poles, slots per pole and per phase, and slot dimensions. In particular, the results for a 4-pole, 2 slots per pole and per phase, distributed winding motor are shown in Fig.3.18. The model has been tested in different supplying

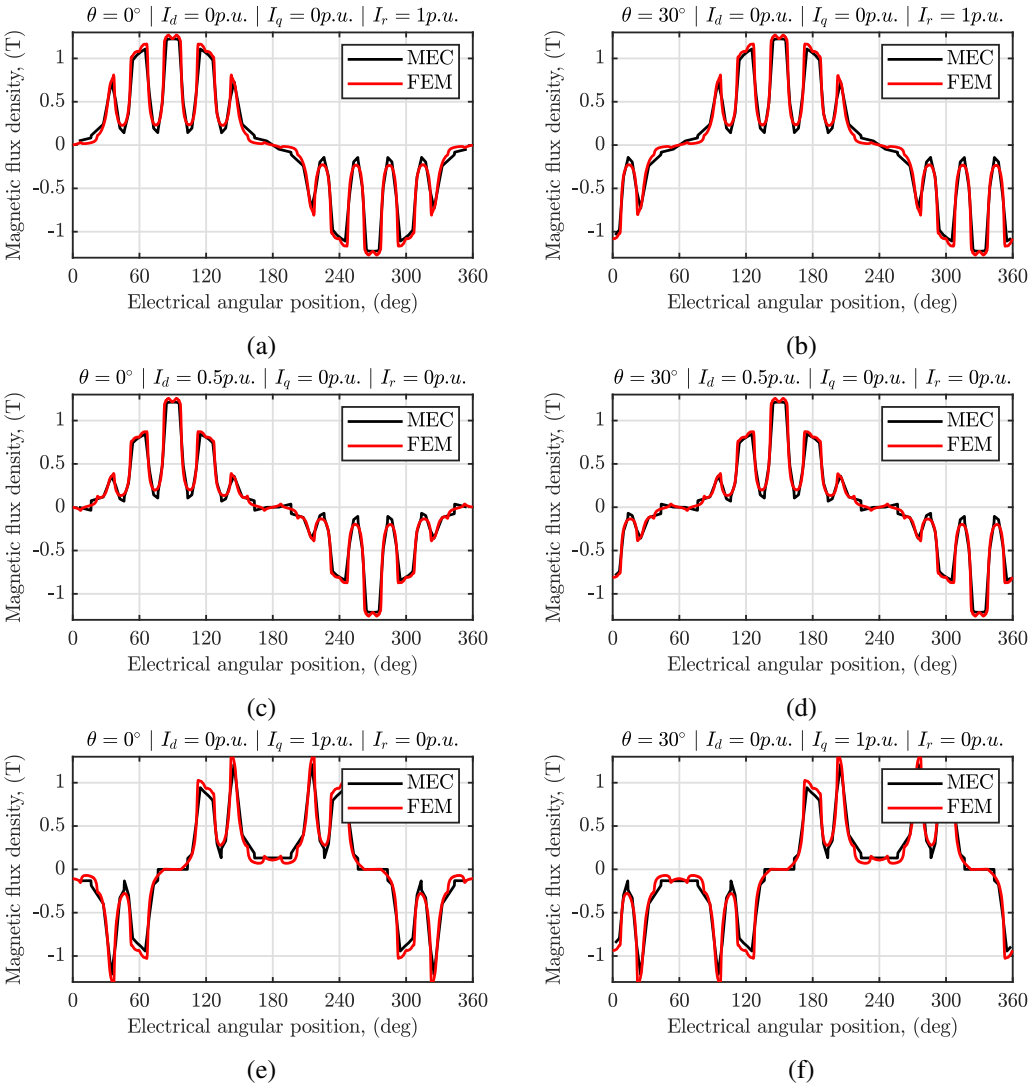

Fig. 3.18 Comparison between MEC and FEM results for the air gap flux density.

Table 3.4 Comparison between MEC and FEM results.

CASE	*Execution time*		*Flux density fundamental*		
	FEM	MEC	FEM	MEC	Err%
(a)	12.50s	1.22s	0.815T	0.787T	-3.5%
(b)	12.16s	0.59s	0.645T	0.619T	-4.0%
(c)	13.06s	1.03s	0.536T	0.556T	3.7%

conditions, aiming at producing a maximum value of the air gap magnetic flux density above 1T. The results are shown for two different rotor positions, i.e. 0° and 30°. Table 3.4 lists the achieved results for the cases at position 0°. The obtained errors with respect to FE simulations are lower than 5%, while the execution time is significantly reduced. Approximately 13s are necessary to obtain the results with the FE simulations, while less than 2s is the time required by the MEC, as evident from Table 3.4.

The case study machine has also been used to test the MEC in load conditions. Different rotor and stator current values have been assessed, considering the stator current vector to be placed in the q-axis. Starting from the loop fluxes in the stator, the flux linkages in the *abc* frame can be computed as in (3.72).

$$\boldsymbol{\Lambda}_{abc} = p \cdot \boldsymbol{N}_{abc} \cdot \boldsymbol{\Phi}_{\boldsymbol{s}} \tag{3.72}$$

Knowing the values of the *abc* fluxes, it is possible to compute the *dq* fluxes and, therefore, the electromagnetic torque through (2.14). The computation has been performed for different rotor positions. The magnetic reluctances of the MEC have been initialized in unsaturated conditions (with the maximum value of the material magnetic permeability) only for the first rotor position. For other rotor positions, the magnetic reluctances have been initialized with the magnetic permeability obtained in the previous step, as this represents a more realistic condition. This is done with the aim of easing the convergence process.

An example of the obtained magnetic fluxes is shown in Fig.3.19, together with the corresponding results obtained via finite element simulations. The obtained results in terms of electromagnetic torque and execution time are listed in Table 3.5 for different supply conditions. The magnetic fluxes of Fig.3.19 correspond to the second supply condition.

The results exhibit consistency with the data obtained through finite element analysis, with significantly reduced computational time. To be specific, half of the electric period has been simulated with a step of 1 electrical degree. Both the MEC and FEM have been tested without parallelization of the cores. The data in Table 3.5 show that the time required by the FEM to complete the simulation is approximately 15 minutes, while the MEC takes less than 1 minute. However, it must be noted that by increasing the currents, and therefore by increasing the machine saturation

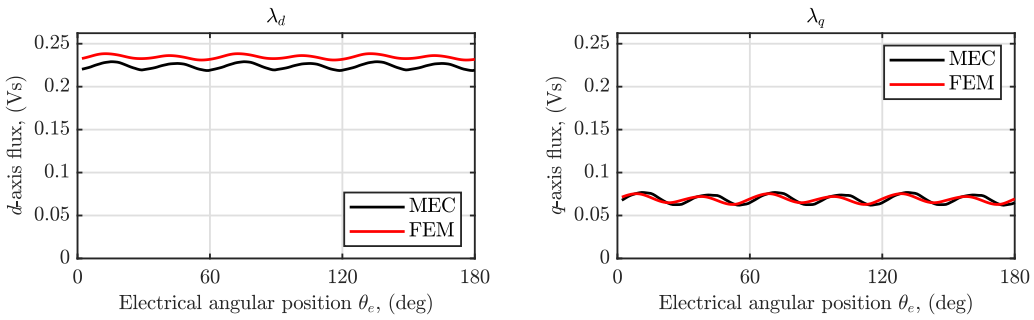

(a) (b)

Fig. 3.19 Comparison between MEC and FEM *dq*-fluxes.

Table 3.5 Comparison between MEC and FEM results for the electromagnetic torque.

Conditions	*Execution time*		*Electromagnetic torque*		
	FEM	MEC	FEM	MEC	Err%
$I_q = 38.2$A $I_r = 1.7$A	919.5s	4.6s	18.47Nm	17.81Nm	-3.6%
$I_q = 50.6$A $I_r = 2.6$A	913.4s	41.5s	35.81Nm	34.17Nm	-4.6%
*$I_q = 61.0$A $I_r = 3.0$A	919.9s	25.1s	47.26Nm	43.94Nm	-7.0%
$I_q = 76.3$A $I_r = 5.2$A	921.0s	DNC	77.66Nm	DNC	-

*The number of rotor sections has been increased to reach convergence.

level, the MEC encounters difficulties in finding convergence. For example, in the third case, the number of rotor sections has been doubled to reach the convergence condition. In this case, the time required by each iteration is still greater, but fewer iterations are needed to find the solution. This is the reason why the third condition, albeit more saturated, takes less than the second one. Finally, in the fourth case, the model does not converge, even with many rotor sections (>1000). To solve the problem, relaxation factors can be implemented in the Newton-Raphson method [131], which will be the object of future studies.

Table 3.6 Required input variables for the FE model.

Main dimensions		*Detailed dimensions*	
p	Number of pole pairs	F_{stat}	Shape of the stator slot
q	Slots per pole and per phase	F_{rot}	Shape of the rotor coil
m	Number of phases	h_{st}	Tooth height
L	Machine axial length	h_1	Inner tooth height
D_{so}	Stator outer diameter	h_2	Tooth tip height
D_{si}	Stator inner diameter	w_{st}	Stator tooth width
g_0	Minimum air gap length	w_{st0}	Stator tooth width at the air gap
D_{ri}	Rotor inner diameter	w_p	Pole body width
h_p	Rotor pole tip height	h_{p1}	Rotor pole body height
k_b	Extension of the pole tip	h_{re}	Lateral height of the rotor tip
BH	Magnetic characteristic	w_{cu}	Rotor winding distance from tip

3.3 The finite element model

In this research context, the last developed wound-field machine model is the finite element simulation, which has already been used as a validation tool for the analytical model and the magnetic equivalent circuit. The FE project is created using the software Matlab linked to the software FEMM, a popular open-source static FE solver [132]. Although the creation of finite element models is a self-explanatory procedure, this section provides a brief description of the parametric definition of the machine geometry and general information on the adopted solving process of the developed FE model. For further information, the complete Matlab code can be found in Appendix B.

3.3.1 The parametric design

The inputs required by the drawing code are listed in Table 3.6. The main machine dimensions and the detailed dimensions are the geometric variables shown in Fig.3.1 and Fig.3.20. The machine geometry is thus built in FEMM by Matlab, on the basis of these variables. The stator and rotor turns are not required by the code as they are fixed numbers. In particular, one turn is considered for the rotor winding and two

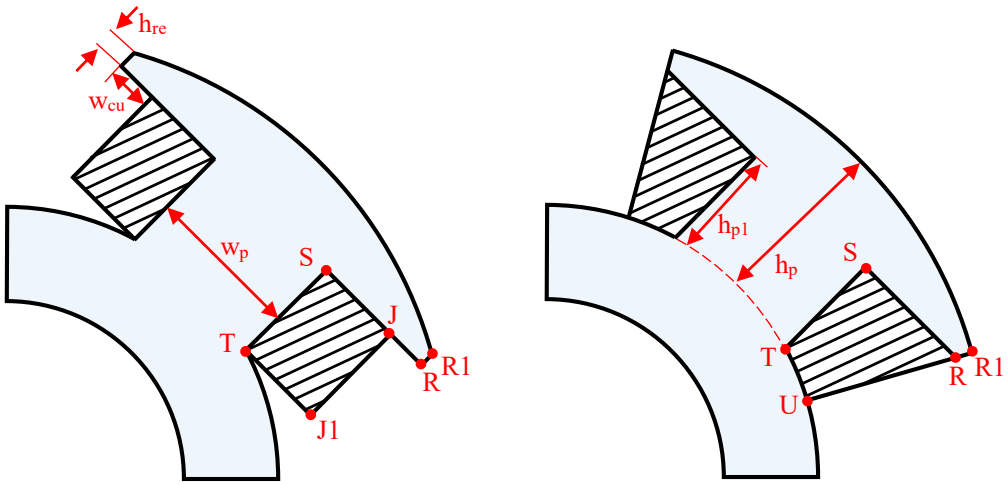

(a) (b)

Fig. 3.20 Considered rotor slot geometries: $F_{rot} = 0$ (a), and $F_{rot} = 1$ (b)

turns in series per slot for the stator winding (the reason is explained later), which are then coherently supplied during the solving process.

The proposed FE model exploits the machine's periodicity to draw only one geometry sector, reducing the required computational time. Moreover, the machine air gap is divided into three regions, and the rotor motion is simulated through the sliding band model [133]. The sliding band model allows keeping the same mesh regardless of the angular position of the rotor, therefore removing a significant cause of numerical errors. Among the inputs of Table 3.6, the only material-related information is the magnetic characteristic of the stator and rotor laminations. The rotor and stator windings are assumed to be made of copper, while air is assigned to the non-conductive and non-magnetic regions.

The two inputs F_{stat} and F_{rot} are two flag variables. If $F_{stat} = 0$ the stator lamination is built with rectangular teeth and trapezoidal slots; otherwise, the slots are considered rectangular and the teeth trapezoidal. Conversely, the variable F_{rot} affects the rotor coil shape. If $F_{rot} = 0$ the rotor coil is assumed to be rectangular; otherwise, the coil sides are drawn as radial lines, as shown in Fig.3.20. The figure also reports the same letters used in the drawing code of Appendix B. Although some error cases are already included and corrected in the drawing of the rotor, the recommendation is to use $F_{rot} = 0$ for small values of k_b, i.e. when the rotor pole tip

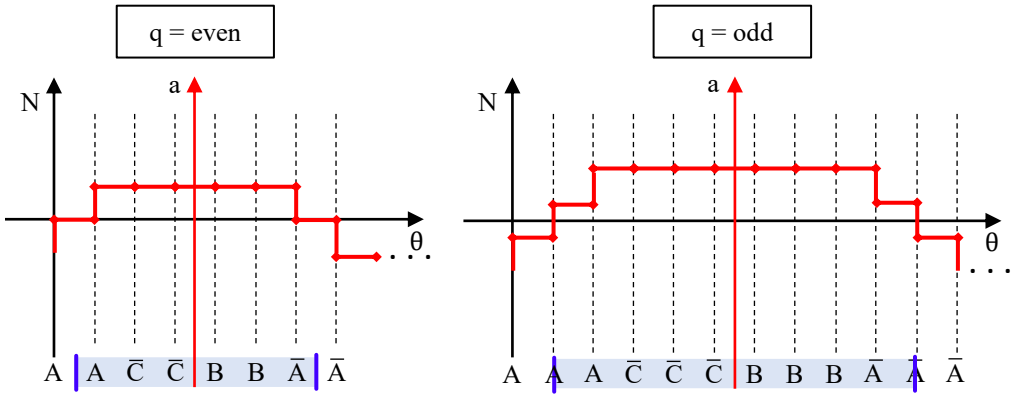

Fig. 3.21 Conductors distribution for even and odd number of slots per pole and per phase.

occupies a small percentage of the pole pitch. In contrast, the geometry with $F_{rot} = 1$ is more suitable for greater values of k_b.

The rotor pole

The considered rotor pole geometry is the inverse of the cosine of the angular coordinate starting from the d-axis, as for the models presented in the previous sections. In the FE model, the rotor pole profile is approximated as a series of arcs built over three points; each point is obtained through the cosine inverse function. The number of discretized points in the rotor profile is the variable *"n_points"* of the drawing code.

The d-axis alignment

The drawing code automatically aligns the rotor pole, i.e. the d-axis, with the magnetic axis of phase A. In particular, for single-layer distributed winding, the conductor distribution of phase A leads to a position of the corresponding magnetic axis in the centre of the tooth between B positive and C negative, as shown in Fig.3.21. Therefore, in order to verify the alignment, a stator tooth must always be placed in the direction of the rotor pole. This leads to two different geometries depending on the value of q, as depicted in Fig.3.21. In particular, for an even value of q, the geometry borders contain stator teeth. On the contrary, for an odd value of q, stator slots must be placed at the machine borders. This is evidenced by the blue lines of the figure, which delimit the drawn machine sector.

Being the rotor geometry fixed, the phases in the slots are thus allocated properly to verify the described alignment. Moreover, as an integer number must be used for the definition of the winding, and in the case of an odd number of q, only half slot is drawn for slot A positive and negative, the fixed number of turns in series per slot for the stator winding is two. Therefore, if I_s is the desired value of the stator current, and Z_c is the turns in series per slot, the stator winding of the FEMM project is supplied with:

$$I_{s,FEMM} = I_s \cdot \frac{Z_c}{2} \tag{3.73}$$

The solving process

The solving procedure of the machine obtained from the drawing model exploits the parallelization over multiple cores. The parallel computing allows for carrying out different computational processes simultaneously. Therefore, once the model is created, the simulations, for instance, of different rotor positions can be run independently and at the same time. This is accomplished by means of the Matlab function *"parfor"*, which divides the tasks assigned to a for loop over the available cores. Therefore, different FE simulations are performed contemporaryly, reducing the required computational time.

3.4 Conclusion

Different WFSM models have been developed and presented with the aim of selecting the most appropriate to be used in a sizing algorithm for the design of wound-field motors for traction applications. The proposed models include an analytical model, a magnetic equivalent circuit and a parametric FE model, which have proven to reach comparable results.

The analytical model features the lowest computational time, even considering the lamination saturation, the distortion of the air gap flux density and the magnetic shunt of the stator slots. However, the procedure is based on the assumption that the magnetic flux is placed only in the d-axis, which makes it unsuitable for evaluations in load conditions, where $I_q \neq 0$. However, the analytical model can efficiently assess the machine's performance in no-load conditions.

The magnetic equivalent circuit requires higher execution times since it is based on the solution of a system of non-linear equations through an iterative procedure, although still significantly reduced if compared to the finite element model. The MEC can asses the no-load and load machine's performance with output results comparable to finite element simulations. However, the main drawback is the difficulty in reaching the convergence for high saturation conditions.

The finite element model has been developed using the FEMM software, and a Matlab code has been built to automate the project creation process. The FEM represents the most accurate and time-consuming model. To address the computational burden, the model has been created by exploiting the machine periodicity, and the solving process has been achieved through parallelization over multiple cores.

The comparison of the three models has led to the conclusion that a combination of the analytical and finite element models represents the winning choice for the sizing code of wound-field motors. Indeed, although the MEC model reaches satisfactory results, further improvements in the convergence procedure are still needed in order to be used in an iterative sizing procedure. Therefore, the idea is to obtain a preliminary lamination geometry only relying on analytical equations in a negligible computational time and subsequently to refine the obtained machine with a limited number of FE simulations. The complete sizing procedure is described in Chapter 4.

Chapter 4

The Sizing Procedure

The focus of this research project has been on the electromagnetic sizing of wound-field synchronous motors. The ultimate goal of this endeavor has been to develop a preliminary, yet accurate, fast-sizing process, presented in [134]. This process has been conceived to provide motor designers and engineers with a reliable and efficient way of determining the preliminary size for these types of motors, starting from a limited number of machine specifications, such as targets and constraints.

The proposed methodology consists of a combination of the analytical and numerical approaches addressed in Chapter 3, to trade-off the fast computation time of the analytical formulations with accurate FEM analyses. The procedure of sizing progressively increases the machine diameter in order to ensure that all the input constraints are met and that the rated performances are guaranteed.

The process of determining the appropriate size for the lamination involves two distinct steps. Initially, strictly analytical equations are utilized to establish a preliminary geometry under no-load conditions. This geometry is then further refined through a limited number of FE simulations to ensure the rated load performances.

The proposed methodology was validated considering, as a case study, a reversely engineered salient-pole wound field synchronous motor used for traction applications, specifically the electric motor that equips the Renault ZOE. The electromagnetic information gathered from the actual machine was utilized as input for the sizing code, obtaining a lamination that closely matches the reference WFSM. The validation is covered in Chapter 5.

Table 4.1 Sizing input data.

Design targets	*Electromagnetic loading limits*
Torque (T)	Air-gap flux density at no-load ($B_{g,max}$)
Speed (n)	Stator yoke flux density at no-load ($B_{sy,max}$)
Stator phase voltage (V_s)	Rotor yoke flux density at no-load ($B_{ry,max}$)
Rotor voltage (V_r)	Teeth flux density at no-load ($B_{t,max}$)
BH-curve and stacking factor (k_{st})	Rotor pole flux density at no-load ($B_{p,max}$)
Power factor, ($cos\varphi$)	Stator current density ($J_{s,max}$)
Target efficiency (η)	Rotor current density ($J_{r,max}$)
Operating temperature (θ_o)	Linear current density ($A_{s,max}$)
Geometrical and winding specifications	
Machine aspect ratio ($\lambda = L/D_g$)	Stator slot opening dimensions (h_1, h_2, w_{t0})
Pole pairs number (p)	Stator slot filling factor (k_{fs})
Slots per pole per phase (q)	Rotor slot filling factors (k_{fr})
Minimum inner diameter (D_{ri})	Rotor pole span (k_b)
Minimum air gap thickness (g_0)	Rotor slot detailed dimensions (h_{re}, w_{cu})

4.1 Procedure inputs & Assumptions

The input data of the electromagnetic sizing algorithm comprehend the desired rated performances, the admissible electromagnetic loadings, some geometrical specifications, and a basic winding layout. Table 4.1 lists all the requested input data.

The rated torque and the rated speed are fundamental inputs to start the sizing process of any kind of rotating electrical motor, as they determine the rated shaft output power. In particular, the electromagnetic torque represents the ultimate target of the proposed algorithm. The stator and rotor voltages are also input data that must be chosen according to the available power source. The power factor is an important parameter to consider, and this is especially true for wound-field synchronous motors, as its value significantly impacts the resulting rotor and stator currents.

Regarding the electromagnetic loadings, which include the stator and rotor current densities, the linear current density, and magnetic flux densities, the maximum allowable values are contingent upon the insulation and cooling of the machine. These factors play a critical role in determining the safe limits for these loadings.

Empirically defined variation ranges of the electromagnetic loadings are well-known to electric machine designers, and their typical values can also be found in textbooks. It is worth noting that low surface current density and high linear current density values are suitable for large machines. Conversely, high current density and low linear current density values are suitable for small machines. In well-designed electric machines, both linear current density and flux density increase proportionally with machine size [79].

Among the geometrical specifications, the machine aspect ratio λ is defined as the ratio of the active core length (L) and the air gap diameter (D_g). Its value characterizes the shape of the machine (pancake or tubular shape) and can be fixed according to the volume constraints dictated by the specific application. The minimum inner diameter is also fixed, depending on the mechanical layout as well as on the shaft diameter that is required to deliver the output torque. The number of poles is also an input for the developed sizing procedure since it must be chosen as a trade-off between the required rotational speed and the supply frequency. Similarly, the slot enclosure dimensions are also imposed by the user according to the winding construction process that is intended to be used.

In the salient-pole WFSMs sizing process, the pole shoe is considered to be shaped such that the magnetic flux density at the air gap is proportional to the cosine of the electrical angle $\mathrm{p}\theta$, as described in Section 2.1.2. The value of the minimum air gap length g_0 of equation (2.3) is set as an input. Theoretically, in order to minimize the magnetizing current, it is ideal for g_0 to be as small as possible. Nevertheless, smaller air gaps produce larger eddy current losses because of the permeance harmonics of the slot openings. According to [79], the minimum value of the air gap length of synchronous machines can be found by imposing the rotor ampere-turns to be higher than the armature ampere-turns, with the aim of limiting the armature reaction. Its formulation is reported in (4.1), where γ is a coefficient that depends on the type of the machine (for the salient pole WFSM, its value is $7 \cdot 10^{-}7$, reported in [79]), and A_s is the stator linear current density. However, in many cases, the definitive minimum air gap also depends on mechanical considerations.

$$g_0 \geq \gamma \cdot \tau_p \cdot \frac{A_s}{B_g} \tag{4.1}$$

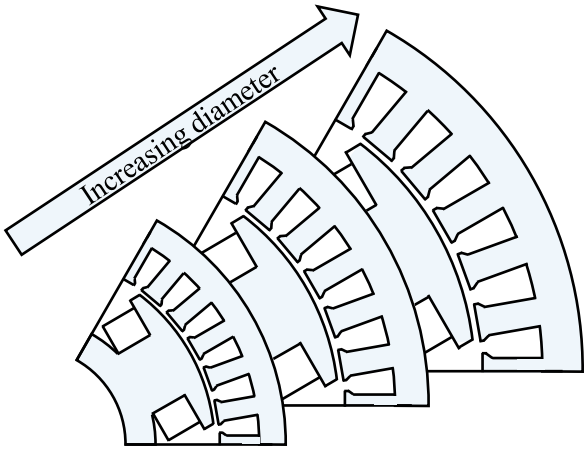

Fig. 4.1 Principle of operation of the sizing procedure.

Finally, the pole shoe width as a fraction of the pole pitch, k_b, is defined by (4.2), where β is the angular span occupied by the rotor pole. Higher values of k_b mean lower values of the saliency ratio; in this case, the resulting geometry features a better mechanical enclosure of the rotor conductors, but also a larger leakage flux among the poles.

$$k_b = \frac{\beta}{\pi/p} \tag{4.2}$$

4.2 The sizing algorithm

The proposed electromagnetic sizing procedure has been implemented in Matlab. However, any programming language or numerical computing language can be used for this purpose. The algorithm considers an initial air gap diameter that is slightly greater than the constrained minimum inner rotor diameter. Therefore, its value is iteratively increased of a predefined quantity until all the input constraints are respected, as shown in Fig.4.1. This methodology allows obtaining the smallest feasible motor for the required input constraints. In achieving the final machine size, the algorithm pursues two subsequent steps. In the first step, a preliminary design is obtained through analytical sizing; while refinements are obtained in the second step with limited FE simulations. The complete procedure is described hereafter and shown in the flow chart of Fig.4.2.

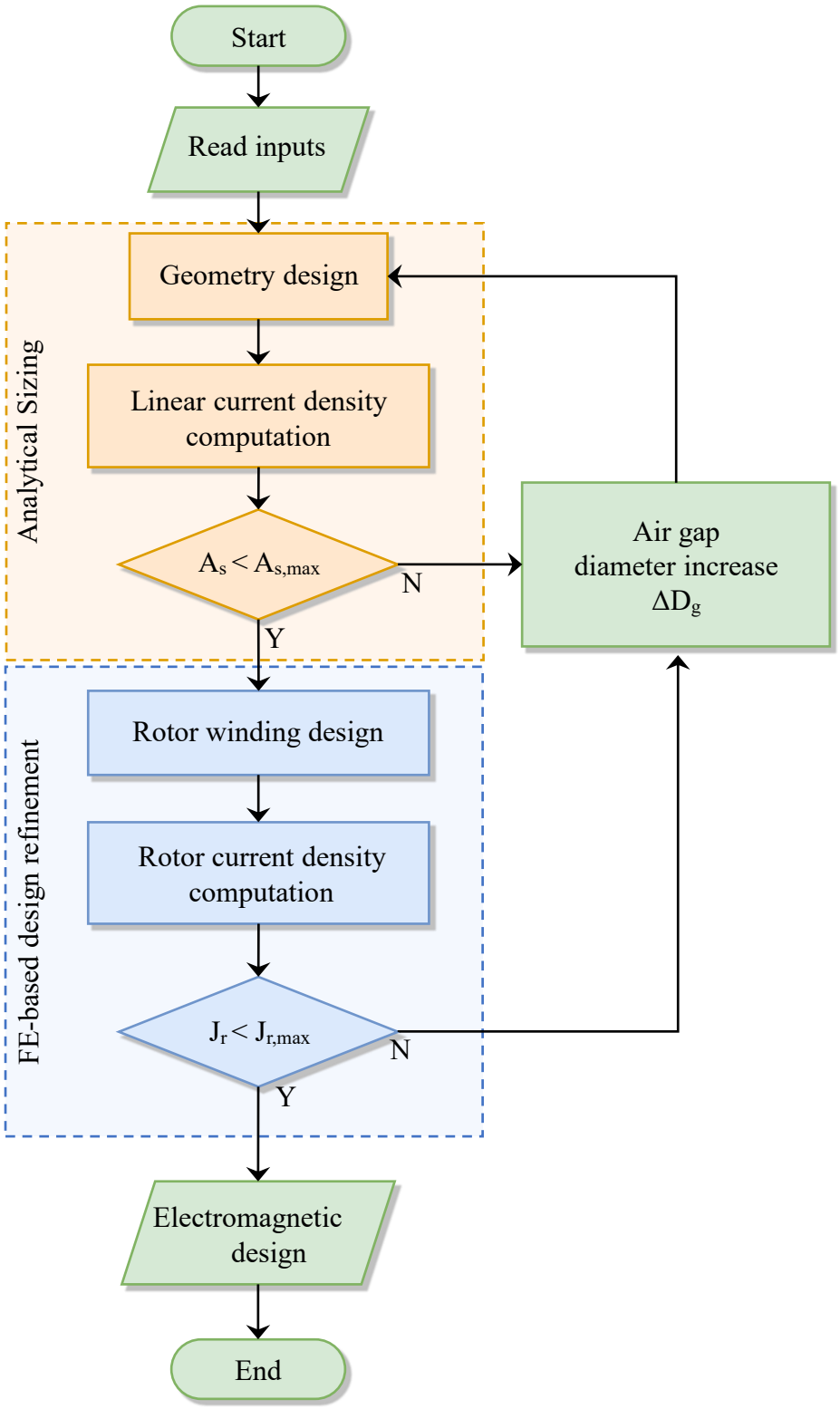

Fig. 4.2 Sizing algorithm flow-chart

4.2.1 Preliminary analytical sizing

The first step of the sizing procedure consists of creating a preliminary lamination geometry only relying on analytical equations and considering the machine magnetic loadings in no-load conditions.

The sizing process starts by computing the main machine's dimensions (D_{ro}, D_{si} and L of Fig.3.1), knowing the air gap diameter.

$$D_{ro} = D_g - g_0 \tag{4.3}$$

$$D_{si} = D_g + g_0 \tag{4.4}$$

$$L = \lambda \cdot D_g \tag{4.5}$$

Therefore, the value of the flux per pole is computed on the basis of the imposed maximum air gap flux density as in (4.6). The parameter α_s is the coefficient of the arithmetical average of the magnetic flux density, which is equal to $2/\pi$ for a sinusoidal distribution, assumed as first initial guess. When the iron lamination saturates, the air gap flux density is distorted, affecting the value of α_s. Therefore, in the developed sizing procedure, the correct value of α_s is iteratively determined once the geometric dimensions are defined, as later explained.

$$\Phi_p = \alpha_s \cdot \tau_p \cdot L \cdot B_{g,max} \tag{4.6}$$

The number of turns in series per phase is determined as in (4.7), where f is the electrical frequency, and E_s is the electromotive force in no load conditions. Considering the impact of the armature reaction, it is assumed that the value of the no-load voltage E_s might exceed of 1.2-1.3 times the stator voltage V_s in load conditions. Such a range is considered reasonable also for high-armature reaction machines [79].

$$N_1 = \frac{E_s}{2\pi/\sqrt{2} \cdot k_w \cdot f \cdot \Phi_p} \tag{4.7}$$

The theoretically obtained value of N_1 is then rounded up to the nearest integer, and the computation of the flux per pole is adjusted accordingly.

The value of the stator current is obtained considering the required stator active power and neglecting the rotor power. Knowing the imposed stator phase voltage, the rotational speed, the efficiency, and the power factor, the stator current amplitude can be computed as:

$$I_s = \frac{T \cdot n \cdot \frac{\pi}{30}}{3 \cdot V_s \cdot \eta \cdot cos\varphi} \tag{4.8}$$

On the basis of the turns in series per phase and the amplitude of the stator current, the stator linear current density is computed through (4.9).

$$A_s = \frac{I_s \cdot m \cdot 2N_1}{\pi D_g} \tag{4.9}$$

If the resulting linear current density exceeds the corresponding imposed constraint ($A_{s,max}$), the air gap diameter is increased by a defined step size ΔD_g, and the computation is repeated. Once the loop is solved, the main preliminary dimensions of the lamination geometry are obtained.

Additional calculations

The remaining geometrical variables are found on the basis of the resulting flux per pole. In detail, the tooth width w_{st} is computed by (4.10), considering the magnetic flux related to one slot pitch.

$$\tau_s \cdot L \cdot B_{g,max} = w_{st} \cdot L \cdot k_{st} \cdot B_{t,max} \tag{4.10}$$

The stator slot area is determined by the stator current density J_s and the linear current density A_s.

$$S_{ss} = \frac{A_s \cdot \tau_s}{k_{fs} \cdot J_s} \tag{4.11}$$

Therefore, the stator slot height h_{us} can be simply determined by geometrical considerations, depending on the desired slot shape. For instance, for a trapezoidal slot shape, knowing the surface (S_{ss}) and the width of both the bases (w_{s1} and w_{s2}) of

the slot trapezoid, the height is simply obtained by solving the second-order equation resulting from (4.12), considering x the unknown value of the slot height.

$$\begin{cases} S_{ss} = \frac{1}{2}\left(w_{s1} + w_{s2}(x)\right) \cdot x \\ w_{s1} \simeq (D_g + 2 \cdot h_2) \cdot \frac{\pi}{N_s} - w_{st} \\ w_{s2}(x) \simeq (D_g + 2 \cdot h_2 + 2 \cdot x) \cdot \frac{\pi}{N_s} - w_{st} \end{cases} \tag{4.12}$$

Taking into account that the developed code is intended for fast lamination sizing, only simple slot geometries, such as rectangular or trapezoidal shapes, have been considered. Further detailed refinements, such as fillets or particular slot shapes, can then be addressed in the project finalization stage without heavily impacting the machine's performance [135, 136].

Once the tooth dimensions have been defined, the teeth' magnetic voltage and the air gap magnetic voltage are computed, as per the explanation provided in Section 3.1.1. Considering k_{sat} to be the ratio between the m.m.f. drop in the teeth and the m.m.f. drop in the air gap, and assuming that the distortion of the magnetic flux density in the air gap is mainly due to the saturation of the teeth, the parameter α_s is updated as in (4.13), according to [79].

$$\alpha_s = \frac{1.24 k_{sat} + 1}{1.42 k_{sat} + 1.57} \tag{4.13}$$

Therefore, a new value for the air gap flux density is computed by (4.6), and the lamination design is recomputed. The process is iteratively repeated until the convergence on α_s is achieved with a defined tolerance.

The width of the rotor yoke, rotor pole and stator yoke are obtained by solving the magnetic circuit in the d-axis for the magnetic flux per pole.

$$h_{ry} = \frac{\Phi_p/2}{B_{ry,max} \cdot L \cdot k_{st}} \tag{4.14}$$

$$w_p = \frac{\Phi_p}{B_{sy,max} \cdot L \cdot k_{st}} \tag{4.15}$$

$$h_{sy} = \frac{\Phi_p/2}{B_{sy,max} \cdot L \cdot k_{st}} \tag{4.16}$$

Finally, the machine geometry is completed by computing the rotor pole height and the stator outer diameter.

$$h_p = \frac{D_{ro}}{2} - h_{ry} - \frac{D_{ri}}{2} \tag{4.17}$$

$$D_{so} = D_{ro} + 2 \cdot g + 2 \cdot h_2 + 2 \cdot h_{us} + 2 \cdot h_{sy} \tag{4.18}$$

The rotor pole height h_p is then divided into h_{p1} and h_{p2}, depending on the selected value of h_{re} and the chosen rotor geometry, according to the two alternatives of Fig.3.20. Also, the rotor 'slot' area S_r is calculated based on the chosen geometry. For example, for the rotor case $F_{rot} = 1$, the surface is computed as in (4.19), where P is the quadrilateral perimeter. For the case $F_{rot} = 0$, S_r is simply the surface of a rectangle.

$$S_r = \sqrt{(P/2 - \overline{ST}) \cdot (P/2 - \overline{TU}) \cdot (P/2 - \overline{UR}) \cdot (P/2 - \overline{RS})} \tag{4.19}$$

4.2.2 The lamination design in load conditions

The second step of the sizing process involves assessing the load conditions to determine the appropriate stator and rotor currents required to ensure the desired rated performance. This is a crucial aspect of the process as it ensures that the machine is capable of handling the required electromagnetic torque. In fact, although the magnitude of the stator current vector has already been defined through (4.8), its orientation in the dq reference frame is still indeterminate. Moreover, the rotor ampere-turns $N_r I_r$, and ultimately, the rotor current, must be determined with the aim of providing the required machine magnetization.

In order to gain a deeper comprehension of the factors involved in the determination of the stator current angle Ψ and the rotor ampere-turns $N_r I_r$, it would be beneficial to rearrange equation (4.8) into (4.20). From this perspective, it is clear that the desired output torque can only be achieved if both the imposed stator voltage V_s and the power factor $\cos\varphi$ are respected, for a fixed efficiency η.

$$T = \frac{3 \cdot V_s \cdot I_s \cdot \eta \cdot cos\varphi}{n \cdot \frac{\pi}{30}} \tag{4.20}$$

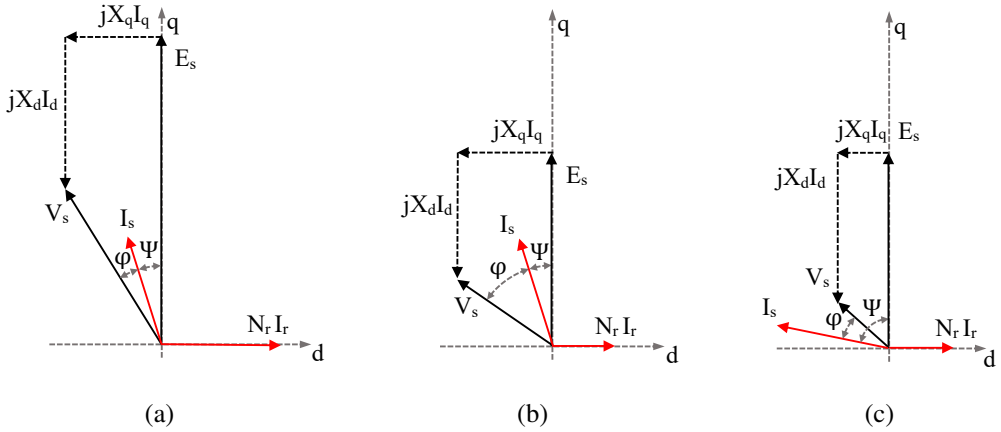

Fig. 4.3 The phasor diagram with negligible stator resistance changing the angle of the stator current (a)-(b) or the rotor ampere-turns (b)-(c).

However, the two unknown variables Ψ and $N_r I_r$ affect both the stator voltage and the power factor, as can be seen from the phasor diagram in Fig. 4.3. For finding the correct pair of Ψ - $N_r I_r$ that achieve the requested V_s - $\cos\varphi$, the developed FE model presented in Section 3.3 is utilized.

Finite element simulations are run for different values of the stator current vector angle and different values of the rotor ampere-turns. In detail, the geometry obtained from the preliminary analytical design is built through the finite element model presented in Chapter 3, and a grid of different combinations of Ψ and $N_r I_r$ is simulated for one magnetic periodicity of the machine [137, 138]. It is worth noticing that, for high power factor values, the investigation range for the stator current vector can be limited to the second quadrant of the dq-frame [139]. Indeed, the stator voltage vector V_s is found in the second quadrant, as it leads the no-load voltage vector E_s, which is placed in the q-axis, as in Fig.4.3. For the rotor ampere-turns, the investigation range is set according to the ampere-turns computed for the no-load operation, as explained in Section 3.1.1. For each rotor position, the Λ_d and Λ_q magnetic linkage fluxes are computed and then averaged over all the simulated rotor positions. From the magnetic flux values, the d- and q-axis voltages are obtained using (2.8), neglecting the stator resistance.

$$\begin{cases} V_d = -\omega\Lambda_q \\ V_q = \omega\Lambda_d \end{cases} \tag{4.21}$$

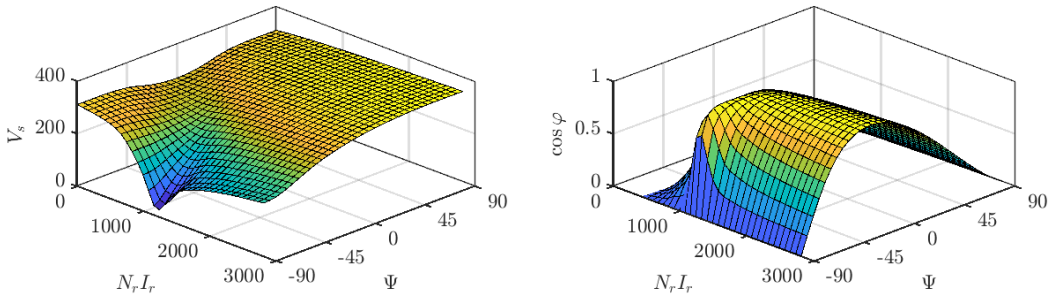

(a) (b)

Fig. 4.4 Stator voltage (a) and power factor (b) as functions of the rotor ampere-turns and the stator vector angle.

The obtained dq voltages allow for the computation of the stator voltage amplitude and angle matrices. The stator voltage angle is then used to compute the matrix of the angle φ, subtracting the matrix of the stator current angle. An example of the obtained results is shown in Fig.4.4. For negative values of the stator current angle, the magnetic flux created by the stator is opposite to that produced by the rotor current, as evident from 4.4a. Indeed, considering, for example, the voltage profile at $\Psi = -90°$, increasing the rotor ampere-turns leads to a decrease of the main flux and thus of the induced voltage, at least for low values of the rotor ampere-turns. An additional increase in the rotor ampere-turns causes the magnetic flux created by the rotor to exceed that generated by the stator current, increasing the stator voltage. On the contrary, for positive values of the stator current angle, the d-component of the flux created by the stator is concordant with the rotor flux, which in turn saturates the machine more easily, as demonstrated by the practically flat surface of the stator voltage in this region.

Among all the simulated points, the sizing algorithm identifies the pair of Ψ and N_rI_r values that satisfies the imposed V_s and $\cos\varphi$ for the specific load condition.

Knowing the requested rotor ampere-turns at load and being ρ the copper resistivity at the selected operating temperature θ_o, the value of the rotor turns is obtained by applying the Ohm law:

$$N_r = \frac{V_r \cdot S_{rs} \cdot k_{fr}}{2p \cdot \rho \cdot L \cdot (N_rI_r)} \tag{4.22}$$

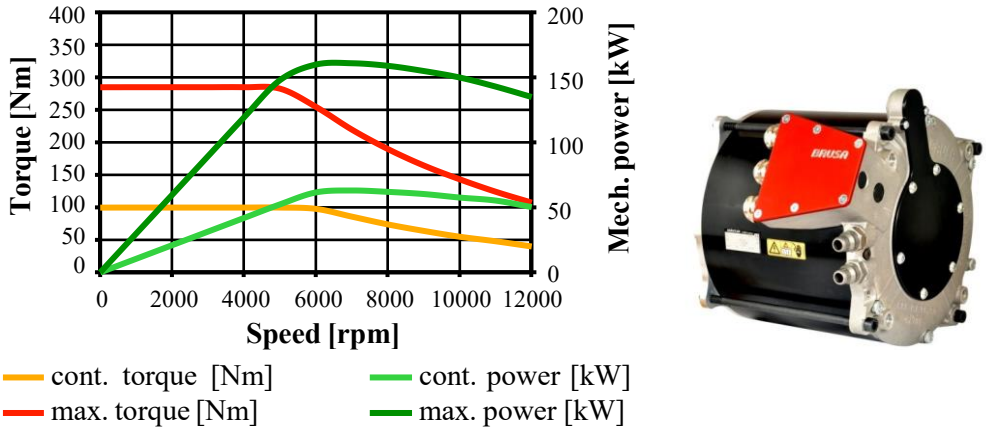

Fig. 4.5 Baseline motor for the preliminary validation of the sizing procedure [140].

The rotor current is obtained by dividing the ampere-turns by the number of rotor turns. Finally, the value of the rotor current density can be easily computed by (12).

$$J_r = \frac{N_r I_r}{S_{rs} \cdot k_{fr}} \tag{4.23}$$

The rotor current density is thus compared to its maximum value set as input. If the obtained value exceeds the limit, as depicted in Fig.4.2, the air gap diameter is again increased of the step size ΔD_g and the computation is repeated; otherwise, the algorithm is ended, and the machine sizing completed.

4.3 The sizing results

Preliminary validation of the sizing tool is achieved by considering as reference the motor shown in Fig.4.5. For this motor, the required specifications are readily available in the literature [38, 140, 141]. According to the torque-speed profile in Fig.4.5, the input operating point for the sizing code is set at an output torque of 100Nm and a base speed of 6000rpm, which means an output power of approximately 60kW. The information on the lamination geometry and material have been recollected from [141], originally obtained through [38]. The supply conditions of such operating point are extrapolated from [38], where the rotor and dq-currents are provided in tabular form for different torques and speeds, allowing for the computation of the linear and surface current densities, as in equations (4.24)-(4.25). The magnetic flux

Table 4.2 Main specifications of the baseline motor.

Sizing code inputs	
Torque (T)	100Nm
Speed (n)	6000rpm
Stator phase voltage (V_s)	160V_{rms}
Power factor, ($cos\varphi$)	1.0
Efficiency, (η)	0.95
Pole pairs number (p)	3
Slots per pole per phase (q)	3
Minimum air gap thickness (g_0)	0.5mm
Rotor pole span (k_b)	0.9
Variables for electromagnetic loadings extrapolation	
Stator current (I_s)	160A_{rms}
Turns in series per slot (Z_c)	7/3
Rotor current (I_r)	1.42A
Rotor turns per pole (N_r)	843
Electromagnetic loadings limits	
Stator current density ($J_{s,max}$)	$9\text{A}/\text{mm}^2$
Rotor current density ($J_{r,max}$)	$5\text{A}/\text{mm}^2$
Linear current density ($A_{s,max}$)	$389\text{A}/\text{cm}$
Air-gap flux density at no-load ($B_{g,max}$)	0.98T
Stator yoke flux density at no-load ($B_{sy,max}$)	1.7T
Rotor yoke flux density at no-load ($B_{ry,max}$)	2.0T
Teeth flux density at no-load ($B_{t,max}$)	1.6T
Rotor pole flux density at no-load ($B_{p,max}$)	1.8T

densities, required as inputs, have been obtained through an FE-simulation performed in no-load conditions for a rotor current equal to its value at load, i.e. $I_r = 1.42\text{A}$. Table 4.2 recollects the extrapolated main specifications and the electromagnetic loadings limits of the baseline motor.

$$J_{s,max} = \frac{Z_c \cdot I_s}{S_{ss} \cdot k_{fs}} = 9\text{A}/\text{mm}^2, \qquad A_{s,max} = J_{s,max} \frac{k_{fs} \cdot S_{ss}}{\tau_s} = 389\text{A}/\text{cm} \tag{4.24}$$

$$J_{r,max} = \frac{N_r \cdot I_r}{S_{rs} \cdot k_{fr}} = 5\text{A}/\text{mm}^2 \tag{4.25}$$

Fig. 4.6 Computed and reference geometry of the baseline motor.

Table 4.3 Main specifications of the baseline motor.

Geometric variable	Computed (mm)	Reference (mm)	Error (%)
L	126.2	123.0	2.6
D_{so}	239.2	240.0	-0.3
D_g	169.0	164.7	2.6
h_{sy}	16.07	16.40	-2.0
h_p	28.00	24.85	12.7
h_{ry}	13.74	14.75	-6.8
w_{st}	5.622	5.459	3.0
w_p	30.16	32.00	-5.8

4.3.1 The resulting WFSM motor

Figure 4.6 shows in dashed red the sized motor using the discussed variables as input for the proposed algorithm, together with the baseline motor. Table 4.3 recollects the main machine dimensions of both the computed and the reference machine, showing the relative percentage errors. The largest error occurs for the length of the rotor pole. This parameter is the consequence of the definition of the air gap diameter and the rotor yoke height, as in equation (4.17). Therefore, also, a limited error in the air gap diameter (2.6%) heavily reflects on the pole height. In any case, the proposed

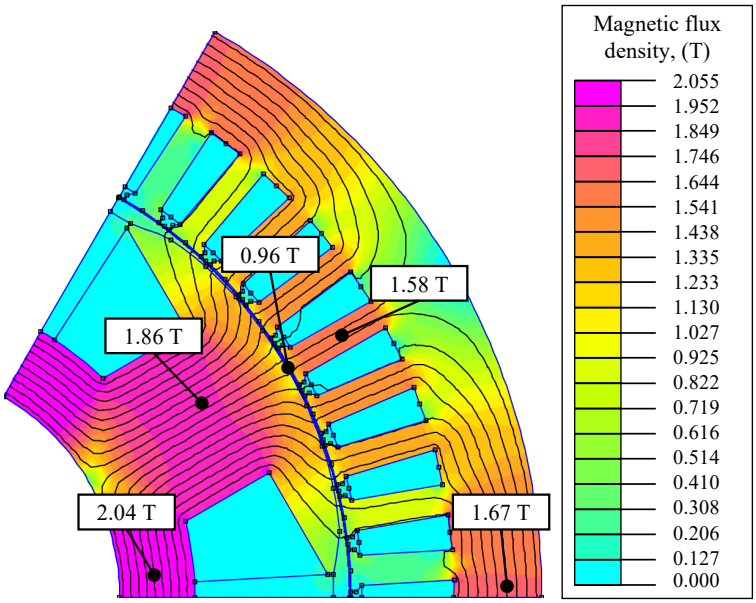

Fig. 4.7 Colour density map of the magnetic flux density of the computed WFSM motor in no-load conditions.

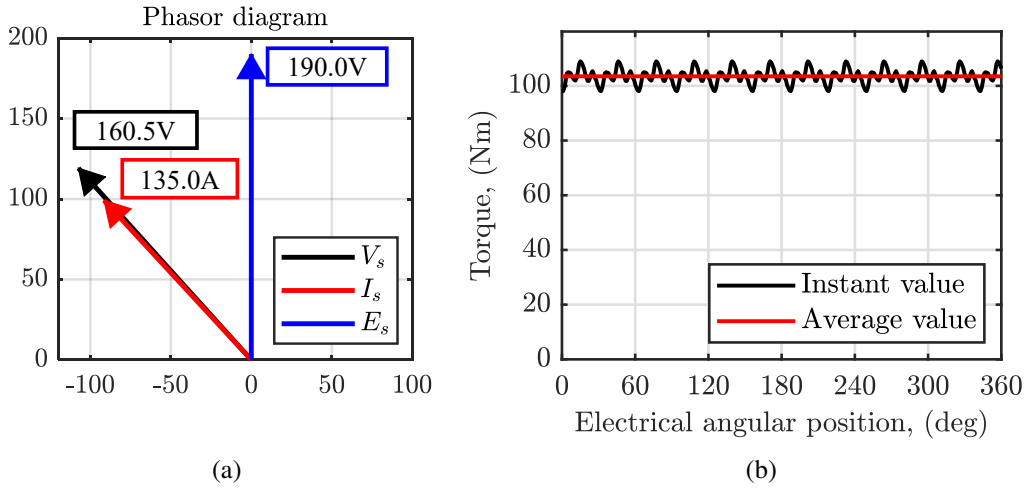

Fig. 4.8 Phasor diagram (a) and output torque (b) of the computed WFSM motor.

sizing algorithm must be intended as a preliminary design tool, and nonetheless, the obtained motor geometry well matches the baseline machine.

Figure 4.7 shows the magnetic flux density colour map of the sized motor in no-load conditions, while the phasor diagram (in rms values) and the output torque in load conditions are shown in Fig.4.8. The value of the average output torque is

103.5Nm, meaning an error of 3.45%. The output torque is reached with a linear current density of 355.5A/cm and rotor current density of 4.86A/mm^2. The value of the stator current density is not used as a check condition, as evident from the flow chart of Fig.4.2; therefore, its value is exactly the requested 9A/mm^2. Figure 4.8a also shows how the stator voltage limit and the power factor are respected with a margin error of less than 0.4%.

4.4 Conclusion

This chapter presented a fast tool for the preliminary electromagnetic sizing of wound-field synchronous motors. The rated data, the permissible electromagnetic loadings, and a few initial geometry and winding specifications are requested as input for the algorithm. The procedure consists of increasing the machine air gap diameter until the performances are obtained, respecting all the imposed constraints. The proposed methodology is based on an analytical-numerical approach, in which analytical equations establish a preliminary geometry and, subsequently, refinements are achieved through finite element simulations. Specifically, a fully analytical procedure establishes the preliminary geometry based on the magnetic flux density in no-load conditions. Subsequently, the rated working point of the preliminary-sized machine is evaluated through finite element simulations, eventually leading to a further increase in the machine's air gap diameter. Although the procedure is validated by means of a motor sample in the following chapter, a preliminary validation has already been presented in this chapter on a case study, whose characteristics were available in the literature. On the basis of the retrieved electromagnetic and geometrical input for the sizing algorithm, the procedure obtains a final geometry comparable to the case study motor.

Chapter 5

Validation Procedure

In order to validate the sizing code presented in Chapter 4, a practical examination was conducted using a WFSM that is typically employed in traction applications. In particular, the Renault ZOE motor R135 has been used as a case study to prove that the machine volume obtained by the sizing code has a valid correspondence with existing machines.

The following sections will then firstly focus on the work of reverse engineering conducted on the ZOE motor and the performed tests, leading to the definition of a reliable FE model. Subsequently, on the basis of the retrieved electromagnetic and geometrical information, the code inputs are defined and given to the sizing algorithm. Finally, the obtained geometry is compared to the actual ZOE motor.

5.1 The baseline motor

The considered wound-field synchronous machine is a 3-phase, 4-pole motor that features a rated power of 51 kW with a base speed of 4000 rpm. The motor is part of a drivetrain architecture supplied by a 400V *dc*-link [142]. The cooling is achieved through the use of a forced air system. The rotor excitation system is composed of brushes and slip rings. The lamination geometry and materials, as well as the winding layout, have been reversely engineered on the sample shown in Fig.5.1.

Fig. 5.1 Sample of the Renault ZOE R135 motor.

5.1.1 Geometrical dimensions

The geometrical motor dimensions have been obtained by both direct measurements with a gauge on the machine sample and through a 3D optical scanner, whose scans are shown in Fig.5.2. The 3D optical scanner provided files containing information on the coordinates, in three-dimensional space, of points belonging to the surface of the real component. The retrieved information was obtained in the SolidWorks environment by sectioning the 3D geometry with a plane perpendicular to the axis of the shaft. The recollected geometrical characteristics and dimensions of the machines are shown in Fig.5.3 and listed in Table 5.1.

The scanner also provided the values of the external rotor diameter and the internal stator diameter, defining the value of the minimum air gap length. However, despite the accuracy of the scanning process, even small errors on the value of g_0 may have a significant impact on the machine model. Therefore, the actual value of the air gap length has been obtained by calibrating the measured no-load characteristic, as later discussed, leading to a value of 0.78mm.

On the contrary, the scanning process is fundamental to determining the rotor pole shape. In particular, Fig.5.2d depicts the sketch of the rotor pole tip obtained in the SolidWorks environment. The final rotor pole profile is then approximated as a group of 20 segments in order to be manageable by FE software.

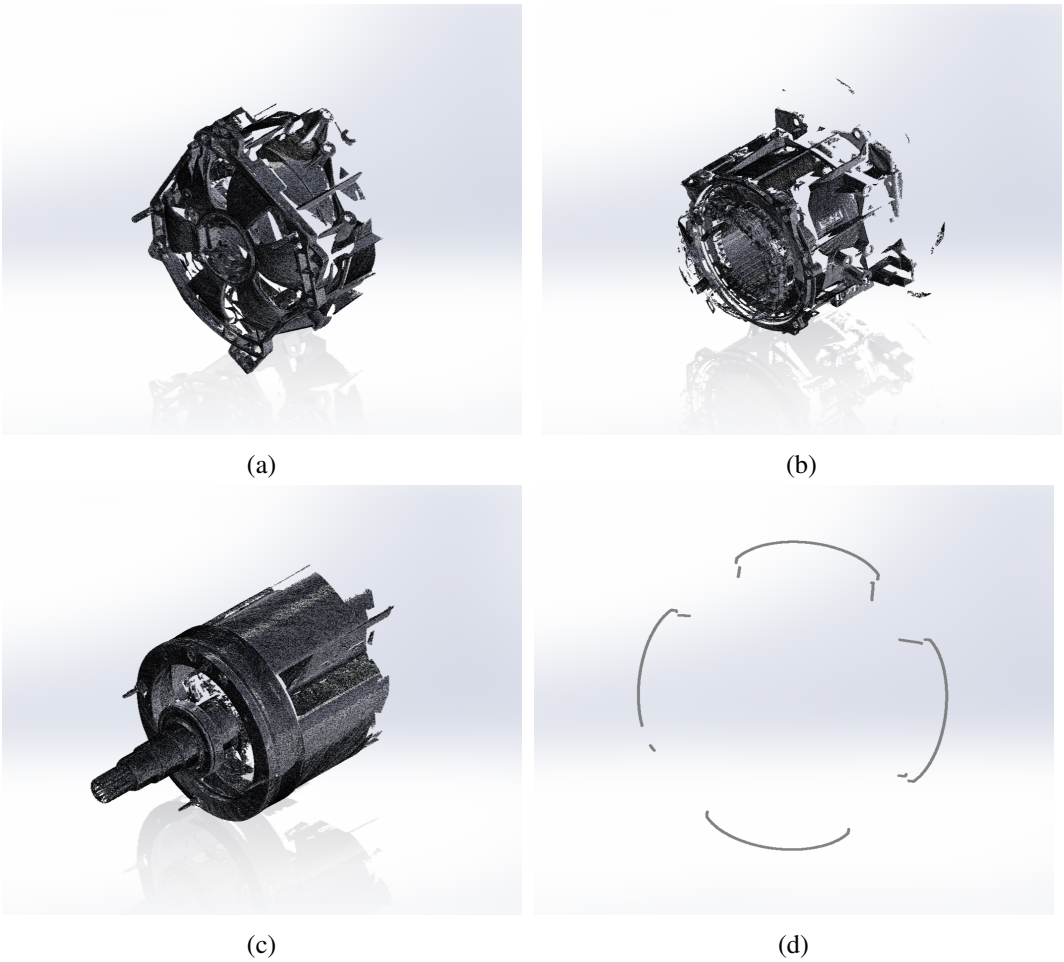

(a) (b)

(c) (d)

Fig. 5.2 3D scans of the ZOE motor.

Table 5.1 ZOE motor main dimensions.

Parameter	*Value*
Number of pole pairs, p	2
Number of phases, m	3
Number of stator slots, N_s	48
Machine axial length, L	175 mm
Stator outer diameter, D_{so}	262.2 mm
Stator inner diameter, D_{si}	156.15 mm
Rotor outer diameter, D_{ro}	154.59 mm
Rotor inner diameter, D_{ri}	41.0 mm

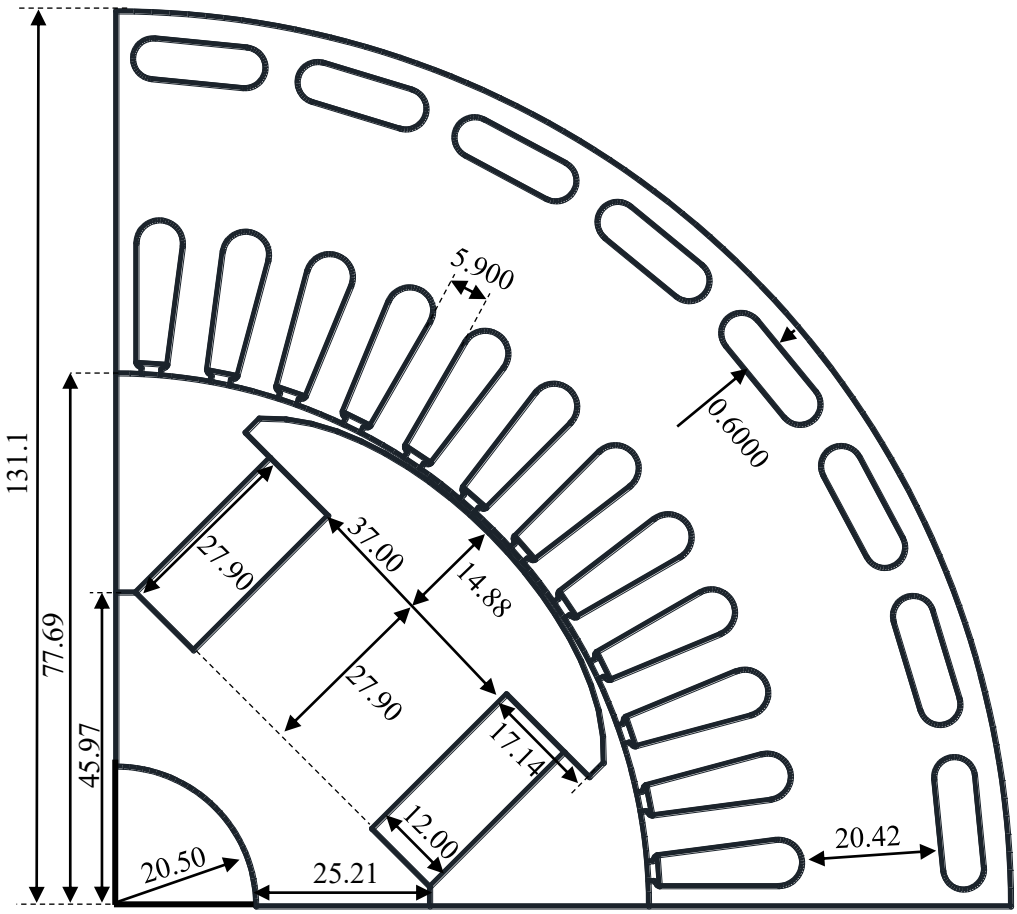

Fig. 5.3 Dimensions of the ZOE motor geometry in mm.

5.1.2 Stator and Rotor winding layout

By inspection of the winding in both the stator and rotor, it was possible to deduce their respective configurations. The details of these configurations are provided in the following sections.

The stator winding

After examining the machine under investigation, it was found that it presents a single-layer distributed stator winding with a total of 48 stator slots. As this is a 3-phase, 4-pole motor, it was deduced that there are 4 slots per pole and per phase,

Table 5.2 Stator winding characteristics.

Parameter	*Value*
Slots per pole and per phase, q	4
Number of conductors in one slot, Z_f	108
Number of external parallels, a_e	4
Number of internal parallels, a_i	12

as indicated in equation (5.1). Upon further inspection, it was observed that there are 108 conductors in each slot, with 4 external parallels (allowing all poles to be in parallel) and 12 internal parallels.

$$q = \frac{N_s}{2 \cdot p \cdot m} = \frac{48}{2 \cdot 2 \cdot 3} = 4 \tag{5.1}$$

The extrapolated data of the stator winding layout are recollected in Table 5.2. Starting from these values, it is possible to compute the number of turns in series per phase and the number of turns in series per slot:

$$N_1 = p \cdot q \cdot \frac{Z_f}{a_i \cdot a_e} = 18 \tag{5.2}$$

$$Z_c = \frac{Z_f}{a_i \cdot a_e} = \frac{9}{4} \tag{5.3}$$

On the basis of the measured conductor diameter, the conductor cross-sectional area, excluding the insulation, can be obtained:

$$S_{cu,s} = \frac{\pi \cdot d_{cu,s}^2}{4} = 0.5027\text{mm}^2 \tag{5.4}$$

The cross-sectional area of the equivalent conductor in the series equivalent stator winding can be computed as in (5.5).

$$S_{cu,eq} = a_i \cdot a_e \cdot S_{cu,s} = 24.13\text{mm}^2 \tag{5.5}$$

Table 5.3 Stator winding resistance.

Parameter	*Value*
Phase 1 resistance , R_{s1}	9.745 $m\Omega$
Phase 2 resistance , R_{s2}	9.816 $m\Omega$
Phase 3 resistance , R_{s3}	9.830 $m\Omega$
$\theta_a = 19.80°C$	

The value of the *dc* resistance of each phase has been measured on the machine sample, employing the accessible star point. The obtained values are reported in Table 5.3, together with the measured ambient temperature.

Therefore, it is possible to compute the average length of the stator turn, considering R_s the average of the measured resistances of Table 5.3:

$$l_{at,s} = \frac{R_s \cdot S_{cu,eq}}{N_1 \cdot \rho} = 763.5\text{mm} \tag{5.6}$$

The end-winding length is:

$$l_{ew,s} = \frac{l_{at,s}}{2} - L = 207.3\text{mm} \tag{5.7}$$

The end-winding shape coefficient can be obtained considering the radius at the centre of the slot (r_s). The obtained value falls into the typical range of variation of $k_{ew,s}$, i.e. 1.45-1.6, as reported in [143].

$$k_{ew,s} = \frac{l_{ew,s}}{2 \cdot \pi r_s} \cdot 2 \cdot p = 1.463\text{mm} \tag{5.8}$$

Finally, on the basis of the retrieved information, it is possible to compute the winding factor of the machine under analysis. Considering that the stator winding is a single-layer, the winding factor coincides with the distribution factor, being the pitch factor unitary.

$$k_w = \frac{\sin(\frac{\pi}{6})}{q \sin(\frac{\pi}{6q})} = 0.9577 \tag{5.9}$$

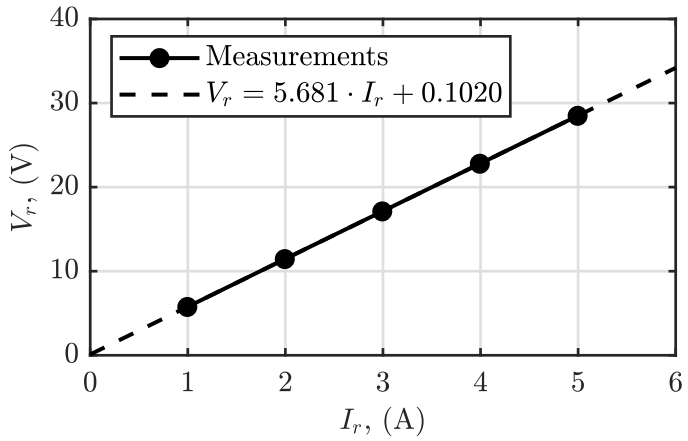

Fig. 5.4 Rotor resistance measurements.

Table 5.4 Rotor winding characteristics.

Parameter	*Value*
Number of rotor turns per pole, N_r	195
Rotor resistance, R_r	5.673 @ $\theta_a = 19.80°C$
Cross-sectional area of the rotor conductor, $S_{cu,r}$	1.131 mm^2

The rotor winding

The assessment of the rotor winding only consists of counting the number of turns per pole, as all the poles are connected in series. All the extrapolated information is gathered in Table 5.4.

The value of the rotor resistance was evaluated by conducting *dc* tests on both the disassembled and complete samples. In the former case, the measured voltage actually corresponds to the rotor winding resistance, obtaining the value reported in Table 5.4. In the closed sample, however, the voltage measurement includes the voltage drop on the brushes. To account for this, different rotor currents have been tested, and the results are shown in Fig.5.4. By linearly extrapolating the results to zero rotor current, it was possible to separate the voltage contribution of the brushes (the y-intercept) by the actual rotor resistance (the angular coefficient), yielding similar R_r values of Table 5.4.

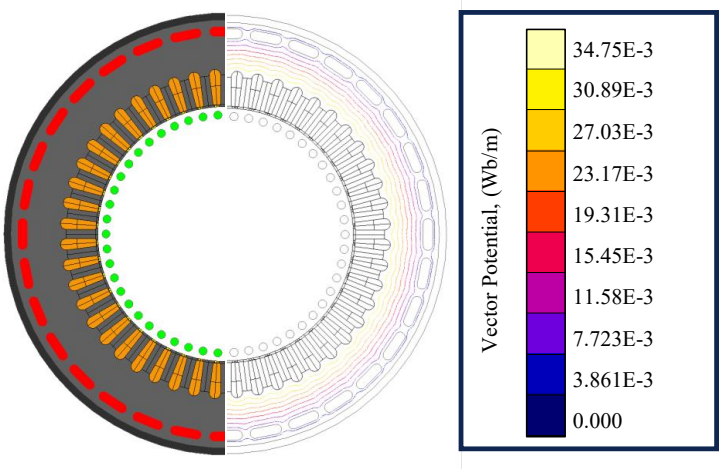

Fig. 5.5 Machine winding for BH-curve measurement.

5.1.3 Measured magnetic material characteristic

The magnetic characteristic of the lamination material has been determined by experimental measurements conducted on the stator core [144]. The measurement of the BH-curve of the core requires the creation of two windings around the stator, forming a ferromagnetic core of toroidal shape. When one winding is supplied in *ac*, an induced voltage is created in the other winding. The test is based on the measurements of the peak values of sinusoidal variables. Therefore, strong saturation conditions of the magnetic material invalidate the measurement results, as the current absorbed on the primary side and the induced voltages at the secondary become distorted. The harmonic content of the induced voltage depends on the operating point of the core on the BH curve, which in turn depends on the values of the excitation field and magnetic flux density in the material. To guarantee the validity of the measurements, it is necessary to evaluate the distortion of the voltage induced on the secondary, verifying that the ratio between the peak value and the rms value remains in the interval $1.1 \pm 1\%$, being 1.1 the value for a perfect sinusoid.

The number of turns of the primary and secondary windings is chosen according to the limits of the available power source. Being the stator inserted into the housing, the conductors are wound on the motor sample through the air gap and the cooling slots, which are circumferentially distributed over the stator yoke. Figure 5.5 shows the cross-section surfaces of the conductors with green circles in the air gap and the cooling slots with red areas. This placement limits the leakage flux with respect

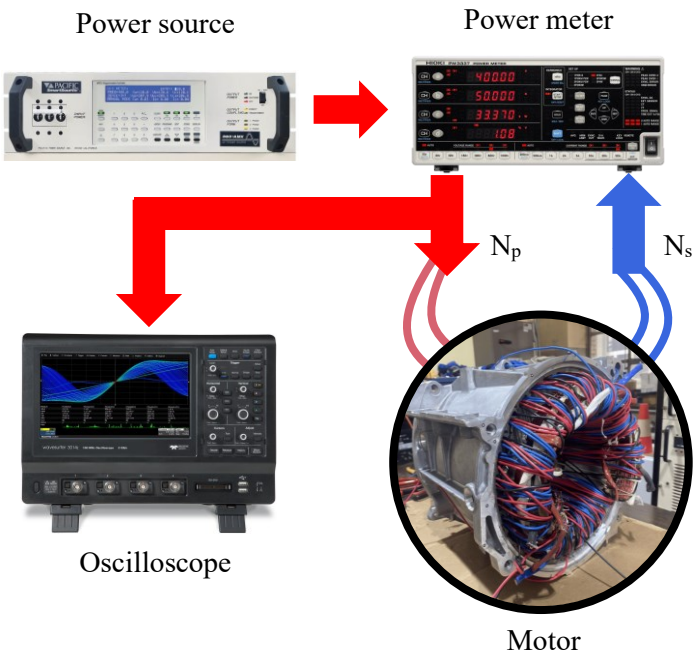

Fig. 5.6 BH-curve measurement schematic.

to positioning the winding externally to the housing. Indeed, through the 2D FE simulation of the stator shown in Fig.5.5, it can be observed that most of the magnetic flux is concentrated internally with respect to the cooling slots.

The adopted measurement setup is shown in Fig.5.6. The equipment consists of a linear power source able to generate sinusoidal voltages used to supply the primary winding, and a high-precision power meter necessary for the measurement of the current absorbed by the primary winding and the voltage induced in the secondary. The voltage measurement is taken in the secondary winding because of the absence of Joule losses. The oscilloscope is used for monitoring the current of the primary side to prevent exceeding the power meter current limits when highly distorted currents are absorbed. Figure 5.6 also shows the motor sample, wound with the primary (in red) and secondary (in blue) winding of N_p and N_s number of turns, respectively. Starting from the measurement of the peak value of the current in the primary winding I_1 and considering l the average length of the stator yoke circumference, the value of the magnetic field H can be computed as in (5.10).

$$H = \frac{N_1 I_1}{l} \tag{5.10}$$

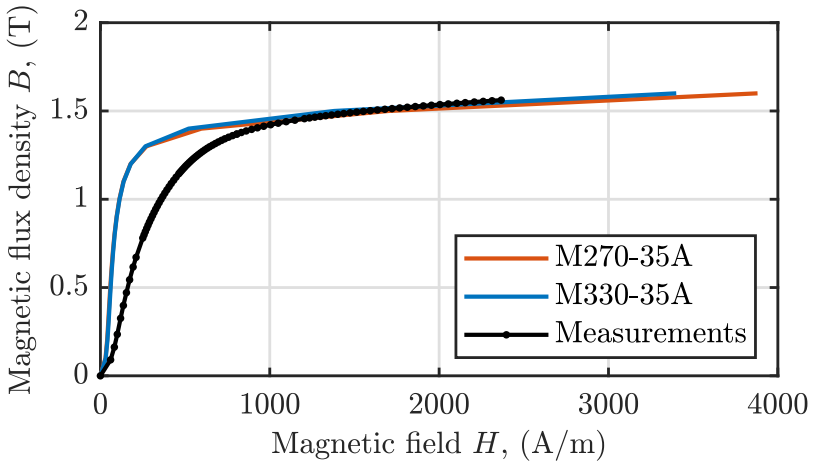

Fig. 5.7 BH-curve measurement results.

The peak value of the magnetic flux in the stator yoke is computed through (5.11), thanks to the measurement of the rectified mean value of the secondary voltage $|\overline{V}_2|$.

$$\Phi = \frac{|\overline{V}_2|}{4fN_2} \tag{5.11}$$

Therefore, the magnetic flux density can be obtained diving by the cross-section area of the stator yoke.

$$B = \frac{\Phi}{h_{sy} \cdot L \cdot k_{st}} \tag{5.12}$$

Measurement results

The BH-curve obtained from the experimental test can be observed in Fig.5.7. In addition, two reference BH-curves of the M270-35A and M330-35A have been included for comparison. Indeed, although the thickness of the actually used lamination material is unknown, based on the inspection of the sample, it is estimated to be around 0.35mm thick. The magnetic properties of the sample are inferior to those of the reference materials, which can be attributed to the material processing and treatment.

Compatible with the limits of the power source, the BH-curve has been measured up to a maximum magnetic flux density of 1.56T, which corresponds to a relative

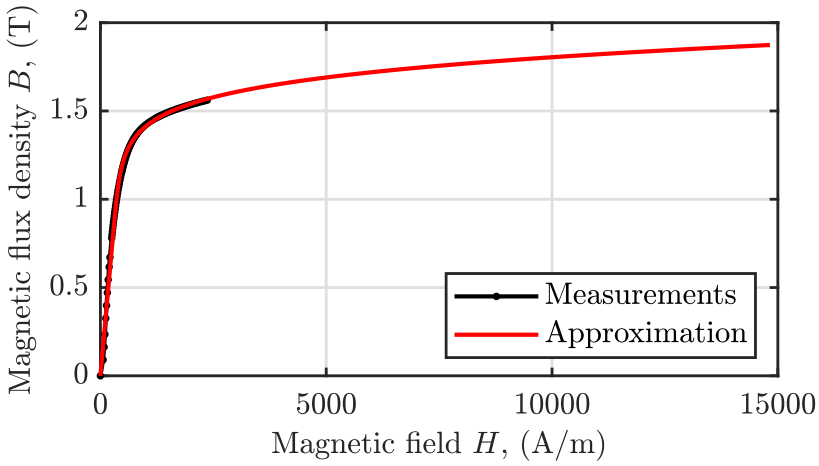

Fig. 5.8 Measured and approximated BH-curve.

permeability value of 525, still far from strong saturation conditions where the relative permeability is close to one. Therefore, using the measured characteristic within finite element software, which extrapolates linearly from the final data points, can result in notable inaccuracies. In order to solve this issue, the relative magnetic permeability μ_r is approximated using the estimation shown in equation (5.13), as proposed in the reference [107].

$$\mu_r(B) = \frac{(1/K)\sum_{k=1}^{K}(|B/m_k|^{n_k} + a_k^{n_k})^{1/n_k}}{(1/K)\sum_{k=1}^{K}(|B/m_k|^{n_k} + a_k^{n_k})^{1/n_k} - 1} \tag{5.13}$$

The values of the parameters m_k, n_k and a_k are obtained through the Particle Swarm Optimization (PSO) technique applied to the error function between the measured and approximated characteristics.

The PSO technique yielded to the set of parameters listed in Table 5.5. In Fig.5.8, both the approximated and measured BH-curves are presented.

Table 5.5 Parameters for the permeability characteristic approximation.

k	m_k	n_k	a_k
1	8.305	98.93	$1.676\text{x}10^3/(1.676\text{x}10^3)$
2	9.892	64.33	$3.878\text{x}10^3/(3.878\text{x}10^3)$
3	2.042	11.33	$2.132\text{x}10^3/(2.132\text{x}10^3)$

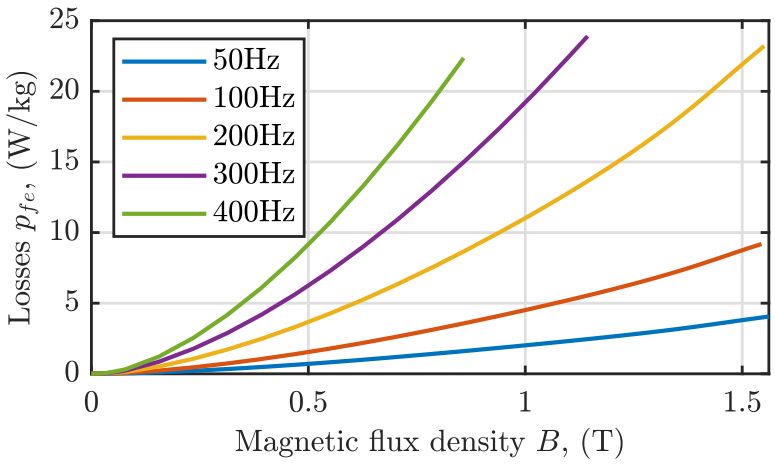

Fig. 5.9 Specific iron losses measurements.

The experiment has been conducted for different frequencies, in order to evaluate the material specific losses, obtained through (5.14), where P_{12} is the power measured by the power meter considering the excitation current and the induced voltage, and m_{sy} is the mass of the stator yoke. The obtained results are shown in Fig.5.9.

$$p_{fe} = \frac{1}{m_{sy}} \cdot \frac{N_p}{N_2} \cdot P_{12} \tag{5.14}$$

As expected, larger iron losses are obtained for higher frequencies. Comparing these specific losses with those of the catalogues of the M270-35A and M330-35A, the sample presents larger iron losses, which again can be attributed to the material processing and treatment.

5.2 Tests on the motor sample

Several experimental tests have been carried out to define the fundamental properties of the baseline motor. These tests involve experiments performed exclusively on the stator and the rotor, as well as experiments conducted on the complete machine sample. The performed tests allowed for the extrapolation of the machine inductances in non-saturation conditions, and the no-load characteristics, as presented in the following sections.

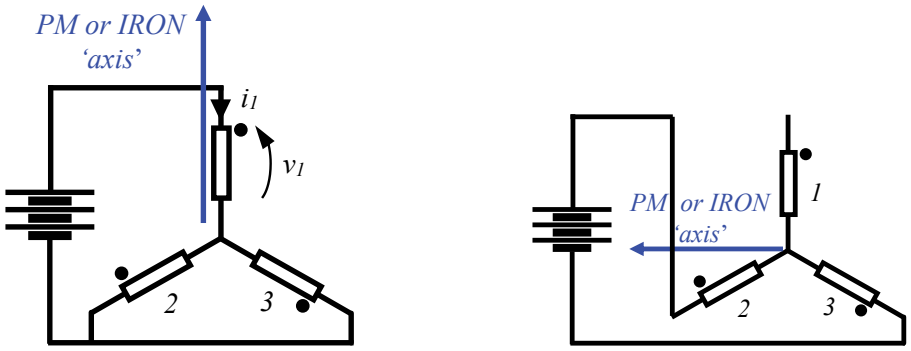

Fig. 5.10 Circuit used for the parallel (a) or perpendicular (b) rotor alignment with the magnetic axis of phase one [145].

5.2.1 Synchronous inductances

The measurement of the inductances L_d and L_q is performed by orienting and locking the rotor in two different positions [145]. The first rotor position consists of aligning the d-axis with the magnetic axis of phase 1, and it can be found supplying the stator winding with a *dc* source according to the circuit depicted in Fig.5.10a. The second rotor position is perpendicular to the magnetic axis of phase 1, obtained by reconfiguring the circuit into the one shown in Fig.5.10b. Although the rotor saliency is already sufficient to drag the rotor into the desired position, the process can be further aided by providing *dc* power supply also to the rotor winding, leading to a more accurate alignment. Injecting the *dc* currents in the rotor winding and in the stator windings as described, the rotor rotates to align the d-axis with the m.m.f. vector, as a consequence of the alignment of the excitation field and the minimization of the magnetic circuit reluctance.

Figure 5.10b illustrates that the three stator windings can be connected as single-phase electrical loads in two fundamental ways: utilizing all three windings (case A) or only two (case B). This gives rise to six possible connection arrangements, as depicted in Fig.5.11. It follows that the space vector produced by a single-phase *ac* current can be oriented in six defined directions, regardless of the rotor position, while considering the m.m.f. sign convention. The d- and q-axis alignment is established only for a relative shift angle of 0° or 90° between the stator m.m.f. and the rotor axis. Thus, among the six configurations displayed in Fig.5.11, only four m.m.f.-rotor relative positions adhere to these conditions, as summarized in Fig.5.12.

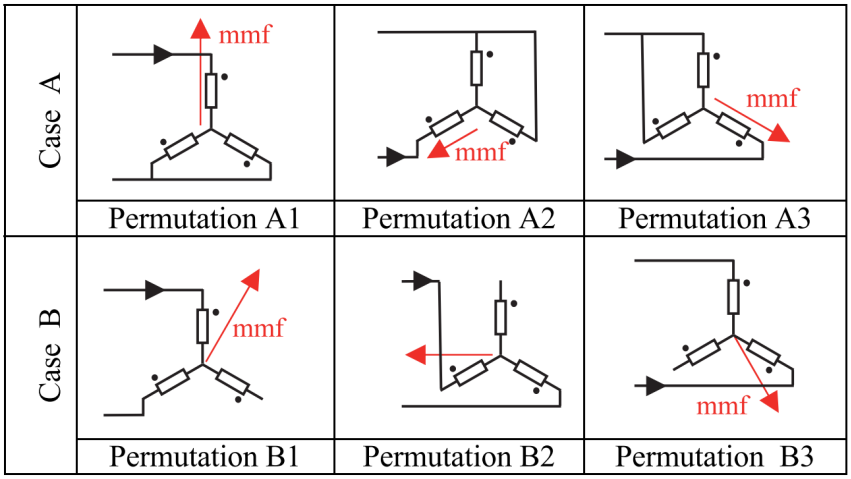

Fig. 5.11 Possible single-phase connection schemes [145].

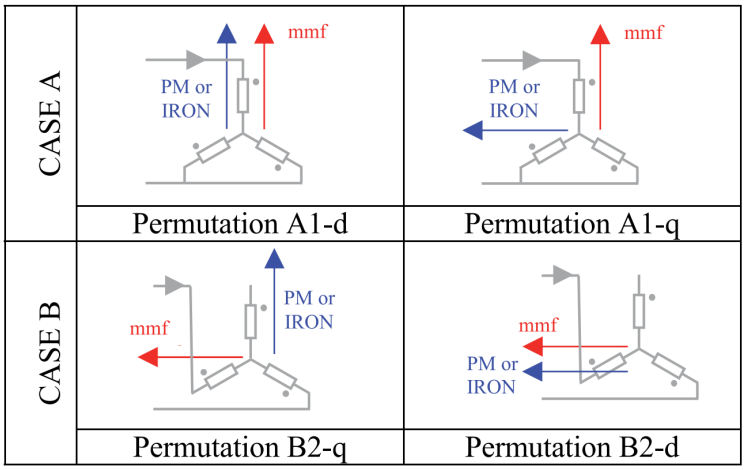

Fig. 5.12 *dq*-axis alignements [145].

In the cases A1-d and B2-d, the *d*-axis is placed in the same direction as the magnetomotive force vector m.m.f.generated by the stator windings. In the cases A1-q and B2-q, the *d*-axis is in quadrature with respect to the m.m.f. vector, i.e. the magnetomotive force vector is oriented along the *q*-axis. The conditions A1-d and B2-d allow obtaining L_d, while the conditions A1-q and B2-q allow obtaining L_q. The two cases (A and B) are described by equations (5.15) and (5.16), respectively.

$$\overline{V}_{12} = \frac{3}{2}\left[R_s + j\omega_e\left(L_{\sigma,s} + \frac{3}{2}M\right)\right]\overline{I_1} \tag{5.15}$$

$$\overline{V}_{22} = \frac{1}{2}\left[R_s + j\omega_e\left(L_{\sigma,s} + \frac{3}{2}M\right)\right]\overline{I_2} \tag{5.16}$$

The coefficients 3/2 and 1/2 are the result of the corresponding circuit connections. Depending on the position of the rotor, the equations present L_d (A1-d and B2-d) or L_q (A1-q and B2-q) as the sum of two terms, one associated with magnetization and one associated with leakage fluxes.

Figure 5.13 depicts the used test setup for the inductances measurement. After supplying the circuits of Fig5.10 with a *dc* power, the rotor is aligned into the desired position and mechanically locked, as shown in Fig.5.14. Therefore, the stator windings have been supplied through the *ac* power source, using PC1, according to the circuits of 5.10b. The power meter is used to measure the current, the voltage and the reactive power absorbed by the stator winding, thus obtaining the value of the inductances. The tests have been performed at a frequency of 50Hz and in the linear region of the material characteristic. The results for the L_d and L_q inductances are reported in Table 5.6 and Table 5.7, respectively.

Table 5.6 Results for the L_d inductance test.

	$I_s, (\mathrm{A})$	$V_s, (\mathrm{V})$	$Q, (\mathrm{var})$	$L_d, (\mathrm{mH})$
A1-d	42.59	37.67	1594	1.865
B2-d	34.06	41.20	1394	1.913

Table 5.7 Results for the L_q inductance test.

	$I_s, (\mathrm{A})$	$V_s, (\mathrm{V})$	$Q, (\mathrm{var})$	$L_q, (\mathrm{mH})$
A1-q	36.02	11.76	422.6	0.6913
B2-q	39.02	16.86	656.9	0.6869

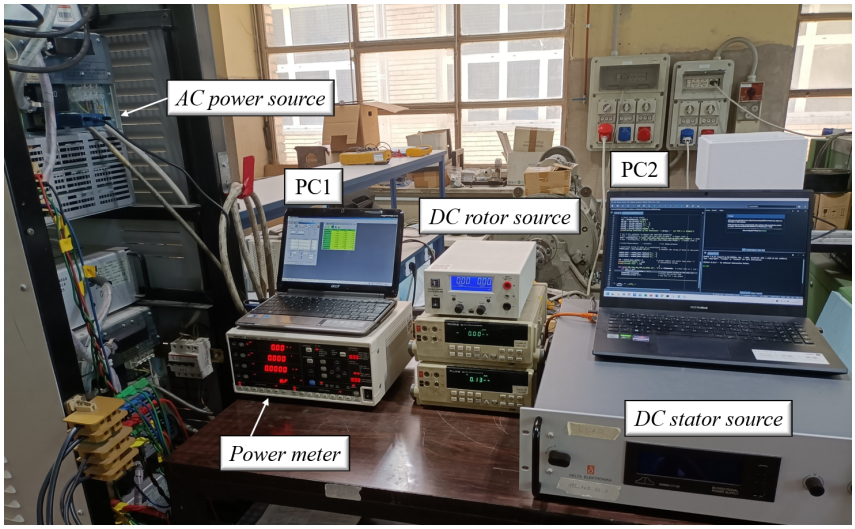

Fig. 5.13 Setup for the measurement of the unsaturated L_d and L_q inductances.

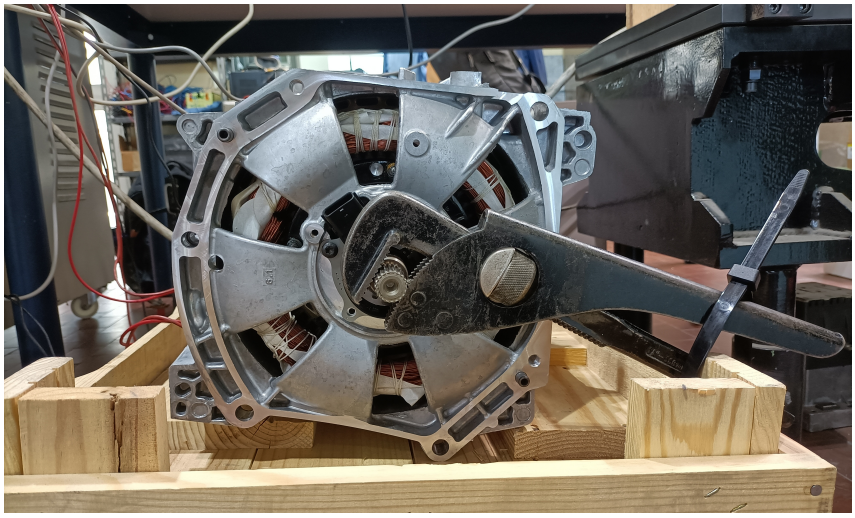

Fig. 5.14 Locking of the rotor into a specific position.

5.2.2 Extracted rotor tests

The extraction of the rotor from the stator allowed for performing tests on the separate motor parts. The test with the removed rotor is also recognized by the standard IEEE Std 112-2017 [146], for determining stray-load loss in polyphase induction motors.

Table 5.8 Results for the stator in the removed rotor test.

$f,(\mathrm{Hz})$	$I_s,(\mathrm{A})$	$V_s,(\mathrm{V})$	$P_s,(\mathrm{W})$	$Z_s,(\mathrm{m\Omega})$	$\cos\varphi_s$	$L_s,(\mu\mathrm{H})$	$R_{s,ac},(\mathrm{m\Omega})$
50	24.76	2.009	22.54	46.86	0.2620	144.0	12.26
50	35.88	2.904	47.23	46.73	0.2620	143.6	12.23
50	50.13	3.978	89.25	45.82	0.2580	140.9	11.84
100	15.46	2.385	8.860	89.08	0.1390	140.4	12.36
100	30.48	4.575	33.44	86.65	0.1380	136.6	12.00
100	45.20	6.756	72.85	86.29	0.1380	136.0	11.88
200	16.85	4.972	11.19	170.4	0.0770	135.2	13.14
200	32.93	9.676	42.59	169.6	0.0770	134.6	13.09
200	49.16	14.43	94.37	169.4	0.0770	134.4	13.02
300	17.79	7.808	14.14	253.4	0.0590	134.2	14.89
300	35.12	15.40	55.10	253.1	0.0590	134.1	14.90
300	52.34	22.95	121.9	253.1	0.0590	134.1	14.83

Test on the machine stator

The three-phase stator winding is supplied with three symmetrical sinusoidal voltages. By measuring the phase currents and the active power, once the line-to-line voltages and the supply frequency are known, the real and imaginary parts of the stator impedance Z_s in this configuration are obtained through the following relations. The obtained results are shown in Table 5.8.

$$|\overline{Z_s}| = \left|\frac{\overline{V_s}}{\overline{I_s}}\right| \tag{5.17}$$

$$\cos\varphi_s = \frac{P_s}{\sqrt{3}\cdot V_s \cdot I_s} \tag{5.18}$$

$$X_s = |\overline{Z_s}|\sin\varphi_s \tag{5.19}$$

$$L_s = \frac{X_s}{2\cdot\pi\cdot f} \tag{5.20}$$

$$R_{s,ac} = |\overline{Z_s}|\cos\varphi_s \tag{5.21}$$

Table 5.9 Results for the rotor in the removed rotor test.

$f,(\mathrm{Hz})$	$I_r,(\mathrm{A})$	$V_r,(\mathrm{V})$	$P_r,(\mathrm{W})$	$Z_r,(\mathrm{m\Omega})$	$\cos\varphi_r$	$L_r,(\mu\mathrm{H})$	$R_{r,ac},(\mathrm{m\Omega})$
10	2.435	34.48	35.17	14.16	0.4190	204.6	5.931
10	3.706	51.85	81.17	13.99	0.4220	201.8	5.911
50	1.319	86.56	16.13	65.62	0.1410	206.8	9.269
50	2.708	173.5	57.55	64.06	0.1230	202.4	7.847
50	4.123	260.9	126.2	63.26	0.1170	200.0	7.422
50	5.529	347.0	221.7	62.77	0.1160	198.5	7.253
50	6.966	434.8	349.0	62.41	0.1150	197.4	7.192
50	8.393	521.5	508.0	62.14	0.1160	196.5	7.212

Test on the machine rotor

The real and imaginary parts of the rotor impedance Z_r are obtained by supplying the rotor winding with a sinusoidal voltage, following a procedure similar to that used for the stator. The following equations refer to a single-phase winding, representing the only difference with respect to the previous formulations. The obtained results are shown in Table 5.9.

$$|\overline{Z_r}| = \left|\frac{\overline{V_r}}{\overline{I_r}}\right| \tag{5.22}$$

$$\cos\varphi_r = \frac{P_r}{V_r \cdot I_r} \tag{5.23}$$

$$X_r = |\overline{Z_r}|\sin\varphi_r \tag{5.24}$$

$$L_r = \frac{X_r}{2\cdot\pi\cdot f} \tag{5.25}$$

$$R_{r,ac} = |\overline{Z_r}|\cos\varphi_r \tag{5.26}$$

5.2.3 No-load test

In order to perform the no-load test on the machine sample, the measurement setup shown in Fig.5.15 and in Fig.5.16 has been used. In particular, the rotor of the motor under test has been kept rotating at a fixed speed (500rpm) using the prime

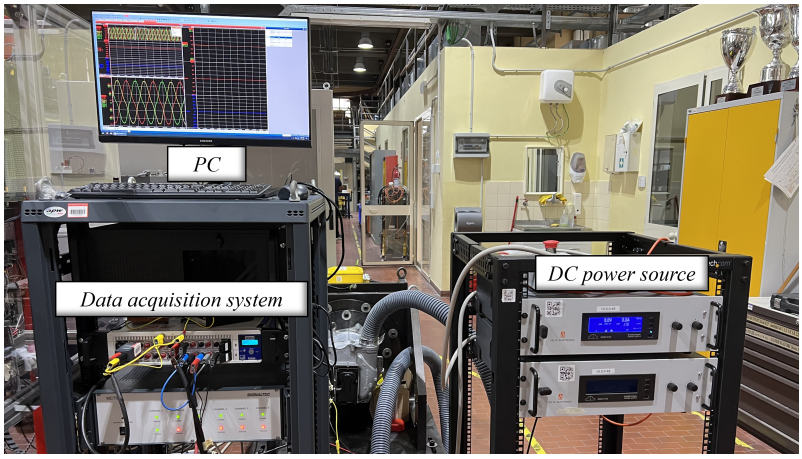

Fig. 5.15 No-load test setup: the equipment.

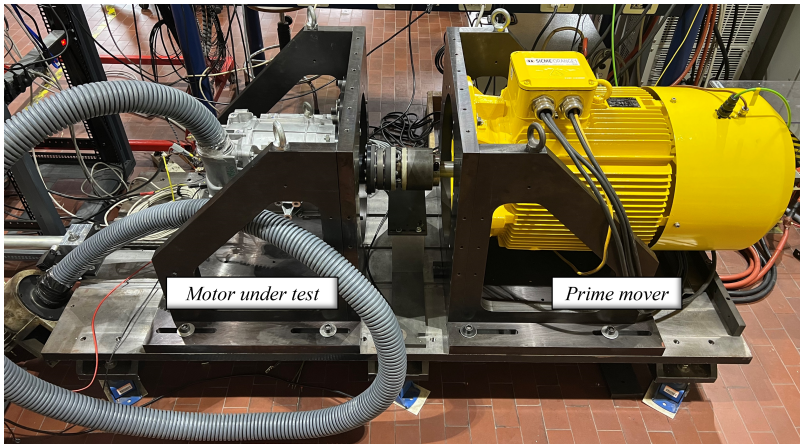

Fig. 5.16 No-load test setup: the motors.

mover, while the rotor winding has been supplied with a *dc* power source. The phase stator voltage has been measured for different values of the rotor current. The rotor current has been measured using the closed-loop current transducer IT200-S Ultrastab from LEM. The three stator phase voltages have been measured using shielded cables connected to voltage cards GN610B from HBM Gmbh. All the data have been measured with a sampling frequency of 500kS/s and collected by the data acquisition system GEN2tB from HBM Gmbh. Figure 5.17 shows four obtained measurements of the induced stator voltage selected from a total number of eighteen tests. Extrapolating the fundamental component of the measured voltages, the no-load characteristic depicted in Fig.5.18 is obtained.

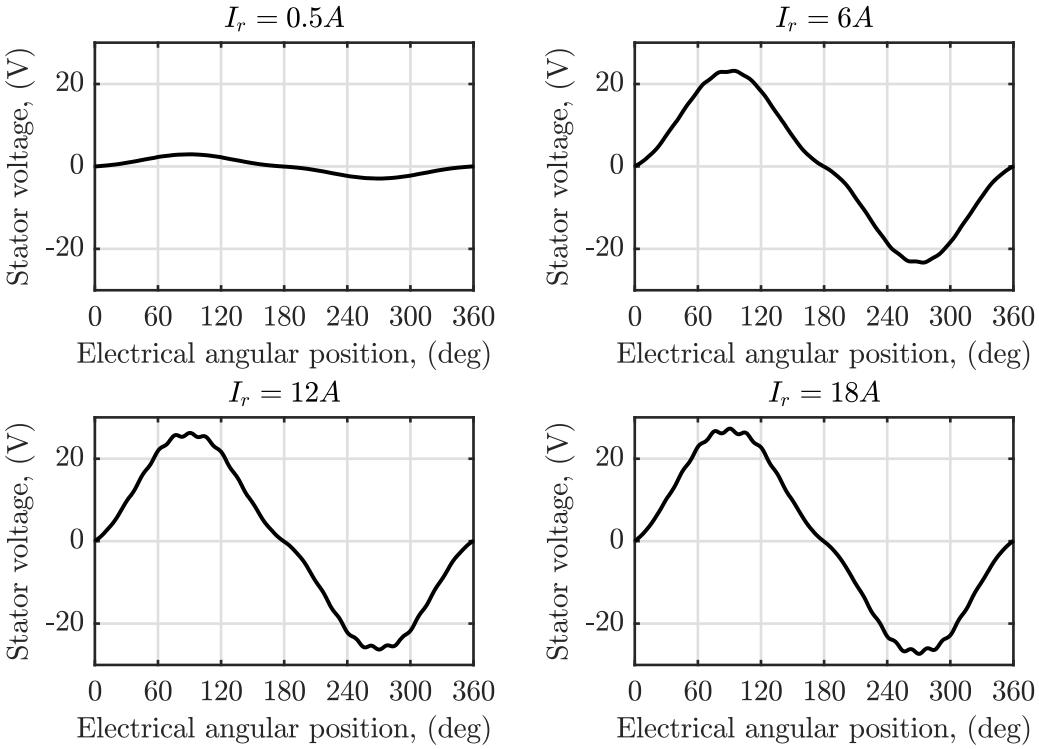

Fig. 5.17 Measured stator voltages for different rotor currents at 500rpm.

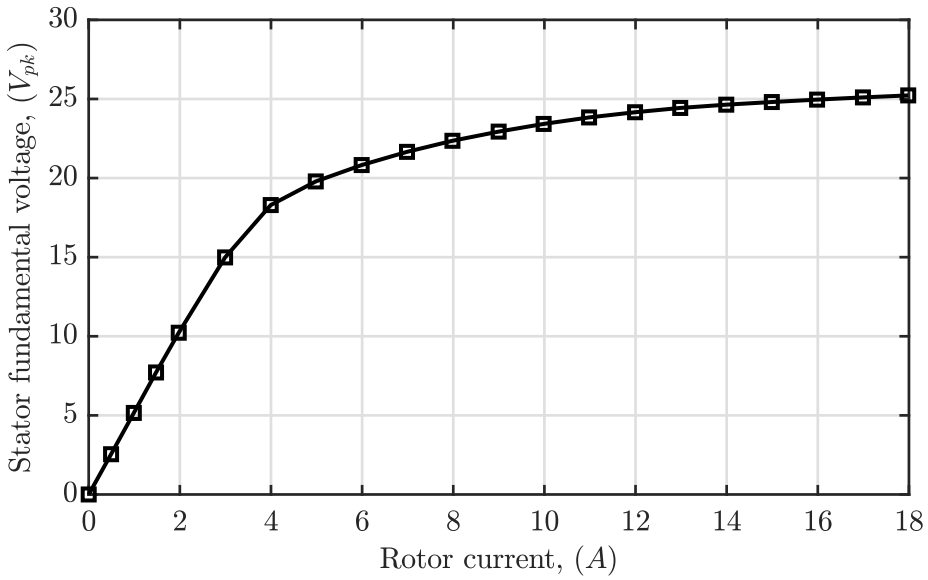

Fig. 5.18 Measured no-load characteristic at 500rpm.

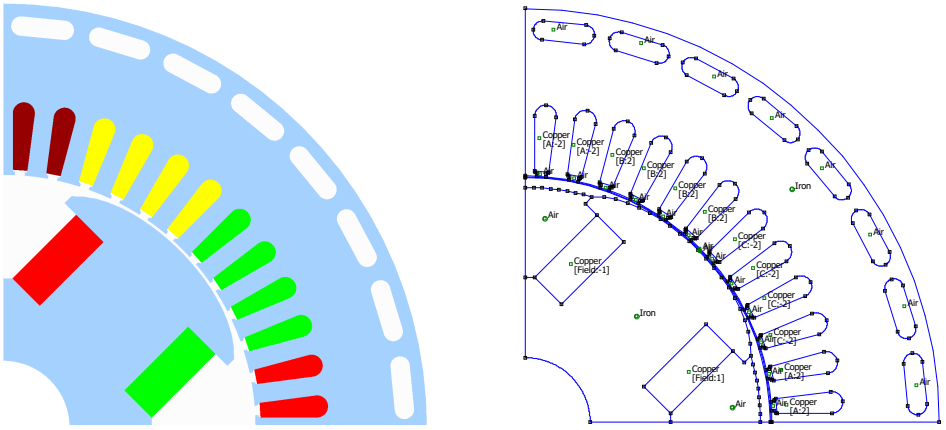

(a) (b)

Fig. 5.19 FE-model of the ZOE motor: in FLUX Altair (a) and FEMM (b).

5.3 The finite element model

Based on the recollected information and measurements, the finite element model of the ZOE motor is developed. The geometric dimensions are the values reported in Fig.5.3, the magnetic material that of Fig.5.8, the stator conductors per slot is $Z_c = 9/4$ and the rotor conductors per pole is $N_r = 195$. Although the proposed drawing code (Section 3.3) could be used to create the FE model of the ZOE motor, many geometry details would be approximated, as only a limited amount of options have been developed. In any case, the main aim of the developed Matlab-FEMM model is to be used in the sizing algorithm. In order to build an accurate FE model, the software FLUX Altair is used for its simplicity in building and modifying the machine geometry with software overlays, except for the rotor pole profile, which is imported via the 3D scans. The parametric FLUX model was also used to easily calibrate the air gap length, which is difficult to obtain from direct measurements on the sample. The calibration has been conducted based on the comparison with the linear part of the measured no-load characteristic. Subsequently, the final machine has been imported into a FEMM model to exploit the parallelization over multiple cores and, above all, to obtain the results as MATLAB data, instead of memory-consuming FE simulations. This is especially welcome in the computation of the current-to-flux linkage model, which requires a significantly large quantity of simulations, particularly for wound-field machines, as the model must be computed for three current variables. Both models are shown in Fig.5.19.

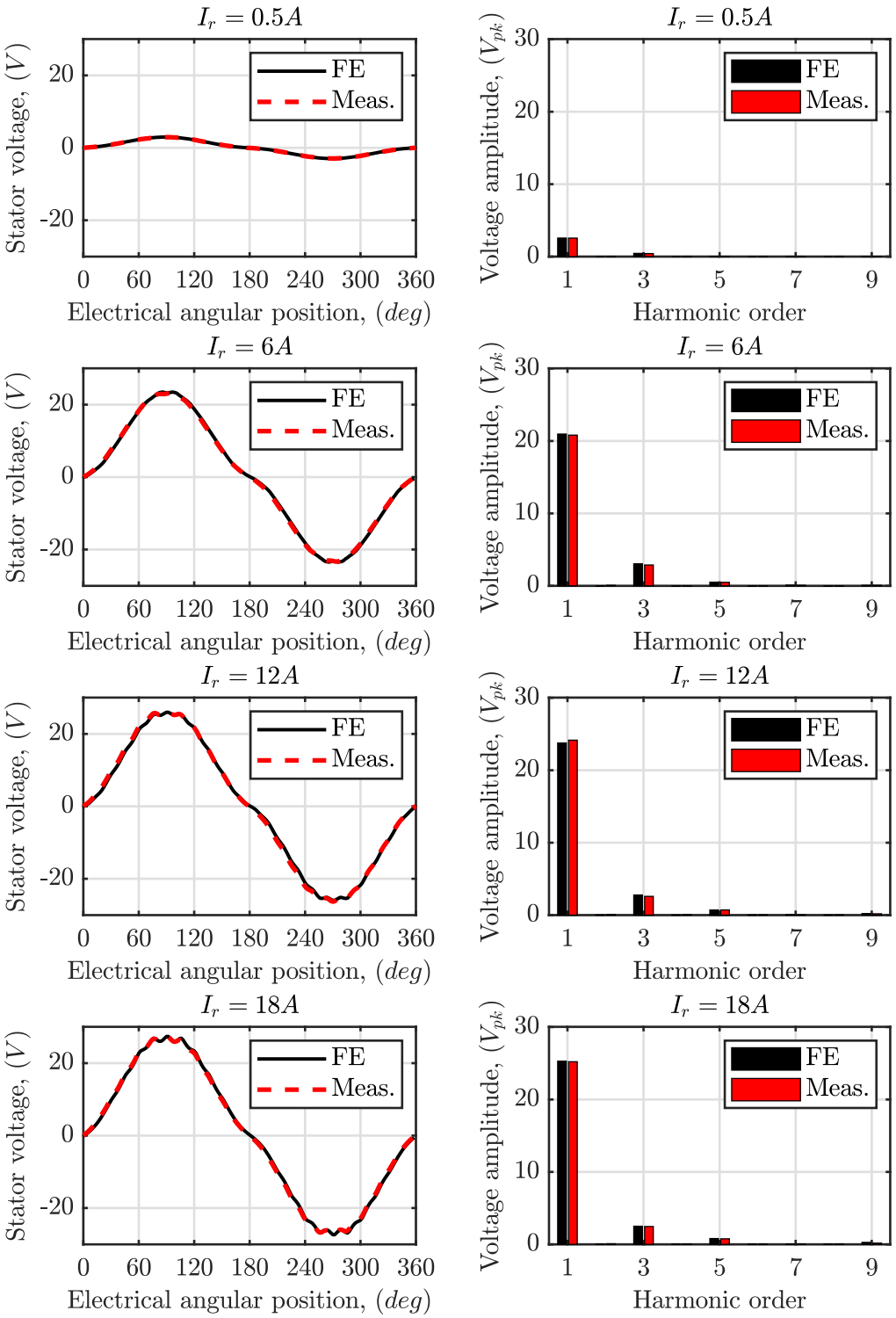

Fig. 5.20 Simulated and measured induced stator voltages at no-load.

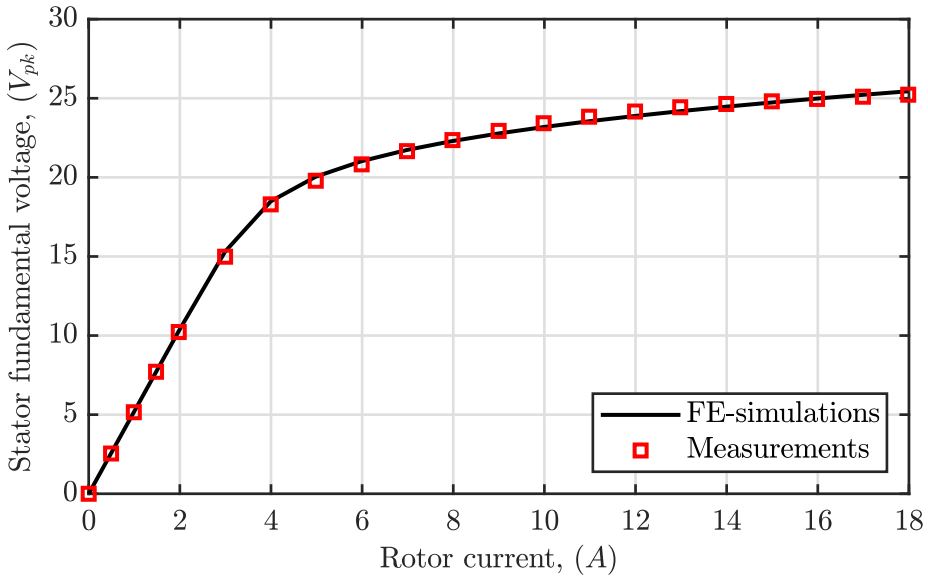

Fig. 5.21 Simulated and measured no-load characteristic.

5.3.1 The simulated no-load characteristic

The induced stator voltages in no-load conditions both measured and simulated via FEMM are shown in Fig.5.20 for a limited number of rotor currents. Figure 5.20 also exhibits the corresponding spectra of the selected results. As shown by the matching between the measured and simulated voltage waveforms, both the air gap length and the rotor pole shape have been modelled with satisfactory accuracy.

The resulting no-load characteristic is shown in Fig.5.21, along with the measured one. The results obtained from the simulations and the no-load test are listed in Table 5.10, together with the percentage error over the peak fundamental induced voltages. From the reported values, it can be seen that the percentage error, as an absolute value, does not exceed 2.2%, while the average error is 0.75%. These values demonstrate that the developed FE-model accurately represents the real motor sample and can be considered reliable, at least in no-load conditions.

On the basis of the FE-model, the current-to-flux linkage model can be computed. The current-to-flux linkage model is the correlation of the dq-fluxes with the d-, q- and rotor currents, generally in the form of lookup tables or multidimensional maps. This is needed for the identification of the rated load point of the motor, used to find the electromagnetic loadings to be used in the sizing algorithm.

Table 5.10 Results for the no-load test and simulation.

Measurements				*FE-simulations*	
$n,(\text{rpm})$	$I_r,(\text{A})$	$V_r,(\text{V})$	$V_{s1,pk},(\text{V})$	$V_{s1,pk},(\text{V})$	$\varepsilon,(\%)$
498.6	0.4910	2.986	2.544	2.558	-0.54
498.5	0.9899	5.960	5.154	5.157	-0.068
498.5	1.478	8.858	7.712	7.697	0.19
498.3	1.976	11.70	10.22	10.28	-0.58
498.6	2.993	17.51	14.98	15.31	-2.2
498.5	3.994	23.32	18.29	18.48	-1.0
498.5	4.983	29.23	19.79	20.04	-1.3
498.4	5.990	35.07	20.82	21.03	-1.0
498.5	6.985	40.94	21.66	21.73	-0.35
498.5	7.982	46.63	22.36	22.30	0.27
498.5	8.996	52.50	22.94	22.77	0.70
498.4	9.983	58.36	23.42	23.18	1.0
498.5	10.98	64.29	23.83	23.55	1.2
498.5	11.99	70.20	24.16	23.88	1.2
498.5	12.98	76.16	24.43	24.18	1.0
498.5	13.99	81.65	24.64	24.47	0.70
498.5	14.99	87.78	24.81	24.73	0.30
498.5	15.98	93.80	24.96	24.98	-0.089
498.5	16.99	100.2	25.10	25.22	-0.48
498.5	17.98	106.7	25.23	25.44	-0.86

5.3.2 Current-to-flux linkage model identification

Based on the information available online [142], the peak motor power is 100kW, the battery voltage 400V, and assuming both the power factor and the efficiency equal to 0.95, the peak value of the stator current is approximately 230A for the peak performances. No information is available on the rotor current; however, with a rotor current of 18A in no load conditions, the magnetic flux density in the rotor pole body is more than 2T, thus already highly saturated. The current-to-flux linkage model is

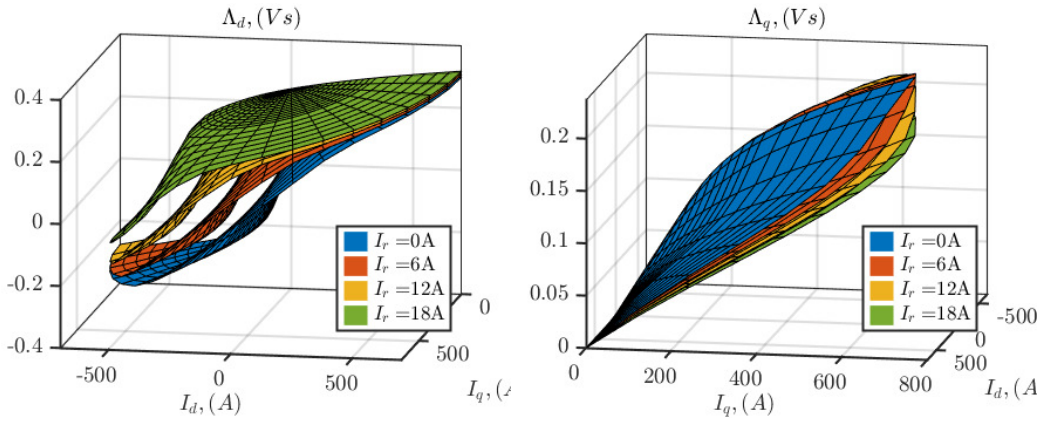

Fig. 5.22 Maps of the *dq*-axis flux for different rotor currents.

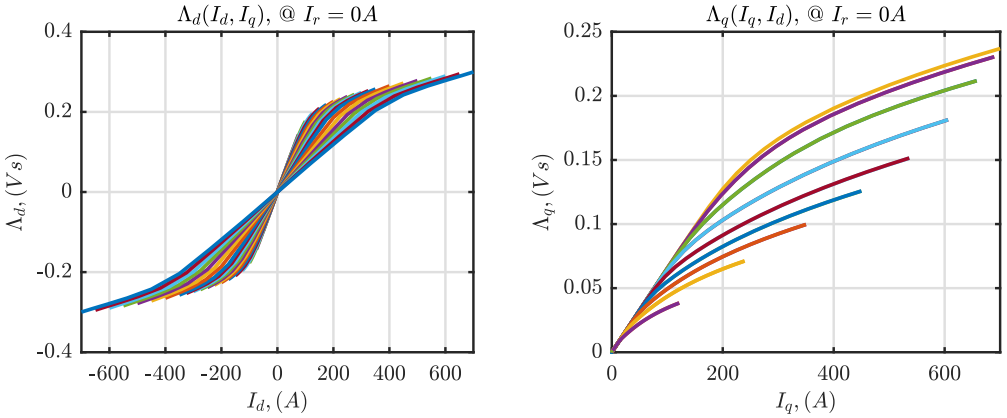

Fig. 5.23 *dq*-axis flux for 0A rotor current.

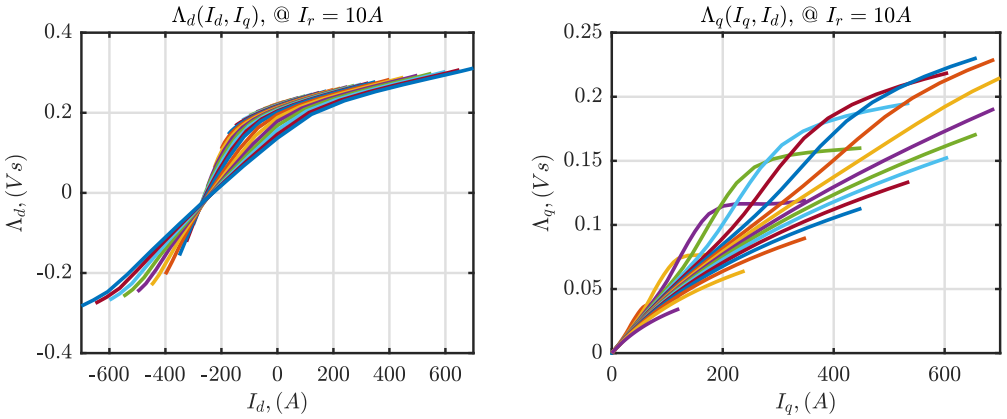

Fig. 5.24 *dq*-axis flux for 10A rotor current.

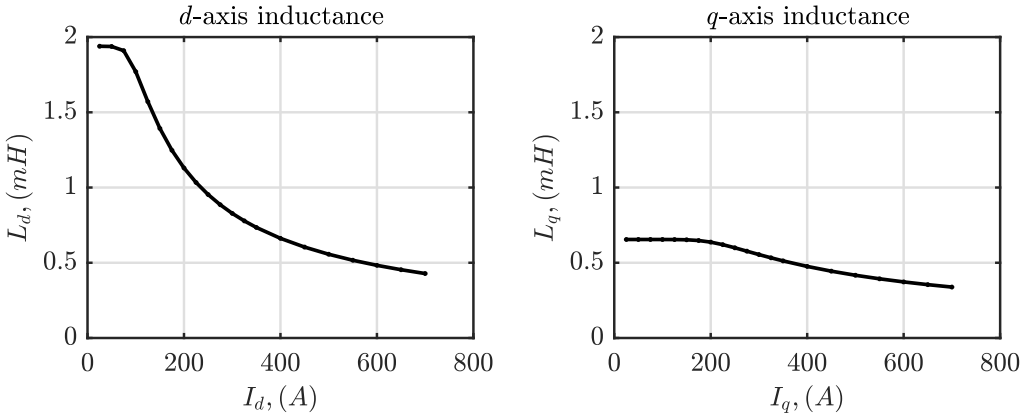

Fig. 5.25 *dq*-axis magnetic inductances.

Table 5.11 Measured and simulated *dq*-axes unsaturated inductances.

	Measurements	FE-simulation	Error
L_q	1.889 mH	1.939 mH	2.65%
L_d	0.6969 mH	0.6547 mH	6.44 %

therefore simulated via FEMM by setting the stator current amplitude to vary from 0 to 700A with a step of 25A up to 350A and then changing it to 50A; the stator current angle is set to vary from negative *d*-axis to positive *d*-axis with a step of 10°. The considered rotor angular positions comprehend one-sixth of the period, averaging the needed variables over 30 points. The rotor current is set to vary from 0 to 18A, with a step of 1A. The amount of simulated points for each rotor current is, therefore, 12540, leading to a total of 238260 simulations. This emphasises how the additional degree of freedom introduced by the rotor current makes the extrapolation of the model not trivial. The simulations have been distributed over 6 PCs with different rated characteristics, and for each of them, the parallelization over the available cores has been exploited. The process was completed in around two days. Figure 5.22 reports the obtained results for 4 simulated rotor currents. Figure 5.23 and Figure 5.24 show the obtained *dq* fluxes for 0A and 10A rotor currents.

The map of the *dq*-fluxes with the rotor current equal to zero can be used to extrapolate the values of the magnetic inductances in the *d*- and *q*-axis. Indeed, the value of L_d inductance can be simply obtained by dividing the *d*-axis flux by the *d*-axis current when the *q*-current is zero, and vice-versa for the computation of the

Table 5.12 Main specifications of the baseline motor.

Sizing code inputs	
Torque (T)	120Nm
Speed (n)	4000rpm
Stator phase voltage (V_s)	160V_{rms}
Pole pairs number (p)	2
Slots per pole per phase (q)	4
Minimum air gap thickness (g_0)	0.78mm
Rotor pole span (k_b)	0.64
Electromagnetic loadings limits	
Stator current density ($J_{s,max}$)	$7.3\text{A}/\text{mm}^2$
Rotor current density ($J_{r,max}$)	$8.4\text{A}/\text{mm}^2$
Linear current density ($A_{s,max}$)	$392\text{A}/\text{cm}$
Air-gap flux density at no-load ($B_{g,max}$)	0.95T
Stator yoke flux density at no-load ($B_{sy,max}$)	1.41T
Rotor yoke flux density at no-load ($B_{ry,max}$)	1.78T
Teeth flux density at no-load ($B_{t,max}$)	1.70T
Rotor pole flux density at no-load ($B_{p,max}$)	1.85T

L_q inductance. The obtained results are shown in Fig.5.25. The unsaturated values of the inductances can be compared to the ones obtained from the test described in Section 5.2.1 as an additional confirmation of the model's reliability. Both the measured and computed via simulation values are reported in Table 5.11, together with the percentage error.

5.4 The validation of the sizing procedure

On the basis of the obtained current-to-flux linkage model, a rated working point has been identified following the strategy adopted for the baseline motor used in the preliminary validation, reported in [38]. Therefore, the rotor and stator currents have been found with the aim of maximizing the power factor, thus leading to the individuation of the electromagnetic loadings, using the formula reported in Section 4.3. The obtained values are recollected in Table 5.12, together with the geometrical and winding layout sizing input parameters.

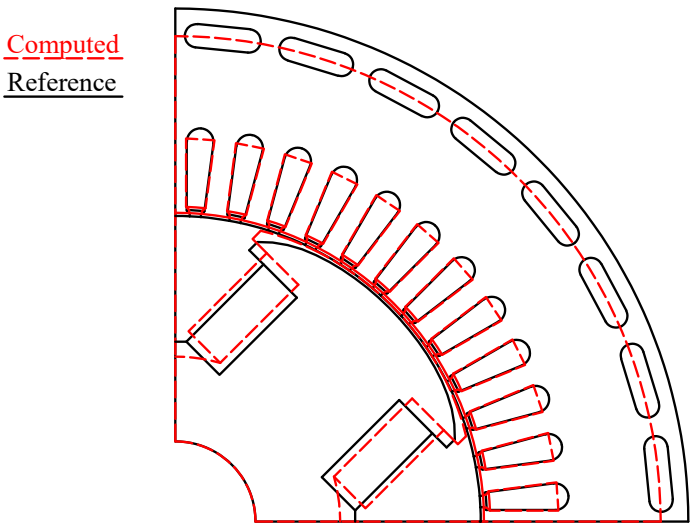

Fig. 5.26 Computed and reference geometry of the baseline motor.

Table 5.13 Main specifications of the baseline motor.

Geometric variable	Computed (mm)	Reference (mm)	Error (%)
L	176.8	175.0	1.0
D_{so}	248.1	248.5	-0.2
D_g	157.0	155.1	1.2
h_{sy}	26.16	23.75	10.1
h_p	35.97	38.13	-5.7
h_{ry}	21.64	18.48	17.1
w_{st}	5.568	5.900	-5.6
w_p	39.44	37.00	6.6

The obtained values are finally used as inputs for the sizing code presented in Chapter 4. The machine obtained by the sizing code is presented in Fig.5.26, together with the baseline ZOE motor. The comparison of the obtained and reference geometric dimensions are listed in Table 5.13. The reported percentage error values indicate that the main dimensions are predicted by the sizing code with sufficient accuracy, although it must be noted that a fair comparison of the outer stator diameter is not trivial to define. In the table, the diameter considered for the reference machine passes through the centres of the cooling slots.

Regarding the other dimensions, the largest errors can be appreciated in the stator and rotor yoke. However, the definition of these two geometric variables for the

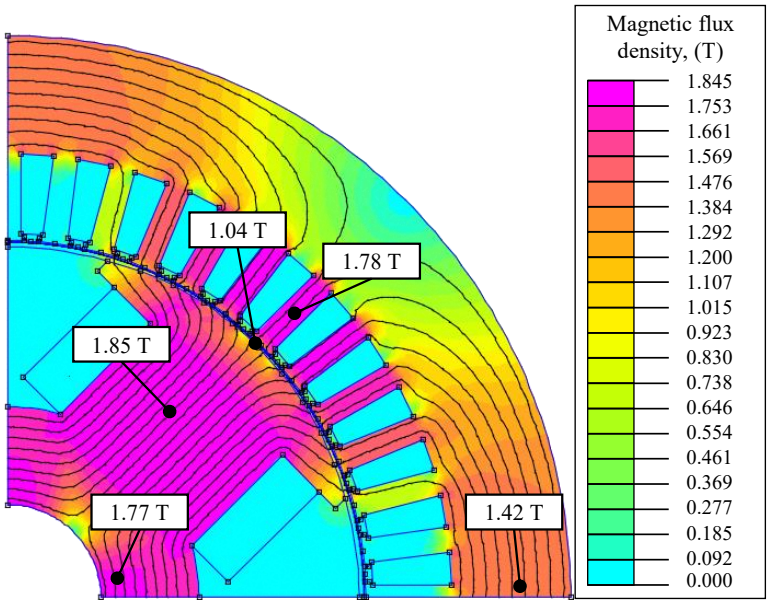

Fig. 5.27 Colour density map of the magnetic flux density of the computed WFSM motor in no-load conditions.

reference machine can be ambiguous. The rotor yoke considered for the comparison is the minimum available. This explains the obtained 17.1% error. The stator yoke has been identified starting from the end of the circular part of the slots up to the centre of the cooling slots. Therefore, such dimension is affected by the real shape of the stator and cooling slots, which are not accounted for in the proposed sizing procedure. In conclusion, the obtained results are considered satisfactory, especially considering that the proposed sizing procedure must be intended as a preliminary design tool to be subjected to refinements for the project finalization.

The colour density map of the magnetic flux density in no-load conditions is shown in Fig.5.27, with labelled values on the main machine parts. The reported no-load air gap flux density (1.04T) shows an error of 9.47% with respect to the one in Table 5.12 (0.95T). However, it must be considered that the pole tip profile of the ZOE motor is shaped differently than the inverse cosine function used in the sizing algorithm, leading to different fundamental values of the magnetic flux density. On the contrary, the motor used for the preliminary validation in Chapter 4 is actually shaped as in the sizing procedure, resulting in more similar results, i.e. a percentage error of 2%.

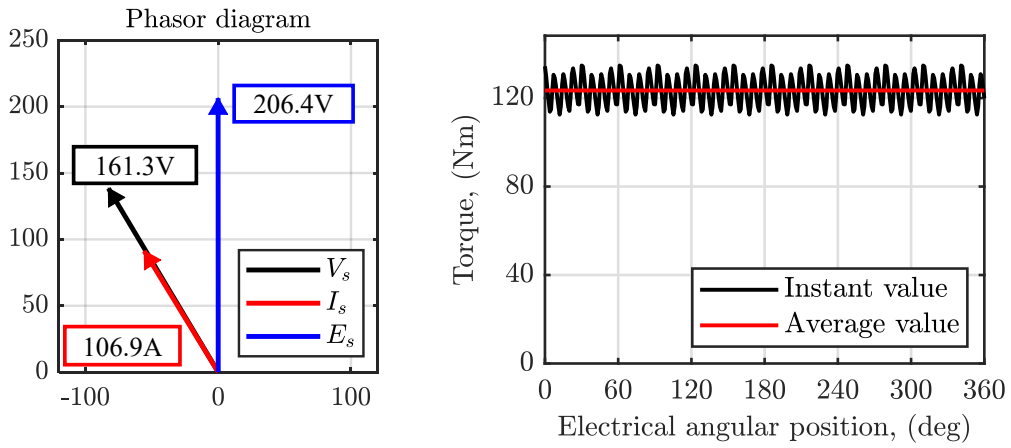

Fig. 5.28 Phasor diagram (a) and output torque (b) of the computed WFSM motor.

The computed machine's load performance is reported in Fig.5.28, regarding the phasor diagram (in rms values) and the output torque. The phasor diagram indicates that both the stator voltage limit and the power factor are respected with a margin error of less than 0.82%. The value of the average output torque is 123.4Nm, meaning an error of 2.86%. The output torque is reached with a linear current density of 338.0A/cm and rotor current density of 8.2A/mm^2. Note again that the value of the stator current density is not used as a check condition; therefore, its value is exactly the requested one.

5.5 Conclusion

The sizing procedure developed in this dissertation has been validated using a sample of the Renault ZOE motor. The sample has been subjected to a work of reverse engineering to extrapolate the motor characteristics necessary for the validation. Both direct measurements and 3D scans have been used to define the motor geometry, while the BH-curve of the employed material has been experimentally measured. Based on this information, the machine finite elements model is built. The goodness of the extrapolated machine information, as well as the developed FE model, has been proven by measuring the no-load characteristics on the sample and comparing the FE and measured no-load characteristics. Therefore, finite element simulations are used to define the machine current-to-flux linkage model and, thus, extrapolate

the electromagnetic inputs required by the developed sizing code. The sizing code with retrieved electromagnetic and geometry information provides a final geometry comparable to the actual ZOE motor, with an accuracy on the main dimensions, i.e. the axial length, the stator outer diameter and the air gap diameter, characterized by a few per cent errors. In conclusion, it has been proven that the proposed sizing procedure is able to obtain machine volumes that have a valid correspondence with existing machines, starting from a limited number of specifications, such as targets and constraints.

Chapter 6

Thermal Aspects & Modeling

Thermal analysis represents a critical factor in electrical machine design due to the impact of temperature increase on insulation lifetime. The literature reports many research papers that focus on the thermal analysis of electric machines. Depending on the analysis techniques used to compute the temperature distribution, thermal models can be mainly categorized as analytical and numerical models [147, 148]. Both modelling methods feature advantages and drawbacks that impact the thermal model complexity, accuracy, and resolution time [149, 150].

Numerical models consist of thermal FE or computational fluid dynamic (CFD) models that allow accurate prediction of the temperatures in the different machine parts [151–154]. However, detailed knowledge of the machine's geometrical dimensions and the characteristics of the used materials is mandatory, as well as knowledge of the details of the cooling system. Moreover, the model setup and its resolution are usually very time-consuming. Because of these drawbacks, engineers working in manufacturing companies often limit numerical thermal analyses only to the final design stage, occasionally using multiphysics models for a comprehensive performance assessment of the electric machines [155, 156]. Electromagnetic and thermal numerical co-simulations are sometimes conducted to assess faulty conditions [157].

Analytical thermal models consist of lumped parameters networks modelled on the basis of the heat transfer theory [158–160]. This approach exploits the modelling equivalence between thermal and electric circuits. In detail, thermal resistances represent the heat transfer due to conduction, convection, and radiation phenomena and allow computation of the steady-state temperatures, while thermal

capacitances represent the energy storage capacity and allow modelling of the thermal transient behaviour. In the thermal network, the heat sources related to the different machine losses are modelled by means of current generators, while the node voltages represent the temperature values for the different machine parts. The lumped nature of this modelling approach considers each machine loss and the corresponding heat source uniformly distributed into the machine components [161]. Similarly, the node voltages represent the average temperatures for the modelled machine parts. Increasing the number of nodes results in a higher-order thermal network that better discretizes the machine under analysis but at the expense of increased model complexity because of the larger number of parameters that must be determined.

The parameter values of the LPTN can be mainly computed using equations reported in literature upon the knowledge of machine dimensions and material properties [158]. In detail, thermal capacitances are derived by the weight and the specific heat capacity of the materials, while thermal resistances are usually determined assuming the different machine parts as hollow cylinders. The heat transfer coefficients due to radiation and convection are typically obtained by empirical formulas [162–165]. However, for particularly complex and high-order LPTNs, as well as for those cases where the assumptions for the thermal parameters computations are not rigorous, the identification of a thermal parameters set that allows accurate replication of the temperature variations measured on the real machine may not be straightforward. In these cases, optimization techniques are often used in conjunction with measurements to properly calibrate the thermal network parameters [166–169].

In this research activity, methodologies for developing lumped parameter thermal networks for synchronous machines are presented, focusing on the identification of the parameters by means of experimental and optimization approaches. In particular, in the absence of a wound-field sample equipped with thermocouples, the study is conducted on small synchronous SPM machines used in automotive actuators [170, 171]. Adjustments are adopted to make the WFSM thermal network suitable for SPM machines, specifically regarding the differences in the rotors. Moreover, for the specific case used for the validation, dedicated lumped parameter thermal networks are proposed to predict operative conditions requiring a non-uniform thermal distribution. Finally, considerations on the heat exchange with the ambient in the absence of force convection are drawn, focusing on the corresponding network parameter computation. The considerations are independent of the machine type.

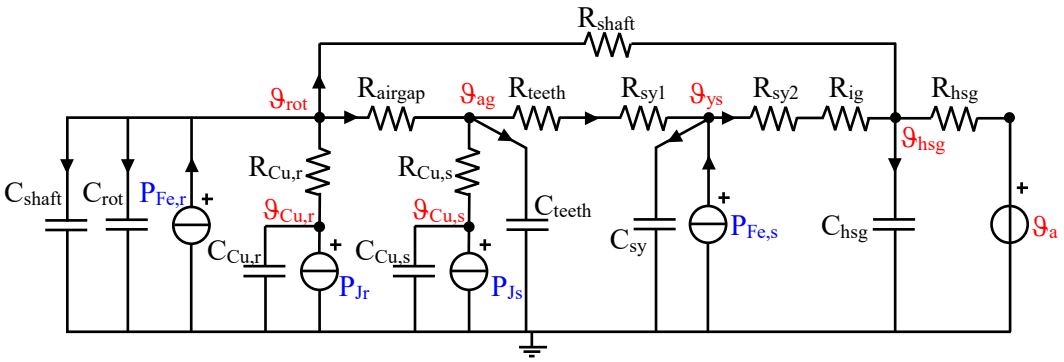

Fig. 6.1 Lumped parameter thermal network for wound-field synchronous machines.

6.1 The Lumped Parameter Thermal Network Approach

The thermal network is developed starting from the Mellor and Turner model, where the machine is subdivided into several parts that are assumed to have the same thermal behaviour, and it is shown in Fig.6.1. In particular, the motor is subdivided into hollow cylinders concentric with the rotor axis [158]. Moreover, as a first approximation, the rotor poles are assessed with the same methodology adopted for the stator teeth. The following hypotheses form the foundation of the developed thermal model:

- motor symmetry around the shaft and about the radial plane through the centre of the machine;
- the influence of the asymmetrical temperature distribution is neglected;
- each cylinder is thermally symmetrical in the radial direction;
- the heat sources are uniformly distributed;
- the heat flux in the axial direction is considered only in the shaft.

The thermal parameters are recollected in Table 6.1. The considered loss sources are:

- $P_{Fe,r}$ and $P_{J,r}$: iron and Joule losses on the rotor, respectively;
- $P_{Fe,s}$ and $P_{J,s}$: iron and Joule losses on the stator, respectively;

Table 6.1 Thermal network parameters.

Parameter	*Description*
	Thermal Capacitance
C_{shaft}	Thermal capacitance of the shaft
C_{rot}	Thermal capacitance of the rotor
$C_{Cu,r}$	Thermal capacitance of the rotor winding
$C_{Cu,s}$	Thermal capacitance of the stator winding
C_{teeth}	Thermal capacitance of the stator teeth
C_{sy}	Thermal capacitance of the stator yoke
C_{hsg}	Thermal capacitance of the housing
	Thermal Resistance
R_{shaft}	Thermal resistance of the shaft
$R_{Cu,r}$	Thermal resistance between rotor winding and rotor core
R_{airgap}	Convection thermal resistance of the air gap
$R_{Cu,s}$	Thermal resistance between stator winding and stator core
R_{teeth}	Radial thermal resistance of the stator teeth
R_{sy1}	Radial thermal resistance of the inner half of the stator yoke
R_{sy2}	Radial thermal resistance of the outer half of the stator yoke
R_{ig}	Radial thermal resistance of the interface gap between stator core and housing
R_{hsg}	Convection thermal resistance between housing and ambient

The temperature evaluated in the different nodes are:

- $\vartheta_{Cu,r}$: temperature of the rotor copper;
- ϑ_{rot}: temperature of the rotor core;
- $\vartheta_{Cu,s}$: temperature of the stator copper;
- ϑ_{ag}: temperature of the air gap;
- ϑ_{sy}: temperature of the stator yoke;
- ϑ_{hsg}: temperature of the housing;
- ϑ_{a}: ambient temperature.

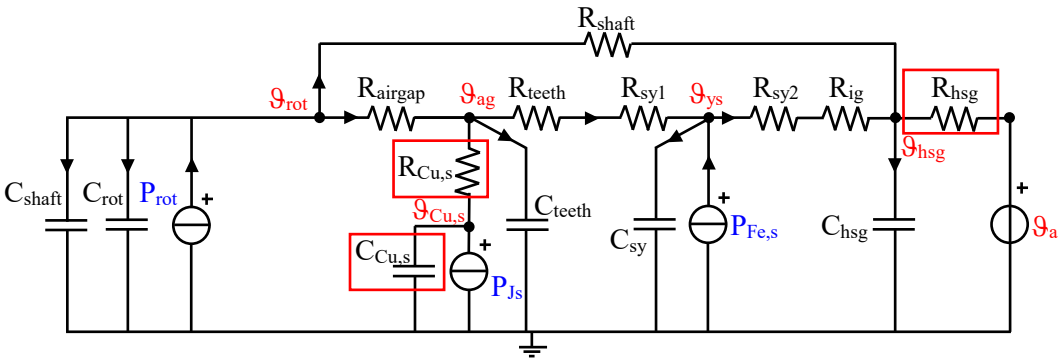

Fig. 6.2 Lumped parameter thermal network for permanent magnets synchronous machines.

The proposed LPTN is also suitable for PM machines adopting some adjustments. In particular, the branch relative to the rotor copper must be removed, and the rotor core losses must include the permanent magnet losses, i.e. $P_{rot} = P_{Fe,r} + P_{PM}$. The resulting network is shown in Fig.6.2. The different motor parts are shown in the sketch of an SPM motor in Fig.6.3.

6.1.1 The thermal parameters

All the parameters of the LPTN can be computed by means of the dimensions of the motor and the thermal characteristics of the used materials, except for the thermal resistance of the housing and the parameters relative to the stator winding, which are all represented in red squares in Fig.6.2. These parameters can be calibrated on a *dc* test, as later explained. In the following sections, the procedure for the computation of the thermal parameters is presented. In particular, thermal capacitances are firstly computed, followed by thermal resistances, and subsequently, the parameters obtainable through calibration are presented.

-The thermal capacitances

The generic thermal capacitance C_{th} of the presented LPTN can be computed by multiplying the weight of the considered motor part and the specific heat capacity of the relative material c_p. Moreover, the weight of the considered motor part can be obtained by multiplying the material specific weight γ by its occupied volume v. In

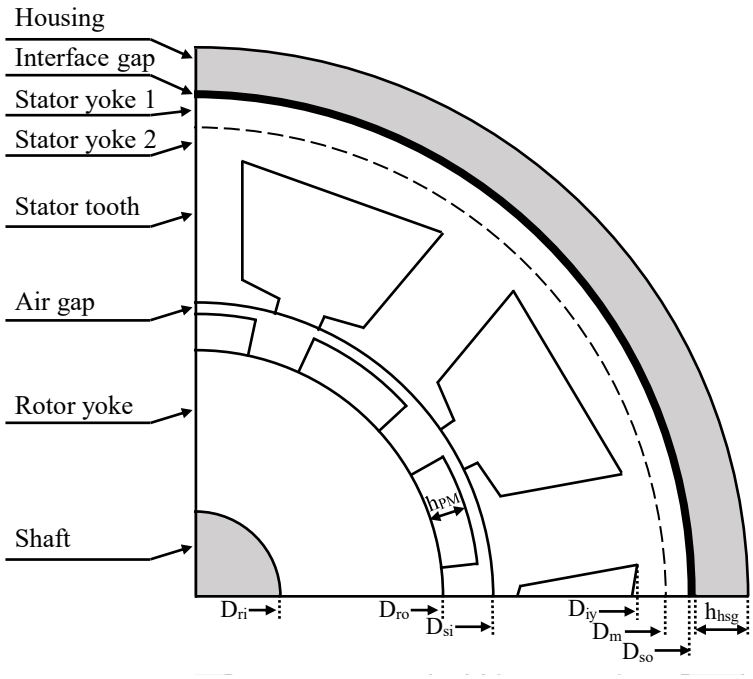

Fig. 6.3 Sketch of a surface permanent magnet motor.

conclusion, the generic thermal capacitance can be computed as in (6.1).

$$C_{th} = c_p \cdot \gamma \cdot v \tag{6.1}$$

Therefore, assuming the specific heat capacity and the specific weight of the material to be known by the catalogue, computing the thermal capacitance means computing the motor part volume.

The thermal capacitance of the shaft

Starting from the left side of the network of Fig.6.2, the thermal capacitance of the shaft (C_{shaft}) is obtained through the volume of the shaft v_{shaft}, which can be computed as the volume of a cylinder.

$$v_{shaft} = \left(\frac{D_{ri}}{2}\right)^2 \cdot \pi \cdot L \tag{6.2}$$

The thermal capacitance of the rotor

The thermal capacitance of the rotor (C_{rot}), for a PM machine, consists of the sum of the thermal capacitance of the rotor yoke and that of the permanent magnets, computed as in (6.3) and (6.4), respectively.

$$v_{ry} = \left(\frac{D_{ro}^2}{4} - \frac{D_{ri}^2}{4} \right) \cdot \pi \cdot L \tag{6.3}$$

$$v_{PM} = k_{PM} \cdot \left(\frac{(D_{ro} + 2 \cdot h_{PM})^2}{4} - \frac{D_{ro}^2}{4} \right) \cdot \pi \cdot L \tag{6.4}$$

In (6.4), k_{PM} is the portion of one pole occupied by the permanent magnet, while h_{PM} is the height of the permanent magnets.

Thermal capacitance of the teeth

The thermal capacitance of the stator teeth (C_{teeth}) is computed through the volume of the stator teeth (v_{teeth}), which depends on the specific shape of the stator teeth/slots. Considering the S_{tooth} the cross-sectional area of one tooth and n_{teeth} the number of teeth, the total volume of the teeth is:

$$v_{teeth} = S_{tooth} \cdot n_{teeth} \cdot L \tag{6.5}$$

Thermal capacitance of the stator yoke and the housing

The thermal capacitance of the stator yoke (C_{sy}) and the housing (C_{hsg}) are obtained by computing their volumes as in (6.6) and (6.7), considering D_{iy} the diameter at the bottom of the stator slots and h_{hsg} the housing height.

$$v_{sy} = \left(\frac{D_{so}^2}{4} - \frac{D_{iy}^2}{4} \right) \cdot \pi \cdot L \tag{6.6}$$

$$v_{hsg} = \left(\frac{(D_{so} + 2 \cdot h_{hsg})^2}{4} - \frac{D_{so}^2}{4} \right) \cdot \pi \cdot L \tag{6.7}$$

-The thermal resistances

The formulations for the computation of the thermal resistances have been elaborated and adapted for SPM machines starting from the equations reported in [158]. The heat flux in the axial direction has been neglected in all the machine parts except for the shaft. Therefore, all the thermal resistances, except R_{shaft}, can be computed using the equations of the hollow cylinders; thus, they can be obtained by knowing the geometric dimensions.

The thermal resistance of the shaft

The thermal resistance of the shaft can be computed as the sum of three contributions, as in (6.8), where k_{ir} is the temperature-dependent iron thermal conduction coefficient, and L_{shaft} is the length of the shaft. The first one represents the radial thermal flux due to the rotor yoke, the second one considers the part of the shaft placed below the rotor core, and the last one is due to the shaft part external to the rotor core length.

$$R_{shaft} = \frac{1}{2 \cdot \pi \cdot k_{ir}} \cdot \ln \frac{D_{ro}}{D_{ri}} + \frac{L}{2 \cdot k_{ir} \cdot \pi \cdot D_{ri}^2} + \frac{L_{shaft} - L}{k_{ir} \cdot \pi \cdot D_{ri}^2} \tag{6.8}$$

The iron thermal conduction coefficient can be expressed as a function of its temperature in kelvin [158].

$$k_{ir} = -0.024 \vartheta_{iron} + 65.552 \tag{6.9}$$

The convection thermal resistance of the air gap

The convection thermal resistance of the air gap can be computed through (6.10), where h_{ag} is the forced convection coefficient of the air [158].

$$R_{airgap} = \frac{1}{\pi \cdot D_{si} \cdot L \cdot h_{ag}} \tag{6.10}$$

The coefficient h_{ag} can be obtained through (6.11), where Nu is the Nusselt number, k_{air} is the thermal conduction coefficient of the air.

$$h_{ag} = \frac{Nu \cdot k_{air}}{2 \cdot g} \tag{6.11}$$

The Nusselt number depends on the comparison between the Reynold number and the Reynolds critical number, which can be respectively computed as in (6.12) and (6.13), where ρ is the fluid density, v is the fluid speed, μ is the fluid dynamic viscosity.

$$Re = \frac{\rho \cdot v \cdot L}{\mu} \tag{6.12}$$

$$Re_{cr} = 100\sqrt{\frac{D_{si}}{2} \cdot g} \tag{6.13}$$

The Nusselt number is 2 if $Re < Re_{cr}$, meaning thermal conduction conditions, otherwise:

$$Nu = 0.386\frac{1}{\sqrt{D_{si}/2 \cdot g}}Pr^{0.27} \tag{6.14}$$

In (6.14), Pr is the Prandtl number, which can be computed as in (6.15).

$$Pr = \frac{c_p \cdot \mu}{k} \tag{6.15}$$

In (6.15), k is the conduction heat coefficient. In the case of air, as considered fluid, the conduction heat coefficient can be obtained as in (6.16), where ϑ_{airgap} is expressed in kelvin [158].

$$k_{air} = -0.0000795\vartheta_{airgap} + 0.00246 \tag{6.16}$$

The thermal resistance of the stator teeth

The thermal resistance of the stator teeth can be computed as in (6.17).

$$R_{teeth} = \frac{1}{2 \cdot \pi \cdot k_{ir} \cdot L \cdot p_{ir}} \cdot \ln\left(\frac{D_{iy}}{D_{si}}\right) \tag{6.17}$$

The coefficient p_{ir} is the percentage of the teeth iron volume with respect to the total teeth plus slots volume, and it is computed as:

$$p_{ir} = \frac{n_{teeth} \cdot S_{tooth}}{\left(\frac{D_{iy}^2}{4} - \frac{D_{si}^2}{4}\right) \cdot \pi \cdot L} \tag{6.18}$$

The thermal resistance of the stator yoke

The stator yoke is subdivided into two hollow cylinders separated at the middle stator yoke diameter. In this way, the loss source corresponding to the stator iron losses can be applied in the middle of the stator yoke. The formulations for the radial conduction stator yoke thermal resistances are reported in (6.19) and (6.20) for the inner and outer stator yoke parts, respectively.

$$R_{sy1} = \frac{1}{2 \cdot \pi \cdot k_{ir} \cdot L} \ln\left(\frac{D_m}{D_{iy}}\right) \tag{6.19}$$

$$R_{sy2} = \frac{1}{2 \cdot \pi \cdot k_{ir} \cdot L} \ln\left(\frac{D_{so}}{D_m}\right) \tag{6.20}$$

The thermal resistance of the interface gap between the stator core and housing

The interface gap accounts for the assembling process of the stator pack into the housing; this conduction thermal resistance is computed by (6.21), where the thermal conduction coefficient has been assumed equal to that of air at the ambient temperature, while h_{ig} is the radial thickness.

$$R_{ig} = \frac{h_{ig}}{2 \cdot \pi \cdot k_{air} \cdot L \cdot D_{so}/2} \tag{6.21}$$

-The thermal parameters obtained through calibration

The definition of the thermal capacitance of the stator winding ($C_{Cu,s}$), the thermal resistance between the stator winding and the stator core ($R_{Cu,s}$), and the thermal resistance between the housing and the ambient (R_{hsg}) are computed by means of a *dc* test. In particular, the first instants of the test are necessary for finding the parameters $C_{Cu,s}$ and $R_{Cu,s}$, while the steady-state conditions must be reached to define R_{hsg}. The *dc* test can be conducted by supplying two of the three stator phases

or by supplying the series of one phase and the parallel of the other two phases. Otherwise, if the neutral is accessible, the three phases can be connected in parallel. The last option results in the most uniform heat distribution in the electric machine.

The thermal capacitance of the stator winding and the thermal resistance between the stator winding and the stator core

The definition of the thermal characteristics of a stator winding must consider that this component of the machine is a distributed composite (combination of the electric insulation, impregnation, and air). Adopting pure material properties as input data for the thermal models returns inaccurate temperature predictions. Hence, a reasonable approach involves determining equivalent properties through measurements of a *dc* test [172–174]. Since the motor is supplied with a *dc* current, the only active loss source is the stator Joule losses in the copper. It is assumed that if the housing temperature does not change more than one degree, the winding can be considered adiabatic with respect to the rest of the motor. This means that all the heat produced by the stator Joule losses is entirely used to heat the winding. In these initial instants, the temperature of the stator winding can be obtained by solving a first-order RC circuit:

$$\vartheta_{Cu,s} = \vartheta_{amb} + R_{Cu,s} \cdot P_{Js}\left(1 - e^{\frac{t}{R_{Cu,s} \cdot C_{Cu,s}}}\right) \tag{6.22}$$

Therefore, by comparison with the measurements, it is possible to find the parameters $R_{Cu,s}$ and $C_{Cu,s}$, which minimize the error between the computed and the measured winding temperature. In this study, this is performed by using the particle swarm optimization technique.

The thermal resistance between the housing and the ambient

The thermal resistance between the housing and the ambient can be obtained through a steady-state *dc* test:

$$R_{hsg} = \frac{\vartheta_{hsg,\infty} - \vartheta_{amb,\infty}}{P_{Js}} \tag{6.23}$$

where $\vartheta_{hsg,\infty}$ and $\vartheta_{amb,\infty}$ are the housing and ambient temperatures in steady-state conditions.

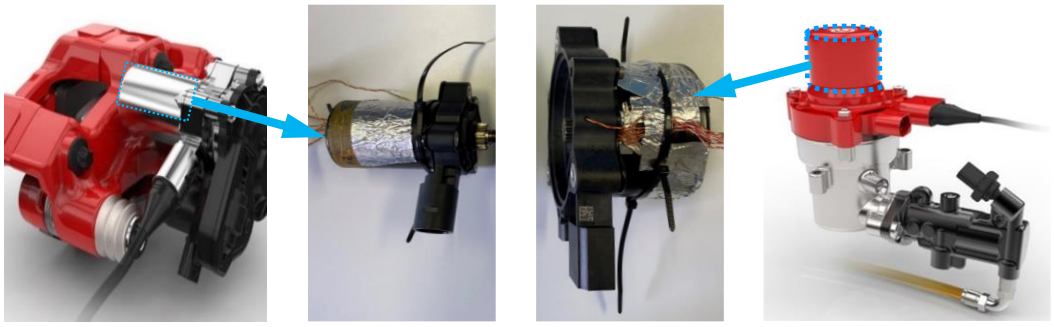

(a) (b)

Fig. 6.4 The SPM motors and their positioning inside the BBW actuators.

6.1.2 Validation on a synchronous machines case study

The presented LPTN is used to predict the temperatures of two different SPM motors used in brake-by-wire (BBW) automotive actuators, which are depicted in Fig.6.4. These machines equip the two different systems shown on the sides of Fig.6.4. The structure on the left is an electromechanical brake calliper in which electric energy is directly converted into clamping force, while the structure on the right side is an electro-hydraulic actuator that converts electric energy into hydraulic pressure on a standard brake calliper.

The two machines are SPM motors, rated a few hundred watts, with a star-connected concentrated winding, and characterized by very different aspect ratios λ, i.e. the ratio between the axial length L over the diameter D_g at the air gap. Hereinafter, the machine with the highest aspect ratio is referred to as the '*slender*' motor, while the machine with the lower aspect is the '*disk-shaped*' machine. The disk-shaped motor features a rated power 1.5 times greater than the slender motor and a lower aspect ratio: $L/D_g = 0.42$ for the disk-shaped motor, $L/D_g = 1.69$ for the slender motor. In their normal working conditions, the machines are low voltage supplied and repetitive pulses of *dc* currents are injected in two of the three phases. This results in an asymmetrical location of the heat sources and, consequently, uneven temperature distributions inside the machines. An extensive thermal test campaign has been conducted on both motors to calibrate and validate the thermal networks.

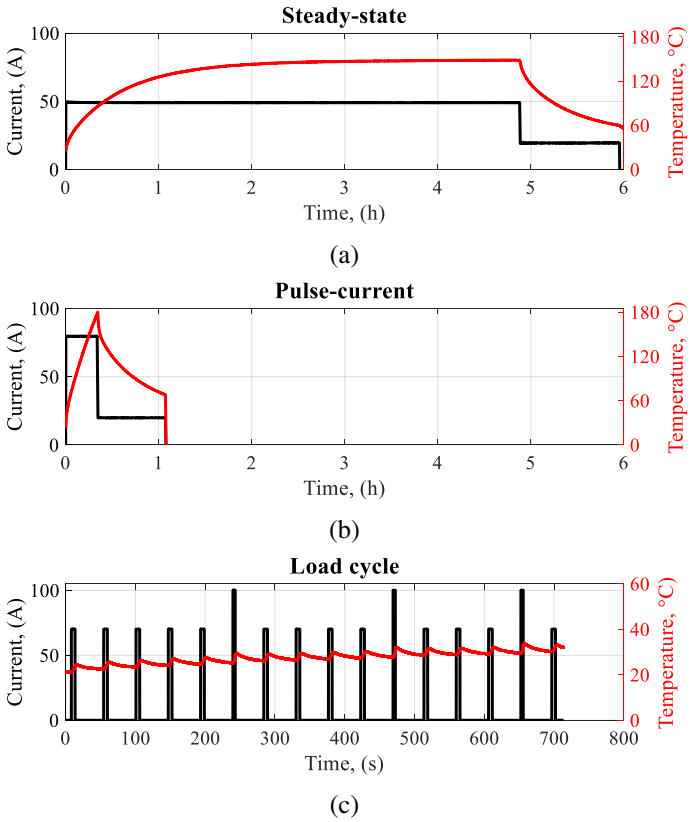

Fig. 6.5 The performed thermal tests:(a) steady-state, (b) pulse-current, (c) load cycle.

6.1.3 The performed thermal tests

The two motors have been equipped with several thermocouples, as depicted in Fig.6.4, and tested in two different ambient conditions: ambient air and climatic chamber. Inside the climatic chamber, the ambient temperature was set to 120°C to consider the operating temperature of the brake-by-wire system. The test campaign was based on three different thermal tests: '*steady-state*', '*pulse-current*' and '*load cycle*' tests. The first consists of injecting a *dc* current until the steady-state conditions are reached, see Fig.6.5a. The second consists of injecting a *dc* current until the maximum admissible temperature (180°C) is reached, as depicted in Fig.6.5b. The third consists of injecting repetitive current pulses to test the motor under working conditions similar to the real ones. Two load cycle tests have been defined. The load cycle 1 consists of injecting repetitive pulses of *dc* currents for a defined time duration; subsequently, another defined time interval waits before the next pulse of current. For the second load cycle, two different values of currents are injected. For

the slender motor, the lower value is injected four consecutive times before supplying the motor with one pulse of the highest current. For the disk-shaped motor, the lower value is injected five consecutive, and, in the following periods, the number of low current injections progressively decreases by one, as shown in Fig.6.5c. The tests performed on the slender motor are one steady-state test, eight pulse-current tests and two load cycles in ambient air, while one steady-state, six pulse-current tests and two load cycles have been performed in the climatic chamber. For the disk-shaped motor, one steady-state test, seven pulse-current tests and two load cycles have been performed in ambient air, while one steady-state test, eight pulse-current tests and two load cycles in the climatic chamber.

The aim is to predict the temperatures of the load cycle tests by using the LPTN of Fig.6.2. The steady-state tests are used for the calibration of the network: the first instants of the test are used for the parameters $C_{Cu,s}$ and $R_{Cu,s}$, and the last instants for R_{hsg}. The pulse-current tests are later used to calibrate the developed '*phase-split*' LPTN, presented in Section 6.2.

6.1.4 The obtained results

The obtained parameters for the LPTN of Fig.6.2 are listed in Table 6.2 for both the slender and the disk-shaped motor in ambient air and climatic chamber conditions. Each motor features different thermal resistances depending on the ambient. Indeed, the thermal resistances are temperature-dependent, and therefore, different values are obtained in the ambient air ($\vartheta_{amb} \approx 20°C$) and climatic chamber ($\vartheta_{amb} \approx 120°C$) conditions. Similarly, the parameters $C_{Cu,s}$, $R_{Cu,s}$ and R_{hsg} are doubly calibrated: on a steady-state test in ambient air and a steady-state test in the climatic chamber. The thermal network is therefore simulated, giving as input the measured ambient temperature and the power losses. The temperatures in the different nodes are computed by solving the corresponding system of differential equations and using Euler's method. Considering that in all the performed tests, *dc* currents are injected in the stator, the only active loss source is represented by the stator Joule losses. The results are shown in Fig.6.6 and Fig.6.7 for the slender motor in the ambient air and the climatic chamber, respectively. The results for the disk-shaped motor are shown in Fig.6.8 and Fig.6.9. Specifically, the reported measured '*Copper Temperature*' is the average of the measured temperatures of the two supplied phases.

Table 6.2 Thermal parameters of the LPTN for the baseline motors - capacitances in $J/°C$ and resistances in $°C/W$.

Parameter	Slender motor		Disk-shaped motor	
	Ambient air	Climatic chamber	Ambient air	Climatic chamber
C_{shaft}	15.74	15.74	10.32	10.32
C_{rot}	49.46	49.46	39.94	39.94
$C_{Cu,s}$	58.05	117.0	114.9	312.0
C_{teeth}	31.04	31.04	44.29	44.29
C_{sy}	40.97	40.97	67.24	67.24
C_{hsg}	46.06	46.06	62.41	62.41
R_{shaft}	11.12	11.08	8.165	8.253
R_{airgap}	4.506	4.634	14.52	13.84
$R_{Cu,s}$	0.4067	0.2400	0.1867	0.1067
R_{teeth}	0.07115	0.07089	0.3298	0.3332
R_{sy1}	0.004620	0.004603	0.01703	0.01721
R_{sy2}	0.004341	0.004326	0.01568	0.01584
R_{ig}	0.1248	0.09672	0.2366	0.1848
R_{hsg}	3.970	2.190	2.500	1.130

The results show that the lumped parameter thermal network accurately predicts the temperatures in the steady-state conditions for both the slender and the disk-shaped motor. This is especially true for the slender motor, whose shape is more consistent with the hypothesis of the proposed model, i.e. the heat flux is considered to be mainly radial. The obtained results for the disk-shaped machine are necessarily less accurate, nonetheless leading to a maximum error of 6.7% for the copper temperature.

The predicted temperatures for the load cycles adequately match the measurements for both motors in ambient air conditions, especially for the copper temperature. However, low-accuracy results are achieved in the climatic chamber for both the copper and the housing temperatures. In all the cases, the proposed network overestimates the housing temperature of the load cycle. Considering that the duration of the load tests is much lower than that of the steady-state tests, the value of the housing thermal capacitance significantly impacts the housing temperature

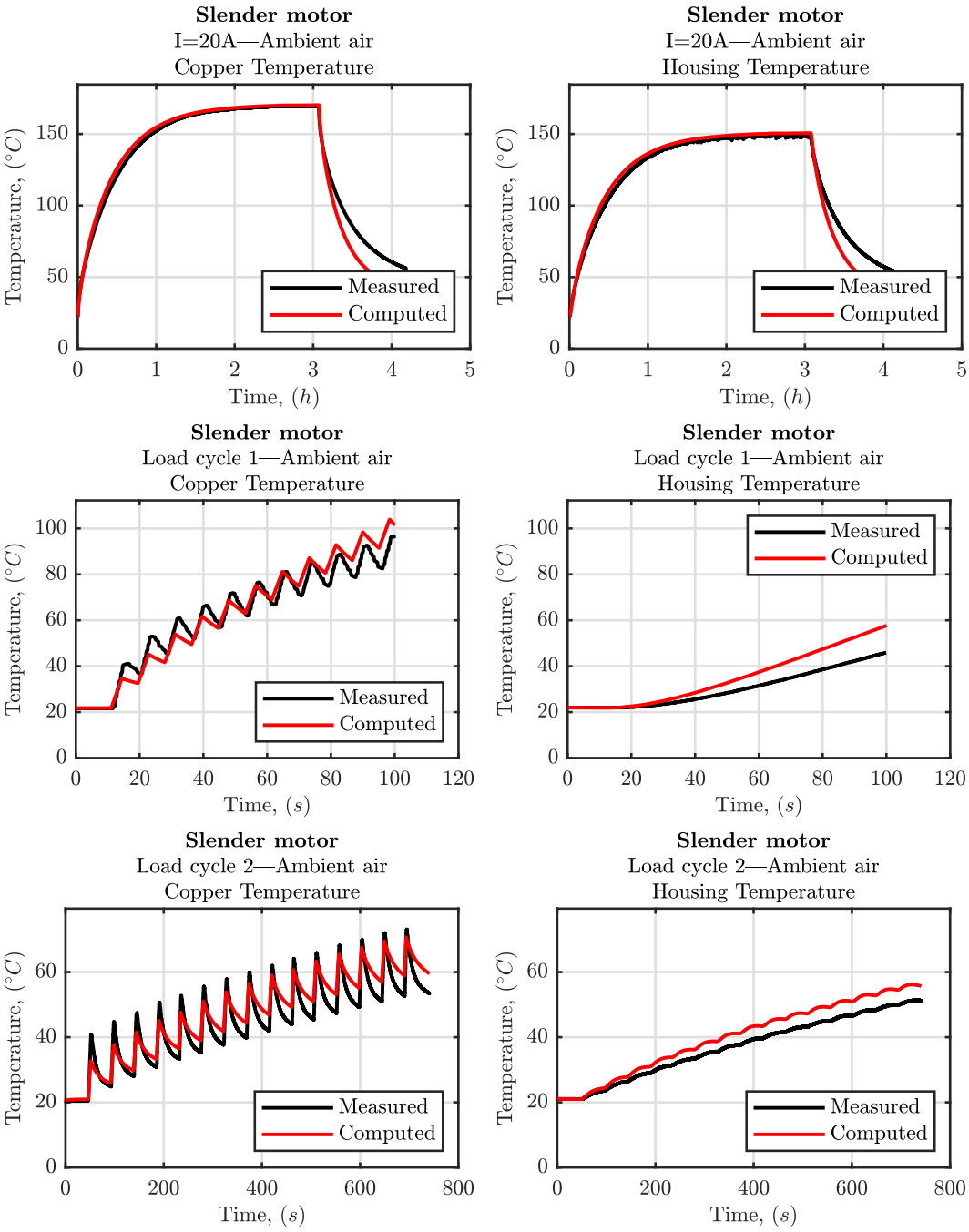

Fig. 6.6 Results for the slender motor in ambient air.

estimation during these first instants. As a consequence, an accurate prediction can be accomplished only by knowing the precise value of the housing mass. However, the proposed LPTN considers the housing as a hollow cylinder and does not take into account additional motor parts external to the housing, such as the end-plates

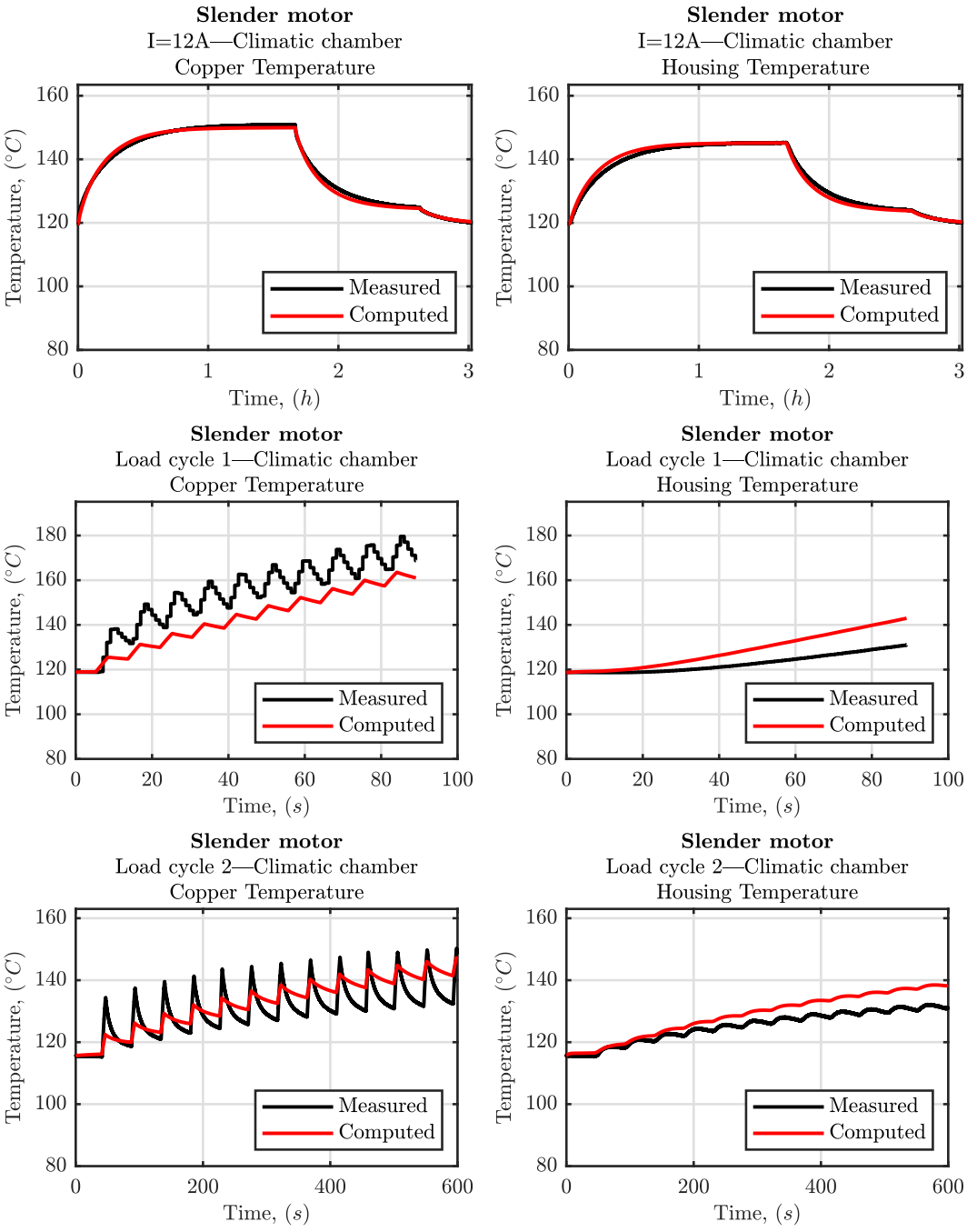

Fig. 6.7 Results for the slender motor in the climatic chamber.

and the mechanical fixture parts that are thermally conductive (see Fig.6.4), hence underestimating the total mass. As a consequence, the housing thermal capacitance is slightly underestimated as well, yielding the overestimation of the thermal dynamics, which in turn causes the housing temperature overestimation in the load cycle tests.

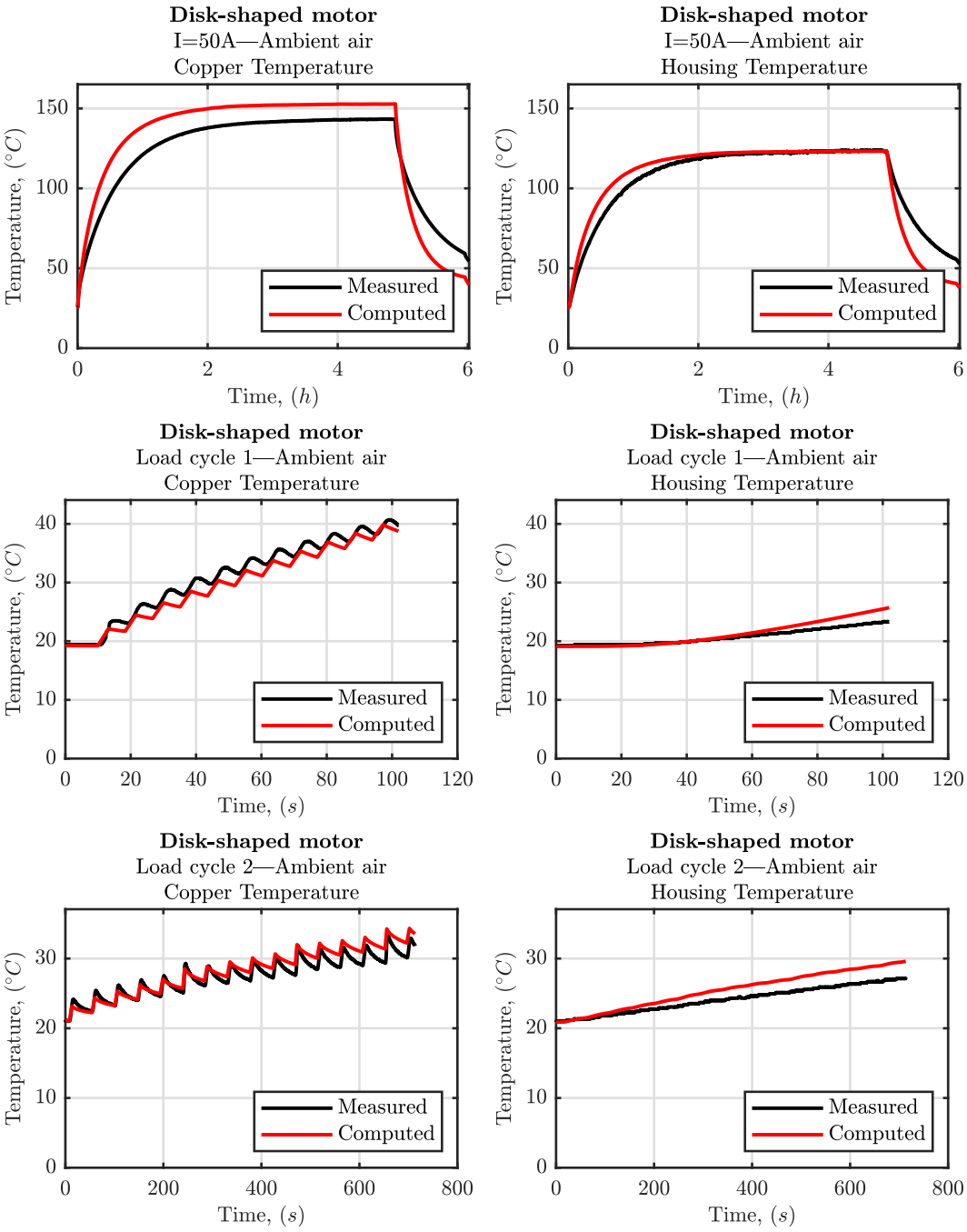

Fig. 6.8 Results for the disk-shaped motor in ambient air.

In conclusion, the proposed LPTN model represents a valid tool for assessing the motor temperatures in steady-state and not-too-harsh load cycles or ambient conditions. However, the specific BBW application of the baseline motors generally requires to operate by injecting *dc* currents in two of the three phases for short

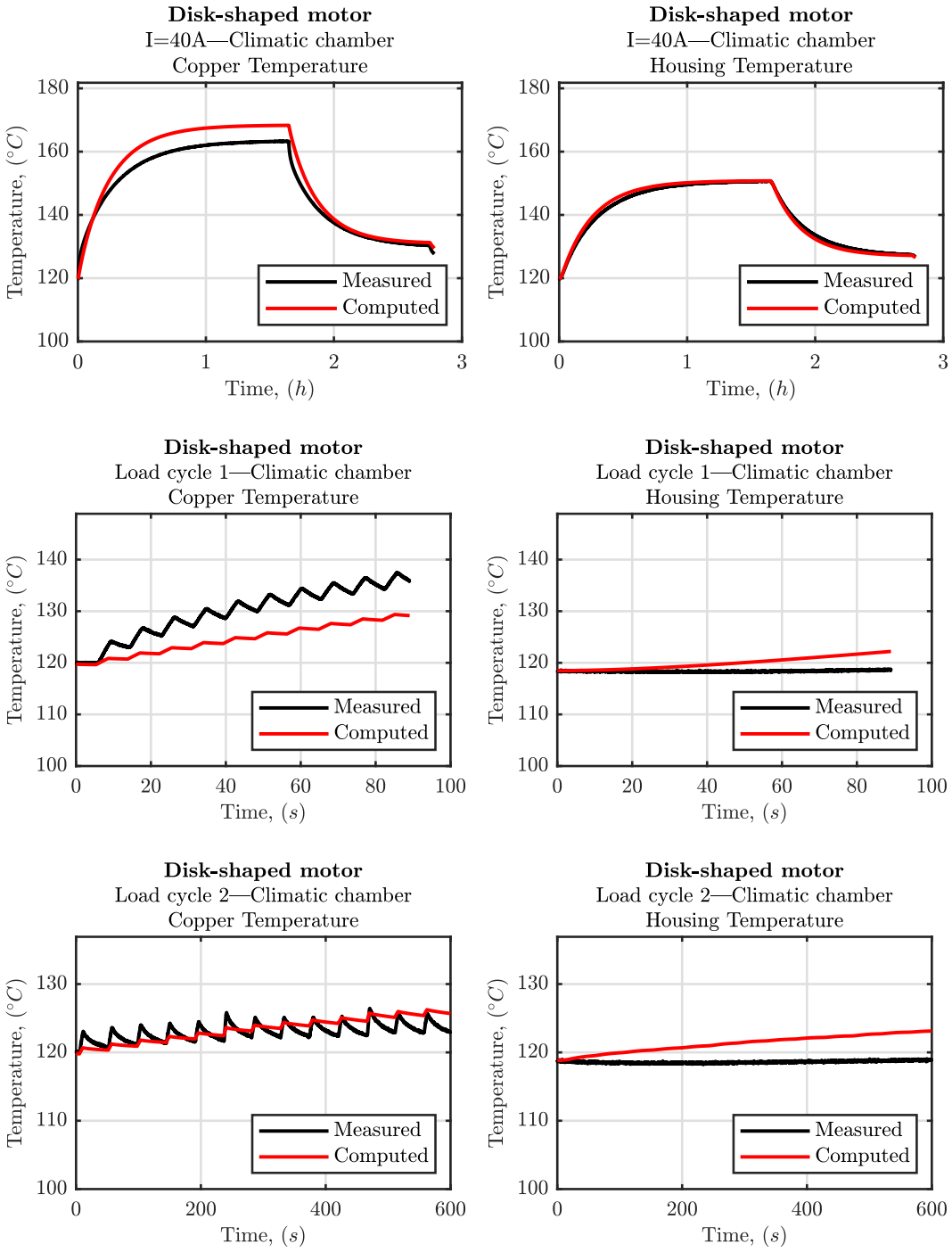

Fig. 6.9 Results for the disk-shaped motor in the climatic chamber.

time intervals, causing an uneven heat distribution in the machine, as anticipated in Section 6.1.2. The proposed model cannot predict uneven heat distributions on the basis of the assumed hypotheses.

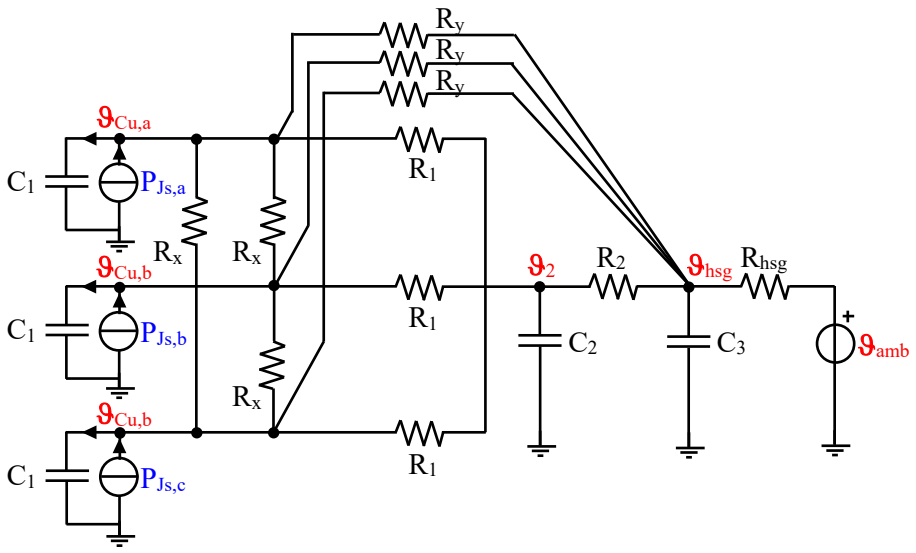

Fig. 6.10 Complete phase-split LPTN

6.2 The phase-split LPTN

A lumped parameters thermal network where the three phases are split is proposed to consider the non-homogeneous heating of the machine. The new model is presented in Fig.6.10. In this version, the winding equivalent thermal resistance (previously referred to as $R_{Cu,s}$) has been split into three different branches of thermal resistance, R_1. Furthermore, a heat exchange among the three phases is considered by adding the three thermal resistances, R_x. Finally, the three parameters R_y introduce an additional heat path representing the heat exchange between the end winding and the housing. The new structure of the network allowed the three phases to be supplied independently.

In the '*phase-split*' network, the definition of practical analytical formulations for the computation of the thermal parameters is highly complex due to unconventional supply conditions. The motor dimensions and the thermal characteristics of the used materials cannot be used to compute the parameters since the hypothesis of motor symmetry is not valid anymore. Therefore, these values are estimated by optimization.

6.2.1 The optimization algorithm for the parameter identification

The thermal parameters of the phase-split network are obtained by means of the particle swarm optimization technique, which is a swarm intelligence-based and stochastic algorithm to solve optimization problems [175, 176]. The procedure is performed in the Matlab environment using the built-in function of the PSO technique. The objective function used in the algorithm is the sum of the quadratic error between the measured and computed temperatures in different conditions, as expressed in (6.24). In the function j is the index that indicates the j-th thermal test (steady-state, pulse-current, load cycle), i is the index that indicates the temperatures of the considered machine parts ($n_\vartheta \leq 4$ is the number of monitored machine parts), and item z is the index that indicates the considered temperature samples (Z is the number of considered samples of the considered thermal test).

$$\varepsilon = \sum_{j=1}^{n_{test}} \sum_{i=1}^{n_\vartheta} \sum_{z=1}^{Z} \left(\vartheta_{measured_{i,z}^{j}} - \vartheta_{computed_{i,z}^{j}} \right)^2 \tag{6.24}$$

Several optimizations with PSO were performed on both motors, varying n_{test} and n_ϑ, always leading to similar parameters. Based on the obtained values, the following considerations can be drawn. A low value of the thermal resistance R_y is found compared to all the other thermal resistances. The values of R_1 and R_2 are practically infinite. This means that most heat flux does not encounter the thermal resistances R_1 and R_2 and does not reach the node ϑ_2, see Fig.6.10. Consequently, the value of the thermal capacitance C_2 does not affect the heat repartition in the thermal network. The heat flux mainly reaches the housing frame through the thermal resistance R_y. These considerations suggest the reduction of the '*complete*' thermal network of 6.10 to the '*simplified*' LPTN shown in Fig.6.11, where the node ϑ_2 is bypassed. The two thermal networks obtain comparable values of thermal capacitances C_1, C_3 and the thermal resistance R_y.

The simplification of the thermal network leads to a sharp reduction of the computational time, as fewer parameters need to be optimized. For example, when one steady-state and seven pulse-current temperature tests are used to determine the model parameters for the slender motor, the computational time reduces from one hour and a half for the complete LTPN to five minutes for the simplified one.

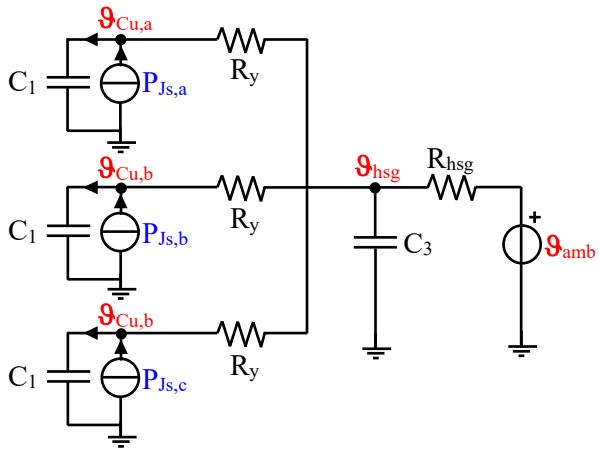

Fig. 6.11 Simplified phase-split LPTN

Table 6.3 Thermal parameters of the phase-split LPTN for the baseline motors - capacitances in $J/°C$ and resistances in $°C/W$.

Parameter	Slender motor		Disk-shaped motor	
	Ambient air	Climatic chamber	Ambient air	Climatic chamber
C_1	22	22	60	50
C_3	245	309	567	641
R_y	1.19	0.80	0.80	0.84
R_{hsg}	3.97	2.20	2.50	1.15

6.2.2 The simplified phase-split LPTN

In Fig.6.11, the optimized thermal network is shown, where the four nodes allow for the computation of the four considered temperatures. Different combinations of thermal tests have been used in the optimization procedure. In particular, for each ambient condition and each baseline motor, the steady-state test and all the performed pulse-current tests have been used for the calibration of the thermal network. The obtained parameters lead to consistent predictions of the monitored temperatures, reported in [170]. However, a further investigation has been carried out to minimize the number of experimental tests that need to be performed to calibrate the simplified phase-split LPTN correctly. The outcome is that only one pulse-current test and the steady-state test are sufficient to find similar thermal parameters. However, the recommendation is to select a pulse-current test that reaches the maximum admissible temperatures in a short time, as this operating condition is more comparable with

the load cycles. The thermal parameters obtained through the PSO with one pulse-current and one steady-state test for the baseline motors in ambient air and climatic chamber conditions are recollected in Table 6.3. The obtained values of the housing thermal resistance (R_{hsg}) are practically the same values used in the conventional high-order network of Fig.6.2.

The temperatures predicted by the simplified phase-split thermal network of Fig.6.11 with the thermal parameters of Table 6.3 are shown hereafter together with the measured temperatures. Specifically, the temperatures for the two thermal tests used for the optimization are presented, followed by the results for the load-cycle tests. Moreover, for space reasons, the temperatures of one of the two '*hot*' phases and the '*cold*' one are shown for the pulse-current test, while the other '*hot*' phase and the housing are selected for the steady-state test. In particular, Fig.6.12-6.14 show the results for the slender motor in ambient air for the optimization tests and the two load cycles, while the results in the climatic chamber are displayed in Fig.6.15-6.17. Regarding the disk-shaped motor, the results in both ambient conditions can be found in Appendix C.

As can be seen, good results are obtained for the three phases and the housing temperatures in all the conditions and for both motors. The difference between the hot phases and the cold one is predicted by the models thanks to the split of the winding branch into three different branches. The maximum percentage error exhibited by the proposed network is approximately 12%, reached by the slender motor in ambient air for the first load cycle, in which, however, the absolute deviation is less than 5°C. Note also that the differences in the electrical resistances of the three phases cause different heating of the two hot phases, while in the proposed model, the three phases are assumed to be perfectly equal in terms of thermal parameters.

In conclusion, the conventional high-order LPTN of Section 6.1 has proven to be essentially appropriate for the temperature estimations of the motors under analysis, but it cannot provide the evolution of the temperatures of the three phases separately, as requested by the specific application. However, the model provided an acceptable estimate of the housing temperatures and the hot phases. The proposed phase-split LPTN, if opportunely optimized as discussed, allows more accurate results for all the monitored parts of the machine. The obtained model was simple and fast in computing. However, an additional thermal test requires to be performed at higher current levels; thus, adequate lab equipment must be available.

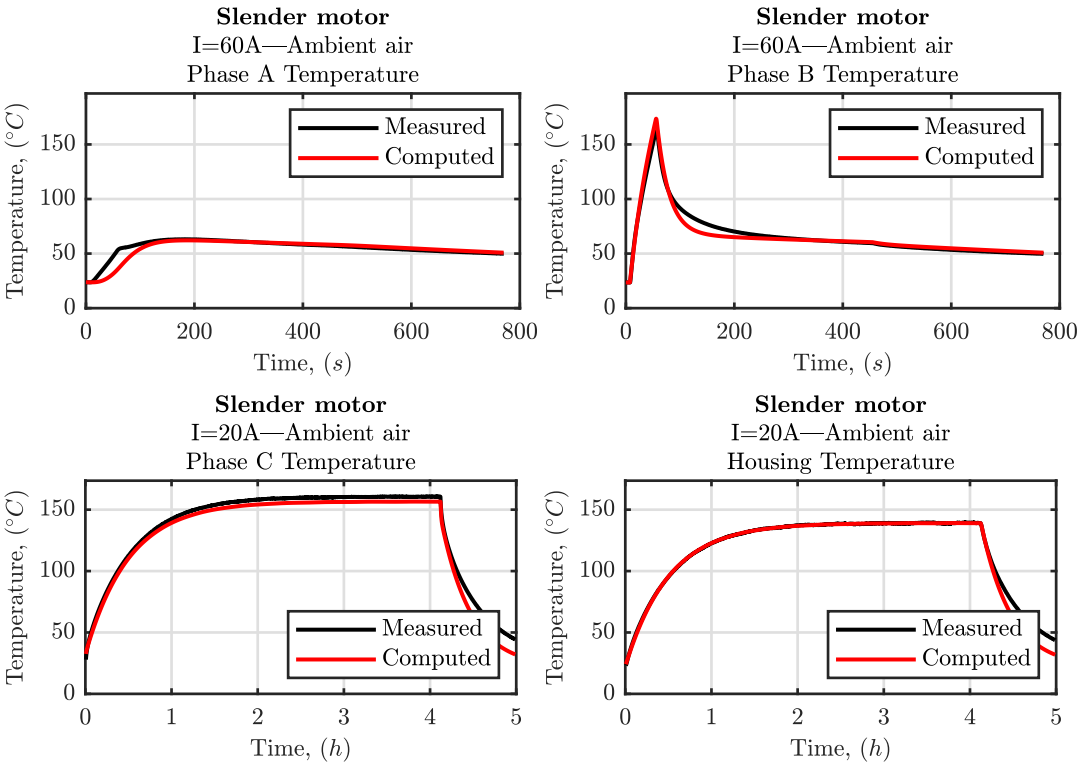

Fig. 6.12 Simplified phase-split LPTN results for the slender motor in ambient air for the tests used in the optimization.

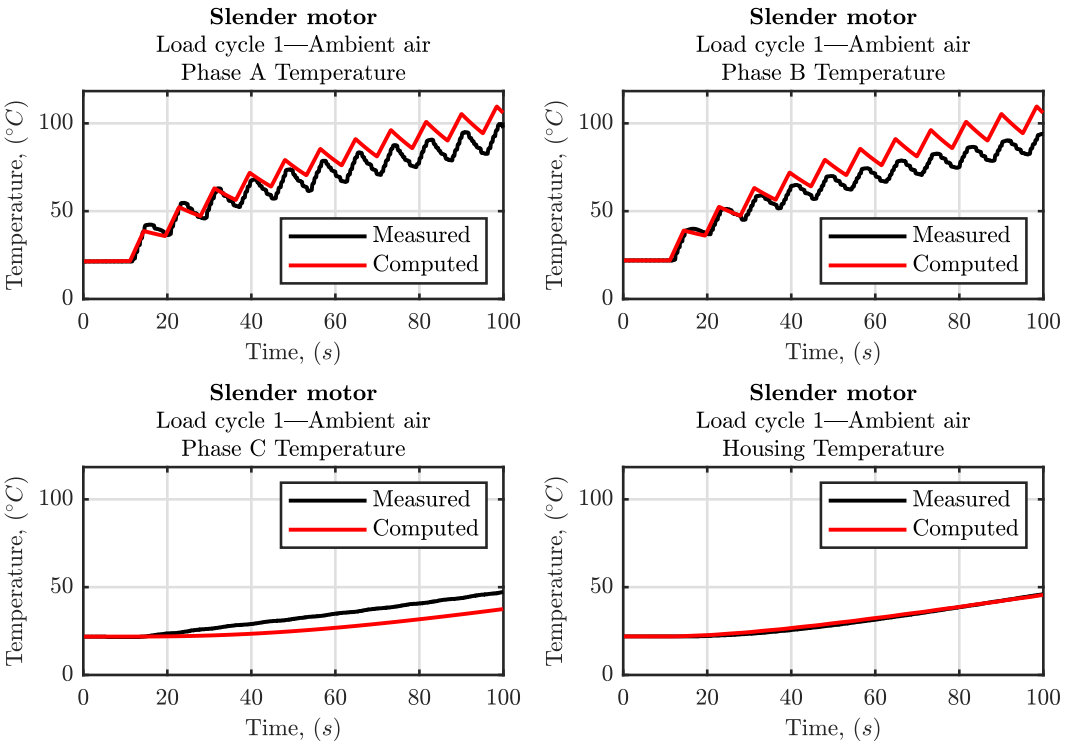

Fig. 6.13 Simplified phase-split LPTN results for the slender motor in ambient air for the load cycle 1.

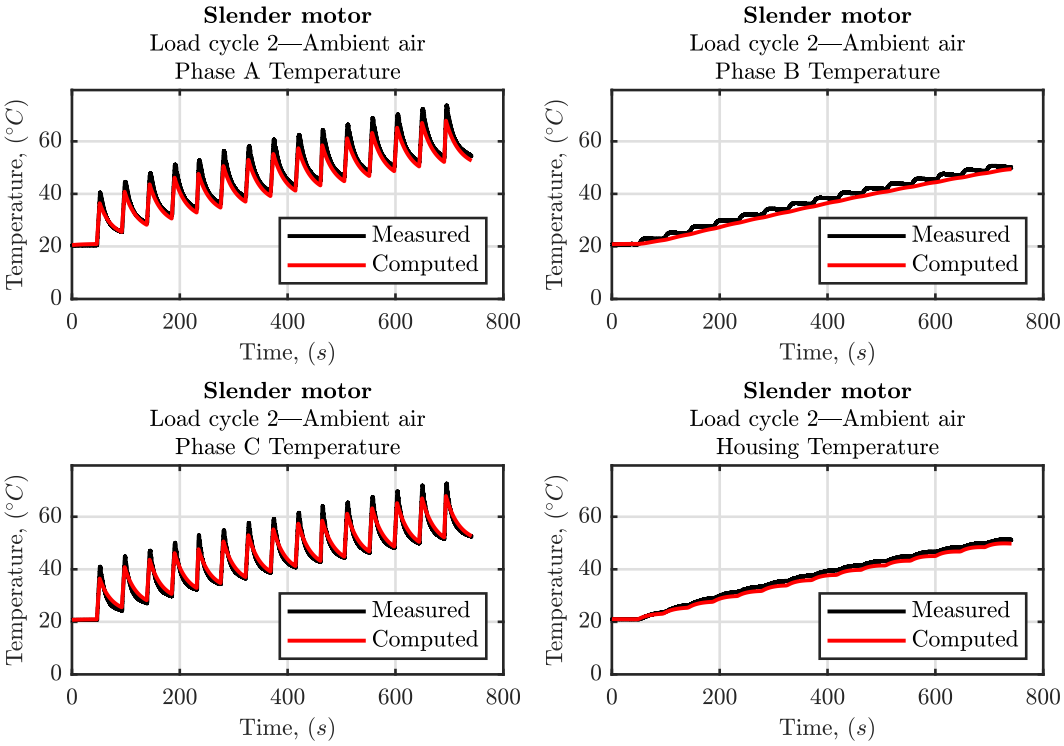

Fig. 6.14 Simplified phase-split LPTN results for the slender motor in ambient air for the load cycle 2.

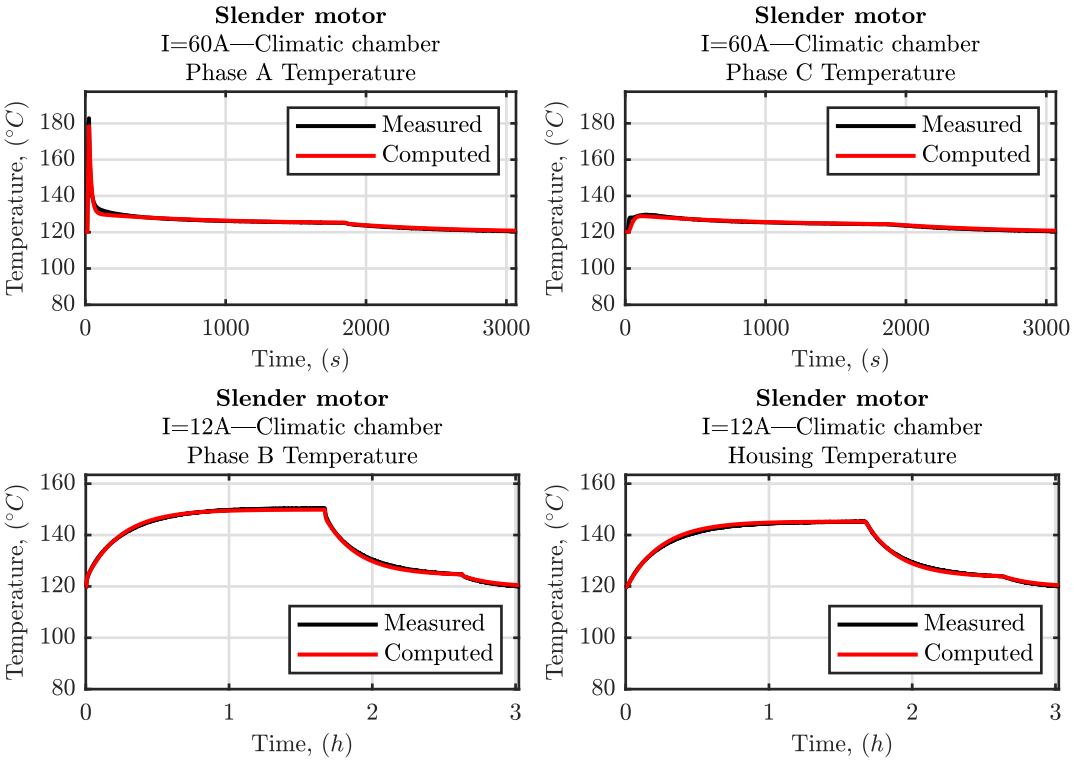

Fig. 6.15 Simplified phase-split LPTN results for the slender motor in the climatic chamber for the tests used in the optimization.

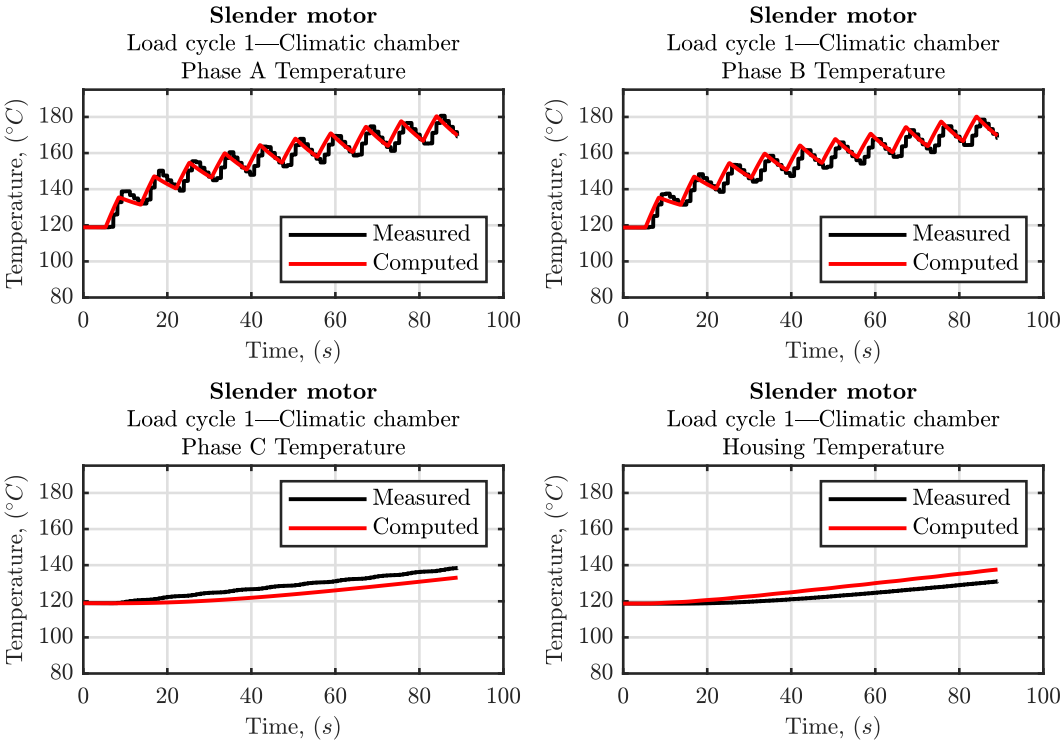

Fig. 6.16 Simplified phase-split LPTN results for the slender motor in the climatic chamber for the load cycle 1.

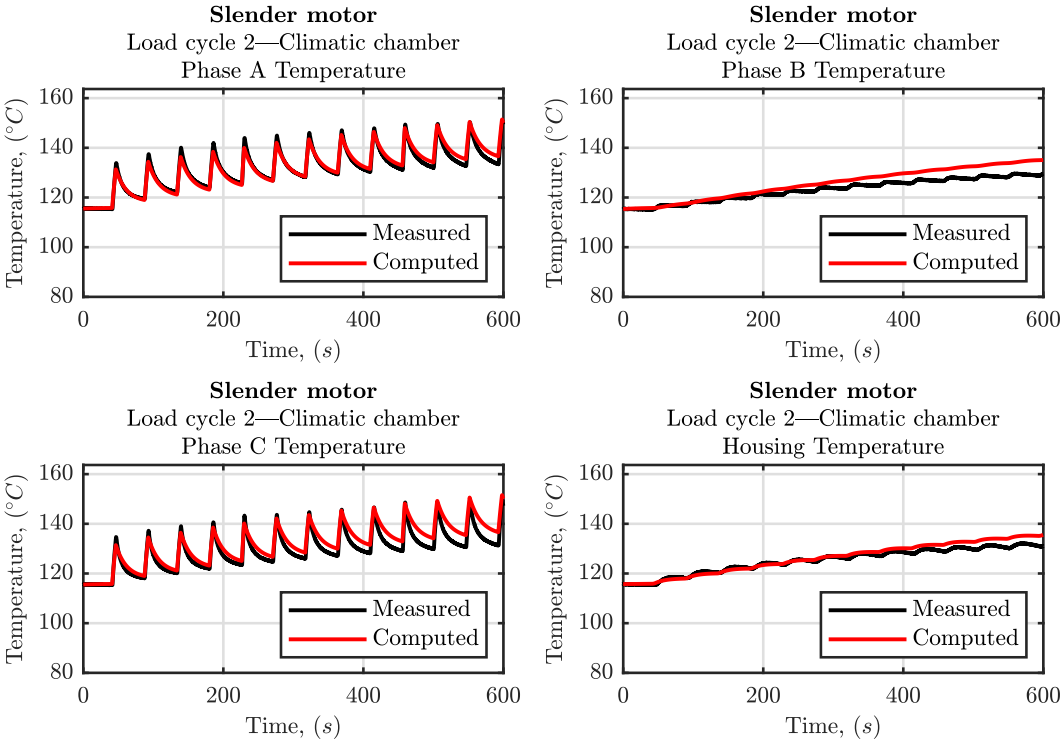

Fig. 6.17 Simplified phase-split LPTN results for the slender motor in the climatic chamber for the load cycle 2.

6.3 Analytical computation of the housing thermal resistance

The thermal resistance R_{hsg} represents the thermal resistance between the housing and the external ambient. The heat flow through this specific path is generated by the parallel contribution of natural convection, forced convection and radiation phenomena. In the proposed LPTNs the parameter R_{hsg} has been either computed through the steady-state *dc*-test or by the PSO technique. In any case, different values have been obtained for each motor, depending on the external ambient (climatic chamber or ambient air), as the parameter is temperature-dependent. In this section, an alternative approach, based on an analytical estimation, is used to determine the value of the parameter R_{hsg} for different ambient temperatures and injected powers. The procedure is validated by a test campaign of *dc* steady-state thermal tests conducted on the disk-shaped motor. The parameter determination is based on the assumption of the absence of forced convection.

Following the work proposed in [177], originally based on [178], the thermal resistance housing-ambient is obtained by computing the thermal convection and radiation coefficients. The following ambient air's thermal properties are obtained through linear interpolation of the data reported in [177], at the film temperature $\vartheta_f = (\vartheta_{hsg} + \vartheta_{hsg})/2$.

Convection from the front surface

Approximating the convection phenomenon in the front and rear cross-sectional area as that of two square plates with height H_{eq}, the Rayleigh number can be computed as in (6.25), where g_a is the gravitational acceleration, β is the air expansion coefficient, nu_k is the air kinematic viscosity, and α_{th} is the air thermal diffusivity.

$$Ra_f = \frac{g_a \beta (\vartheta_{hsg} - \vartheta_{amb}) H_{eq}^3}{\nu_k \alpha_{th}} \tag{6.25}$$

The value of H_{eq} can be obtained by imposing the same surface for the front/rear surface and the square plate.

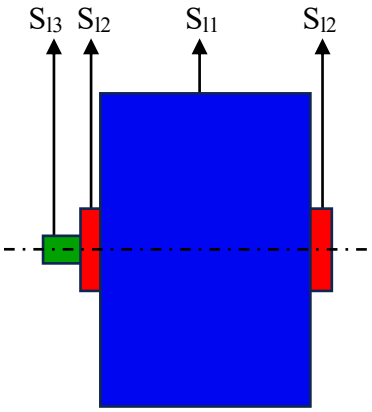

Fig. 6.18 Sketch of the motor housing.

$$\frac{D_e^2\pi}{4} = H_{eq}^2 \qquad \rightarrow \qquad H_{eq} = \frac{\sqrt{\pi}}{2} D_e \tag{6.26}$$

Therefore, the Nusselt number can be computed as in 6.27, where h_f is the convection coefficient of the front/rear area.

$$Nu_f = \frac{h_f \cdot H_{eq}}{k_{air}} = \left(0.825 + \frac{0.387 Ra_f^{1/6}}{(1 + (0.492/Pr)^{9/16})^{8/27}} \right)^2 \tag{6.27}$$

Convection from the lateral surface

In order to compute the lateral surface convection coefficient h_l, it must be considered that the total lateral surface is composed of three different cylinders, as depicted in Fig.6.18.

For the biggest lateral surface S_{l1}, the Rayleigh number can be computed considering the convection over a long horizontal cylinder.

$$Ra_{l1} = \frac{g_a \beta (\vartheta_{hsg} - \vartheta_{amb}) D_e^3}{\nu_k \alpha_{th}} \tag{6.28}$$

Considering:

$$D_e = D_{so} + h_{ig} + h_{hsg} \tag{6.29}$$

The Nusselt number is given by 6.30, where h_{l1} is the convection coefficient for the lateral surface S_{l1}

$$Nu_{l1} = \frac{h_{l1} \cdot D_e}{k_{air}} = \left(0.60 + \frac{0.387 Ra_{l1}^{1/6}}{(1 + (0.559/Pr)^{9/16})^{8/27}} \right)^2 \tag{6.30}$$

Repeating the procedure for the other surfaces, the equivalent convection coefficient from the lateral surface can be computed, considering $S_l = S_{l1} + S_{l2} + S_{l3}$.

$$h_l \cdot S_l = h_{l1} \cdot S_{l1} + h_{l2} \cdot S_{l2} + h_{l3} \cdot S_{l3} \tag{6.31}$$

Convection thermal coefficient

Therefore, the equivalent convection thermal coefficient given by the lateral, front and rear surfaces can be obtained as in (6.32), where $S = S_l + 2S_f$.

$$h_c = \frac{h_l S_l + 2 h_f S_f}{S} \tag{6.32}$$

Radiation from the motor surface

The surface heat density dissipated by radiation can be computed as in (6.33), where ε_r is the emissivity coefficient (assumed to be 0.97) and σ_c is the Stefan-Boltzmann constant ($5.67x10^{-8} W/m^2/K^4$), while h_r is the unknown radiation coefficient.

$$q_r = \varepsilon_r \sigma_c \left(\vartheta_{hsg}^4 - \vartheta_{amb}^4 \right) = h_r \left(\vartheta_{hsg} - \vartheta_{amb} \right) \tag{6.33}$$

Thus, the value of the radiation coefficient is:

$$h_r = \varepsilon_r \sigma_c \left(\vartheta_{hsg} + \vartheta_{amb} \right) \left(\vartheta_{hsg}^2 + \vartheta_{amb}^2 \right) \tag{6.34}$$

The housing-ambient thermal resistance

Finally, the equivalent value of the coefficient h_t, which includes both the natural convection and the radiation, can be obtained by summing two convection and

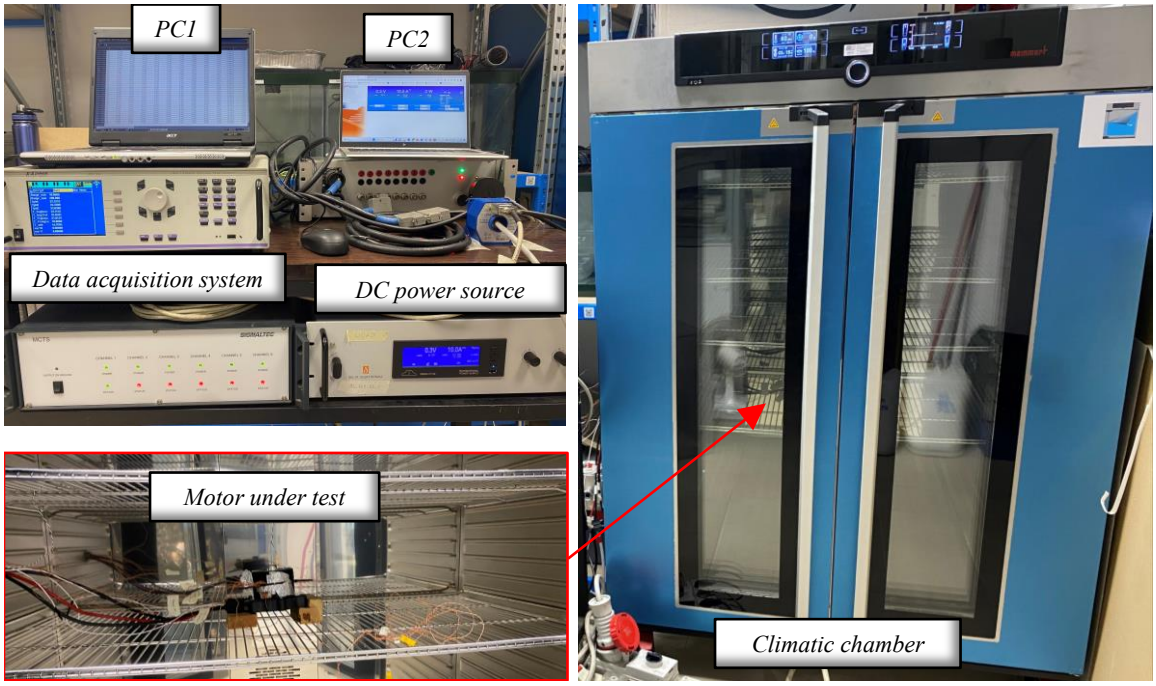

Fig. 6.19 Measurements setup for the housing-ambient thermal resistance

radiation coefficients.

$$h_t = h_c + h_r \tag{6.35}$$

Therefore, the value of the parameter R_{hsg} is:

$$R_{hsg} = \frac{1}{h_t \cdot S} \tag{6.36}$$

6.3.1 The validation procedure

In order to validate the analytical computation of the parameter R_{hsg}y, nineteen steady-state tests have been performed on the disk-shaped motor. As evident from equations (6.30), (6.27) and (6.34), the thermal coefficients h_c and h_r depend on both the ambient and housing temperatures. Therefore, the performed tests have been conducted for different ambient temperatures, controlled through a climatic chamber, and for different housing temperatures by varying the injected power in the motor. Figure 6.19 shows the used measurements setup, which consists of a *dc* power source used to supply two of the three phases of the disk-shaped motor under test, a data acquisition system and the climatic chamber. The latter is specifically used as a static

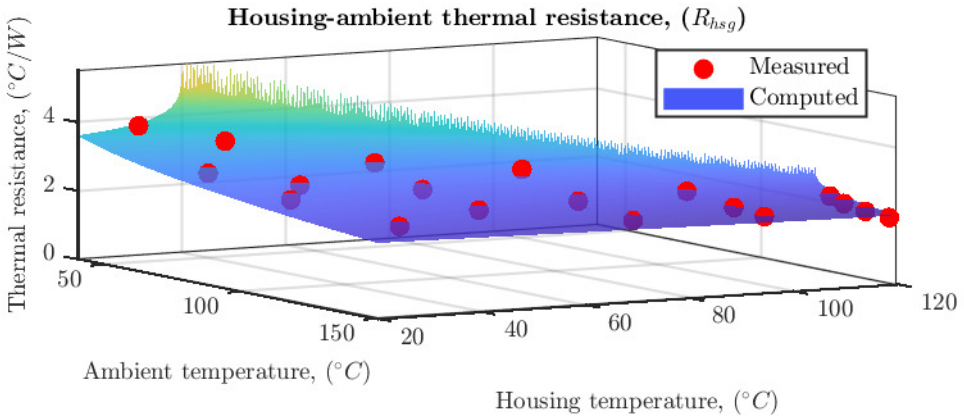

Fig. 6.20 Measured and computed housing-ambient thermal resistance.

Table 6.4 Results of the parameter R_{hsg} : part I

$\vartheta_{amb}, (°C)$	27.23	29.65	31.75	35.19	38.35	39.33	56.49
$\vartheta_{hsg}, (°C)$	48.67	69.5	95.72	129	86.55	57.27	117.5
Computed $R_{hsg}, (°C/W)$	3.45	3.03	2.67	2.34	2.78	3.34	2.41
Measured $R_{hsg}, (°C/W)$	3.96	2.87	2.5	2.21	2.71	3.52	2.29
Error (%)	-12.9	5.3	7.1	6.0	2.9	-5.3	5.5

Table 6.5 Results of the parameter R_{hsg} : part II

$\vartheta_{amb}, (°C)$	57.63	58.37	77.15	77.34	77.86	97.81
$\vartheta_{hsg}, (°C)$	94.73	75.81	134.7	93.62	113.3	115
Computed $R_{hsg}, (°C/W)$	2.68	3.03	2.22	2.75	2.44	2.44
Measured $R_{hsg}, (°C/W)$	2.52	2.99	2.05	2.90	2.27	2.38
Error (%)	6.3	1.1	8.2	-5.0	7.4	2.4

Table 6.6 Results of the parameter R_{hsg} : part III

$\vartheta_{amb}, (°C)$	98.00	98.30	118.5	118.7	118.7	118.8
$\vartheta_{hsg}, (°C)$	131.8	142.5	133.1	149.3	140.6	127.5
Computed $R_{hsg}, (°C/W)$	2.22	2.11	2.21	2.02	2.11	2.31
Measured $R_{hsg}, (°C/W)$	2.18	2.08	2.11	1.95	1.99	2.23
Error (%)	1.8	1.7	5.0	3.5	6.0	3.5

oven, thus disabling the fan's functioning. This procedure is necessary to ensure the absence of forced convection phenomena.

Figure 6.20 shows the map of the measured and computed housing-ambient thermal resistance as a function of the ambient and housing temperatures. The shape of the computed map is justified by the fact that, as ϑ_{hsg} and ϑ_{amb} become similar, their difference tends to zero, and, thus, the parameter R_{hsg} tends to infinite. The results show that the computed map and the measured points overlap in most cases. In general, the absolute value of the minimum obtained percentage error is 1.08%, while for the maximum error is 12.9%. The average value of the absolute percentage error is 5.1%. However all the obtained computed and measured housing-ambient thermal resistances are listed in Table 6.4 - 6.6, together with their percentage errors.

In conclusion, the presented method can analytically define the housing-ambient thermal resistance for different housing and ambient temperatures in the absence of forced ventilation. The obtained parameter can be used in the proposed LPTNs, therefore replacing the calibration or optimization procedure, although higher percentage errors must be acceptable for the specific application.

Chapter 7

Conclusions and Future Works

In the context of transport decarbonization, and specifically regarding the production of electric motors free from critical materials, the work presented in this dissertation deals with the modelling and the sizing of wound-field synchronous machines. The general purpose is to provide motor designers and engineers with reliable and efficient tools for the modeling and design of wound-field synchronous motors for traction applications.

Different models of wound-field synchronous machines are developed and presented in this dissertation. Specifically, an analytical model, a magnetic equivalent circuit and a parametric finite element model are proposed. The analytical model consists of a straightforward computation of the no-load characteristic, considering the iron saturation, the distortion of the air gap flux density and the magnetic shunt of the stator slots on the basis of the machine geometry and material properties. The analytical model obtains accurate results in a negligible computation time. However, the procedure is unsuitable for evaluations in load conditions, as the magnetic flux is assumed to be placed in the d-axis. The magnetic equivalent circuit and the finite element model are proposed to assess the machine performances at load. The magnetic equivalent circuit includes non-linear reluctances, thus being suitable in saturation conditions, and it incorporates rotor rotation. The required computational time for a single rotational step is greater than the analytical model, as a system of non-linear equations is solved through the Newton-Raphson method. However, the computational burden is still significantly reduced with respect to the finite element analysis. The main drawback is the difficulty in reaching the convergence for high saturation

conditions. The finite element model is created using the FEMM software, and a Matlab code is built to automate the project creation process. The model exploits the machine periodicity, and the solving process is achieved through parallelization over multiple cores. The comparison of the three models has led to the conclusion that a combination of the analytical and finite element models represents the most appropriate choice to be used in the sizing process of wound-field motors.

In the frame of wound-field motor design, this research activity provides a fast and reliable tool for the preliminary electromagnetic sizing of the machine, starting from a limited number of specifications, such as targets and constraints. The proposed methodology consists of an analytical-numerical approach in which analytical equations establish a preliminary geometry, and subsequently, refinements are achieved through finite element simulations. The developed approach combines the reduced computational time of analytical models with the accuracy of finite element methods. The procedure is validated by means of the wound-field motor equipping the Renault ZOE. On the basis of the retrieved electromagnetic and geometrical information on the tested motor sample, the inputs of the sizing algorithm are defined. The procedure obtains a final geometry comparable to the actual ZOE motor, with an accuracy on the main dimensions, i.e. the axial length, the stator outer diameter and the air gap diameter, characterized by a few per cent errors.

Finally, methodologies for developing lumped parameter thermal networks for synchronous machines are presented, focusing on identifying the parameters through experimental and optimization approaches. In the absence of a wound-field sample equipped with thermocouples, the study is conducted on two small synchronous SPM machines used in automotive actuators, characterized by two different aspect ratios. Different thermal networks are developed and validated through thermal tests conducted on the prototypes. Specifically, a high-order thermal network operating under conventional assumptions is presented, whose parameters are obtained by the motor dimensions and the material characteristics. Moreover, a dedicated '*phase-split*' thermal network, able to predict non-uniform thermal operative conditions, is developed for the specific application requirements. Finally, considerations on the heat exchange with the ambient in the absence of force convection are drawn for the motor with the lowest aspect ratio, focusing on the corresponding network parameter computation.

Future Works

Among the potential future works, in the context of the proposed magnetic equivalent circuit of wound-field motors, there is room for improvements regarding the convergence procedure. One possibility is to introduce a relaxation factor to enforce global convergence. In this process, selecting the proper relaxation factor is a crucial step, which is currently under investigation. The relaxation factor must be small enough to ensure stability without strongly affecting the convergence speed. Moreover, the success of the convergence procedure is affected by the selected initial conditions. In the proposed model, all the reluctances are assumed to be unsaturated, which generally represents a condition far from reality. If the model is used to simulate the rotor rotation, the convergence process is aided by assuming as initial conditions of the current rotor step, the magnetic permeabilities of the reluctances computed in the previous step. However, this is valid only from the second simulated rotor position. Based on these considerations, an idea could be to use finite element simulations to find the initial magnetic permeabilities only for the first rotor step. Thus, apart from the time required for a single finite element simulation, the complete rotation is performed through the magnetic equivalent circuit.

In the case of reaching better convergence properties with the adoption of the proposed improvements, the magnetic equivalent circuit could replace the finite element model in the sizing algorithm, reducing the required computational time. Additionally, regarding the developed sizing procedure, efforts are being made to develop a user-friendly graphical interface in Matlab. This interface would make it easier for potential users to employ the sizing tool.

In the validation procedure of the sizing algorithm, the current-to-flux linkage model of the ZOE motor is obtained through FE simulations, whose model is validated by means of the performed no-load test on the motor sample. The future plans include obtaining the current-to-flux linkage model directly by measurements on the motor and comparing the results to the simulated maps.

In the frame of the thermal aspects, the considerations on the heat exchange with the ambient drawn for the motor with the lowest aspect ratio are intended to be extended to the other synchronous motor. The thermal test campaign of *dc* steady-state tests needs to be performed on the motor with the highest aspect ratio.

Because of its slender shape, more accurate results are expected as the analytical computation assumed the motor to be approximated as a long cylinder.

Furthermore, the lumped parameter thermal networks can be extended to wound-field synchronous machines in the availability of a motor sample equipped with thermocouples. The network adjustment must consider the specific pole shape to compute the rotor parameters. Moreover, on a higher level of detail, non-uniform thermal conditions must be considered for the rotor pole. Indeed, depending on the rotation direction, one side of the rotor pole receives more airflow, enhancing the heat transfer.

References

[1] *The challenge of decarbonizing heavy transport*. Brookings, 2020.

[2] *CO2 Emissions in 2022*. International Energy Agency, 2022.

[3] *How to decarbonise European transport by 2050*. Transport & Environment, 2018.

[4] *Share of transport greenhouse gas emissions*. European Environment Agency, 2019.

[5] *Electric Vehicle Life Cycle Analysis and Raw Material Availability*. Transport & Environment, 2017.

[6] *Ready or Not. Who are the frontrunners in the global race to clean up trucks and gain technology leadership?* Transport & Environment, 2023.

[7] *Analysis: Aviation could consume a quarter of 1.5C carbon budget by 2050*. https://www.carbonbrief.org/aviation-consume-quarter-carbon-budget. Accessed: 23-Aug-23.

[8] B. A. Adu-Gyamfi and C. Good. "Electric aviation: A review of concepts and enabling technologies". In: *Transportation Engineering* (2022). DOI: https://doi.org/10.1016/j.treng.2022.100134.

[9] G. Bailey, N. Mancheri, and K. Van Acker. "Sustainability of Permanent Rare Earth Magnet Motors in (H)EV Industry". In: *Journal of Sustainable Metallurgy* 3.3 (2017), pp. 611–626. DOI: 10.1007/s40831-017-0118-4.

[10] S. Zheng, X. Zhu, Z. Xiang, L. Xu, L. Zhang, and C. H. Lee. "Technology trends, challenges, and opportunities of reduced-rare-earth PM motor for modern electric vehicles". In: *Green Energy and Intelligent Transportation* 1.1 (2022), p. 100012. DOI: 10.1016/j.geits.2022.100012.

[11] *The Guardian view on rare earths: mining them can't cost the Earth*. https://www.theguardian.com/commentisfree/2022/aug/18/the-guardian-view-on-rare-earths-mining-them-cant-cost-the-earth. Accessed: 27-Aug-23.

[12] *Rare earth mining may be key to our renewable energy future. But at what cost?* https://www.sciencenews.org/article/rare-earth-mining-renewable-energy-future. Accessed: 27-Aug-23.

[13] *Not So "Green" Technology: The Complicated Legacy of Rare Earth Mining*. https://hir.harvard.edu/not-so-green-technology-the-complicated-legacy-of-rare-earth-mining. Accessed: 27-Aug-23.

[14] S. R. Golroudbary, I. Makarava, A. Kraslawski, and E. Repo. "Global environmental cost of using rare earth elements in green energy technologies". In: *Science of The Total Environment* 832 (2022), p. 155022. DOI: https://doi.org/10.1016/j.scitotenv.2022.155022.

[15] J. D. Widmer, R. Martin, and M. Kimiabeigi. "Electric vehicle traction motors without rare earth magnets". In: *Sustainable Materials and Technologies* (2015). DOI: 10.1016/j.susmat.2015.02.001.

[16] P. Zapp, A. Schreiber, J. Marx, and W. Kuckshinrichs. "Environmental impacts of rare earth production". In: *MRS Bulletin* (2022), pp. 267–275. DOI: 10.1557/s43577-022-00286-6.

[17] *REE - Rare Earth Elements and their Uses*. https://geology.com/articles/rare-earth-elements. Accessed: 27-Aug-23.

[18] V. Fernandez. "Rare-earth elements market: A historical and financial perspective". In: *Resources Policy* 53 (2017), pp. 26–45. DOI: 10.1016/j.resourpol.2017.05.010.

[19] European Commission. Directorate General for Internal Market, Industry, Entrepreneurship and SMEs., Deloitte Sustainability., British Geological Survey., Bureau de Recherches Géologiques et Minières, and Toegepast natuurwetenschappelijk onderzoek. *Study on the review of the list of critical raw materials: critical raw materials factsheets.* LU: Publications Office, 2017.

[20] D. G. Dorrell, A. M. Knight, M. Popescu, L. Evans, and D. A. Staton. "Comparison of different motor design drives for hybrid electric vehicles". In: *2010 IEEE Energy Conversion Congress and Exposition*. 2010, pp. 3352–3359. DOI: 10.1109/ECCE.2010.5618318.

[21] L. Mantione, L. Frosini, and M. Minervini. "Evaluation of Different Magnet Materials and Skewed Geometries for IPMSM at High Speed". In: *2022 International Conference on Electrical Machines (ICEM)*. 2022, pp. 2297–2303. DOI: 10.1109/ICEM51905.2022.9910949.

[22] T. Burress. *Electrical Performance, Reliability Analysis, and Characterization*. https://www.energy.gov/sites/prod/files/2017/06/f34/edt087_burress_2017_o.pdf. Accessed: 29-Aug-23.

[23] *Tesla Model 3 Powertrain Fun. From Carburetors To Carborundum. You've Come A Long Way, Baby!* https://cleantechnica.com/2018/05/28/more-tesla-model-3-powertrain-fun-from-carburetors-to-carborundum-youve-come-a-long-way-baby. Accessed: 29-Aug-23.

[24] T. Jahns. "Getting Rare-Earth Magnets Out of EV Traction Machines: A review of the many approaches being pursued to minimize or eliminate rare-earth magnets from future EV drivetrains". In: *IEEE Electrification Magazine* 5.1 (2017), pp. 6–18. DOI: 10.1109/MELE.2016.2644280.

[25] E. Agamloh, A. Von Jouanne, and A. Yokochi. "An Overview of Electric Machine Trends in Modern Electric Vehicles". en. In: *Machines* 8.2 (Apr. 2020). DOI: 10.3390/machines8020020.

[26] G. Petrelli, S. Nuzzo, T. Zou, D. Barater, G. Franceschini, and C. Gerada. "Review and Future Developments of Wound Field Synchronous Motors in Automotive". In: *2023 IEEE International Conference on Electrical Systems for Aircraft, Railway, Ship Propulsion and Road Vehicles & International Transportation Electrification Conference (ESARS-ITEC)*. 2023, pp. 1–6. DOI: 10.1109/ESARS-ITEC57127.2023.10114826.

[27] J. Jenkins. *A closer look at brushed AC motors in EVs*. https://chargedevs.com/features/a-closer-look-at-brushed-ac-motors-in-evs. Accessed: 01-Sept-23. 2022.

[28] F. Graffeo, O. Stiscia, S. Vaschetto, A. Cavagnino, and A. Tenconi. "Doubly Excitated Synchronous Machines for Traction Applications". In: *2021 IEEE 30th International Symposium on Industrial Electronics (ISIE)*. 2021, pp. 1–8. DOI: 10.1109/ISIE45552.2021.9576244.

[29] L. Cinti, D. Michieletto, N. Bianchi, and M. Bertoluzzo. "A Comparison between Hybrid Excitation and Interior Permanent Magnet Motors". In: *2021 IEEE Workshop on Electrical Machines Design, Control and Diagnosis (WEMDCD)*. 2021, pp. 10–15. DOI: 10.1109/WEMDCD51469.2021.9425634.

[30] J. Merwerth, J. Halbedel, and G. Schlangens. *Electrical drive motor for a vehicle*. U.S. Patent 8 575 807 B2, Nov. 2013.

[31] G. Du, G. Zhang, H. Li, and C. Hu. "Comprehensive Comparative Study on Permanent-Magnet-Assisted Synchronous Reluctance Motors and Other Types of Motor". en. In: *Applied Sciences* 13.14 (July 2023), p. 8557. DOI: 10.3390/app13148557.

[32] C. Rossi, D. Casadei, A. Pilati, and M. Marano. "Wound Rotor Salient Pole Synchronous Machine Drive for Electric Traction". In: *Conference Record of the 2006 IEEE Industry Applications Conference Forty-First IAS Annual Meeting*. Vol. 3. 2006, pp. 1235–1241. DOI: 10.1109/IAS.2006.256689.

[33] G. Friedrich. "Comparative study of three control strategies for the synchronous salient poles and wound rotor machine in automotive applications with on board energy". en. In: *Proceedings of 5th International Conference on Power Electronics and Variable-Speed Drives*. Vol. 1994. London, UK: IEE, 1994, pp. 706–709. DOI: 10.1049/cp:19941051.

[34] J. de Santiago, H. Bernhoff, B. Ekergård, S. Eriksson, S. Ferhatovic, R. Waters, and M. Leijon. "Electrical Motor Drivelines in Commercial All-Electric Vehicles: A Review". In: *IEEE Transactions on Vehicular Technology* 61.2 (2012), pp. 475–484. DOI: 10.1109/TVT.2011.2177873.

[35] A. M. EL-Refaie. "Electrical Machines for Traction and Propulsion Applications". In: *Transportation Electrification: Breakthroughs in Electrified Vehicles, Aircraft, Rolling Stock, and Watercraft*. Wiley-IEEE Press, 2023, pp. 1–26. DOI: 10.1002/9781119812357.ch1.

[36] J. K. Nøland, S. Nuzzo, A. Tessarolo, and E. F. Alves. "Excitation System Technologies for Wound-Field Synchronous Machines: Survey of Solutions and Evolving Trends". In: *IEEE Access* 7 (2019), pp. 109699–109718. DOI: 10.1109/ACCESS.2019.2933493.

[37] D. Fallows, S. Nuzzo, and M. Galea. "Exciterless Wound-Field Medium-Power Synchronous Machines: Their History and Future". In: *IEEE Industrial Electronics Magazine* 16.4 (2022), pp. 44–51. DOI: 10.1109/MIE.2021.3093024.

[38] E. M. Illiano. "Design of a highly efficient brushless current excited synchronous motor for automotive purposes". PhD thesis. ETH, 2014.

[39] T. Raminosoa and R. Wiles. "Contactless Rotor Excitation for Traction Motors". In: *2018 IEEE Energy Conversion Congress and Exposition (ECCE)*. 2018, pp. 6448–6453. DOI: 10.1109/ECCE.2018.8557553.

[40] J. Legranger, G. Friedrich, S. Vivier, and J. C. Mipo. "Comparison of Two Optimal Rotary Transformer Designs for Highly Constrained Applications". In: *2007 IEEE International Electric Machines & Drives Conference*. Vol. 2. 2007, pp. 1546–1551. DOI: 10.1109/IEMDC.2007.383658.

[41] K. D. Papastergiou and D. E. Macpherson. "An Airborne Radar Power Supply With Contactless Transfer of Energy—Part II: Converter Design". In: *IEEE Transactions on Industrial Electronics* 54.5 (2007), pp. 2885–2893. DOI: 10.1109/TIE.2007.901370.

[42] K. D. Papastergiou and D. E. Macpherson. "An Airborne Radar Power Supply With Contactless Transfer of Energy—Part I: Rotating Transformer". In: *IEEE Transactions on Industrial Electronics* 54.5 (2007), pp. 2874–2884. DOI: 10.1109/TIE.2007.902044.

[43] D. C. Ludois, J. K. Reed, and K. Hanson. "Capacitive Power Transfer for Rotor Field Current in Synchronous Machines". In: *IEEE Transactions on Power Electronics* 27.11 (2012), pp. 4638–4645. DOI: 10.1109/TPEL.2012.2191160.

[44] A. Di Gioia, I. P. Brown, Y. Nie, R. Knippel, D. C. Ludois, J. Dai, S. Hagen, and C. Alteheld. "Design and Demonstration of a Wound Field Synchronous Machine for Electric Vehicle Traction With Brushless Capacitive Field Excitation". In: *IEEE Transactions on Industry Applications* 54.2 (2018), pp. 1390–1403. DOI: 10.1109/TIA.2017.2784799.

[45] J. Ritonja. *Robust and Adaptive Control for Synchronous Generator's Operation Improvement*. Section: 10. Rijeka: IntechOpen, 2020. DOI: 10.5772/intechopen.92558.

[46] C. Stancu, T. Ward, K. M. Rahman, R. Dawsey, and P. Savagian. "Separately Excited Synchronous Motor With Rotary Transformer for Hybrid Vehicle Application". In: *IEEE Transactions on Industry Applications* 54.1 (2018), pp. 223–232. DOI: 10.1109/TIA.2017.2757019.

[47] *ZF makes magnet-free electric motor uniquely compact and competitive*. https://press.zf.com/press/en/releases/release_60480.html. Accessed: 13-Sept-23.

[48] J. L. Kirtley, A. Banerjee, and S. Englebretson. "Motors for Ship Propulsion". In: *Proceedings of the IEEE* 103.12 (2015), pp. 2320–2332. DOI: 10.1109/JPROC.2015.2487044.

[49] K. H. Chu, J. Pou, S. Ramakrishna, and A. K. Gupta. "Salient pole wound field synchronous machine for marine propulsors with outboard drives: Analysis and design". en. In: *IECON 2017 - 43rd Annual Conference of the IEEE Industrial Electronics Society*. Beijing: IEEE, Oct. 2017, pp. 3754–3759. DOI: 10.1109/IECON.2017.8216639.

[50] Y. Terao, W. Kong, H. Ohsaki, H. Oyori, and N. Morioka. "Electromagnetic Design of Superconducting Synchronous Motors for Electric Aircraft Propulsion". In: *IEEE Transactions on Applied Superconductivity* 28.4 (2018), pp. 1–5. DOI: 10.1109/TASC.2018.2823503.

[51] *Renault Zoe's new electric motor to be built at Cléon*. https://paultan.org/2015/06/19/renault-zoe-new-electric-motor-cleon-plant/. Accessed: 13-Sept-23.

[52] *Unità e-drive BMW Gen5, Smontata: la fine di vari mondi motoristici ma si può ancora riparare*. https://www.automoto.it/elettrico/unita-e-drive-bmw-gen5-smontata-la-fine-di-vari-mondi-motoristici-e-tutta-qui-ma-si-puo-ancora-riparare.html. Accessed: 01-Sept-23.

[53] A. Frias, P. Pellerey, A. K. Lebouc, C. Chillet, V. Lanfranchi, G. Friedrich, L. Albert, and L. Humbert. "Rotor and stator shape optimization of a synchronous machine to reduce iron losses and acoustic noise". en. In: *2012 IEEE Vehicle Power and Propulsion Conference*. Seoul, Korea (South): IEEE, Oct. 2012, pp. 98–103. DOI: 10.1109/VPPC.2012.6422572.

[54] A. Di Gioia, I. P. Brown, Y. Nie, R. Knippel, D. C. Ludois, J. Dai, S. Hagen, and C. Alteheld. "Design and Demonstration of a Wound Field Synchronous Machine for Electric Vehicle Traction With Brushless Capacitive Field Excitation". en. In: *IEEE Transactions on Industry Applications* 54.2 (Mar. 2018), pp. 1390–1403. DOI: 10.1109/TIA.2017.2784799.

[55] M.-R. Park, D.-M. Kim, Y.-H. Jung, M.-S. Lim, and J.-P. Hong. "Modeling, Design and Control of Wound-Field Synchronous Motor for High Energy Efficiency of Electric Vehicle". en. In: *2019 IEEE Energy Conversion Congress and Exposition (ECCE)*. Baltimore, MD, USA: IEEE, Sept. 2019, pp. 3960–3967. DOI: 10.1109/ECCE.2019.8912279.

[56] F. Guo, M. Salameh, M. Krishnamurthy, and I. P. Brown. "Multimaterial Magneto-Structural Topology Optimization of Wound Field Synchronous Machine Rotors". en. In: *IEEE Transactions on Industry Applications* 56.4 (July 2020), pp. 3656–3667. DOI: 10.1109/TIA.2020.2989682.

[57] D. Grauvogl, P. Stauder, B. Hopfensperger, and D. Gerling. "Multiphysics Design of a Wound Field Synchronous Machine with Magnetic Asymmetry". en. In: *2021 IEEE International Electric Machines & Drives Conference (IEMDC)*. Hartford, CT, USA: IEEE, May 2021, pp. 1–8. DOI: 10.1109/IEMDC47953.2021.9449564.

[58] I. Boldea. *Synchronous Generators*. CRC Press, 2015.

[59] G. Klempner and I. Kerszenbaum. *Handbook of Large Turbo-Generator Operation and Maintenance*. Wiley-IEEE Press, 2018.

[60] M. Kostenko and L. Piotrovsky. *Electrical Machines - Vol. 2*. Mir Publishers, 1968.

[61] F. Graffeo, S. Vaschetto, M. Cossale, M. Kerschbaumer, E. C. Bortoni, and A. Cavagnino. "Cylindrical Wound-Rotor Synchronous Machines for Traction Applications". In: *2020 International Conference on Electrical Machines (ICEM)*. Vol. 1. 2020, pp. 1736–1742. DOI: 10.1109/ICEM49940.2020.9270992.

[62] D. Duricic, Z. El Khawly, D. Loos, M. Bauer, and A. Mayr. *Rotor for an electrical machine with push-on windings*. Patent number: WO2018091210 (A1) — 2018-05-24.

[63] *BMW Factory - Electric Motor and High Voltage Battery Production | BMW iX3 drivetrain*. https://www.youtube.com/watch?v=ncfmLxKXzPw. Accessed: 01-Sept-23.

[64] M. Biasion, D. Kowal, R. R. Moghaddam, and M. Pastorelli. "Influence of the Lamination Material and Rotor Pole Geometry on the Performance of Wound Field Synchronous Machines". In: *2022 IEEE Energy Conversion Congress and Exposition (ECCE)*. 2022, pp. 1–8. DOI: 10.1109/ECCE50734.2022.9948038.

[65] L. Cinti and N. Bianchi. "Optimal Shaping for Electrically Excited Synchronous Motor". In: *2023 IEEE International Conference on Electrical Systems for Aircraft, Railway, Ship Propulsion and Road Vehicles & International Transportation Electrification Conference (ESARS-ITEC)*. 2023, pp. 1–6. DOI: 10.1109/ESARS-ITEC57127.2023.10114885.

[66] S.-I. Park and K.-C. Kim. "Torque Ripple Reduction Method With Asymmetric Pole for Wound-Field Synchronous Motor". In: *IEEE Transactions on Magnetics* 51.3 (2015), pp. 1–4. DOI: 10.1109/TMAG.2014.2357853.

[67] G. Bramerdorfer, E. Marth, S. Nuzzo, and M. Galea. "Multi-Objective Optimization of Medium-Scale Wound-Field Electric Generators". In: *2020 IEEE 19th Biennial Conference on Electromagnetic Field Computation (CEFC)*. 2020, pp. 1–4. DOI: 10.1109/CEFC46938.2020.9451327.

[68] R. H. Park. "Two-reaction theory of synchronous machines generalized method of analysis-part I". In: *Transactions of the American Institute of Electrical Engineers* 48.3 (1929), pp. 716–727. DOI: 10.1109/T-AIEE.1929.5055275.

[69] W. C. Duesterhoeft, M. W. Schulz, and E. Clarke. "Determination of Instantaneous Currents and Voltages by Means of Alpha, Beta, and Zero Components". In: *Transactions of the American Institute of Electrical Engineers* 70.2 (1951), pp. 1248–1255. DOI: 10.1109/T-AIEE.1951.5060554.

[70] L. Olivieri and E. Ravelli. *Elettrotecnica - Macchine elettriche*. Vol. second. Cedam, 1972.

[71] M. Margner and W. Hackmann. “Control challenges of an externally excited synchronous machine in an automotive traction drive application”. en. In: *2010 Emobility - Electrical Power Train*. Leipzig, Germany: IEEE, Nov. 2010, pp. 1–6. DOI: 10.1109/EMOBILITY.2010.5668056.

[72] Y. Kim and K. Nam. “Copper-Loss-Minimizing Field Current Control Scheme for Wound Synchronous Machines”. en. In: *IEEE Transactions on Power Electronics* 32.2 (Feb. 2017), pp. 1335–1345. DOI: 10.1109/TPEL.2016.2547953.

[73] Q. K. Nguyen, J. Schuster, and J. Roth-Stielow. “Energy optimal control of an electrically excited synchronous motor used as traction drive”. en. In: *2015 9th International Conference on Power Electronics and ECCE Asia (ICPE-ECCE Asia)*. Seoul, South Korea: IEEE, June 2015, pp. 2789–2795. DOI: 10.1109/ICPE.2015.7168165.

[74] D. Hwang and B.-G. Gu. “Field Current Control Strategy for Wound-Rotor Synchronous Motors Considering Coupled Stator Flux Linkage”. en. In: *IEEE Access* 8 (2020), pp. 111811–111821. DOI: 10.1109/ACCESS.2020.3001866.

[75] S. Shinnaka and T. Sagawa. “New Optimal Current Control Methods for Energy-Efficient and Wide Speed-Range Operation of Hybrid-Field Synchronous Motor”. en. In: *IEEE Transactions on Industrial Electronics* 54.5 (Oct. 2007), pp. 2443–2450. DOI: 10.1109/TIE.2007.900356.

[76] O. Haala, B. Wagner, M. Hofmann, and M. Marz. “Optimal Current Control of Externally Excited Synchronous Machines in Automotive Traction Drive Applications”. en. In: *International Journal of Electrical and Computer Engineering* 7.9 (2013).

[77] M. Imecs, C. Szabo, and I. I. Incze. “Stator-field-oriented vectorial control for VSI-fed wound-excited synchronous motor”. en. In: *2007 International Aegean Conference on Electrical Machines and Power Electronics*. Bodrum, Turkey: IEEE, Sept. 2007, pp. 303–308. DOI: 10.1109/ACEMP.2007.4510519.

[78] C. Szabo, M. Imecs, and I. Incze. “Double-field orientation of unity power factor synchronous motor drive”. en. In: *2010 IEEE 14th International Conference on Intelligent Engineering Systems*. Las Palmas, Spain: IEEE, 2010, pp. 237–242. DOI: 10.1109/INES.2010.5483842.

[79] J. Pyrhönen, T. Jokinen, and V. Hrabovcová. *Design of Rotating Electrical Machines*. John Wiley & Sons, 2014.

[80] T. D. P. M. Bazzo, V. D. O. Moura, and R. Carlson. “A Step-by-Step Procedure to Perform Preliminary Designs of Salient-Pole Synchronous Generators”. en. In: *Energies* 14.16 (Aug. 2021), p. 4989. DOI: 10.3390/en14164989.

[81] A. Di Gioia, I. P. Brown, Y. Nie, R. Knippel, D. C. Ludois, J. Dai, S. Hagen, and C. Alteheld. "Design of a wound field synchronous machine for electric vehicle traction with brushless capacitive field excitation". en. In: *2016 IEEE Energy Conversion Congress and Exposition (ECCE)*. Milwaukee, WI, USA: IEEE, Sept. 2016, pp. 1–8. DOI: 10.1109/ECCE.2016.7855023.

[82] D. C. Ludois and I. Brown. *Brushless and Permanent Magnet Free Wound Field Synchronous Motors for EV Traction*. en. Tech. rep. DOE-Wisconsin–6849, 1349258. University of Wisconsin -Madison, Mar. 2017. DOI: 10.2172/1349258.

[83] Y. Kano. "Design optimization of brushless synchronous machines with wound-field excitation for hybrid electric vehicles". In: *2015 IEEE Energy Conversion Congress and Exposition (ECCE)*. 2015, pp. 2769–2775. DOI: 10.1109/ECCE.2015.7310048.

[84] A. Gneiting and N. Parspour. "Multi-Objective Optimization of a Quadruple 3-Phase Inductive Electrically Excited Synchronous Machine for 48V Traction Drives". en. In: *IECON 2021 – 47th Annual Conference of the IEEE Industrial Electronics Society*. Toronto, ON, Canada: IEEE, Oct. 2021, pp. 1–6. DOI: 10.1109/IECON48115.2021.9589771.

[85] J. Jurgens, A. Brune, and B. Ponick. "Electromagnetic design and analysis of a salient-pole synchronous machine with tooth-coil windings for use as a wheel hub motor in an electric vehicle". en. In: *2014 International Conference on Electrical Machines (ICEM)*. Berlin, Germany: IEEE, Sept. 2014, pp. 744–750. DOI: 10.1109/ICELMACH.2014.6960264.

[86] N. Tang, D. Sossong, and I. P. Brown. "Design and Metamodel-Based Optimization of a High Power Density Wound Field Traction Motor". en. In: *2021 IEEE Energy Conversion Congress and Exposition (ECCE)*. Vancouver, BC, Canada: IEEE, Oct. 2021, pp. 4267–4274. DOI: 10.1109/ECCE47101.2021.9595403.

[87] N. Tang and I. P. Brown. "Comparison of Candidate Designs and Performance Optimization for an Electric Traction Motor Targeting 50 kW/L Power Density". In: *2021 IEEE Energy Conversion Congress and Exposition (ECCE)*. 2021, pp. 3675–3682. DOI: 10.1109/ECCE47101.2021.9595839.

[88] C. Stancu, T. Ward, K. Rahman, R. Dawsey, and P. Savagian. "Separately excited synchronous motor with rotary transformer for hybrid vehicle application". In: *2014 IEEE Energy Conversion Congress and Exposition (ECCE)*. 2014, pp. 5844–5851. DOI: 10.1109/ECCE.2014.6954203.

[89] S. Udema and C. Fraeger. "Design of a Highly Efficient Electrical Excited Salient-Pole Synchronous Machine Utilizing an Optimization Algorithm". In: *Innovative Small Drives and Micro-Motor Systems; 11th GMM/ETG-Symposium*. 2017, pp. 1–6.

[90] M. L. Bash and S. Pekarek. "Analysis and Validation of a Population-Based Design of a Wound-Rotor Synchronous Machine". en. In: *IEEE Transactions on Energy Conversion* 27.3 (Sept. 2012), pp. 603–614. DOI: 10.1109/TEC.2012.2203136.

[91] H.-J. Park and M.-S. Lim. "Design of High Power Density and High Efficiency Wound-Field Synchronous Motor for Electric Vehicle Traction". en. In: *IEEE Access* 7 (2019), pp. 46677–46685. DOI: 10.1109/ACCESS.2019.2907800.

[92] Q. Ali, T. A. Lipo, and B.-I. Kwon. "Design and Analysis of a Novel Brushless Wound Rotor Synchronous Machine". In: *IEEE Transactions on Magnetics* 51.11 (2015), pp. 1–4. DOI: 10.1109/TMAG.2015.2440433.

[93] M.-S. Lim and J.-P. Hong. "Design of High Efficiency Wound Field Synchronous Machine With Winding Connection Change Method". In: *IEEE Transactions on Energy Conversion* 33.4 (2018), pp. 1978–1987. DOI: 10.1109/TEC.2018.2847728.

[94] O. Laldin, S. D. Sudhoff, and S. Pekarek. "An Analytical Design Model for Wound Rotor Synchronous Machines". en. In: *IEEE Transactions on Energy Conversion* 30.4 (Dec. 2015), pp. 1299–1309. DOI: 10.1109/TEC.2014.2366472.

[95] H. Bali, Y. Amara, G. Barakat, R. Ibtiouen, and M. Gabsi. "Analytical Modeling of Open Circuit Magnetic Field in Wound Field and Series Double Excitation Synchronous Machines". In: *IEEE Transactions on Magnetics* 46.10 (2010), pp. 3802–3815. DOI: 10.1109/TMAG.2010.2053039.

[96] T. A. Lipo. *Analysis of Synchronous Machines*. CRC Press, 2012.

[97] Z. Delirani, A. Rahideh, and M. Mardaneh. "Analytical calculations of electromagnetic quantities for wound rotor salient-pole synchronous machines". en. In: *COMPEL - The international journal for computation and mathematics in electrical and electronic engineering* 40.3 (Aug. 2021), pp. 325–357. DOI: 10.1108/COMPEL-03-2020-0115.

[98] R. Hamidouche, S. Mezani, T. Lubin, and T. Hamiti. "Analytical Model of Wound Rotor Synchronous Machine for Electric Vehicle Traction". en. In: *2022 Joint MMM-Intermag Conference (INTERMAG)*. New Orleans, LA, USA: IEEE, Jan. 2022, pp. 1–5. DOI: 10.1109/INTERMAG39746.2022.9827802.

[99] M. Strauch, S. Dewenter, A. Binder, and K. H. Nam. "Calculation of the electromagnetic characteristics of an electrically excited synchronous motor for an EV". en. In: *2012 IEEE Vehicle Power and Propulsion Conference*. Seoul, Korea (South): IEEE, Oct. 2012, pp. 1086–1091. DOI: 10.1109/VPPC.2012.6422786.

[100] O. Laldin, S. D. Sudhoff, and S. Pekarek. "Modified Carter's Coefficient". en. In: *IEEE Transactions on Energy Conversion* 30.3 (Sept. 2015), pp. 1133–1134. DOI: 10.1109/TEC.2015.2415457.

[101] M. Carpenter and D. Macdonald. "Circuit representation of inverter-fed synchronous motors". en. In: *IEEE Transactions on Energy Conversion* 4.3 (Sept. 1989), pp. 531–537. DOI: 10.1109/60.43259.

[102] A. Di Gerlando. "A field-circuit approach to the design oriented evaluation of the no-load voltage harmonics of salient pole synchronous generators". en. In: *Seventh International Conference on Electrical Machines and Drives*. Vol. 1995. Durham, UK: IEE, 1995, pp. 390–394. DOI: 10.1049/cp:19950900.

[103] J. Law, T. Busch, and T. Lipo. "Magnetic circuit modelling of the field regulated reluctance machine. Part I: model development". In: *IEEE Transactions on Energy Conversion* 11.1 (1996), pp. 49–55. DOI: 10.1109/60.486575.

[104] K. Bradley and A. Tami. "Reluctance mesh modelling of induction motors with healthy and faulty rotors". In: *IAS '96. Conference Record of the 1996 IEEE Industry Applications Conference Thirty-First IAS Annual Meeting*. Vol. 1. 1996, 625–632 vol.1. DOI: 10.1109/IAS.1996.557101.

[105] C. Rasmussen and E. Ritchie. "A magnetic equivalent circuit approach for predicting PM motor performance". In: *IAS '97. Conference Record of the 1997 IEEE Industry Applications Conference Thirty-Second IAS Annual Meeting*. Vol. 1. 1997, 10–17 vol.1. DOI: 10.1109/IAS.1997.643001.

[106] G. Slemon. "An equivalent circuit approach to analysis of synchronous machines with saliency and saturation". en. In: *IEEE Transactions on Energy Conversion* 5.3 (Sept. 1990), pp. 538–545. DOI: 10.1109/60.105279.

[107] M. L. Bash, J. M. Williams, and S. D. Pekarek. "Incorporating Motion in Mesh-Based Magnetic Equivalent Circuits". en. In: *IEEE Transactions on Energy Conversion* 25.2 (June 2010), pp. 329–338. DOI: 10.1109/TEC.2009.2035513.

[108] M. L. Bash and S. D. Pekarek. "Modeling of Salient-Pole Wound-Rotor Synchronous Machines for Population-Based Design". en. In: *IEEE Transactions on Energy Conversion* 26.2 (June 2011), pp. 381–392. DOI: 10.1109/TEC.2011.2105874.

[109] A. Larson, S. Pekarek, R. Wang, M. L. Bash, and R. Van Maaren. "An efficient circuit model for design of synchronous machines". en. In: *2015 IEEE International Electric Machines & Drives Conference (IEMDC)*. Coeur d'Alene, ID: IEEE, May 2015, pp. 84–89. DOI: 10.1109/IEMDC.2015.7409041.

[110] R. Wang, S. Pekarek, M. L. Bash, A. Larson, and R. V. Maaren. "Incorporating Dynamics in a Mesh-Based Magnetic Equivalent Circuit Model of Synchronous Machines". en. In: *IEEE Transactions on Energy Conversion* 30.3 (Sept. 2015), pp. 821–832. DOI: 10.1109/TEC.2015.2403773.

[111] R. Wang, S. Pekarek, and M. Bash. "Alternative excitation strategies for a wound rotor synchronous machine drive". en. In: *2012 IEEE Energy Conversion Congress and Exposition (ECCE)*. Raleigh, NC, USA: IEEE, Sept. 2012, pp. 2300–2307. DOI: 10.1109/ECCE.2012.6342467.

[112] J.-J. Lee, J. Lee, and K.-S. Kim. "Design of a WFSM for an Electric Vehicle Based on a Nonlinear Magnetic Equivalent Circuit". en. In: *IEEE Transactions on Applied Superconductivity* 28.3 (Apr. 2018), pp. 1–4. DOI: 10.1109/TASC.2018.2807438.

[113] G. Traxler-Samek, T. Lugand, and A. Schwery. "Additional Losses in the Damper Winding of Large Hydrogenerators at Open-Circuit and Load Conditions". In: *IEEE Transactions on Industrial Electronics* 57.1 (2010), pp. 154–160. DOI: 10.1109/TIE.2009.2026773.

[114] Fang Deng and N. Demerdash. "Comprehensive salient-pole synchronous machine parametric design analysis using time-step finite element-state space modeling techniques". en. In: *IEEE Transactions on Energy Conversion* 13.3 (Sept. 1998), pp. 221–229. DOI: 10.1109/60.707599.

[115] N. Bianchi. *Electrical Machine Analysis Using Finite Elements*. CRC Press, 2005.

[116] D. B. Pinhal and D. Gerling. "Driving Cycle Simulation of Wound-Rotor Synchronous Machine with Hairpin Windings Considering AC-Losses". en. In: *2019 IEEE Transportation Electrification Conference and Expo (ITEC)*. Detroit, MI, USA: IEEE, June 2019, pp. 1–7. DOI: 10.1109/ITEC.2019.8790556.

[117] D. B. Pinhal and D. Gerling. "Performance Map Calculation of a Salient-Pole Synchronous Motor with Hairpin Winding". en. In: *2019 IEEE 28th International Symposium on Industrial Electronics (ISIE)*. Vancouver, BC, Canada: IEEE, June 2019, pp. 359–365. DOI: 10.1109/ISIE.2019.8781339.

[118] M. G. Pasquinelli, P. Bolognesi, A. Guiducci, S. Nuzzo, and M. Galea. "Design of a High-Speed Wound-Field Synchronous Generator for the More Electric Aircraft". In: *2021 IEEE Workshop on Electrical Machines Design, Control and Diagnosis (WEMDCD)*. 2021, pp. 64–69. DOI: 10.1109/WEMDCD51469.2021.9425625.

[119] D. G. Dorrell. "Are wound-rotor synchronous motors suitable for use in high efficiency torque-dense automotive drives?" In: *IECON 2012 - 38th Annual Conference on IEEE Industrial Electronics Society*. 2012, pp. 4880–4885. DOI: 10.1109/IECON.2012.6389578.

[120] A. Tessarolo, C. Bassi, and D. Giulivo. "Time-Stepping Finite-Element Analysis of a 14-MVA Salient-Pole Shipboard Alternator for Different Damper Winding Design Solutions". In: *IEEE Transactions on Industrial Electronics* 59.6 (2012), pp. 2524–2535. DOI: 10.1109/TIE.2011.2157294.

[121] A. Tessarolo. "Accurate Computation of Multiphase Synchronous Machine Inductances Based on Winding Function Theory". In: *IEEE Transactions on Energy Conversion* 27.4 (2012), pp. 895–904. DOI: 10.1109/TEC.2012.2219050.

[122] Q. H. Quadri, S. Nuzzo, M. Rashed, C. Gerada, and M. Galea. "Modeling of Classical Synchronous Generators Using Size-Efficient Lookup Tables With Skewing Effect". In: *IEEE Access* 7 (2019), pp. 174551–174561. DOI: 10.1109/ACCESS.2019.2957102.

[123] S. Nuzzo, P. Bolognesi, C. Gerada, and M. Galea. "Simplified Damper Cage Circuital Model and Fast Analytical–Numerical Approach for the Analysis of Synchronous Generators". In: *IEEE Transactions on Industrial Electronics* 66.11 (2019), pp. 8361–8371. DOI: 10.1109/TIE.2018.2885737.

[124] S. Keller, M. T. Xuan, and J.-J. Simond. "Computation of the no-load voltage waveform of laminated salient-pole synchronous generators". In: *IEEE Transactions on Industry Applications* 42.3 (2006), pp. 681–687. DOI: 10.1109/TIA.2006.873663.

[125] A. Z. Gbégbé, B. Rouached, J. Cros, M. Bergeron, and P. Viarouge. "Damper Currents Simulation of Large Hydro-Generator Using the Combination of FEM and Coupled Circuits Models". In: *IEEE Transactions on Energy Conversion* 32.4 (2017), pp. 1273–1283. DOI: 10.1109/TEC.2017.2719120.

[126] F. Graffeo, S. Vaschetto, A. Tenconi, and A. Cavagnino. "No-Load Characteristic Computation for Wound Field Synchronous Propulsion Motors". In: *2023 IEEE International Conference on Electrical Systems for Aircraft, Railway, Ship Propulsion and Road Vehicles & International Transportation Electrification Conference (ESARS-ITEC)*. 2023, pp. 1–6. DOI: 10.1109/ESARS-ITEC57127.2023.10114874.

[127] A. Boglietti, A. Cavagnino, and M. Lazzari. "Computational Algorithms for Induction Motor Equivalent Circuit Parameter Determination—Part II: Skin Effect and Magnetizing Characteristics". In: *IEEE Transactions on Industrial Electronics* 58.9 (2011), pp. 3734–3740. DOI: 10.1109/TIE.2010.2084975.

[128] A. Boglietti, A. Cavagnino, and M. Lazzari. "Computational Algorithms for Induction Motor Equivalent Circuit Parameter Determination—Part II: Skin Effect and Magnetizing Characteristics". In: *IEEE Transactions on Industrial Electronics* 58.9 (2011), pp. 3734–3740. DOI: 10.1109/TIE.2010.2084975.

[129] H. W. Derbas, J. M. Williams, A. C. Koenig, and S. D. Pekarek. "A Comparison of Nodal- and Mesh-Based Magnetic Equivalent Circuit Models". In: *IEEE Transactions on Energy Conversion* 24.2 (2009), pp. 388–396. DOI: 10.1109/TEC.2008.2002037.

[130] T. A. Lipo. "Introduction to AC Machine Design". In: IEEE Press Wiley, 2004. Chap. 4, pp. 129–134.

[131] J. O'Dwyer and T. O'Donnell. "Choosing the relaxation parameter for the solution of nonlinear magnetic field problems by the Newton-Raphson method". In: *IEEE Transactions on Magnetics* 31.3 (1995), pp. 1484–1487. DOI: 10.1109/20.376310.

[132] D. Meeker. *FEMM: Finite Element Method Magnetics*. https://www.femm.info/wiki/HomePage. Accessed: 17-Sept-23.

[133] D. Meeker. *Sliding band motion model for electric machines*. https://www.femm.info/wiki/SlidingBand. Accessed: 18-Sept-23.

[134] F. Graffeo, S. Vaschetto, A. Tenconi, and A. Cavagnino. "Fast Sizing Procedure for Salient-Pole Wound Field Synchronous Motors for Transportation Electrification". In: *2023 IEEE International Electric Machines & Drives Conference (IEMDC)*. 2023, pp. 1–7. DOI: 10.1109/IEMDC55163.2023.10239093.

[135] A. Boglietti, A. Cavagnino, M. Lazzari, and S. Vaschetto. "Preliminary induction motor electromagnetic sizing based on a geometrical approach". In: *Electric Power Applications, IET* 6 (Nov. 2012), pp. 583–592. DOI: 10.1049/iet-epa.2012.0037.

[136] S. Vaschetto, A. Tenconi, and G. Bramerdorfer. "Sizing procedure of surface mounted PM machines for fast analytical evaluations". In: *2017 IEEE International Electric Machines and Drives Conference (IEMDC)*. 2017, pp. 1–8. DOI: 10.1109/IEMDC.2017.8002223.

[137] S. Ferrari, G. Dilevrano, P. Ragazzo, and G. Pellegrino. "The dq-theta Flux Map Model of Synchronous Machines". In: *2021 IEEE Energy Conversion Congress and Exposition (ECCE)*. 2021, pp. 3716–3723. DOI: 10.1109/ECCE47101.2021.9595187.

[138] R. Bojoi, A. Cavagnino, M. Cossale, and S. Vaschetto. "Methodology for the IPM motor magnetic model computation based on finite element analysis". In: *IECON 2014 - 40th Annual Conference of the IEEE Industrial Electronics Society*. 2014, pp. 722–728. DOI: 10.1109/IECON.2014.7048580.

[139] D. Hwang and B.-G. Gu. "Field Current Control Strategy for Wound-Rotor Synchronous Motors Considering Coupled Stator Flux Linkage". In: *IEEE Access* 8 (2020), pp. 111811–111821. DOI: 10.1109/ACCESS.2020.3001866.

[140] *Design of a Brushless Separately Excited Synchronous Motor*. https://ethz.ch/content/dam/ethz/special-interest/mavt/energy-science-center-dam/events/frontiers-presentations/140218_FiER_Illiano.pdf. Accessed: 29-Sept-23.

[141] F. Graffeo. "Design and analysis of different rotor configurations for wound field synchronous machines". Master thesis. 2020.

[142] *Renault Zoe*. https://de.wikipedia.org/wiki/Renault_Zoe. Accessed: 24-Sept-23.

[143] A. Boglietti, A. Cavagnino, and M. Lazzari. "Computational Algorithms for Induction-Motor Equivalent Circuit Parameter Determination—Part I: Resistances and Leakage Reactances". In: *IEEE Transactions on Industrial Electronics* 58.9 (2011), pp. 3723–3733. DOI: 10.1109/TIE.2010.2084974.

[144] S. Vaschetto, Z. Gmyrek, C. Dobler, G. Bramerdorfer, and A. Cavagnino. "Experimental Assessment and Modeling of Losses in Interlocked Magnetic Cores". In: *IEEE Transactions on Industry Applications* 58.4 (2022), pp. 4450–4460. DOI: 10.1109/TIA.2022.3163073.

[145] A. Cavagnino, G. Pellegrino, S. Vaschetto, and E. B. Agamloh. "Contribution to Offline Measurements of PMSM and SyRM Inductances". In: *IEEE Transactions on Industry Applications* 55.1 (2019), pp. 407–416. DOI: 10.1109/TIA.2018.2869100.

[146] IEEE. "IEEE Standard Test Procedure for Polyphase Induction Motors and Generators". In: *IEEE Std 112-2017 (Revision of IEEE Std 112-2004)* (2018), pp. 1–115. DOI: 10.1109/IEEESTD.2018.8291810.

[147] F. Nishanth, M. Johnson, and E. L. Severson. "A Review of Thermal Analysis and Management of Power Dense Electric Machines". In: *2021 IEEE International Electric Machines & Drives Conference (IEMDC)*. 2021, pp. 1–8. DOI: 10.1109/IEMDC47953.2021.9449520.

[148] A. Boglietti, A. Cavagnino, D. Staton, M. Shanel, M. Mueller, and C. Mejuto. "Evolution and Modern Approaches for Thermal Analysis of Electrical Machines". In: *IEEE Transactions on Industrial Electronics* 56.3 (2009), pp. 871–882. DOI: 10.1109/TIE.2008.2011622.

[149] R. Camilleri and M. D. McCulloch. "Integrating a Heat Sink into Concentrated Wound Coils to Improve the Current Density of an Axial Flux, Direct Liquid Cooled Electrical Machine with Segmented Stator". In: *Energies* 14.12 (2021). DOI: 10.3390/en14123619.

[150] R. Li, P. Cheng, H. Lan, W. Li, D. Gerada, and Y. Hong. "Stator Non-Uniform Radial Ventilation Design Methodology for a 15 MW Turbo-Synchronous Generator Based on Single Ventilation Duct Subsystem". In: *Energies* 14.10 (2021). DOI: 10.3390/en14102760.

[151] Y. Tang, L. Chen, F. Chai, and T. Chen. "Thermal Modeling and Analysis of Active and End Windings of Enclosed Permanent-Magnet Synchronous In-Wheel Motor Based on Multi-Block Method". In: *IEEE Transactions on Energy Conversion* 35.1 (2020), pp. 85–94. DOI: 10.1109/TEC.2019.2946384.

[152] M. Tosetti, P. Maggiore, A. Cavagnino, and S. Vaschetto. "Conjugate heat transfer analysis of integrated brushless generators for more electric engines". In: *2013 IEEE Energy Conversion Congress and Exposition*. 2013, pp. 1518–1525. DOI: 10.1109/ECCE.2013.6646885.

[153] Z. Rehman and K. Seong. "Three-D Numerical Thermal Analysis of Electric Motor with Cooling Jacket". In: *Energies* 11.1 (2018). DOI: 10.3390/en11010092.

[154] A. H. Mohamed, A. Hemeida, A. Rasekh, H. Vansompel, A. Arkkio, and P. Sergeant. "A 3D Dynamic Lumped Parameter Thermal Network of Air-Cooled YASA Axial Flux Permanent Magnet Synchronous Machine". In: *Energies* 11.4 (2018). DOI: 10.3390/en11040774.

[155] P. Taras, G.-J. Li, Z.-Q. Zhu, M. P. Foster, and D. A. Stone. "Combined Multiphysics Model of Switched Flux PM Machines Under Fault Operations". In: *IEEE Transactions on Industrial Electronics* 66.9 (2019), pp. 6737–6745. DOI: 10.1109/TIE.2018.2877089.

[156] Y. Moreno, G. Almandoz, A. Egea, P. Madina, and A. J. Escalada. "Multi-Physics Tool for Electrical Machine Sizing". In: *Energies* 13.7 (2020).

[157] F. Hoffmann, S. Foitzik, and M. Doppelbauer. "Thermal 3D Modeling and Analysis of PMSMs with Inter-Turn Faults". In: *2021 IEEE International Electric Machines & Drives Conference (IEMDC)*. 2021, pp. 1–7. DOI: 10.1109/IEMDC47953.2021.9449573.

[158] A. Boglietti, A. Cavagnino, M. Lazzari, and M. Pastorelli. "A simplified thermal model for variable-speed self-cooled industrial induction motor". In: *IEEE Transactions on Industry Applications* 39.4 (2003), pp. 945–952. DOI: 10.1109/TIA.2003.814555.

[159] J. Nerg, M. Rilla, and J. Pyrhonen. "Thermal Analysis of Radial-Flux Electrical Machines With a High Power Density". In: *IEEE Transactions on Industrial Electronics* 55.10 (2008), pp. 3543–3554. DOI: 10.1109/TIE.2008.927403.

[160] Y. Wang, S. Nuzzo, C. Gerada, W. Zhao, H. Zhang, and M. Galea. "3D Lumped Parameter Thermal Network for Wound-Field Synchronous Generators". In: *2021 IEEE Workshop on Electrical Machines Design, Control and Diagnosis (WEMDCD)*. 2021, pp. 5–9. DOI: 10.1109/WEMDCD51469.2021.9425624.

[161] R. Wrobel, P. H. Mellor, M. Popescu, and D. A. Staton. "Power Loss Analysis in Thermal Design of Permanent-Magnet Machines—A Review". In: *IEEE Transactions on Industry Applications* 52.2 (2016), pp. 1359–1368. DOI: 10.1109/TIA.2015.2489599.

[162] A. J. Grobler, S. R. Holm, and G. van Schoor. "Empirical Parameter Identification for a Hybrid Thermal Model of a High-Speed Permanent Magnet Synchronous Machine". In: *IEEE Transactions on Industrial Electronics* 65.2 (2018), pp. 1616–1625. DOI: 10.1109/TIE.2017.2733499.

[163] D. Liang, Z. Q. Zhu, Y. Zhang, J. Feng, S. Guo, Y. Li, J. Wu, and A. Zhao. "A Hybrid Lumped-Parameter and Two-Dimensional Analytical Thermal Model for Electrical Machines". In: *IEEE Transactions on Industry Applications* 57.1 (2021), pp. 246–258. DOI: 10.1109/TIA.2020.3029997.

[164] A. Boglietti, A. Cavagnino, and D. Staton. "Determination of Critical Parameters in Electrical Machine Thermal Models". In: *IEEE Transactions on Industry Applications* 44.4 (2008), pp. 1150–1159. DOI: 10.1109/TIA.2008.926233.

[165] D. A. Staton and A. Cavagnino. "Convection Heat Transfer and Flow Calculations Suitable for Electric Machines Thermal Models". In: *IEEE Transactions on Industrial Electronics* 55.10 (2008), pp. 3509–3516. DOI: 10.1109/TIE.2008.922604.

[166] Y. Shi, J. Wang, and B. Wang. "Transient 3-D Lumped Parameter and 3-D FE Thermal Models of a PMASynRM Under Fault Conditions With Asymmetric Temperature Distribution". In: *IEEE Transactions on Industrial Electronics* 68.6 (2021), pp. 4623–4633. DOI: 10.1109/TIE.2020.2988224.

[167] O. Wallscheid and J. Böcker. "Global Identification of a Low-Order Lumped-Parameter Thermal Network for Permanent Magnet Synchronous Motors". In: *IEEE Transactions on Energy Conversion* 31.1 (2016), pp. 354–365. DOI: 10.1109/TEC.2015.2473673.

[168] H. Zhang, P. Giangrande, G. Sala, Z. Xu, W. Hua, V. Madonna, D. Gerada, and C. Gerada. "Thermal Model Approach to Multisector Three-Phase Electrical Machines". In: *IEEE Transactions on Industrial Electronics* 68.4 (2021), pp. 2919–2930. DOI: 10.1109/TIE.2020.2977559.

[169] D. Wöckinger, G. Bramerdorfer, S. Drexler, S. Vaschetto, A. Cavagnino, A. Tenconi, W. Amrhein, and F. Jeske. "Measurement-Based Optimization of Thermal Networks for Temperature Monitoring of Outer Rotor PM Machines". In: *2020 IEEE Energy Conversion Congress and Exposition (ECCE)*. 2020, pp. 4261–4268. DOI: 10.1109/ECCE44975.2020.9236388.

[170] F. Graffeo, S. Vaschetto, A. Miotto, F. Carbone, A. Tenconi, E. Agamloh, and A. Cavagnino. "Simplified Thermal Model of Disk-Shaped Automotive Smart Braking Actuators". In: *2022 IEEE Energy Conversion Congress and Exposition (ECCE)*. 2022, pp. 1–8. DOI: 10.1109/ECCE50734.2022.9947428.

[171] F. Graffeo, S. Vaschetto, A. Miotto, F. Carbone, A. Tenconi, and A. Cavagnino. "Lumped-Parameters Thermal Network of PM Synchronous Machines for Automotive Brake-by-Wire Systems". In: *Energies* 14.18 (2021). DOI: 10.3390/en14185652.

[172] A. Boglietti, M. Cossale, S. Vaschetto, and T. Dutra. "Thermal Conductivity Evaluation of Fractional-Slot Concentrated-Winding Machines". In: *IEEE Transactions on Industry Applications* 53.3 (2017), pp. 2059–2065. DOI: 10.1109/TIA.2017.2672518.

[173] A. Boglietti, M. Cossale, S. Vaschetto, and T. Dutra. "Winding Thermal Model for Short-Time Transient: Experimental Validation in Operative Conditions". In: *IEEE Transactions on Industry Applications* 54.2 (2018), pp. 1312–1319. DOI: 10.1109/TIA.2017.2777920.

[174] A. Boglietti, E. Carpaneto, M. Cossale, S. Vaschetto, M. Popescu, and D. Staton. "Stator winding thermal conductivity evaluation: An industrial production assessment". In: *2015 IEEE Energy Conversion Congress and Exposition (ECCE)*. 2015, pp. 4865–4871. DOI: 10.1109/ECCE.2015.7310346.

[175] J. Kennedy and R. Eberhart. "Particle swarm optimization". In: *Proceedings of ICNN'95 - International Conference on Neural Networks*. Vol. 4. 1995, 1942–1948 vol.4. DOI: 10.1109/ICNN.1995.488968.

[176] M. Anantathanavit and M.-A. Munlin. "Radius Particle Swarm Optimization". In: *2013 International Computer Science and Engineering Conference (ICSEC)*. 2013, pp. 126–130. DOI: 10.1109/ICSEC.2013.6694765.

[177] M. Markovic, L. Saunders, and Y. Perriard. "Determination of the Thermal Convection Coefficient for a Small Electric Motor". In: *Conference Record of the 2006 IEEE Industry Applications Conference Forty-First IAS Annual Meeting*. Vol. 1. 2006, pp. 58–61. DOI: 10.1109/IAS.2006.256520.

[178] F. P. Incropera and D. P. DeWitt. *Fundamentals of Heat and Mass Transfer*. 4th Edition. John Wiley & Sons, Inc., 1996.

Appendix A

The Jacobian matrix

The Jacobian matrix J_R is the matrix of all the first-order partial derivatives of f, defined as in (A.1).

$$\boldsymbol{J_R} = \begin{bmatrix} \frac{\partial f_1(\boldsymbol{\Phi})}{\partial \Phi_1} & \cdots & \frac{\partial f_1(\boldsymbol{\Phi})}{\partial \Phi_n} \\ \vdots & \ddots & \vdots \\ \frac{\partial f_m(\boldsymbol{\Phi})}{\partial \Phi_1} & \cdots & \frac{\partial f_m(\boldsymbol{\Phi})}{\partial \Phi_n} \end{bmatrix} \tag{A.1}$$

In order to gain a better understanding of how to construct the Jacobian matrix, let's expand the first term of the function f of (3.67).

$$f_1(\boldsymbol{\Phi}) = (R_{st,1} + R_{sy,1} + R_{st,2} + R_{ss}) \cdot \Phi_{s,1} - R_{st,1} \cdot \Phi_{s,n_s} - R_{st,2} \cdot \Phi_{s,2} - R_{ss} \cdot \Phi_{a,2} - F_1 \tag{A.2}$$

The first term of J_R is, thus, the partial derivative of function f_1 with respect to the flux of loop 1. Considering that the first n_s elements of $\boldsymbol{\Phi}$ coincide with the vector $\boldsymbol{\Phi}_s$, the first element of $\boldsymbol{J_R}$ can be written as:

$$\frac{\partial f_1(\boldsymbol{\Phi})}{\partial \Phi_1} = \frac{\partial \left[(R_{st,1} + R_{sy,1} + R_{st,2} + R_{ss}) \cdot \Phi_1 - R_{st,1} \cdot \Phi_{n_s} - R_{st,2} \cdot \Phi_2 - R_{ss} \cdot \Phi_{a,2} - F_1 \right]}{\partial \Phi_1} \tag{A.3}$$

Each term of (A.3) is computed in the forthcoming. The first term recollects the reluctances multiplying Φ_1:

$$\begin{aligned}\frac{\partial\left[(R_{st,1}+R_{sy,1}+R_{st,2}+R_{ss})\cdot\Phi_1\right]}{\partial\Phi_1} &= R_{st,1}+R_{sy,1}+R_{st,2}+R_{ss}+\\ &+\left(\frac{\partial R_{st,1}}{\partial\Phi_1}+\frac{\partial R_{sy,1}}{\partial\Phi_1}+\frac{\partial R_{st,2}}{\partial\Phi_1}\right)\Phi_1\end{aligned} \tag{A.4}$$

Considering that the sum of $R_{st,1}$, $R_{sy,1}$, $R_{st,2}$, and R_{ss} is the first term of the reluctance matrix, equation (A.4) becomes:

$$\frac{\partial\left[(R_{st,1}+R_{sy,1}+R_{st,2}+R_{ss})\cdot\Phi_1\right]}{\partial\Phi_1} = A_{R,11}+\frac{\partial R_{st,1}}{\partial\Phi_1}\Phi_1+\frac{\partial R_{sy,1}}{\partial\Phi_1}\Phi_1+\frac{\partial R_{st,2}}{\partial\Phi_1}\Phi_1 \tag{A.5}$$

As the derivative of the other loop fluxes with respect to loop flux 1 is zero, the other two terms are found by (A.6) and (A.7).

$$\frac{\partial\left[R_{st,1}\Phi_{n_s}\right]}{\partial\Phi_1} = \frac{\partial R_{st,1}}{\partial\Phi_1}\Phi_{n_s} \tag{A.6}$$

$$\frac{\partial\left[R_{st,2}\Phi_2\right]}{\partial\Phi_1} = \frac{\partial R_{st,2}}{\partial\Phi_1}\Phi_2 \tag{A.7}$$

Since $\Phi_{a,2}$ is independent of Φ_1 and R_{ss} represents a flux tube of non-magnetic material, the third term partial derivative is zero.

$$\frac{\partial\left[R_{ss}\Phi_{a,2}\right]}{\partial\Phi_1} = 0 \tag{A.8}$$

Finally, F_1 is a input of the circuit and does not depend on Φ_1.

$$\frac{\partial F_1}{\partial\Phi_1} = 0 \tag{A.9}$$

In conclusion, the first term of $\boldsymbol{J_R}$ is:

$$\frac{\partial f_1(\boldsymbol{\Phi})}{\partial \Phi_1} = A_{R,11} + \frac{\partial R_{st,1}}{\partial \Phi_1}(\Phi_1 - \Phi_{n_s}) + \frac{\partial R_{sy,1}}{\partial \Phi_1}\Phi_1 + \frac{\partial R_{st,2}}{\partial \Phi_1}(\Phi_1 - \Phi_2) \tag{A.10}$$

The computation of the partial derivative of the reluctances with respect to a loop flux is described in [129]. Let's consider, for example, the partial derivative of $R_{st,1}$:

$$\frac{\partial R_{st,1}}{\partial \Phi_1} = \frac{\partial R_{st,1}}{\partial \mu_{st,1}} \cdot \frac{\partial \mu_{st,1}}{\partial B_{st,1}} \cdot \frac{\partial B_{st,1}}{\partial \Phi_{st,1}} \cdot \frac{\partial \Phi_{st,1}}{\partial \Phi_1} \tag{A.11}$$

Each multiplication factor can be easily computed. The first factor is the derivative of the reluctance with respect to the magnetic permeability, which simply is in its denominator.

$$\frac{\partial R_{st,1}}{\partial \mu_{st,1}} = -\frac{1}{\mu_{st,1}} R_{st,1} \tag{A.12}$$

Considering that the flux is defined by the multiplication of the magnetic flux density and the surface of the flux tube, the next derivative is simply the inverse of such surface.

$$\frac{\partial B_{st,1}}{\partial \Phi_{st,1}} = \frac{1}{A_{st,1}} \tag{A.13}$$

Finally, being $\Phi_{st,1}$ the difference between Φ_{n_s} and Φ_1:

$$\frac{\partial \Phi_{st,1}}{\partial \Phi_1} = \frac{\partial (\Phi_{n_s} - \Phi_1)}{\partial \Phi_1} = -1 \tag{A.14}$$

The factor $\partial \mu_{st,1} / \partial B_{st,1}$ is obtained by the material characteristic.

Repeating the procedure for all the other terms, the Jacobian matrix is populated. However, it is possible to demonstrate that each element of the matrix is the sum of the reluctance matrix in the same position and the partial derivatives of the flux-dependent reluctances multiplied by the relative flux.

$$J_{R,xy} = A_{R,xy} + pA_{R,xy} \tag{A.15}$$

Appendix B

Matlab code for WFSM drawing in FEMM

```
function femm_design(filename, path, pp, q, m, L, Dso, Dsi, g0, Dri, hp, kb, BH, Frot, Fstat, hst, h1, h2, wst
    , wst0, wp, hp1, hre, wcu)
% Fstat     : 0-> Parellel side tooth;      1-> Parellel side slot
% Frot      : 0-> Rectangular rotor coil;   1-> Radial rotor coil sides

%% Preliminary settings and computations
openfemm(1);
newdocument(0);
mi_saveas(strcat(path,'\',filename,'.fem'))

df      = 1/12;                         % Air gap pole arc discretization (half air gap)(p.u.)
Ns      = 2*q*m*pp;                     % Number of stator slots                          (-)
betam   = kb*180;                       % Pole arc extension                              (deg)
p       = pp*2;                         % Number of poles                                 (-)
tau     = 360/p;                        % Pole pitch                                      (deg)
sp      = 360/Ns;                       % Slot pitch                                      (deg)
hry     = Dsi/2-g0-hp-Dri/2;            % Rotor yoke                                      (m)
hp2     = hp-hp1;                       % Rotor pole head height                          (m)
npoints = 20;                           % Pole arc discretization                         (-)

mi_probdef(0,'meters','planar',1e-008,L,20,0)
smartmesh(1)

%% Main geometry design

mi_drawarc(Dri/2,0,Dri/2*cosd(tau),Dri/2*sind(tau), tau, 30)
mi_drawarc(Dso/2,0,Dso/2*cosd(tau),Dso/2*sind(tau), tau, 30)

if rem(q, 2)==0
    mi_drawline(Dri/2,0,(Dsi/2-g0/cosd(pp*betam/p)),0)
    mi_drawline((Dsi/2-g0/cosd(pp*betam/p)),0,(Dsi/2-g0/2-g0*df),0)
    mi_drawline((Dsi/2-g0/2+g0*df),0,Dsi/2,0)
    mi_drawline(Dsi/2,0,Dso/2,0)

    mi_drawline(Dri/2*cosd(tau),Dri/2*sind(tau),(Dsi/2-g0/cosd(pp*betam/p))*cosd(tau),(Dsi/2-g0/cosd(pp*betam/
        p))*sind(tau))
    mi_drawline((Dsi/2-g0/cosd(pp*betam/p))*cosd(tau),(Dsi/2-g0/cosd(pp*betam/p))*sind(tau),(Dsi/2-g0/2-g0*df)
        *cosd(tau),(Dsi/2-g0/2-g0*df)*sind(tau))
    mi_drawline((Dsi/2-g0/2+g0*df)*cosd(tau),(Dsi/2-g0/2+g0*df)*sind(tau),Dsi/2*cosd(tau),Dsi/2*sind(tau))
    mi_drawline(Dsi/2*cosd(tau),Dsi/2*sind(tau),Dso/2*cosd(tau),Dso/2*sind(tau))
else
    mi_drawline(Dri/2,0,(Dsi/2-g0/cosd(pp*betam/p)),0)
    mi_drawline((Dsi/2-g0/cosd(pp*betam/p)),0,(Dsi/2-g0/2-g0*df),0)
```

```
    mi_drawline((Dsi/2-g0/2+g0*df),0,Dsi/2,0)
    mi_drawline(Dsi/2,0,Dsi/2+h2,0)
    mi_drawline(Dsi/2+h2,0,Dsi/2+hst,0)
    mi_drawline(Dsi/2+hst,0,Dso/2,0)

    mi_drawline(Dri/2*cosd(tau),Dri/2*sind(tau),(Dsi/2-g0/cosd(pp*betam/p))*cosd(tau),(Dsi/2-g0/cosd(pp*betam/
        p))*sind(tau))
    mi_drawline((Dsi/2-g0/cosd(pp*betam/p))*cosd(tau),(Dsi/2-g0/cosd(pp*betam/p))*sind(tau),(Dsi/2-g0/2-g0*df)
        *cosd(tau),(Dsi/2-g0/2-g0*df)*sind(tau))
    mi_drawline((Dsi/2-g0/2+g0*df)*cosd(tau),(Dsi/2-g0/2+g0*df)*sind(tau),Dsi/2*cosd(tau),Dsi/2*sind(tau))
    mi_drawline(Dsi/2*cosd(tau),Dsi/2*sind(tau),(Dsi/2+h2)*cosd(tau),(Dsi/2+h2)*sind(tau))
    mi_drawline((Dsi/2+h2)*cosd(tau),(Dsi/2+h2)*sind(tau),(Dsi/2+hst)*cosd(tau),(Dsi/2+hst)*sind(tau))
    mi_drawline((Dsi/2+hst)*cosd(tau),(Dsi/2+hst)*sind(tau),Dso/2*cosd(tau),Dso/2*sind(tau))
end

%% Slot design
ja = atand((wst0/2)/(Dsi/2));
ra = Dsi/2;
xa = ra*cosd(ja);
ya = ra*sind(ja);

rb = Dsi/2+h1;
jb = ja;
xb = rb*cosd(jb);
yb = rb*sind(jb);

rc = Dsi/2 + h2;
yc = wst/2;
xc = sqrt(rc^2-yc^2);
jc = atand(yc/xc);

if Fstat==0
    rd = sqrt((wst0/2)^2 + (Dsi/2)^2) + hst;
    yd = wst/2;
    xd = sqrt(rd^2-yd^2);
    jd = atand(yd/xd);
elseif Fstat==1
    xz = (Dsi/2+hst)*cosd(sp/2);
    yz = (Dsi/2+hst)*sind(sp/2);
    mz = tand(sp/2);
    xd = (mz+1/mz)^-1*(mz*xc+1/mz*xz-yc+yz);
    yd = yc+mz*(xd-xc);
    jd = atand(yd/xd);
    rd = hypot(xd,yd);
end

if rem(q, 2)==0
    mi_drawline(ra*cosd(ja),ra*sind(ja), rb*cosd(jb),rb*sind(jb));
    mi_drawline(rb*cosd(jb),rb*sind(jb), xc, yc);
    mi_drawline(xc, yc, xd, yd);
    mi_drawline(xd, yd, rd*cosd(sp-jd),rd*sind(sp-jd));
    mi_drawline(rd*cosd(sp-jd),rd*sind(sp-jd), rc*cosd(sp-jc), rc*sind(sp-jc));
    mi_drawline(rc*cosd(sp-jc), rc*sind(sp-jc), rb*cosd(sp-jb), rb*sind(sp-jb));
    mi_drawline(rb*cosd(sp-jb), rb*sind(sp-jb), ra*cosd(sp-ja), ra*sind(sp-ja));
    mi_drawarc(xc, yc, rc*cosd(sp-jc), rc*sind(sp-jc), sp-2*jc, 20);

    mi_selectsegment((xa+xb)/2, (ya+yb)/2);
    mi_selectsegment((xb+xc)/2, (yb+yc)/2);
    mi_selectsegment((xc+xd)/2, (yc+yd)/2);
    mi_selectsegment((rc*cosd(sp-jc)+rd*cosd(sp-jd))/2, (rc*sind(sp-jc)+rd*sind(sp-jd))/2);
    mi_selectsegment((rb*cosd(sp-jb)+rc*cosd(sp-jc))/2, (rb*sind(sp-jb)+rc*sind(sp-jc))/2);
    mi_selectsegment((ra*cosd(sp-ja)+rb*cosd(sp-jb))/2, (ra*sind(sp-ja)+rb*sind(sp-jb))/2);
    mi_selectsegment((xd+rd*cosd(sp-jd))/2, (yd+rd*sind(sp-jd))/2);
    mi_copyrotate2(0, 0, sp, Ns/p-1, 1);
    mi_clearselected;
    mi_selectarcsegment((xc+rc*cosd(sp-jc))/2, (rc*sind(sp-jc)+yc)/2);
    mi_copyrotate2(0, 0, sp, Ns/p-1, 3);

    mi_addnode(Dsi/2*cosd(sp/2), Dsi/2*sind(sp/2));
    mi_addarc(Dsi/2,0,Dsi/2*cosd(sp/2), Dsi/2*sind(sp/2), sp/2, 100);
    mi_addnode(Dsi/2*cosd(sp),Dsi/2*sind(sp));
    mi_addarc(Dsi/2*cosd(sp/2), Dsi/2*sind(sp/2),Dsi/2*cosd(sp),Dsi/2*sind(sp), sp/2, 200);

```

```
    mi_selectarcsegment(Dsi/2*cosd(ja/2), Dsi/2*sind(ja/2));
    mi_selectarcsegment(Dsi/2*cosd(sp-ja/2), Dsi/2*sind(sp-ja/2));
    mi_selectarcsegment(Dsi/2*cosd(sp/2-(sp/2-ja)/2), Dsi/2*sind(sp/2-(sp/2-ja)/2));
    mi_selectarcsegment(Dsi/2*cosd(sp/2+(sp/2-ja)/2), Dsi/2*sind(sp/2+(sp/2-ja)/2));
    mi_copyrotate2(0, 0, sp, Ns/p-1, 3 );
    mi_clearselected
else
    mi_drawline(rd*cosd(sp/2-jd),rd*sind(sp/2-jd), rc*cosd(sp/2-jc), rc*sind(sp/2-jc));
    mi_drawline(rc*cosd(sp/2-jc), rc*sind(sp/2-jc), rb*cosd(sp/2-jb), rb*sind(sp/2-jb));
    mi_drawline(rb*cosd(sp/2-jb), rb*sind(sp/2-jb), ra*cosd(sp/2-ja), ra*sind(sp/2-ja));

    mi_drawline(Dsi/2+hst,0, rd*cosd(sp/2-jd),rd*sind(sp/2-jd));
    mi_selectsegment(((Dsi/2+hst)+rd*cosd(sp/2-jd))/2, rd*sind(sp/2-jd)/2);
    mi_mirror2(0,0, Dsi*cosd(sp/2), Dsi*sind(sp/2), 1);
    mi_clearselected

    mi_addnode(Dsi/2*cosd(sp/2), Dsi/2*sind(sp/2))
    mi_addarc(Dsi/2, 0, Dsi/2*cosd(sp/2), Dsi/2*sind(sp/2), sp/2, 100)
    mi_drawarc(Dsi/2+h2, 0,rc*cosd(sp/2-jc), rc*sind(sp/2-jc), sp/2-jc, 20);

    mi_drawline(rd*cosd(sp/2+jd),rd*sind(sp/2+jd), rc*cosd(sp/2+jc), rc*sind(sp/2+jc));
    mi_drawline(rc*cosd(sp/2+jc), rc*sind(sp/2+jc), rb*cosd(sp/2+jb), rb*sind(sp/2+jb));
    mi_drawline(rb*cosd(sp/2+jb), rb*sind(sp/2+jb), ra*cosd(sp/2+ja), ra*sind(sp/2+ja));
    mi_drawarc(rc*cosd(sp/2+jc), rc*sind(sp/2+jc),rc*cosd(sp), rc*sind(sp), sp/2-jc, 20);
    mi_drawarc(Dsi/2*cosd(sp/2), Dsi/2*sind(sp/2), Dsi/2*cosd(sp), Dsi/2*sind(sp), sp/2, 100)

    mi_selectsegment((rd*cosd(sp/2-jd)+rc*cosd(sp/2-jc))/2, (rd*sind(sp/2-jd)+rc*sind(sp/2-jc))/2);
    mi_selectsegment((rb*cosd(sp/2-jb)+rc*cosd(sp/2-jc))/2, (rb*sind(sp/2-jb)+rc*sind(sp/2-jc))/2);
    mi_selectsegment((rb*cosd(sp/2-jb)+ra*cosd(sp/2-ja))/2, (rb*sind(sp/2-jb)+ra*sind(sp/2-ja))/2);
    mi_selectsegment((rd*cosd(sp/2+jd)+rc*cosd(sp/2+jc))/2, (rd*sind(sp/2+jd)+rc*sind(sp/2+jc))/2);
    mi_selectsegment((rc*cosd(sp/2+jc)+rb*cosd(sp/2+jb))/2, (rc*sind(sp/2+jc)+rb*sind(sp/2+jb))/2);
    mi_selectsegment((rb*cosd(sp/2+jb)+ra*cosd(sp/2+ja))/2, (rb*sind(sp/2+jb)+ra*sind(sp/2+ja))/2);
    mi_selectsegment((Dsi/2+hst)*cosd(sp/8), (Dsi/2+hst)*sind(sp/8));
    mi_selectsegment((Dsi/2+hst)*cosd(sp), (Dsi/2+hst)*sind(sp));

    mi_copyrotate2(0, 0, sp, Ns/p-1, 1);
    mi_clearselected

    mi_selectarcsegment(Dsi/2*cosd(sp/4-ja/2), Dsi/2*sind(sp/4-ja/2));
    mi_selectarcsegment(Dsi/2*cosd(sp/2-ja/2), Dsi/2*sind(sp/2-ja/2));
    mi_selectarcsegment(Dsi/2*cosd(sp/2+ja/2), Dsi/2*sind(sp/2+ja/2));
    mi_selectarcsegment(Dsi/2*cosd(3*sp/4+ja/2), Dsi/2*sind(3*sp/4+ja/2));
    mi_selectarcsegment((Dsi/2+h2)*cosd(sp/4-jc/2), (Dsi/2+h2)*sind(sp/4-jc/2));
    mi_selectarcsegment((Dsi/2+h2)*cosd(sp-sp/4+jc/2), (Dsi/2+h2)*sind(sp-sp/4+jc/2));

    mi_copyrotate2(0, 0, sp, Ns/p-1, 3 );
    mi_clearselected
end

%% Air gap design

mi_drawarc((Dsi/2-g0/2-g0*df),0,(Dsi/2-g0/2-g0*df)*cosd(tau),(Dsi/2-g0/2-g0*df)*sind(tau), tau, 1000)
mi_drawarc((Dsi/2-g0/2+g0*df),0,(Dsi/2-g0/2+g0*df)*cosd(tau),(Dsi/2-g0/2+g0*df)*sind(tau), tau, 1000)

%% Rotor design
delta = betam/p/npoints;

x = (Dsi/2-g0./(cosd((0:npoints)*delta*pp))).*cosd(tau/2-(0:npoints)*delta);
y = (Dsi/2-g0./(cosd((0:npoints)*delta*pp))).*sind(tau/2-(0:npoints)*delta);

for i = 0:npoints
    xtmp = x(i+1);
    ytmp = y(i+1);
    mi_addnode(xtmp, ytmp)
    if i>0
        mi_selectnode(xtmp, ytmp);
        mi_mirror(0,0,x(1),y(1));
        if floor(i/2)==ceil(i/2)
            deg = fnc_ang(x(i-1),y(i-1), x(i+1), y(i+1), x(i), y(i));
            mi_drawarc(x(i+1),y(i+1),x(i-1),y(i-1),deg, 30)
            mi_selectarcsegment((x(i+1)+x(i))/2,(y(i+1)+y(i))/2);
            mi_selectarcsegment((x(i-1)+x(i))/2,(y(i-1)+y(i))/2);
            mi_setarcsegmentprop(2.5,'<none>', 0, 1)
```

```
185             mi_mirror2(0,0,x(1),y(1),3);
186             mi_clearselected;
187         elseif i==npoints && rem(npoints, 2)>0
188             mi_drawarc(x(i+1),y(i+1),x(i),y(i),deg/2, 30)
189             mi_selectarcsegment((x(i+1)+x(i))/2,(y(i+1)+y(i))/2);
190             mi_setarcsegmentprop(2.5,'<none>', 0, 1)
191             mi_mirror2(0,0,x(1),y(1),3);
192             mi_clearselected;
193         end
194     end
195 end
196
197 mi_addarc((Dsi/2-g0/cosd(pp*betam/p)),0, (Dsi/2-g0/cosd(pp*betam/p))*cosd(tau/2-betam/p), (Dsi/2-g0/cosd(pp*
        betam/p))*sind(tau/2-betam/p), tau/2-betam/p, 30)
198 mi_addarc((Dsi/2-g0/cosd(pp*betam/p))*cosd(tau/2+betam/p),(Dsi/2-g0/cosd(pp*betam/p))*sind(tau/2+betam/p), (
        Dsi/2-g0/cosd(pp*betam/p))*cosd(tau), (Dsi/2-g0/cosd(pp*betam/p))*sind(tau), tau/2-betam/p, 30)
199 mi_selectarcsegment((Dsi/2-g0/cosd(pp*betam/p))*cosd(tau/4-betam/p/2), (Dsi/2-g0/cosd(pp*betam/p))*sind(tau/4-
        betam/p/2));
200 mi_selectarcsegment((Dsi/2-g0/cosd(pp*betam/p))*cosd(tau-tau/4+betam/p/2), (Dsi/2-g0/cosd(pp*betam/p))*sind(
        tau-tau/4+betam/p/2));
201 mi_setarcsegmentprop(2.5,'<none>', 0, 1)
202 mi_clearselected;
203
204 xR1 = (Dsi/2-g0/cosd(pp*betam/p))*cosd(tau/2-betam/p);
205 yR1 = (Dsi/2-g0/cosd(pp*betam/p))*sind(tau/2-betam/p);
206
207 if Frot == 0
208     xR = xR1-hre*cosd(180/(2*pp));
209     yR = yR1-hre*sind(180/(2*pp));
210 elseif Frot==1
211     xR = (Dsi/2-g0/cosd(pp*betam/p)-hre)*cosd(tau/2-betam/p);
212     yR = (Dsi/2-g0/cosd(pp*betam/p)-hre)*sind(tau/2-betam/p);
213 end
214
215 mi_addnode(xR,yR);
216
217 r       = Dsi/2-g0-hp1-hp2;
218 alpha_d = asind((wp/2)/r);
219 xT      = r*cosd(tau/2-alpha_d);
220 yT      = r*sind(tau/2-alpha_d);
221 mi_addnode(xT,yT);
222
223 mTS     = tand(tau/2);
224 xS      = (mTS*yR-mTS*yT+mTS^2*xT+xR)/(mTS^2+1);
225 yS      = yT+mTS*(xS-xT);
226 mi_addnode(xS,yS);
227
228 mi_addsegment(xR1, yR1, xR, yR)
229 mi_addsegment(xR, yR, xS, yS);
230 mi_addsegment(xT, yT, xS, yS);
231
232 mi_selectsegment((xR+xR1)/2,(yR+yR1)/2);
233 mi_selectsegment((xT+xS)/2,(yT+yS)/2);
234 mi_selectsegment((xR+xS)/2,(yR+yS)/2);
235 mi_setsegmentprop('<none>', 1, 1, 0, 1)
236 mi_mirror2(0,0,x(1),y(1),1);
237 mi_clearselected;
238
239 mi_addnode(r,0);
240 mi_addarc(r,0,r*cosd(tau/2-alpha_d),r*sind(tau/2-alpha_d), tau/2-alpha_d, 30);
241
242 mi_addnode(r*cosd(tau),r*sind(tau));
243 mi_addarc(r*cosd(tau/2+alpha_d),r*sind(tau/2+alpha_d),r*cosd(tau),r*sind(tau), tau/2-alpha_d, 30);
244
245 % Assign group 1 to the rotor
246 mi_selectarcsegment((r + r*cosd(tau/2-alpha_d))/2,r*sind(tau/2-alpha_d)/2);
247 mi_selectarcsegment(r*cosd(tau/2+alpha_d+(tau/2+alpha_d)/2),r*sind(tau/2+alpha_d+(tau/2+alpha_d)/2));
248 mi_setarcsegmentprop(2.5,'<none>', 0, 1)
249 mi_clearselected;
250
251 %% Rotor coil design
252
253 xJ = xR-wcu*sind(180/(2*pp));
```

```
yJ = yR+wcu*cosd(180/(2*pp));

xJ1 = (yT-yJ)*mTS/(mTS^2+1)+xJ*mTS^2/(mTS^2+1)+xT/(mTS^2+1);
yJ1 = yJ+mTS*(xJ1-xJ);

xU = (Dri/2+hry)*cosd(atand(yR/xR));
yU = (Dri/2+hry)*sind(atand(yR/xR));

if Frot==0
    flag_rotcoil=0;
    mi_addnode(xJ,yJ);
    if yJ1<=0
        yJ1 = Dso/2*1e-3;
    end
    mi_addnode(xJ1,yJ1);
    mi_addsegment(xJ, yJ, xJ1, yJ1);
    mi_addsegment(xJ1, yJ1, xT, yT);

    mi_selectsegment((xJ1+xT)/2,(yJ1+yT)/2);
    mi_selectsegment((xJ+xJ1)/2,(yJ+yJ1)/2);
    mi_setsegmentprop('<none>', 1, 1, 0, 1)
    mi_mirror2(0,0,x(1),y(1),1);

    mm1     = (yS-yJ1)/(xS-xJ1);
    mm2     = (yJ-yT)/(xJ-xT);
    xm      = (yS-yJ-mm1*xS+mm2*xJ)/(mm2-mm1);
    ym      = yS+mm1*(xm-xS);

    rLA     = hypot((xS+xT+xJ1+xJ)/4, (yS+yT+yJ1+yJ)/4);
    xLA     = rLA*cosd((1-kb)/8*180/pp);
    yLA     = rLA*sind((1-kb)/8*180/pp);
    xLA1    = rLA*cosd(tau-(1-kb)/8*180/pp);
    yLA1    = rLA*sind(tau-(1-kb)/8*180/pp);

    if yJ1 == Dso/2*1e-3
        xLA     = 0.98*(Dsi/2-g0/cosd(pp*betam/p))*cosd((tau/2-betam/p)/8);
        yLA     = 0.98*(Dsi/2-g0/cosd(pp*betam/p))*sind((tau/2-betam/p)/8);
        xLA1    = 0.98*(Dsi/2-g0/cosd(pp*betam/p))*cosd(tau-(tau/2-betam/p)/8);
        yLA1    = 0.98*(Dsi/2-g0/cosd(pp*betam/p))*sind(tau-(tau/2-betam/p)/8);
    end

elseif Frot==1
    if atand(yU/xU)>atand(yT/xT)
        mi_addsegment(xT, yT, xR, yR);
        flag_rotcoil=1;
    else
        mi_addnode(xU,yU)
        flag_rotcoil=0;
        mi_addsegment(xU, yU, xR, yR);
    end

    mi_addsegment(xU, yU, xR, yR);

    mi_selectsegment((xU+xR)/2,(yU+yR)/2);
    mi_setsegmentprop('<none>', 1, 1, 0, 1)
    mi_mirror2(0,0,x(1),y(1),1);

    mm1     = (yS-yU)/(xS-xU);
    mm2     = (yR-yT)/(xR-xT);
    xm      = (yS-yR-mm1*xS+mm2*xR)/(mm2-mm1);
    ym      = yS+mm1*(xm-xS);

    xLA = (Dri/2+hry+0.5*(hypot((xU-xR), (yU-yR))))*cosd((1-kb)/8*180/pp);
    yLA = (Dri/2+hry+0.5*(hypot((xU-xR), (yU-yR))))*sind((1-kb)/8*180/pp);
    xLA1 = (Dri/2+hry+0.5*(hypot((xU-xR), (yU-yR))))*cosd(tau-(1-kb)/8*180/pp);
    yLA1 = (Dri/2+hry+0.5*(hypot((xU-xR), (yU-yR))))*sind(tau-(1-kb)/8*180/pp);
end

cf      = y(1)/x(1);
y_mir   = (2*cf*xm-ym+cf^2*ym)/(1+cf^2);
x_mir   = xm + cf*ym-cf*y_mir;

%% Boundaries
```

```
327
328 mi_addboundprop('dir', 0, 0, 0, 0, 0, 0, 0, 0, 0);
329 mi_addboundprop('ap1', 0, 0, 0, 0, 0, 0, 0, 0, 5);
330 mi_addboundprop('ap12', 0, 0, 0, 0, 0, 0, 0, 0, 5);
331 mi_addboundprop('ap2', 0, 0, 0, 0, 0, 0, 0, 0, 5);
332 mi_addboundprop('ap3', 0, 0, 0, 0, 0, 0, 0, 0, 5);
333 mi_addboundprop('ap4', 0, 0, 0, 0, 0, 0, 0, 0, 5);
334 mi_addboundprop('sb', 0, 0, 0, 0, 0, 0, 0, 0, 7);
335
336 % Rotor
337 mi_selectarcsegment(Dri/2*cosd(tau/2),Dri/2*sind(tau/2));
338 mi_setarcsegmentprop(2.5,'dir', 0, 1)
339 mi_clearselected
340
341 % Stator
342 mi_selectarcsegment(Dso/2*cosd(tau/2),Dso/2*sind(tau/2));
343 mi_setarcsegmentprop(2.5,'dir', 0, 0)
344 mi_clearselected
345
346 mi_selectsegment(Dri/2*cosd(0),Dri/2*sind(0));
347 mi_selectsegment(Dri/2*cosd(tau),Dri/2*sind(tau));
348 mi_setsegmentprop('ap1', 1, 1, 0, 1)
349 mi_clearselected
350
351 mi_selectsegment(Dri/2+((Dsi/2-g0/cosd(pp*betam/p))-Dri/2)/2,0);
352 mi_selectsegment((Dri/2+((Dsi/2-g0/cosd(pp*betam/p))-Dri/2)/2)*cosd(tau),(Dri/2+((Dsi/2-g0/cosd(pp*betam/p))-
      Dri/2)/2)*sind(tau));
353 mi_setsegmentprop('ap12', 1, 1, 0, 1)
354 mi_clearselected
355
356 mi_selectsegment((Dsi/2-g0/2-g0*df)*cosd(0),(Dsi/2-g0/2-g0*df)*sind(0));
357 mi_selectsegment((Dsi/2-g0/2-g0*df)*cosd(tau),(Dsi/2-g0/2-g0*df)*sind(tau));
358 mi_setsegmentprop('ap2', 1, 1, 0, 2)
359 mi_clearselected
360
361 mi_selectsegment((Dsi/2-g0/2+g0*df)*cosd(0),(Dsi/2-g0/2+g0*df)*sind(0));
362 mi_selectsegment((Dsi/2-g0/2+g0*df)*cosd(tau),(Dsi/2-g0/2+g0*df)*sind(tau));
363 mi_setsegmentprop('ap3', 1, 1, 0, 0)
364 mi_clearselected
365
366 mi_selectsegment((3*Dsi/2)*cosd(0),(3*Dsi/2)*sind(0));
367 mi_selectsegment((3*Dsi/2)*cosd(tau),(3*Dsi/2)*sind(tau));
368 mi_setsegmentprop('ap4', 1, 1, 0, 0)
369 mi_clearselected
370
371 if rem(q, 2)>0
372     mi_addboundprop('ap5', 0, 0, 0, 0, 0, 0, 0, 0, 5);
373     mi_selectsegment((Dsi/2+hst/2)*cosd(0),(Dsi/2+hst/2)*sind(0));
374     mi_selectsegment((Dsi/2+hst/2)*cosd(tau),(Dsi/2+hst/2)*sind(tau));
375     mi_setsegmentprop('ap5', 1, 1, 0, 0)
376     mi_clearselected
377     mi_addboundprop('ap6', 0, 0, 0, 0, 0, 0, 0, 0, 5);
378     mi_selectsegment((Dsi/2+h2/2)*cosd(0),(Dsi/2+h2/2)*sind(0));
379     mi_selectsegment((Dsi/2+h2/2)*cosd(tau),(Dsi/2+h2/2)*sind(tau));
380     mi_setsegmentprop('ap6', 1, 1, 0, 0)
381     mi_clearselected
382 end
383
384 mi_selectarcsegment((Dsi/2-g0/2-g0*df),0);
385 mi_setarcsegmentprop(1,'sb', 0, 2)
386 mi_clearselected
387
388 mi_selectarcsegment((Dsi/2-g0/2+g0*df),0);
389 mi_setarcsegmentprop(1,'sb', 0, 0)
390 mi_clearselected
391
392 %% Materials and circuits
393 mi_getmaterial('Air')
394 mi_getmaterial('Copper')
395
396 mi_addmaterial('Iron', 2100, 2100, 0, 0, 0, 0, 0, 1, 0, 0, 0);
397 mi_addbhpoints('Iron', BH);
398 mi_addcircprop('Field', 0, 1);
```

```
399 if m==3
400     mi_addcircprop('A', 0, 1);
401     mi_addcircprop('B', 0, 1);
402     mi_addcircprop('C', 0, 1);
403 elseif m>3
404     for h=1:m/3
405         mi_addcircprop(['A', num2str(h)], 0, 1);
406         mi_addcircprop(['B', num2str(h)], 0, 1);
407         mi_addcircprop(['C', num2str(h)], 0, 1);
408     end
409 end
410 %% Block Labels
411
412 % Stator
413 mi_addblocklabel(Dso/2*0.99*cosd(tau/2),Dso/2*0.99*sind(tau/2));
414 mi_selectlabel(Dso/2*0.99*cosd(tau/2),Dso/2*0.99*sind(tau/2));
415 mi_setblockprop('Iron', 0, 0, '<None>', 0, 100, 0);
416 mi_clearselected
417
418 % Stator copper
419 if rem(q, 2)==0
420     mi_addblocklabel((Dsi/2+hst/2)*cosd(sp/2), (Dsi/2+hst/2)*sind(sp/2));
421     mi_addblocklabel((Dsi/2+h2/2)*cosd(sp/2), (Dsi/2+h2/2)*sind(sp/2));
422     mi_selectlabel((Dsi/2+hst/2)*cosd(sp/2), (Dsi/2+hst/2)*sind(sp/2));
423     mi_selectlabel((Dsi/2+h2/2)*cosd(sp/2), (Dsi/2+h2/2)*sind(sp/2));
424     mi_copyrotate2(0, 0, sp, Ns/p-1, 4)
425     for i=0:(q -1)
426         if i<q/2
427             mi_selectlabel((Dsi/2+hst/2)*cosd(sp/2+sp*i), (Dsi/2+hst/2)*sind(sp/2+sp*i));
428             mi_setblockprop('Copper', 0, 0, 'A', 0, 0, 2);
429             mi_clearselected
430         end
431
432         mi_selectlabel((Dsi/2+h2/2)*cosd(sp/2+sp*i), (Dsi/2+h2/2)*sind(sp/2+sp*i));
433         mi_setblockprop('Air', 0, 0, '<None>', 0, 0, 0);
434         mi_clearselected
435
436         mi_selectlabel((Dsi/2+hst/2)*cosd(sp/2+sp*(i+q)-sp*q/2), (Dsi/2+hst/2)*sind(sp/2+sp*(i+q)-sp*q/2));
437         mi_setblockprop('Copper', 0, 0, 'C', 0, 0, -2);
438         mi_clearselected
439
440         mi_selectlabel((Dsi/2+h2/2)*cosd(sp/2+sp*(i+q)), (Dsi/2+h2/2)*sind(sp/2+sp*(i+q)));
441         mi_setblockprop('Air', 0, 0, '<None>', 0, 0, 0);
442         mi_clearselected
443
444         mi_selectlabel((Dsi/2+hst/2)*cosd(sp/2+sp*(i+2*q)-sp*q/2), (Dsi/2+hst/2)*sind(sp/2+sp*(i+2*q)-sp*q/2))
                ;
445         mi_setblockprop('Copper', 0, 0, 'B', 0, 0, 2);
446         mi_clearselected
447
448         mi_selectlabel((Dsi/2+h2/2)*cosd(sp/2+sp*(i+2*q)), (Dsi/2+h2/2)*sind(sp/2+sp*(i+2*q)));
449         mi_setblockprop('Air', 0, 0, '<None>', 0, 0, 0);
450         mi_clearselected
451
452         if i>=q/2
453             mi_selectlabel((Dsi/2+hst/2)*cosd(tau-sp/2-sp*(q-1-i)), (Dsi/2+hst/2)*sind(tau-sp/2-sp*(q-1-i)));
454             mi_setblockprop('Copper', 0, 0, 'A', 0, 0, -2);
455             mi_clearselected
456         end
457     end
458 else
459     mi_addblocklabel((Dsi/2+hst/2)*cosd((sp/2-ja)/2), (Dsi/2+hst/2)*sind((sp/2-ja)/2));
460     mi_addblocklabel((Dsi/2+h2/2)*cosd((sp/2-ja)/2), (Dsi/2+h2/2)*sind((sp/2-ja)/2));
461     mi_selectlabel((Dsi/2+hst/2)*cosd((sp/2-ja)/2), (Dsi/2+hst/2)*sind((sp/2-ja)/2));
462     mi_selectlabel((Dsi/2+h2/2)*cosd((sp/2-ja)/2), (Dsi/2+h2/2)*sind((sp/2-ja)/2));
463     mi_copyrotate2(0, 0, sp, Ns/p-1, 4)
464     mi_addblocklabel((Dsi/2+hst/2)*cosd(tau-(sp/2-ja)/2), (Dsi/2+hst/2)*sind(tau-(sp/2-ja)/2));
465     mi_addblocklabel((Dsi/2+h2/2)*cosd(tau-(sp/2-ja)/2), (Dsi/2+h2/2)*sind(tau-(sp/2-ja)/2));
466
467     for i=0:(q -1)
468         if i<q/2
469             if i==0
470                 mi_selectlabel((Dsi/2+hst/2)*cosd((sp/2-ja)/2+sp*i), (Dsi/2+hst/2)*sind((sp/2-ja)/2+sp*i));
```

```
471                 mi_setblockprop('Copper',  0, 0, 'A', 0, 0, 1);
472                 mi_clearselected
473             else
474                 mi_selectlabel((Dsi/2+hst/2)*cosd((sp/2-ja)/2+sp*i), (Dsi/2+hst/2)*sind((sp/2-ja)/2+sp*i));
475                 mi_setblockprop('Copper',  0, 0, 'A', 0, 0, 2);
476                 mi_clearselected
477             end
478         end
479
480         mi_selectlabel((Dsi/2+h2/2)*cosd((sp/2-ja)/2+sp*i), (Dsi/2+h2/2)*sind((sp/2-ja)/2+sp*i));
481         mi_setblockprop('Air',  0, 0,  '<None>', 0, 0, 0);
482         mi_clearselected
483
484         mi_selectlabel((Dsi/2+hst/2)*cosd((sp/2-ja)/2+sp*(i+q)-sp*(q-1)/2), (Dsi/2+hst/2)*sind((sp/2-ja)/2+sp
                *(i+q)-sp*(q-1)/2));
485         mi_setblockprop('Copper', 0, 0, 'C', 0, 0, -2);
486         mi_clearselected
487
488         mi_selectlabel((Dsi/2+h2/2)*cosd((sp/2-ja)/2+sp*(i+q)), (Dsi/2+h2/2)*sind((sp/2-ja)/2+sp*(i+q)));
489         mi_setblockprop('Air',  0, 0,  '<None>', 0, 0, 0);
490         mi_clearselected
491
492         mi_selectlabel((Dsi/2+hst/2)*cosd((sp/2-ja)/2+sp*(i+2*q)-sp*(q-1)/2), (Dsi/2+hst/2)*sind((sp/2-ja)/2+
                sp*(i+2*q)-sp*(q-1)/2));
493         mi_setblockprop('Copper', 0, 0, 'B', 0, 0, 2);
494         mi_clearselected
495
496         mi_selectlabel((Dsi/2+h2/2)*cosd((sp/2-ja)/2+sp*(i+2*q)), (Dsi/2+h2/2)*sind((sp/2-ja)/2+sp*(i+2*q)));
497         mi_setblockprop('Air',  0, 0,  '<None>', 0, 0, 0);
498         mi_clearselected
499
500         if i>=q/2
501             mi_selectlabel((Dsi/2+hst/2)*cosd(tau-((sp/2-ja)/2)-sp*(q-i)), (Dsi/2+hst/2)*sind(tau-((sp/2-ja)
                    /2)-sp*(q-i)));
502             mi_setblockprop('Copper',  0, 0, 'A', 0, 0, -2);
503             mi_clearselected
504         end
505     end
506     mi_selectlabel((Dsi/2+hst/2)*cosd(tau-(sp/2-ja)/2), (Dsi/2+hst/2)*sind(tau-(sp/2-ja)/2));
507     mi_setblockprop('Copper',  0, 0, 'A', 0, 0, -1);
508     mi_clearselected
509     mi_selectlabel((Dsi/2+h2/2)*cosd(tau-(sp/2-ja)/2), (Dsi/2+h2/2)*sind(tau-(sp/2-ja)/2));
510     mi_setblockprop('Air',  0, 0,  '<None>', 0, 0, 0);
511     mi_clearselected
512 end
513
514 % Stator air
515 Dro = Dsi -2*g0;
516 mi_addblocklabel((Dro/2+g0/2+df*g0*1.2)*cosd(tau/2),(Dro/2+g0/2+df*g0*1.2)*sind(tau/2));
517 mi_selectlabel((Dro/2+g0/2+df*g0*1.2)*cosd(tau/2),(Dro/2+g0/2+df*g0*1.2)*sind(tau/2));
518 mi_setblockprop('Air', 0, 0, '<None>', 0, 0, 0);
519 mi_clearselected
520
521 % Rotor air
522 mi_addblocklabel((Dsi/2-g0/2-df*g0*1.2)*cosd(tau/2),(Dsi/2-g0/2-df*g0*1.2)*sind(tau/2));
523 mi_selectlabel((Dsi/2-g0/2-df*g0*1.2)*cosd(tau/2),(Dsi/2-g0/2-df*g0*1.2)*sind(tau/2));
524 mi_setblockprop('Air', 0, 0, '<None>', 0, 2, 0);
525 mi_clearselected
526
527 % Rotor
528 mi_addblocklabel((Dri/2+hp1)*cosd(tau/2),(Dri/2+hp1)*sind(tau/2));
529 mi_selectlabel((Dri/2+hp1)*cosd(tau/2),(Dri/2+hp1)*sind(tau/2));
530 mi_setblockprop('Iron', 0, 0, '<None>', 0, 200, 0);
531 mi_clearselected
532
533 %Rotor copper
534 if flag_rotcoil==0
535     mi_addblocklabel(xm, ym)
536     mi_selectlabel(xm, ym);
537     mi_setblockprop('Copper', 0, 0, 'Field', 0, 1, 1);
538     mi_clearselected
539     mi_addblocklabel(x_mir, y_mir)
540     mi_selectlabel(x_mir, y_mir);
```

```
541     mi_setblockprop('Copper', 0, 0, 'Field', 0, 1, -1);
542     mi_clearselected
543 elseif flag_rotcoil==1
544     mi_addblocklabel(hypot(xS,yS)*cosd(atand(yS/xS)-1), hypot(xS,yS)*sind(atand(yS/xS)-1))
545     mi_selectlabel(hypot(xS,yS)*cosd(atand(yS/xS)-1), hypot(xS,yS)*sind(atand(yS/xS)-1));
546     mi_setblockprop('Copper', 0, 0, 'Field', 0, 1, 1);
547     mi_clearselected
548     mi_addblocklabel(hypot(xS,yS)*cosd(tau-atand(yS/xS)+1),hypot(xS,yS)*sind(tau-atand(yS/xS)+1))
549     mi_selectlabel(hypot(xS,yS)*cosd(tau-atand(yS/xS)+1),hypot(xS,yS)*sind(tau-atand(yS/xS)+1));
550     mi_setblockprop('Copper', 0, 0, 'Field', 0, 1, -1);
551     mi_clearselected
552 end
553
554 %Rotor lateral air
555 mi_addblocklabel(xLA, yLA);
556 mi_addblocklabel(xLA1, yLA1);
557 mi_selectlabel(xLA, yLA);
558 mi_selectlabel(xLA1, yLA1);
559 mi_setblockprop('Air', 0, 0, '<None>', 0, 1, 0);
```

Appendix C

Results of the phase-split Thermal Network for the Disk-Shaped Motor

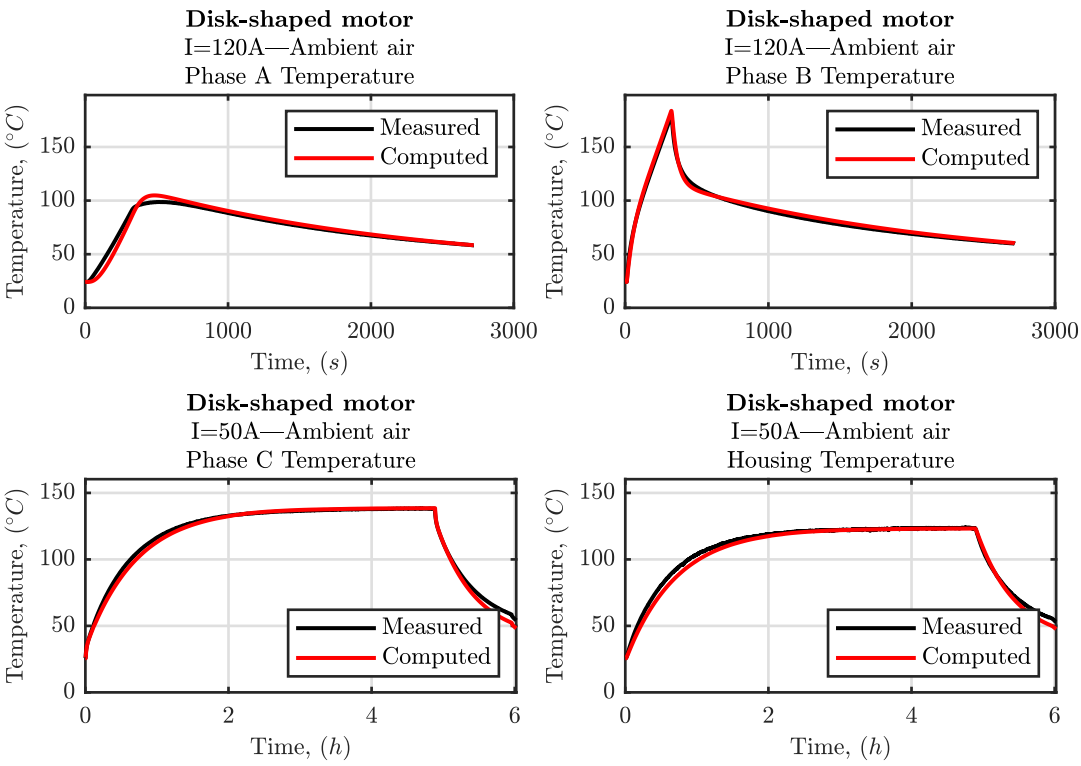

Fig. C.1 Simplified phase-split LPTN results for the disk-shaped motor in ambient air for the tests used in the optimization.

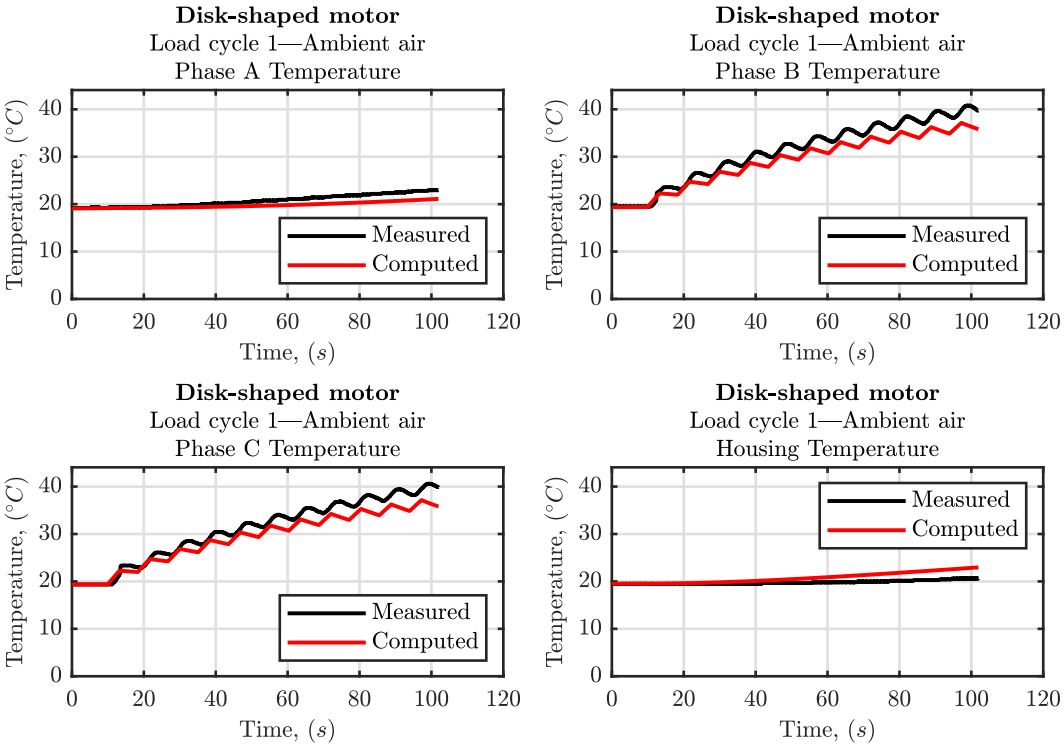

Fig. C.2 Simplified phase-split LPTN results for the disk-shaped motor in ambient air for the load cycle 1.

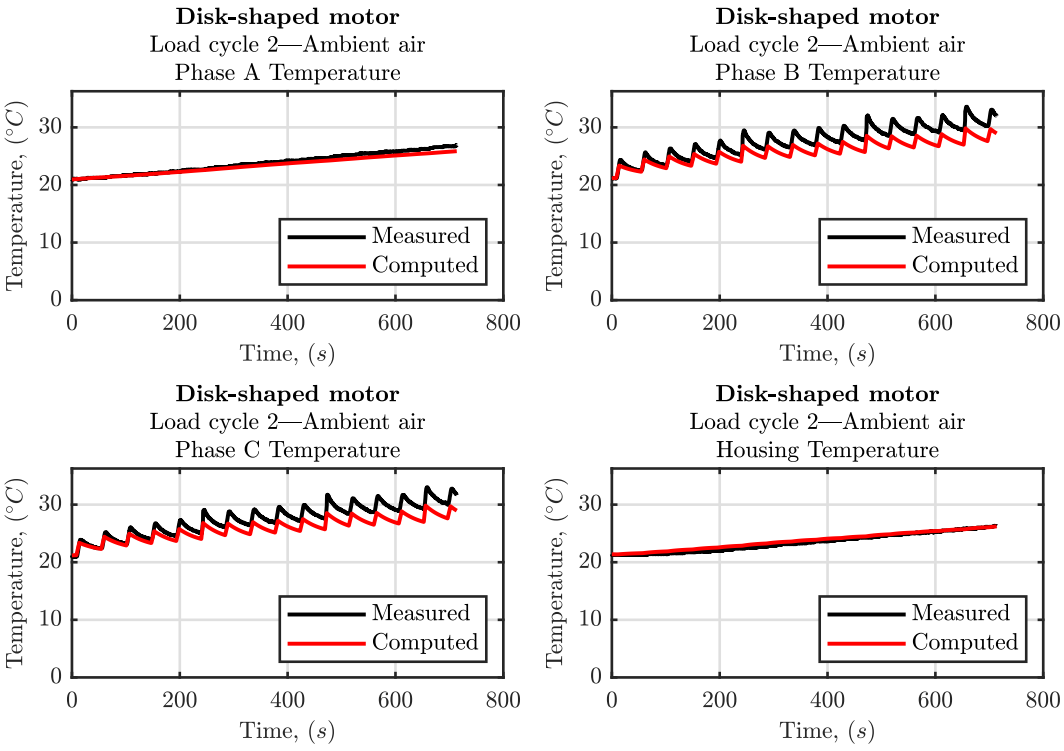

Fig. C.3 Simplified phase-split LPTN results for the disk-shaped motor in ambient air for the load cycle 2.

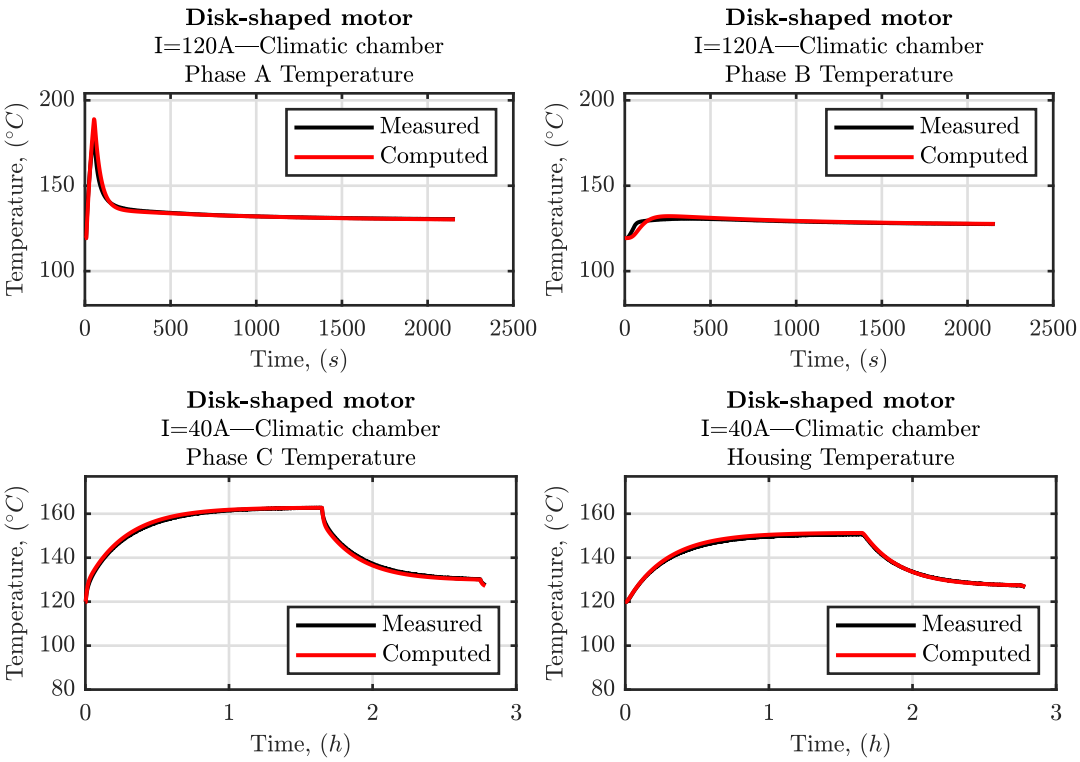

Fig. C.4 Simplified phase-split LPTN results for the disk-shaped motor in the climatic chamber for the tests used in the optimization.

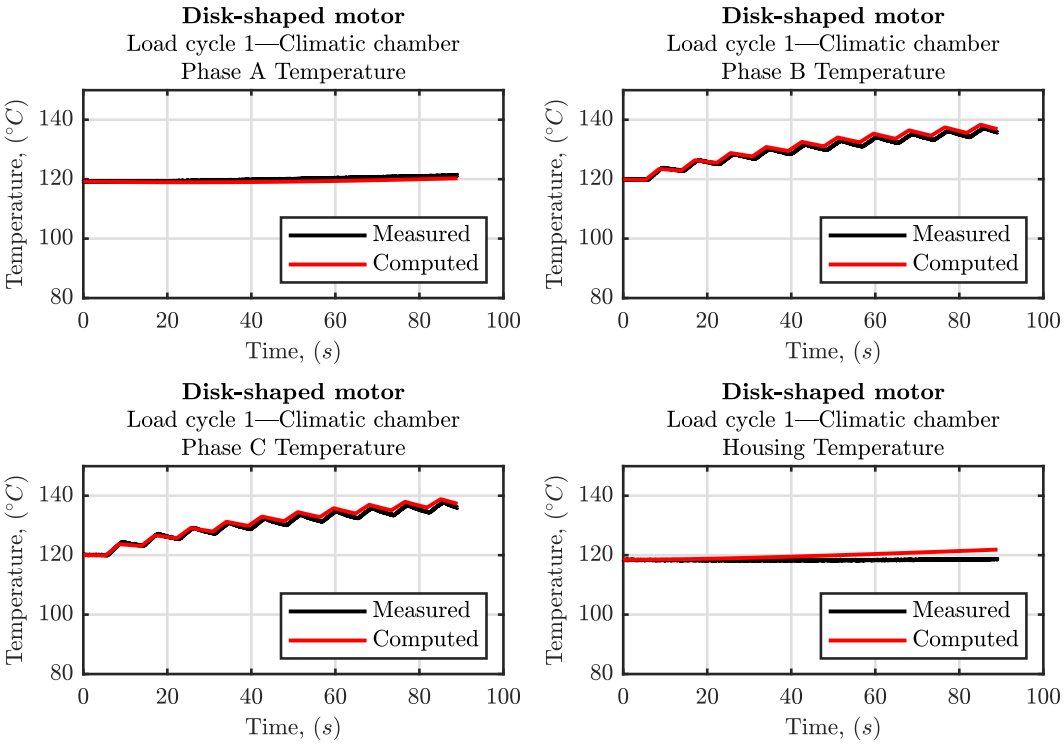

Fig. C.5 Simplified phase-split LPTN results for the disk-shaped motor in the climatic chamber for the load cycle 1.

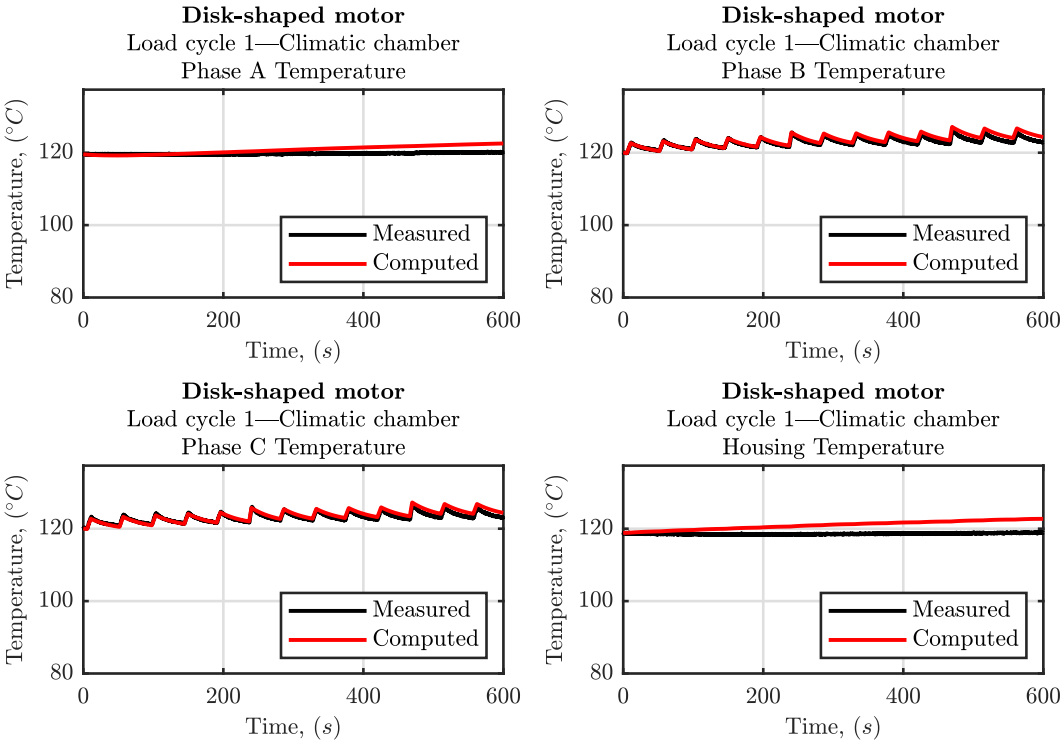

Fig. C.6 Simplified phase-split LPTN results for the disk-shaped motor in the climatic chamber for the load cycle 2.